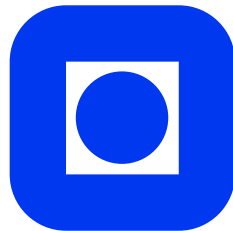# Modelling and Control of Fluid Flows
and Marine Structures

A thesis submitted in partial fulfillment of the requirements for the degree of
Doktor Ingeniør

by

Ole Morten Aamo

Summary

The contributions of this thesis fall naturally into two main categories: Part I: Feedback control of fluid flows, and; Part II: Modelling and control of marine structures.

Main Contributions of Part I

Part I presents new results on stabilization (for the purpose of drag reduction or vortex shedding suppression) and destabilization (for the purpose of mixing) of channel, pipe and cylinder flows. In order to provide a stand-alone reference on this topic, the thesis also contains a comprehensive review of the research carried out in this field over the last decade or so, along with introductory chapters on fluid mechanics and control theory. The review also serves the purpose of placing the contributions by the author into the wider context of the field. The contributions by the author are the following:

Section 4.3.1: A new boundary feedback control law for stabilization of the parabolic equilibrium flow in 2D channel flow is derived using Lyapunov stability theory. The controller uses pressure measurements taken on the channel wall, and applies actuation in the form of wall transpiration, that is, suction and blowing of fluid across the wall. Although the analysis is valid for small Reynolds numbers, only, simulations indicate that the control is very efficient in stabilizing the flow at Reynolds numbers several orders of magnitude higher. The pressure-based control law performed much better than other Lyapunov-based control laws studied.

Section 4.3.3: The simple pressure-based control law derived in Section 4.3.1 is generalized to the 3D pipe flow. As for the 2D channel flow, the analysis is valid for small Reynolds numbers, only.

Section 4.3.4: The pressure-based feedback control law derived in Section 4.3.1 for the 2D channel flow results in flow transients with instantaneous drag far lower than that of the corresponding laminar flow. In fact, for the first time, instantaneous total drag in a constant-mass-flow 2D channel flow is driven to *negative* levels. The physical mechanisms by which this phenomenon occur is explained, and the possibility of achieving sustained drag reductions to below the laminar level by initiating such low-drag transients on a periodic basis is explored. The results add to the evidence that the laminar flow represents a fundamental limit to the drag reduction achievable by wall transpiration.

Section 4.4: A state feedback controller that achieves global asymptotic stabilization of a nonlinear Ginzburg-Landau model of vortex shedding from bluff bodies is designed using backstepping. Stabilization is obtained in two steps. First, the upstream and downstream parts of the system are shown to exhibit the input-to-state stability property with respect to certain boundary input terms governed by the core flow in the vicinity of the bluff body. Second, a finite difference approximation of arbitrary order of the core flow is stabilized using the backstepping method. Consequently, all the states in the core flow are driven to zero, including the boundary input terms of the upstream and downstream subsystems. The control design is valid for any Reynolds number, and simulations demonstrate its performance.

Section 5.2: For the first time, active feedback control is used to enhance mixing by exploiting the natural tendency in the flow to mix. By applying the pressure-based feedback control law derived for stabilizing the 2D channel flow in Section 4.3.1, with the sign of the input reversed, enhanced instability of the parabolic equilibrium flow is obtained, which leads rapidly to highly complex flow patterns. The mixing enhancement is quantified using various diagnostic tools.

Section 5.3: A Lyapunov based boundary feedback controller for achieving mixing in a 3D pipe flow governed by the Navier-Stokes equation is designed. It is shown that the control law maximizes a measure of mixing that incorporates stretching and folding of material elements, while at the same time minimizing the control effort and the sensing effort. The penalty on sensing results in a static *output*-feedback control law (rather than full-state feedback). A lower bound on the gain from the control effort to the mixing measure is also derived. For the open-loop system, input/output-to-state stability properties are established, which show a form of detectability of mixing in the interior of the pipe from the chosen outputs on the wall. The effectiveness of the optimal control in achieving mixing enhancement is demonstrated in numerical simulations. Simulation results also show that the spatial changes in the control velocity are smooth and small, promising that a low number of actuators will suffice in practice.

Section 5.4: Motivated by the mixing results for channels and pipes in Sections 5.2 and 5.3, a simulation study that investigates the feasibility of enhancing particle dispersion in the wake of a circular cylinder is carried out. For a subcritical case, vortex shedding is successfully provoked using feedback.

Main Contributions of Part II

Part II deals with modelling and control of slender marine structures and marine vessels.

Chapter 8: A new finite element model for a cable suspended in water is developed. Global existence and uniqueness of solutions of the truncated system is shown for a slightly simplified equation describing the motion of a cable with negligible added mass and supported by fixed end-points. Based on this, along with well known results on local existence and uniqueness of solutions for symmetrizable hyperbolic systems, a global result for the initial-boundary value problem

is conjectured. The FEM model for the cable is assembled to give a model of a multi-cable mooring system, which, in turn, is coupled to a rigid body model of the floating vessel. The result is a coupled dynamical model of a moored vessel, which can be applied to applications such as turret-based moored ships, or tension leg platforms. As a simple application of the simulator, controlling the line tensions dynamically as an additional means of station keeping is explored.

Chapter 9: Output feedback tracking control laws for a class of Euler-Lagrange systems subject to nonlinear dissipative loads are designed. By imposing a monotone damping condition on the nonlinearities of the unmeasured states, the common restriction that the nonlinearities be globally Lipschitz is removed. The proposed observer-controller scheme renders the origin of the error dynamics uniformly globally asymptotically stable, in the general case. Under certain additional assumptions, the result continue to hold for a simplified control law that is less sensitive to noise and unmodeled phenomena.

Publications

The main results in this thesis have been accepted or submitted for publication in international journals, as well as presented or submitted to international conferences. The most important papers are:

- "Finite element modelling of moored vessels," *Mathematical and Computer Modelling of Dynamical Systems*, vol. 7, no. 1, 2001, with T.I. Fossen.

- "Global output tracking control of a class of Euler-Lagrange systems with monotonic nonlinearities in the velocities," *International Journal of Control*, vol. 74, no. 7, 2001, with M. Arcak, T.I. Fossen, and P.V. Kokotović.

- "Control of mixing by boundary feedback in 2d channel flow," submitted to *Automatica*, with M. Krstić and T.R. Bewley.

- "On the search for fundamental performance limitations in fluid-mechanical systems," Proceedings of the 2002 ASME Fluids Engineering Division Summer Meeting, Montreal, Quebec, Canada, with T.R. Bewley.

- "Optimal mixing enhancement in 3d pipe flow," submitted to *IEEE Transactions on Control Systems Technology*, with A. Balogh and M. Krstić.

- "Global stabilization of a nonlinear Ginzburg-Landau model of vortex shedding," submitted to the *European Journal of Control*, with M. Krstić.

Acknowledgements

Contents

Part I

Feedback Control of Fluid Flows

Chapter 1

Introduction

1.1 Why Flow Control?

Flow control involves controlling a flow field using passive or active devices in order to bring on desired changes in the behavior of the flow. For instance, *laminar* flow, which is characterized by parallel layers of fluid moving in a very regular and deterministic way, is associated with considerable less drag, or friction, at wall-fluid interfaces, than its counterpart, *turbulent* flow, which is characterized by small scale velocity components that appear to be stochastic in nature. On the other hand, turbulent flow may exhibit better mixing properties than laminar flows. Usually, laminar flows are unstable, and will unless controlled, evolve into turbulent flows. Common control objectives include [47]:

- Delaying or advancing transition from laminar to turbulent flow;

- Suppressing or enhancing turbulence, and;

- Preventing or provoking separation.

The benefits that can be gained from these control objectives include drag reduction, lift enhancement, mixing enhancement, and flow-induced noise suppression. For example, a turbulent pipe flow induces considerable drag, or friction, at the bounding wall. It is the resulting overall drag force that the compressor has to overcome in order to pump fluid through the pipe. Increasing the throughput can be achieved by simply installing a more powerful compressor, but the result would be increased energy consumption. Since laminar flow induces much less drag, designing a flow control system that relaminarizes the flow will permit higher throughput without increasing energy consumption.

In flows past bluff bodies, the phenomenon of vortex shedding occurs. For flow past a 2D circular cylinder, which is a prototype model flow for studying vortex shedding, vortices are alternatively shed from the upper and lower sides of the

cylinder, subjecting the cylinder to periodic forcing. In practice the periodic forcing leads to structural vibrations, which are associated with penalties ranging from passenger discomfort to structural damage or failure from fatigue. Consequently, suppression of vortex shedding is of great importance in many engineering applications. By applying flow control, one may alter the behavior of the flow around the structure in such a manner that vortex shedding is suppressed or dampened.

Mixing processes are encountered frequently in applications, and the quality of the resulting mixture directly affects the quality of the end product. This is the case, for instance, in combustion, where the quality of the fuel-air mixture is essential for power generation, and in process industry, where the quality of various mixtures affect chemical reaction rates and the purity of end products. Mixing is usually obtained using "brute-force" techniques, such as mechanical stirring, jet injection and stirring valves. These methods, and all other methods for mixing, are associated with a drag penalty. The application of flow control to mixing problems seeks to minimize this penalty.

The feedback control laws designed for these problems are allowed to be distributed. That is, sensing and actuation may be applied at every point on the boundary of the flow domain. While this may sound unrealistic, the micromachining technology that emerged in the 1980s, permits rapid sensing and actuation on the micron scale, and thereby enables real-time distributed control of fluid flows.

It is clear from the examples mentioned above that the main objective in flow control is to lower operational expenses. We conclude this motivational section with a quote from [47]: "The potential benefits of realizing efficient flow-control systems range from saving billions of dollars in annual fuel costs for land, air, and sea vehicles to achieving economically and environmentally more competitive industrial processes involving fluid flows."

1.2   Scope of this Report

The concept of flow control contains a wide variety of theoretical and technological branches, as the previous section suggests. In this report the treatment is limited to recent developments in two problem areas that have attracted much attention. The first is *stabilization* of a selection of popular prototype flows, namely the channel flow (2D or 3D), the pipe flow, and the cylinder flow (2D). The channel flow is the flow contained between two parallel plates, the pipe flow is the flow contained in the interior of a cylinder with circular cross section, and the cylinder flow is the flow past a cylinder with circular cross section. The second problem we will study, is *mixing* in flows. In the next two sections, recent efforts in these areas are reviewed briefly. Then, selected works are treated in detail in Chapters 4 and 5. First, though, the equations of fluid mechanics are reviewed in Chapter 2, and some control theoretic results are reviewed in Chapter 3. Following the core chapters on stabilization and mixing, a review of the state-of-the-art in sensing and actuation for fluid mechanical systems is presented in Chapter 6. The report ends with some concluding remarks in Chapter 7.

1.2.1 Stabilization

Incompressible fluid flow in a plane channel has been studied quite extensively, and the wall sensing/actuation of this flow has become a standard benchmark problem in the area of flow control, see, e.g., [21] and [46] for recent reviews. In [70] stabilizing PI controllers for two-dimensional channel flow were designed for a reduced-order model of the linearized Navier-Stokes equation, obtained by a standard Galerkin procedure. The work was continued in [71], where LQG design was applied in order to obtain optimal controllers for this reduced-order model. LQG/LTR of the streamfunction formulation of the Navier-Stokes equation was also the focus of [37] and [36], where the latter reference reports the remarkable result of drag reduction to 50% below the laminar level. In [73], a reduced-order model of 3D perturbations (at a single wavenumber pair $\{k_x, k_z\}$) was developed, and LQG control design was applied to this model. Drag reduction by means of body forcing inside the domain applied through electromagnetic forcing was suggested in [13], where an observer-based approach was applied to a reduced order, linearized model. A nonlinear attempt was presented in [33], where Galerkin's method was used to derive a reduced-order model of the full, nonlinear, two-dimensional Navier-Stokes equation. A nonlinear control law was given, along with conditions under which closed-loop stability is obtained. The results were applied to Burger's equation, which is the one-dimensional Navier-Stokes equation, including the nonlinear advective term. In [20], LQG and $\mathcal{H}_\infty$ control theories were applied to the linearized three-dimensional channel flow. A major finding of this paper was that properly-applied controls significantly reduce the nonorthogonality leading to energy amplification mechanisms in such systems. The three-dimensional nonlinear problem was tackled by the application of optimal control theory in a finite-horizon predictive setting (Model Predictive Control) in [23], resulting in relaminarization of $Re = 1700$ turbulent channel flow. Optimal controllers are generally not decentralized, but recent results on the structure of controllers for spatially-invariant systems indicate that one can obtain *localized* controllers arbitrarily close to optimal [17]. This result has been confirmed for plane channel flow in [64], where the Fourier-space control problem formulated in [20] was modified and successfully inverse-transformed to the physical domain, resulting in well-resolved, spatially-localized convolution kernels with exponential decay far from the origin. Such spatial localization is an important ingredient both in relaxing the nonphysical assumption of spatial periodicity in the controller formulation and in facilitating decentralized control in massive arrays of sensors and actuators (see discussion in [21]). The mathematical details of controllability and optimal control theory applied to the Navier-Stokes equation, such as existence and uniqueness of solutions, and proofs of convergence of proposed numerical algorithms, are discussed in [7, 18, 19, 24, 34, 35, 40, 41, 43, 51, 52, 61, 65, 66, 82, 109, 110].

Global stabilization by boundary control of Burgers' equation was achieved in [81]. For the 2D channel flow governed by the Navier-Stokes equation, globally stabilizing boundary control laws were presented in [15], where wall-tangential actuation was used, and in [1], where wall-normal actuation was used. These control laws were fully decentralized, and numerical simulations showed their ability to stabilize flows at large Reynolds numbers, although the mathematical analysis was valid

for small Reynolds numbers, only. As noted in [15] and [21], fully decentralized controllers have an implementational advantage in that they can be embedded into MEMS (Micro-Electro-Mechanical-Systems) hardware, minimizing the communication requirements of centralized computations and facilitating scaling to massive arrays of sensors and actuators. Using the wall-tangential control law, Balogh (private communication) was able to relaminarize a simulated turbulent 3D channel flow at $Re = 4000$.

The flow past a 2D circular cylinder has been a popular model flow for studying vortex suppression by means of open-loop or feedback control. For Reynolds numbers slightly larger than the critical value for onset of vortex shedding (which is approximately $Re_c = 47$), several authors have successfully suppressed vortex shedding in numerical simulations using various simple feedback control configurations. In [99], a pair of suction/blowing slots positioned on the cylinder wall were used for actuation, and shedding was suppressed for $Re = 60$, using proportional feedback from a single velocity measurement taken some distance downstream of the cylinder. For $Re = 80$, vortex shedding was reduced, but not completely suppressed. In [53], the same actuation configuration was tried using feedback from a pair of pressure sensors located on the cylinder wall for $Re = 60$. This attempt was unsuccessful, but by adding a third actuation slot, shedding was reduced considerably, even at $Re = 80$. Although some success in controlling vortex shedding has been achieved in numerical simulations, rigorous control designs are scarce due to the complexity of designing controllers based on the Navier-Stokes equation. A much simpler model, the Ginzburg-Landau equation with appropriate coefficients, has been found to model well the dynamics of vortex shedding near the critical value of the Reynolds number [63]. In [103], it was shown numerically that the Ginzburg-Landau model for Reynolds numbers close to Re_c can be stabilized using proportional feedback from a single measurement downstream of the cylinder, to local forcing at the location of the cylinder. In [83], using the model from [103], stabilization was obtained in numerical simulations for $Re = 100$, with an LQG controller designed for the linearized Ginzburg-Landau equation. In [4], a controller that globally stabilized the equilibrium at zero of a finite difference discretization of any order of the nonlinear Ginzburg-Landau model presented in [103] was designed using backstepping. The design was valid for any Reynolds number.

1.2.2   Mixing

In many engineering applications, the mixing of two or more fluids is essential to obtaining good performance in some downstream process (a prime example is the mixing of air and fuel in combustion engines [48, 10]). As a consequence, mixing has been the focus of much research, but without reaching a unified theory, either for the generation of flows that mix well due to external forcing, or for the quantification of mixing in such flows. A thorough review is given in [96]. Approaches range from experimental design and testing to modern applications of dynamical systems theory. The latter was initiated by Aref [11], who studied chaotic advection in the setting of an incompressible, inviscid fluid contained in

a (2D) circular domain, and agitated by a point vortex. This flow is commonly called the blinking vortex flow. Ottino and coworkers studied a number of various flows, examining mixing properties based on dynamical systems techniques [32, 75, 85, 111]. Later Rom-Kedar et al. [102] applied Melnikov's method and KAM (Kolmogorov-Arnold-Moser) theory to quantify transport in a flow governed by an oscillating vortex pair. For general treatments of dynamical systems theory and transport in dynamical systems, see [50, 116, 117]. An obvious shortcoming of this theory is the requirement that the flow must be periodic, as such methods rely on the existence of a Poincaré map for which some periodic orbit of the flow induces a hyperbolic fixed point. Another shortcoming is that they can only handle small perturbations from integrability, whereas effective mixing usually occurs for large perturbations [97]. A third shortcoming is that traditional dynamical systems theory is concerned with asymptotic, or long-time, behavior, rather than quantifying rate processes which are of interest in mixing applications. In order to overcome some of these shortcomings, recent advances in dynamical systems theory have focused on finding coherent structures and invariant manifolds in experimental datasets, which are finite in time and generally aperiodic. This has led to the notions of finite-time hyperbolic trajectories with corresponding finite-time stable and unstable manifolds [55, 56, 57, 58]. The results include estimates for the transport of initial conditions across the boundaries of coherent structures. In [101] these concepts were applied to a time-dependent velocity field generated by a double-gyre ocean model, in order to study the fluid transport between dynamic eddies and a jet stream. An application to meandering jets was described in [93]. Another method for identifying regions in a flow that have similar finite-time statistical properties based on ergodic theory was developed and applied in [90, 88, 91]. The relationship between the two methods mentioned, focusing on geometrical and statistical properties of particle motion, respectively, was examined in [100].

As these developments have partly been motivated by applications in geophysical flows, they are diagnostic in nature and lend little help to the problem of *generating* a fluid flow that mixes well. The problem of generating effective mixing in a fluid flow is usually approached by trial and error using various "brute force" open-loop controls, such as mechanical stirring, jet injection or mixing valves. However, in the recent papers [38, 39], control systems theory was used to rigorously derive the mixing protocol that maximizes entropy among all the possible periodic sequences composed of two shear flows orthogonal to each other. In [94], the optimal vortex trajectory in the flow induced by a single vortex in a corner subject to a controlled external strain field was found using tools from dynamical systems theory. The resulting trajectory was stabilized using control theory.

In [1], feedback control was applied in order to enhance existing instability mechanisms in a 2D model of plane channel flow. By applying boundary control intelligently in a feedback loop, mixing was considerably enhanced with relatively small control effort. The control law was decentralized and designed using Lyapunov stability analysis. These efforts have recently been extended successfully to 3D pipe flow [16], where certain optimality properties were shown as well. Motivated by these results [1, 16], a simulation study was carried out in [6], aiming at en-

hancing particle dispersion in the wake of a 2D cylinder. For the subcritical case of $Re = 45$, vortex shedding was successfully initiated using feedback control.

Chapter 2

Governing Equations

This introductory chapter on fluid mechanics is based on [27].

2.1 Kinematics

We will be studying the behavior of a fluid contained in the domain Ω, as shown schematically in Figure 2.1. Associated with the fluid is its density, $\rho : \Omega \times \mathbb{R}_+ \to \mathbb{R}$. At every time instant $t > 0$, and to every point $p \in \Omega$, we assign a vector valued quantity which is the velocity, $\mathbf{W}$, of the fluid at that point in time and space. That is, we are interested in the evolution of a vector field $\mathbf{W} : \Omega \times \mathbb{R}_+ \to \mathbb{R}^n$, where n is the *dimension* of the problem. Associated with the velocity field is a pressure field, which is a scalar valued function $P : \Omega \times \mathbb{R}_+ \to \mathbb{R}$. We will study problems in 2 and 3 dimensions (2D and 3D), using cartesian and cylindrical coordinates. In cartesian coordinates, we denote a point $p \in \Omega$ with (x, y) in 2D and (x, y, z) in 3D. In cylindrical coordinates, we denote a point $p \in \Omega$ with (r, θ, z). The two coordinate systems are shown schematically in Figure 2.1. The velocity field is denoted $\mathbf{W}(x, y, z, t) = (U(x, y, z, t), V(x, y, z, t), W(x, y, z, t))$ in 3D cartesian coordinates, where U, V and W are the velocity components in the x, y and z directions, respectively ($\mathbf{W}(x, y, t) = (U(x, y, t), V(x, y, t))$ in 2D). In cylindrical coordinates, we denote the velocity field $\mathbf{W}(r, \theta, z, t) = (V_r(x, y, z, t), V_\theta(x, y, z, t), V_z(x, y, z, t))$, where V_r, V_θ, and V_z are the velocity components in the r, θ and z directions, respectively. The density, ρ, and the pressure, P, take the same arguments as the velocity, but are scalar valued. Below we will derive the conservation equations in cartesian coordinates, and state the corresponding equations in cylindrical coordinates.

2.2 Conservation of Mass

Consider the stationary volume element in Figure 2.2. Writing a mass balance
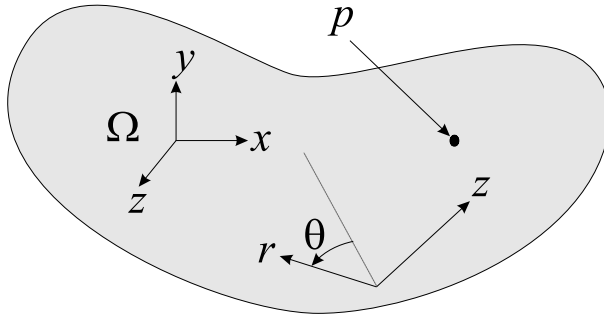
Figure 2.1: The domain in which the fluid is contained is denoted Ω. Two coordinate systems will be used in this report: cartesian coordinates, denoted (x, y, z), and cylindrical coordinates, denoted (r, θ, z).
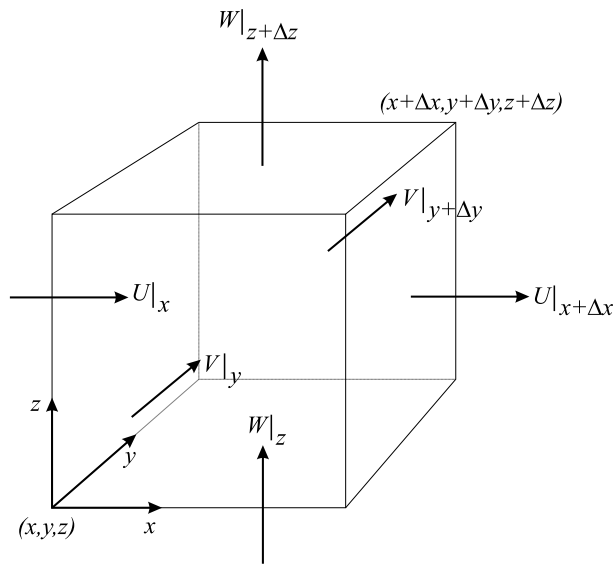
Figure 2.2: Control volume for derivation of the governing equations.

over the volume, we have

rate of mass accumulation = rate of mass in − rate of mass out

where

$$
\begin{aligned}
\text{rate of mass in} &= \left. (\rho U) \right|_x \Delta y \Delta z + \left. (\rho V) \right|_y \Delta x \Delta z + \left. (\rho W) \right|_z \Delta x \Delta y \\
\text{rate of mass out} &= \left. (\rho U) \right|_{x+\Delta x} \Delta y \Delta z + \left. (\rho V) \right|_{y+\Delta y} \Delta x \Delta z + \left. (\rho W) \right|_{z+\Delta z} \Delta y \Delta z.
\end{aligned}
$$

Thus, we get

$$
\begin{aligned}
\frac{\partial \rho}{\partial t} \Delta x \Delta y \Delta z = & -\left(\left. (\rho U) \right|_{x+\Delta x} - \left. (\rho U) \right|_x \right) \Delta y \Delta z \\
& - \left(\left. (\rho V) \right|_{y+\Delta y} - \left. (\rho V) \right|_y \right) \Delta x \Delta z - \left(\left. (\rho W) \right|_{z+\Delta z} - \left. (\rho W) \right|_z \right) \Delta y \Delta z.
\end{aligned}
$$

Dividing by the volume and letting Δx, Δy, and Δz approach zero, we get

$$
\frac{\partial \rho}{\partial t} = -\frac{\partial (\rho U)}{\partial x} - \frac{\partial (\rho V)}{\partial y} - \frac{\partial (\rho W)}{\partial z}.
$$

We will be dealing exclusively with incompressible fluids, for which ρ is constant. Consequently,

$$
\frac{\partial U}{\partial x} + \frac{\partial V}{\partial y} + \frac{\partial W}{\partial z} = 0. \tag{2.1}
$$

Equation (2.1) is referred to as the *equation of continuity*.

2.3 Conservation of Momentum

Again consider the stationary volume element in Figure 2.2. Writing a momentum balance over the volume, we have

rate of momentum accumulation =

rate of momentum in − rate of momentum out

+ sum of forces acting on system.

So for the momentum in the x-direction, we have

rate of momentum in =

$$
\left. \left(\rho U^2 \right) \right|_x \Delta y \Delta z + \left. (\rho U V) \right|_y \Delta x \Delta z + \left. (\rho U W) \right|_z \Delta x \Delta y
$$

rate of momentum out =

$$
\left. \left(\rho U^2 \right) \right|_{x+\Delta x} \Delta y \Delta z + \left. (\rho U V) \right|_{y+\Delta y} \Delta x \Delta z + \left. (\rho U W) \right|_{z+\Delta z} \Delta x \Delta y
$$

sum of forces acting on system =

$$\left(\tau_{xx}|_x - \tau_{xx}|_{x+\Delta x} \right) \Delta y \Delta z + \left(\tau_{yx}|_y - \tau_{yx}|_{y+\Delta y} \right) \Delta x \Delta z$$
$$+ \left(\tau_{zx}|_z \Delta x \Delta y - \tau_{zx}|_{z+\Delta z} \right) \Delta x \Delta y + \left(P|_x - P|_{x+\Delta x} \right) \Delta y \Delta z$$

where τ_{ij} denotes the viscous force (per unit area) acting in the direction of j on a face normal to the i-direction, and P is the pressure (i.e. the pressure force per unit area). We get

$$\frac{\partial (\rho U)}{\partial t} \Delta x \Delta y \Delta z = - \left((\rho U^2)|_{x+\Delta x} - (\rho U^2)|_x \right) \Delta y \Delta z$$
$$- \left((\rho U V)|_{y+\Delta y} - (\rho U V)|_y \right) \Delta x \Delta z - \left((\rho U W)|_{z+\Delta z} - (\rho U W)|_z \right) \Delta x \Delta y$$
$$- \left(\tau_{xx}|_{x+\Delta x} - \tau_{xx}|_x \right) \Delta y \Delta z - \left(\tau_{yx}|_{y+\Delta y} - \tau_{yx}|_y \right) \Delta x \Delta z$$
$$- \left(\tau_{zx}|_{z+\Delta z} - \tau_{zx}|_z \right) \Delta x \Delta y - \left(P|_{x+\Delta x} - P|_x \right) \Delta y \Delta z.$$

Dividing by the volume and letting Δx, Δy, and Δz approach zero, we get

$$\frac{\partial (\rho U)}{\partial t} + \frac{\partial (\rho U^2)}{\partial x} + \frac{\partial (\rho U V)}{\partial y} + \frac{\partial (\rho U W)}{\partial z} = - \frac{\partial P}{\partial x} - \frac{\partial \tau_{xx}}{\partial x} - \frac{\partial \tau_{yx}}{\partial y} - \frac{\partial \tau_{zx}}{\partial z}.$$

For constant density ρ, we get

$$\rho \frac{\partial U}{\partial t} + \rho \left(U \frac{\partial U}{\partial x} + V \frac{\partial U}{\partial y} + W \frac{\partial U}{\partial z} \right) + \rho U \left(\frac{\partial U}{\partial x} + \frac{\partial V}{\partial y} + \frac{\partial W}{\partial z} \right) =$$
$$- \frac{\partial P}{\partial x} - \frac{\partial \tau_{xx}}{\partial x} - \frac{\partial \tau_{yx}}{\partial y} - \frac{\partial \tau_{zx}}{\partial z}$$

and using (2.1) yields

$$\rho \frac{\partial U}{\partial t} + \rho \left(U \frac{\partial U}{\partial x} + V \frac{\partial U}{\partial y} + W \frac{\partial U}{\partial z} \right) = - \frac{\partial P}{\partial x} - \frac{\partial \tau_{xx}}{\partial x} - \frac{\partial \tau_{yx}}{\partial y} - \frac{\partial \tau_{zx}}{\partial z}.$$

Similar derivations for the momentum in the y and z directions yield the complete set of equations

$$\rho \frac{\partial U}{\partial t} + \rho \left(U \frac{\partial U}{\partial x} + V \frac{\partial U}{\partial y} + W \frac{\partial U}{\partial z} \right) = - \frac{\partial P}{\partial x} - \frac{\partial \tau_{xx}}{\partial x} - \frac{\partial \tau_{yx}}{\partial y} - \frac{\partial \tau_{zx}}{\partial z} \qquad (2.2)$$

$$\rho \frac{\partial V}{\partial t} + \rho \left(U \frac{\partial V}{\partial x} + V \frac{\partial V}{\partial y} + W \frac{\partial V}{\partial z} \right) = - \frac{\partial P}{\partial y} - \frac{\partial \tau_{xy}}{\partial x} - \frac{\partial \tau_{yy}}{\partial y} - \frac{\partial \tau_{zy}}{\partial z} \qquad (2.3)$$

$$\rho \frac{\partial W}{\partial t} + \rho \left(U \frac{\partial W}{\partial x} + V \frac{\partial W}{\partial y} + W \frac{\partial W}{\partial z} \right) = - \frac{\partial P}{\partial z} - \frac{\partial \tau_{xz}}{\partial x} - \frac{\partial \tau_{yz}}{\partial y} - \frac{\partial \tau_{zz}}{\partial z}. \qquad (2.4)$$

It remains to insert a constitutive equation relating the viscous forces τ_{ij} to the fluid motion $\mathbf{W} = (U, V, W)$. We will exclusively consider Newtonian fluids, which in conjunction with incompressibility yield the following relations [27]

$$\tau_{xx} = -2\mu\frac{\partial U}{\partial x}, \ \tau_{yy} = -2\mu\frac{\partial V}{\partial y}, \ \tau_{zz} = -2\mu\frac{\partial W}{\partial z} \tag{2.5}$$

$$\tau_{xy} = \tau_{yx} = -\mu\left(\frac{\partial U}{\partial y} + \frac{\partial V}{\partial x}\right) \tag{2.6}$$

$$\tau_{yz} = \tau_{zy} = -\mu\left(\frac{\partial V}{\partial z} + \frac{\partial W}{\partial y}\right) \tag{2.7}$$

$$\tau_{zx} = \tau_{xz} = -\mu\left(\frac{\partial W}{\partial x} + \frac{\partial U}{\partial z}\right) \tag{2.8}$$

where the coefficient μ is called the viscosity of the fluid. Inserting (2.5)–(2.8) into (2.2)–(2.4) yields

$$\rho\frac{\partial U}{\partial t} + \rho\left(U\frac{\partial U}{\partial x} + V\frac{\partial U}{\partial y} + W\frac{\partial U}{\partial z}\right) =$$
$$-\frac{\partial P}{\partial x} + \mu\left(\frac{\partial^2 U}{\partial x^2} + \frac{\partial^2 U}{\partial y^2} + \frac{\partial^2 U}{\partial z^2}\right) + \mu\frac{\partial}{\partial x}\left(\frac{\partial U}{\partial x} + \frac{\partial V}{\partial y} + \frac{\partial W}{\partial z}\right)$$

$$\rho\frac{\partial V}{\partial t} + \rho\left(U\frac{\partial V}{\partial x} + V\frac{\partial V}{\partial y} + W\frac{\partial V}{\partial z}\right) =$$
$$-\frac{\partial P}{\partial y} + \mu\left(\frac{\partial^2 V}{\partial x^2} + \frac{\partial^2 V}{\partial y^2} + \frac{\partial^2 V}{\partial z^2}\right) + \mu\frac{\partial}{\partial y}\left(\frac{\partial U}{\partial x} + \frac{\partial V}{\partial y} + \frac{\partial W}{\partial z}\right)$$

$$\rho\frac{\partial W}{\partial t} + \rho\left(U\frac{\partial W}{\partial x} + V\frac{\partial W}{\partial y} + W\frac{\partial W}{\partial z}\right) =$$
$$-\frac{\partial P}{\partial z} + \mu\left(\frac{\partial^2 W}{\partial x^2} + \frac{\partial^2 W}{\partial y^2} + \frac{\partial^2 W}{\partial z^2}\right) + \mu\frac{\partial}{\partial z}\left(\frac{\partial U}{\partial x} + \frac{\partial V}{\partial y} + \frac{\partial W}{\partial z}\right)$$

and using (2.1) we finally get

$$\rho\left(\frac{\partial U}{\partial t} + U\frac{\partial U}{\partial x} + V\frac{\partial U}{\partial y} + W\frac{\partial U}{\partial z}\right) =$$
$$-\frac{\partial P}{\partial x} + \mu\left(\frac{\partial^2 U}{\partial x^2} + \frac{\partial^2 U}{\partial y^2} + \frac{\partial^2 U}{\partial z^2}\right) \tag{2.9}$$

$$\rho\left(\frac{\partial V}{\partial t} + U\frac{\partial V}{\partial x} + V\frac{\partial V}{\partial y} + W\frac{\partial V}{\partial z}\right) =$$
$$-\frac{\partial p}{\partial y} + \mu\left(\frac{\partial^2 V}{\partial x^2} + \frac{\partial^2 V}{\partial y^2} + \frac{\partial^2 V}{\partial z^2}\right) \tag{2.10}$$

$$\rho \left(\frac{\partial W}{\partial t} + U \frac{\partial W}{\partial x} + V \frac{\partial W}{\partial y} + W \frac{\partial W}{\partial z} \right) =$$

$$- \frac{\partial P}{\partial z} + \mu \left(\frac{\partial^2 W}{\partial x^2} + \frac{\partial^2 W}{\partial y^2} + \frac{\partial^2 W}{\partial z^2} \right). \quad (2.11)$$

Equation (2.9)–(2.11) is the celebrated *Navier-Stokes equation*. In vector form, equations (2.1) and (2.9)–(2.11) can be written compactly as

$$\boxed{div\,(\mathbf{W}) = 0}$$

$$\boxed{\frac{\partial \mathbf{W}}{\partial t} + (\mathbf{W} \cdot \nabla)\,\mathbf{W} = -\frac{1}{\rho} \nabla P + \frac{\mu}{\rho} \Delta \mathbf{W}}$$

where ∇ denotes the gradient operator, Δ denotes the Laplace operator, and *div* is short for divergence.

2.4 The Dimensionless Navier-Stokes Equation

2.4.1 Cartesian Coordinates

Given a flow geometry, the Navier-Stokes equation can be written in dimensionless form by introducing a characteristic length and a characteristic velocity. Denoting the characteristic length $\breve{D}$, and the characteristic velocity $\breve{V}$, we can perform a change of variables in such a way that the new variables are dimensionless

$$\begin{aligned}
(U^*, V^*, W^*) &= \left(\frac{U}{\breve{V}}, \frac{V}{\breve{V}}, \frac{W}{\breve{V}} \right),\ P^* = \frac{P}{\rho \breve{V}^2},\ t^* = \frac{\breve{V}}{\breve{D}} t \\
x^* &= \frac{x}{\breve{D}},\ y^* = \frac{y}{\breve{D}},\ z^* = \frac{z}{\breve{D}}.
\end{aligned}$$

So we get

$$\begin{aligned}
\frac{\partial U}{\partial t} &= \breve{V} \frac{\partial U^*}{\partial t^*} \frac{\partial t^*}{\partial t} = \frac{\breve{V}^2}{\breve{D}} \frac{\partial U^*}{\partial t^*} \\
\frac{\partial U}{\partial x} &= \breve{V} \frac{\partial U^*}{\partial x^*} \frac{\partial x^*}{\partial x} = \frac{\breve{V}}{\breve{D}} \frac{\partial U^*}{\partial x^*} \\
\frac{\partial P}{\partial x} &= \rho \breve{V}^2 \frac{\partial P^*}{\partial x^*} \frac{\partial x^*}{\partial x} = \frac{\rho \breve{V}^2}{\breve{D}} \frac{\partial P^*}{\partial x^*} \\
\frac{\partial^2 U}{\partial x^2} &= \frac{\partial}{\partial x^*} \left(\frac{\breve{V}}{\breve{D}} \frac{\partial U^*}{\partial x^*} \right) \frac{\partial x^*}{\partial x} = \frac{\breve{V}}{\breve{D}^2} \frac{\partial^2 U^*}{\partial x^{*2}}
\end{aligned}$$

and similarly for the other derivatives occurring in (2.1) and (2.9)–(2.11). Inserting these relations into (2.1) and (2.9)–(2.11) yields

$$\frac{\partial U}{\partial x} + \frac{\partial V}{\partial y} + \frac{\partial W}{\partial z} = 0 \qquad (2.12)$$

$$\frac{\partial U}{\partial t} + U\frac{\partial U}{\partial x} + V\frac{\partial U}{\partial y} + W\frac{\partial U}{\partial z} =$$
$$-\frac{\partial P}{\partial x} + \frac{1}{Re}\left(\frac{\partial^2 U}{\partial x^2} + \frac{\partial^2 U}{\partial y^2} + \frac{\partial^2 U}{\partial z^2}\right) \qquad (2.13)$$

$$\frac{\partial V}{\partial t} + U\frac{\partial V}{\partial x} + V\frac{\partial V}{\partial y} + W\frac{\partial V}{\partial z} =$$
$$-\frac{\partial P}{\partial y} + \frac{1}{Re}\left(\frac{\partial^2 V}{\partial x^2} + \frac{\partial^2 V}{\partial y^2} + \frac{\partial^2 V}{\partial z^2}\right) \qquad (2.14)$$

$$\frac{\partial W}{\partial t} + U\frac{\partial W}{\partial x} + V\frac{\partial W}{\partial y} + W\frac{\partial W}{\partial z} =$$
$$-\frac{\partial P}{\partial z} + \frac{1}{Re}\left(\frac{\partial^2 W}{\partial x^2} + \frac{\partial^2 W}{\partial y^2} + \frac{\partial^2 W}{\partial z^2}\right) \qquad (2.15)$$

where we have defined $Re = \rho\breve{D}\breve{V}/\mu$, and skipped the superscript * for notational convenience. Re is called the Reynolds number, and is the only parameter in equations (2.13)–(2.15). In vector notation, equations (2.12) and (2.13)–(2.15) become

$$\boxed{div\,(\mathbf{W}) = 0}$$

$$\boxed{\frac{\partial \mathbf{W}}{\partial t} + (\mathbf{W}\cdot\nabla)\,\mathbf{W} = -\nabla P + \frac{1}{Re}\Delta\mathbf{W}}.$$

2.4.2   Cylindrical Coordinates

In cylindrical coordinates, equations (2.12)–(2.15) become (see, for instance, [27]),

$$\frac{1}{r}\frac{\partial}{\partial r}\left(rV_r\right) + \frac{1}{r}\frac{\partial V_\theta}{\partial \theta} + \frac{\partial V_z}{\partial z} = 0 \qquad (2.16)$$

$$\frac{\partial V_r}{\partial t} + V_r\frac{\partial V_r}{\partial r} + \frac{V_\theta}{r}\frac{\partial V_r}{\partial \theta} - \frac{V_\theta^2}{r} + V_z\frac{\partial V_r}{\partial z} =$$
$$-\frac{\partial P}{\partial r} + \frac{1}{Re}\left(\frac{\partial}{\partial r}\left(\frac{1}{r}\frac{\partial}{\partial r}\left(rV_r\right)\right) + \frac{1}{r^2}\frac{\partial^2 V_r}{\partial \theta^2} - \frac{2}{r^2}\frac{\partial V_\theta}{\partial \theta} + \frac{\partial^2 V_r}{\partial z^2}\right) \qquad (2.17)$$

$$\frac{\partial V_\theta}{\partial t} + V_r \frac{\partial V_\theta}{\partial r} + \frac{V_\theta}{r} \frac{\partial V_\theta}{\partial \theta} + \frac{V_r V_\theta}{r} + V_z \frac{\partial V_\theta}{\partial z} =$$
$$- \frac{1}{r} \frac{\partial P}{\partial \theta} + \frac{1}{Re} \left(\frac{\partial}{\partial r} \left(\frac{1}{r} \frac{\partial}{\partial r} \left(r V_\theta \right) \right) + \frac{1}{r^2} \frac{\partial^2 V_\theta}{\partial \theta^2} + \frac{2}{r^2} \frac{\partial V_r}{\partial \theta} + \frac{\partial^2 V_\theta}{\partial z^2} \right) \quad (2.18)$$

$$\frac{\partial V_z}{\partial t} + V_r \frac{\partial V_z}{\partial r} + \frac{V_\theta}{r} \frac{\partial V_z}{\partial \theta} + V_z \frac{\partial V_z}{\partial z} =$$
$$- \frac{\partial P}{\partial z} + \frac{1}{Re} \left(\frac{1}{r} \frac{\partial}{\partial r} \left(r \frac{\partial V_z}{\partial r} \right) + \frac{1}{r^2} \frac{\partial^2 V_z}{\partial \theta^2} + \frac{\partial^2 V_z}{\partial z^2} \right). \quad (2.19)$$

2.5 Perturbations and the Linearized Navier-Stokes Equation

2.5.1 Cartesian Coordinates

Suppose $(\tilde{U}, \tilde{V}, \tilde{W}, \tilde{P})$ is a steady state solution of (2.12) and (2.13)–(2.15), that is

$$\left(\frac{\partial \tilde{U}}{\partial t}, \frac{\partial \tilde{V}}{\partial t}, \frac{\partial \tilde{W}}{\partial t}, \frac{\partial \tilde{P}}{\partial t} \right) = (0, 0, 0, 0) \quad (2.20)$$

and

$$\frac{\partial \tilde{U}}{\partial x} + \frac{\partial \tilde{V}}{\partial y} + \frac{\partial \tilde{W}}{\partial z} = 0 \quad (2.21)$$

$$\tilde{U} \frac{\partial \tilde{U}}{\partial x} + \tilde{V} \frac{\partial \tilde{U}}{\partial y} + \tilde{W} \frac{\partial \tilde{U}}{\partial z} = -\frac{\partial \tilde{P}}{\partial x} + \frac{1}{Re} \left(\frac{\partial^2 \tilde{U}}{\partial x^2} + \frac{\partial^2 \tilde{U}}{\partial y^2} + \frac{\partial^2 \tilde{U}}{\partial z^2} \right) \quad (2.22)$$

$$\tilde{U} \frac{\partial \tilde{V}}{\partial x} + \tilde{V} \frac{\partial \tilde{V}}{\partial y} + \tilde{W} \frac{\partial \tilde{V}}{\partial z} = -\frac{\partial \tilde{P}}{\partial y} + \frac{1}{Re} \left(\frac{\partial^2 \tilde{V}}{\partial x^2} + \frac{\partial^2 \tilde{V}}{\partial y^2} + \frac{\partial^2 \tilde{V}}{\partial z^2} \right) \quad (2.23)$$

$$\tilde{U} \frac{\partial \tilde{W}}{\partial x} + \tilde{V} \frac{\partial \tilde{W}}{\partial y} + \tilde{W} \frac{\partial \tilde{W}}{\partial z} = -\frac{\partial \tilde{P}}{\partial z} + \frac{1}{Re} \left(\frac{\partial^2 \tilde{W}}{\partial x^2} + \frac{\partial^2 \tilde{W}}{\partial y^2} + \frac{\partial^2 \tilde{W}}{\partial z^2} \right). \quad (2.24)$$

Defining the perturbations $\mathbf{w} = (u, v, w)$ and p as

$$u \triangleq U - \tilde{U}$$
$$v \triangleq V - \tilde{V}$$
$$w \triangleq W - \tilde{W}$$
$$p \triangleq P - \tilde{P}$$

and inserting into (2.12) and (2.13)–(2.15), yield

$$\frac{\partial u}{\partial x} + \frac{\partial v}{\partial y} + \frac{\partial w}{\partial z} + \frac{\partial \tilde{U}}{\partial x} + \frac{\partial \tilde{V}}{\partial y} + \frac{\partial \tilde{W}}{\partial z} = 0$$

$$\frac{\partial u}{\partial t} + \frac{\partial \tilde{U}}{\partial t} + u\frac{\partial u}{\partial x} + u\frac{\partial \tilde{U}}{\partial x} + \tilde{U}\frac{\partial u}{\partial x} + v\frac{\partial u}{\partial y} + v\frac{\partial \tilde{U}}{\partial y} + \tilde{V}\frac{\partial u}{\partial y}$$

$$+ w\frac{\partial u}{\partial z} + w\frac{\partial \tilde{U}}{\partial z} + \tilde{W}\frac{\partial u}{\partial z} + \tilde{U}\frac{\partial \tilde{U}}{\partial x} + \tilde{V}\frac{\partial \tilde{U}}{\partial y} + \tilde{W}\frac{\partial \tilde{U}}{\partial z} =$$

$$- \frac{\partial p}{\partial x} - \frac{\partial \tilde{P}}{\partial x} + \frac{1}{Re}\left(\frac{\partial^2 u}{\partial x^2} + \frac{\partial^2 u}{\partial y^2} + \frac{\partial^2 u}{\partial z^2} + \frac{\partial^2 \tilde{U}}{\partial x^2} + \frac{\partial^2 \tilde{U}}{\partial y^2} + \frac{\partial^2 \tilde{U}}{\partial z^2}\right)$$

$$\frac{\partial v}{\partial t} + \frac{\partial \tilde{V}}{\partial t} + u\frac{\partial v}{\partial x} + \tilde{U}\frac{\partial v}{\partial x} + \frac{\partial \tilde{V}}{\partial x}u + v\frac{\partial v}{\partial y} + v\frac{\partial \tilde{V}}{\partial y} + \tilde{V}\frac{\partial v}{\partial y}$$

$$+ w\frac{\partial v}{\partial z} + w\frac{\partial \tilde{V}}{\partial z} + \tilde{W}\frac{\partial v}{\partial z} + \tilde{U}\frac{\partial \tilde{V}}{\partial x} + \tilde{V}\frac{\partial \tilde{V}}{\partial y} + \tilde{W}\frac{\partial \tilde{V}}{\partial z} =$$

$$- \frac{\partial p}{\partial y} - \frac{\partial \tilde{P}}{\partial y} + \frac{1}{Re}\left(\frac{\partial^2 v}{\partial x^2} + \frac{\partial^2 v}{\partial y^2} + \frac{\partial^2 v}{\partial z^2} + \frac{\partial^2 \tilde{V}}{\partial x^2} + \frac{\partial^2 \tilde{V}}{\partial y^2} + \frac{\partial^2 \tilde{V}}{\partial z^2}\right)$$

$$\frac{\partial w}{\partial t} + \frac{\partial \tilde{W}}{\partial t} + u\frac{\partial w}{\partial x} + u\frac{\partial \tilde{W}}{\partial x} + \tilde{U}\frac{\partial w}{\partial x} + v\frac{\partial w}{\partial y} + v\frac{\partial \tilde{W}}{\partial y} + \tilde{V}\frac{\partial w}{\partial y}$$

$$+ w\frac{\partial w}{\partial z} + w\frac{\partial \tilde{W}}{\partial z} + \tilde{W}\frac{\partial w}{\partial z} + \tilde{U}\frac{\partial \tilde{W}}{\partial x} + \tilde{V}\frac{\partial \tilde{W}}{\partial y} + \tilde{W}\frac{\partial \tilde{W}}{\partial z} =$$

$$- \frac{\partial p}{\partial z} - \frac{\partial \tilde{P}}{\partial z} + \frac{1}{Re}\left(\frac{\partial^2 w}{\partial x^2} + \frac{\partial^2 w}{\partial y^2} + \frac{\partial^2 w}{\partial z^2} + \frac{\partial^2 \tilde{W}}{\partial x^2} + \frac{\partial^2 \tilde{W}}{\partial y^2} + \frac{\partial^2 \tilde{W}}{\partial z^2}\right).$$

In view of (2.20)–(2.24), we get the perturbation equations

$$\frac{\partial u}{\partial x} + \frac{\partial v}{\partial y} + \frac{\partial w}{\partial z} = 0 \tag{2.25}$$

$$\frac{\partial u}{\partial t} + u\frac{\partial u}{\partial x} + u\frac{\partial \tilde{U}}{\partial x} + \tilde{U}\frac{\partial u}{\partial x} + v\frac{\partial u}{\partial y} + v\frac{\partial \tilde{U}}{\partial y} + \tilde{V}\frac{\partial u}{\partial y} + w\frac{\partial u}{\partial z} + w\frac{\partial \tilde{U}}{\partial z} + \tilde{W}\frac{\partial u}{\partial z} =$$

$$- \frac{\partial p}{\partial x} + \frac{1}{Re}\left(\frac{\partial^2 u}{\partial x^2} + \frac{\partial^2 u}{\partial y^2} + \frac{\partial^2 u}{\partial z^2}\right) \tag{2.26}$$

$$\frac{\partial v}{\partial t} + u\frac{\partial v}{\partial x} + \tilde{U}\frac{\partial v}{\partial x} + \frac{\partial \tilde{V}}{\partial x}u + v\frac{\partial v}{\partial y} + v\frac{\partial \tilde{V}}{\partial y} + \tilde{V}\frac{\partial v}{\partial y} + w\frac{\partial v}{\partial z} + w\frac{\partial \tilde{V}}{\partial z} + \tilde{W}\frac{\partial v}{\partial z} =$$

$$- \frac{\partial p}{\partial y} + \frac{1}{Re}\left(\frac{\partial^2 v}{\partial x^2} + \frac{\partial^2 v}{\partial y^2} + \frac{\partial^2 v}{\partial z^2}\right) \tag{2.27}$$

$$\frac{\partial w}{\partial t} + u\frac{\partial w}{\partial x} + u\frac{\partial \tilde{W}}{\partial x} + \tilde{U}\frac{\partial w}{\partial x} + v\frac{\partial w}{\partial y} + v\frac{\partial \tilde{W}}{\partial y} + \tilde{V}\frac{\partial w}{\partial y} + w\frac{\partial w}{\partial z} + w\frac{\partial \tilde{W}}{\partial z} + \tilde{W}\frac{\partial w}{\partial z} =$$

$$- \frac{\partial p}{\partial z} + \frac{1}{Re}\left(\frac{\partial^2 w}{\partial x^2} + \frac{\partial^2 w}{\partial y^2} + \frac{\partial^2 w}{\partial z^2}\right). \tag{2.28}$$

The linearized equations are now obtained by omitting terms that are second order in the perturbations. Thus, we get

$$\frac{\partial u}{\partial x} + \frac{\partial v}{\partial y} + \frac{\partial w}{\partial z} = 0 \tag{2.29}$$

$$\frac{\partial u}{\partial t} + u\frac{\partial \tilde{U}}{\partial x} + \tilde{U}\frac{\partial u}{\partial x} + v\frac{\partial \tilde{U}}{\partial y} + \tilde{V}\frac{\partial u}{\partial y} + w\frac{\partial \tilde{U}}{\partial z} + \tilde{W}\frac{\partial u}{\partial z} =$$
$$-\frac{\partial p}{\partial x} + \frac{1}{Re}\left(\frac{\partial^2 u}{\partial x^2} + \frac{\partial^2 u}{\partial y^2} + \frac{\partial^2 u}{\partial z^2}\right) \tag{2.30}$$

$$\frac{\partial v}{\partial t} + \tilde{U}\frac{\partial v}{\partial x} + \frac{\partial \tilde{V}}{\partial x}u + v\frac{\partial \tilde{V}}{\partial y} + \tilde{V}\frac{\partial v}{\partial y} + w\frac{\partial \tilde{V}}{\partial z} + \tilde{W}\frac{\partial v}{\partial z} =$$
$$-\frac{\partial p}{\partial y} + \frac{1}{Re}\left(\frac{\partial^2 v}{\partial x^2} + \frac{\partial^2 v}{\partial y^2} + \frac{\partial^2 v}{\partial z^2}\right) \tag{2.31}$$

$$\frac{\partial w}{\partial t} + u\frac{\partial \tilde{W}}{\partial x} + \tilde{U}\frac{\partial w}{\partial x} + v\frac{\partial \tilde{W}}{\partial y} + \tilde{V}\frac{\partial w}{\partial y} + w\frac{\partial \tilde{W}}{\partial z} + \tilde{W}\frac{\partial w}{\partial z} =$$
$$-\frac{\partial p}{\partial z} + \frac{1}{Re}\left(\frac{\partial^2 w}{\partial x^2} + \frac{\partial^2 w}{\partial y^2} + \frac{\partial^2 w}{\partial z^2}\right). \tag{2.32}$$

2.5.2   Cylindrical Coordinates

Suppose $(\tilde{V}_r, \tilde{V}_\theta, \tilde{V}_z, \tilde{P})$ is a steady state solution of (2.16) and (2.17)–(2.19). Defining the perturbation

$$
\begin{aligned}
v_r &\triangleq V_r - \tilde{V}_r \\
v_\theta &\triangleq V_\theta - \tilde{V}_\theta \\
v_z &\triangleq V_z - \tilde{V}_z \\
p &\triangleq P - \tilde{P}
\end{aligned}
$$

we get the perturbation equations

$$\frac{1}{r}\frac{\partial}{\partial r}\left(rv_r\right) + \frac{1}{r}\frac{\partial v_\theta}{\partial \theta} + \frac{\partial v_z}{\partial z} = 0 \tag{2.33}$$

$$\frac{\partial v_r}{\partial t} + v_r\frac{\partial v_r}{\partial r} + v_r\frac{\partial \tilde{V}_r}{\partial r} + \tilde{V}_r\frac{\partial v_r}{\partial r} + \frac{v_\theta}{r}\frac{\partial v_r}{\partial \theta} + \frac{v_\theta}{r}\frac{\partial \tilde{V}_r}{\partial \theta} + \frac{\tilde{V}_\theta}{r}\frac{\partial v_r}{\partial \theta}$$
$$-\frac{v_\theta^2}{r} - 2\frac{v_\theta}{r}\tilde{V}_\theta + v_z\frac{\partial v_r}{\partial z} + v_z\frac{\partial \tilde{V}_r}{\partial z} + \tilde{V}_z\frac{\partial v_r}{\partial z} =$$
$$-\frac{\partial p}{\partial r} + \frac{1}{Re}\left(\frac{\partial}{\partial r}\left(\frac{1}{r}\frac{\partial}{\partial r}\left(rv_r\right)\right) + \frac{1}{r^2}\frac{\partial^2 v_r}{\partial \theta^2} - \frac{2}{r^2}\frac{\partial v_\theta}{\partial \theta} + \frac{\partial^2 v_r}{\partial z^2}\right) \tag{2.34}$$

$$\frac{\partial v_\theta}{\partial t} + v_r \frac{\partial v_\theta}{\partial r} + v_r \frac{\partial \tilde{V}_\theta}{\partial r} + \tilde{V}_r \frac{\partial v_\theta}{\partial r} + \frac{v_\theta}{r} \frac{\partial v_\theta}{\partial \theta} + \frac{v_\theta}{r} \frac{\partial \tilde{V}_\theta}{\partial \theta} + \frac{\tilde{V}_\theta}{r} \frac{\partial v_\theta}{\partial \theta}$$

$$+ \frac{v_r v_\theta}{r} + \frac{v_r V_\theta}{r} + \frac{V_r v_\theta}{r} + v_z \frac{\partial v_\theta}{\partial z} + v_z \frac{\partial \tilde{V}_\theta}{\partial z} + \tilde{V}_z \frac{\partial v_\theta}{\partial z} =$$

$$- \frac{1}{r} \frac{\partial p}{\partial \theta} + \frac{1}{Re} \left(\frac{\partial}{\partial r} \left(\frac{1}{r} \frac{\partial}{\partial r} \left(r v_\theta \right) \right) + \frac{1}{r^2} \frac{\partial^2 v_\theta}{\partial \theta^2} + \frac{2}{r^2} \frac{\partial v_r}{\partial \theta} + \frac{\partial^2 v_\theta}{\partial z^2} \right) \quad (2.35)$$

$$\frac{\partial v_z}{\partial t} + v_r \frac{\partial v_z}{\partial r} + v_r \frac{\partial \tilde{V}_z}{\partial r} + \tilde{V}_r \frac{\partial v_z}{\partial r} + \frac{v_\theta}{r} \frac{\partial v_z}{\partial \theta} + \frac{v_\theta}{r} \frac{\partial \tilde{V}_z}{\partial \theta} + \frac{\tilde{V}_\theta}{r} \frac{\partial v_z}{\partial \theta}$$

$$+ v_z \frac{\partial v_z}{\partial z} + v_z \frac{\partial \tilde{V}_z}{\partial z} + \tilde{V}_z \frac{\partial v_z}{\partial z} =$$

$$- \frac{\partial p}{\partial z} + \frac{1}{Re} \left(\frac{1}{r} \frac{\partial}{\partial r} \left(r \frac{\partial v_z}{\partial r} \right) + \frac{1}{r^2} \frac{\partial^2 v_z}{\partial \theta^2} + \frac{\partial^2 v_z}{\partial z^2} \right) \quad (2.36)$$

and the linearized equations

$$\frac{1}{r} \frac{\partial}{\partial r} \left(r v_r \right) + \frac{1}{r} \frac{\partial v_\theta}{\partial \theta} + \frac{\partial v_z}{\partial z} = 0 \quad (2.37)$$

$$\frac{\partial v_r}{\partial t} + v_r \frac{\partial \tilde{V}_r}{\partial r} + \tilde{V}_r \frac{\partial v_r}{\partial r} + \frac{v_\theta}{r} \frac{\partial \tilde{V}_r}{\partial \theta} + \frac{\tilde{V}_\theta}{r} \frac{\partial v_r}{\partial \theta} - 2 \frac{v_\theta}{r} \tilde{V}_\theta + v_z \frac{\partial \tilde{V}_r}{\partial z} + \tilde{V}_z \frac{\partial v_r}{\partial z} =$$

$$- \frac{\partial p}{\partial r} + \frac{1}{Re} \left(\frac{\partial}{\partial r} \left(\frac{1}{r} \frac{\partial}{\partial r} \left(r v_r \right) \right) + \frac{1}{r^2} \frac{\partial^2 v_r}{\partial \theta^2} - \frac{2}{r^2} \frac{\partial v_\theta}{\partial \theta} + \frac{\partial^2 v_r}{\partial z^2} \right) \quad (2.38)$$

$$\frac{\partial v_\theta}{\partial t} + v_r \frac{\partial \tilde{V}_\theta}{\partial r} + \tilde{V}_r \frac{\partial v_\theta}{\partial r} + \frac{v_\theta}{r} \frac{\partial \tilde{V}_\theta}{\partial \theta} + \frac{\tilde{V}_\theta}{r} \frac{\partial v_\theta}{\partial \theta} + \frac{v_r V_\theta}{r} + \frac{V_r v_\theta}{r} + v_z \frac{\partial \tilde{V}_\theta}{\partial z} + \tilde{V}_z \frac{\partial v_\theta}{\partial z} =$$

$$- \frac{1}{r} \frac{\partial p}{\partial \theta} + \frac{1}{Re} \left(\frac{\partial}{\partial r} \left(\frac{1}{r} \frac{\partial}{\partial r} \left(r v_\theta \right) \right) + \frac{1}{r^2} \frac{\partial^2 v_\theta}{\partial \theta^2} + \frac{2}{r^2} \frac{\partial v_r}{\partial \theta} + \frac{\partial^2 v_\theta}{\partial z^2} \right) \quad (2.39)$$

$$\frac{\partial v_z}{\partial t} + v_r \frac{\partial \tilde{V}_z}{\partial r} + \tilde{V}_r \frac{\partial v_z}{\partial r} + \frac{v_\theta}{r} \frac{\partial \tilde{V}_z}{\partial \theta} + \frac{\tilde{V}_\theta}{r} \frac{\partial v_z}{\partial \theta} + v_z \frac{\partial \tilde{V}_z}{\partial z} + \tilde{V}_z \frac{\partial v_z}{\partial z} =$$

$$- \frac{\partial p}{\partial z} + \frac{1}{Re} \left(\frac{1}{r} \frac{\partial}{\partial r} \left(r \frac{\partial v_z}{\partial r} \right) + \frac{1}{r^2} \frac{\partial^2 v_z}{\partial \theta^2} + \frac{\partial^2 v_z}{\partial z^2} \right). \quad (2.40)$$

2.6 Prototype Flows

So far, the domain on which the Navier-Stokes equation is defined has not entered the picture. In this report, the focus is on three prototype flows that have been studied quite extensively in the literature: 1) *channel flow*, which is the flow contained between two parallel plates; 2) *pipe flow*, which is the flow contained in the interior of a cylinder with circular cross section, and; 3) *cylinder flow*, which is the flow past a cylinder with circular cross section. The particularly simple
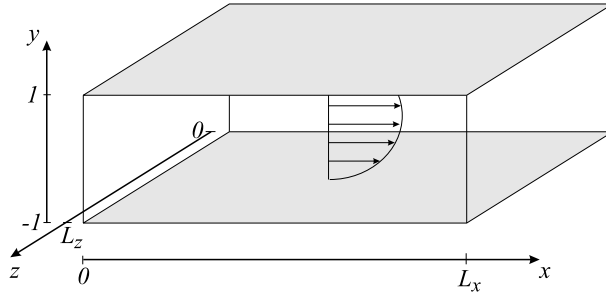
Figure 2.3: Geometry of the 3D channel flow.

geometries of these flows make the problems mathematically tractable, as well as numerically feasible. In addition, the pipe is encountered frequently in practice, so understanding how to control this flow is of great importance in engineering applications.

2.6.1 3D Channel Flow

The domain in this case is the box $\Omega = \{(x, y, z) \in [0, L_x) \times (-1, 1) \times [0, L_z)\}$, which is shown in Figure 2.3. The flow problem is completed by specifying boundary conditions on the boundary of the box. In the streamwise (x) and spanwise (z) directions, we use periodic boundary conditions. That is, we equate the flow quantities at $x = 0$ and $x = L_x$, and at $z = 0$ and $z = L_z$. At the walls, the boundary conditions will eventually be specified by the result of some boundary control design, but for the time being, we select no-slip boundary conditions, i.e. $U = V = W = 0$ at the walls ($y = \pm 1$). Given the boundary conditions, we are now in the position to solve (2.12)–(2.15) for a steady-state solution. In solving the Navier-Stokes equations for a steady-state solution in channel flow with no-slip boundary conditions at the walls, we assume that the velocity field is independent of the streamwise and spanwise directions. Thus, setting the time derivatives and the spatial derivatives with respect to x and z in (2.12)–(2.15) to zero, we get

$$\frac{\partial V}{\partial y} = 0 \tag{2.41}$$

$$V\frac{\partial U}{\partial y} = -\frac{\partial P}{\partial x} + \frac{1}{Re}\frac{\partial^2 U}{\partial y^2} \tag{2.42}$$

$$V\frac{\partial V}{\partial y} = -\frac{\partial P}{\partial y} + \frac{1}{Re}\frac{\partial^2 V}{\partial y^2} \tag{2.43}$$

$$V\frac{\partial W}{\partial y} = -\frac{\partial P}{\partial z} + \frac{1}{Re}\frac{\partial^2 W}{\partial y^2}. \tag{2.44}$$

From (2.41) we have that $V = constant$, and since we are employing no-slip boundary conditions, we obtain $V = 0$. So, from (2.42)–(2.44) we have that

$$\frac{\partial P}{\partial x} = \frac{1}{Re}\frac{\partial^2 U}{\partial y^2} \tag{2.45}$$

$$\frac{\partial P}{\partial y} = 0 \tag{2.46}$$

$$\frac{\partial P}{\partial z} = \frac{1}{Re}\frac{\partial^2 W}{\partial y^2}. \tag{2.47}$$

From (2.46), we have that $P = P(x, z)$, and since $U = U(y)$ by assumption, we get

$$\frac{\partial P}{\partial x} = c_1 = \frac{1}{Re}\frac{\partial^2 U}{\partial y^2} \tag{2.48}$$

$$\frac{\partial P}{\partial z} = c_2 = \frac{1}{Re}\frac{\partial^2 W}{\partial y^2} \tag{2.49}$$

where c_1 and c_2 are constants. Thus, we can solve for each side of (2.48) and (2.49) separately, to get

$$P = c_1 x + c_2 z + c_3$$

where c_3 is a constant, and

$$U(y) = \frac{c_1 Re}{2}y^2 + c_4 y + c_5$$

$$W(y) = \frac{c_2 Re}{2}y^2 + c_6 y + c_7$$

where c_4, c_5, c_6 and c_7 are constants. Since only the gradient of P enters the Navier-Stokes equations, c_3 may be arbitrarily chosen, so we set $c_3 = 0$. By employing no slip boundary conditions we obtain the set of equations

$$\frac{c_1 Re}{2} - c_4 + c_5 = 0$$

$$\frac{c_1 Re}{2} + c_4 + c_5 = 0$$

$$\frac{c_2 Re}{2} - c_6 + c_7 = 0$$

$$\frac{c_2 Re}{2} + c_6 + c_7 = 0$$

so that

$$c_4 = c_6 = 0$$

$$c_5 = -\frac{c_1 Re}{2}$$

$$c_7 = -\frac{c_2 Re}{2}.$$

Without loss of generality we select the direction of flow along the positive x-axis, and the center velocity, $U(0) = 1$. We get

$$c_1 = -\frac{2}{Re}, \quad c_2 = 0, \quad c_5 = 1, \quad \text{and } c_7 = 0.$$

So we have the steady state solution

$$\left(\tilde{U}, \tilde{V}, \tilde{W}, \tilde{P}\right) = \left(1 - y^2, 0, 0, -\frac{2}{Re}x\right). \tag{2.50}$$

Inserting (2.50) into the perturbation equations (2.25)–(2.28) yields

$$\frac{\partial u}{\partial x} + \frac{\partial v}{\partial y} + \frac{\partial w}{\partial z} = 0 \tag{2.51}$$

$$\frac{\partial u}{\partial t} + u\frac{\partial u}{\partial x} + \tilde{U}\frac{\partial u}{\partial x} + v\frac{\partial u}{\partial y} + v\frac{\partial \tilde{U}}{\partial y} + w\frac{\partial u}{\partial z} = $$
$$-\frac{\partial p}{\partial x} + \frac{1}{Re}\left(\frac{\partial^2 u}{\partial x^2} + \frac{\partial^2 u}{\partial y^2} + \frac{\partial^2 u}{\partial z^2}\right) \tag{2.52}$$

$$\frac{\partial v}{\partial t} + u\frac{\partial v}{\partial x} + \tilde{U}\frac{\partial v}{\partial x} + v\frac{\partial v}{\partial y} + w\frac{\partial v}{\partial z} = $$
$$-\frac{\partial p}{\partial y} + \frac{1}{Re}\left(\frac{\partial^2 v}{\partial x^2} + \frac{\partial^2 v}{\partial y^2} + \frac{\partial^2 v}{\partial z^2}\right) \tag{2.53}$$

$$\frac{\partial w}{\partial t} + u\frac{\partial w}{\partial x} + \tilde{U}\frac{\partial w}{\partial x} + v\frac{\partial w}{\partial y} + w\frac{\partial w}{\partial z} = $$
$$-\frac{\partial p}{\partial z} + \frac{1}{Re}\left(\frac{\partial^2 w}{\partial x^2} + \frac{\partial^2 w}{\partial y^2} + \frac{\partial^2 w}{\partial z^2}\right). \tag{2.54}$$

The linearized equations are

$$\frac{\partial u}{\partial x} + \frac{\partial v}{\partial y} + \frac{\partial w}{\partial z} = 0 \tag{2.55}$$

$$\frac{\partial u}{\partial t} + \tilde{U}\frac{\partial u}{\partial x} + v\frac{\partial \tilde{U}}{\partial y} = -\frac{\partial p}{\partial x} + \frac{1}{Re}\left(\frac{\partial^2 u}{\partial x^2} + \frac{\partial^2 u}{\partial y^2} + \frac{\partial^2 u}{\partial z^2}\right) \tag{2.56}$$

$$\frac{\partial v}{\partial t} + \tilde{U}\frac{\partial v}{\partial x} = -\frac{\partial p}{\partial y} + \frac{1}{Re}\left(\frac{\partial^2 v}{\partial x^2} + \frac{\partial^2 v}{\partial y^2} + \frac{\partial^2 v}{\partial z^2}\right) \tag{2.57}$$

$$\frac{\partial w}{\partial t} + \tilde{U}\frac{\partial w}{\partial x} = -\frac{\partial p}{\partial z} + \frac{1}{Re}\left(\frac{\partial^2 w}{\partial x^2} + \frac{\partial^2 w}{\partial y^2} + \frac{\partial^2 w}{\partial z^2}\right). \tag{2.58}$$

Choosing the channel half width (which is 1) as the characteristic length, and the center velocity (which is 1) as the characteristic velocity, the Reynolds number is simply $Re = \rho/\mu$.

Figure 2.4: Geometry of the pipe flow.

2.6.2 3D Pipe Flow

The domain in this case is the cylinder $\Omega = \{(r, \theta, z) \in [0, 1) \times [0, 2\pi) \times [0, L)\}$, which is shown in Figure 2.4. In the angular (θ) direction the boundary conditions are clearly periodic. In the streamwise (z) direction, we also use periodic boundary conditions. That is, we equate the flow quantities at $\theta = 0$ and $\theta = 2\pi$, and at $z = 0$ and $z = L$. In the radial direction (r) we impose the boundary conditions that the velocity be finite at $r = 0$, and no-slip at the wall ($r = 1$). We are now in the position to solve (2.16)–(2.19) for a steady-state solution, which we assume is independent of the angular (θ) and streamwise (z) directions with $V_r = V_\theta = 0$. Thus, we get

$$0 = \frac{\partial P}{\partial r} \tag{2.59}$$

$$0 = \frac{\partial P}{\partial \theta} \tag{2.60}$$

$$\frac{\partial P}{\partial z} = \frac{1}{Re} \frac{1}{r} \frac{\partial}{\partial r} \left(r \frac{\partial V_z}{\partial r} \right). \tag{2.61}$$

From (2.59) and (2.60) we have that $P = P(z)$, and since $V_z = V_z(r)$ by assumption, we get

$$\frac{\partial P}{\partial z} = -c = \frac{1}{Re} \frac{1}{r} \frac{\partial}{\partial r} \left(r \frac{\partial V_z}{\partial r} \right) \tag{2.62}$$

where c is a constant. The left hand side of (2.62) can be integrated to obtain

$$P = -cz + c_1$$

and the right hand side of (2.62) is separable, so we can solve it to obtain

$$V_z(r) = -\frac{cRe}{4} r^2 + c_2 \ln r + c_3.$$

Imposing the boundary conditions in the radial direction, yields

$$c_2 = 0 \text{ and } c_3 = \frac{cRe}{4}$$

and without loss of generality we select the center velocity, $V_z(0) = 1$, so that $c = \frac{4}{Re}$. Thus, we have the steady state solution

$$\left(\tilde{V}_r, \tilde{V}_\theta, \tilde{V}_z, \tilde{P} \right) = \left(0, 0, 1 - r^2, -\frac{4}{Re} z \right). \tag{2.63}$$

The perturbation equations are

$$\frac{1}{r} \frac{\partial}{\partial r} (r v_r) + \frac{1}{r} \frac{\partial v_\theta}{\partial \theta} + \frac{\partial v_z}{\partial z} = 0 \tag{2.64}$$

$$\frac{\partial v_r}{\partial t} + v_r \frac{\partial v_r}{\partial r} + \frac{v_\theta}{r} \frac{\partial v_r}{\partial \theta} - \frac{v_\theta^2}{r} + v_z \frac{\partial v_r}{\partial z} + \tilde{V}_z \frac{\partial v_r}{\partial z} =$$
$$- \frac{\partial p}{\partial r} + \frac{1}{Re} \left(\frac{\partial}{\partial r} \left(\frac{1}{r} \frac{\partial}{\partial r} (r v_r) \right) + \frac{1}{r^2} \frac{\partial^2 v_r}{\partial \theta^2} - \frac{2}{r^2} \frac{\partial v_\theta}{\partial \theta} + \frac{\partial^2 v_r}{\partial z^2} \right) \tag{2.65}$$

$$\frac{\partial v_\theta}{\partial t} + v_r \frac{\partial v_\theta}{\partial r} + \frac{v_\theta}{r} \frac{\partial v_\theta}{\partial \theta} + \frac{v_r v_\theta}{r} + v_z \frac{\partial v_\theta}{\partial z} + \tilde{V}_z \frac{\partial v_\theta}{\partial z} =$$
$$- \frac{1}{r} \frac{\partial p}{\partial \theta} + \frac{1}{Re} \left(\frac{\partial}{\partial r} \left(\frac{1}{r} \frac{\partial}{\partial r} (r v_\theta) \right) + \frac{1}{r^2} \frac{\partial^2 v_\theta}{\partial \theta^2} + \frac{2}{r^2} \frac{\partial v_r}{\partial \theta} + \frac{\partial^2 v_\theta}{\partial z^2} \right) \tag{2.66}$$

$$\frac{\partial v_z}{\partial t} + v_r \frac{\partial v_z}{\partial r} + v_r \frac{\partial \tilde{V}_z}{\partial r} + \frac{v_\theta}{r} \frac{\partial v_z}{\partial \theta} + v_z \frac{\partial v_z}{\partial z} + \tilde{V}_z \frac{\partial v_z}{\partial z} =$$
$$- \frac{\partial p}{\partial z} + \frac{1}{Re} \left(\frac{1}{r} \frac{\partial}{\partial r} \left(r \frac{\partial v_z}{\partial r} \right) + \frac{1}{r^2} \frac{\partial^2 v_z}{\partial \theta^2} + \frac{\partial^2 v_z}{\partial z^2} \right) \tag{2.67}$$

and the linearized equations are

$$\frac{1}{r} \frac{\partial}{\partial r} (r v_r) + \frac{1}{r} \frac{\partial v_\theta}{\partial \theta} + \frac{\partial v_z}{\partial z} = 0 \tag{2.68}$$

$$\frac{\partial v_r}{\partial t} + \tilde{V}_z \frac{\partial v_r}{\partial z} =$$
$$- \frac{\partial p}{\partial r} + \frac{1}{Re} \left(\frac{\partial}{\partial r} \left(\frac{1}{r} \frac{\partial}{\partial r} (r v_r) \right) + \frac{1}{r^2} \frac{\partial^2 v_r}{\partial \theta^2} - \frac{2}{r^2} \frac{\partial v_\theta}{\partial \theta} + \frac{\partial^2 v_r}{\partial z^2} \right) \tag{2.69}$$

$$\frac{\partial v_\theta}{\partial t} + \tilde{V}_z \frac{\partial v_\theta}{\partial z} =$$
$$- \frac{1}{r} \frac{\partial p}{\partial \theta} + \frac{1}{Re} \left(\frac{\partial}{\partial r} \left(\frac{1}{r} \frac{\partial}{\partial r} (r v_\theta) \right) + \frac{1}{r^2} \frac{\partial^2 v_\theta}{\partial \theta^2} + \frac{2}{r^2} \frac{\partial v_r}{\partial \theta} + \frac{\partial^2 v_\theta}{\partial z^2} \right) \tag{2.70}$$

$$\frac{\partial v_z}{\partial t} + v_r \frac{\partial \tilde{V}_z}{\partial r} + \tilde{V}_z \frac{\partial v_z}{\partial z} =$$
$$- \frac{\partial p}{\partial z} + \frac{1}{Re} \left(\frac{1}{r} \frac{\partial}{\partial r} \left(r \frac{\partial v_z}{\partial r} \right) + \frac{1}{r^2} \frac{\partial^2 v_z}{\partial \theta^2} + \frac{\partial^2 v_z}{\partial z^2} \right). \tag{2.71}$$
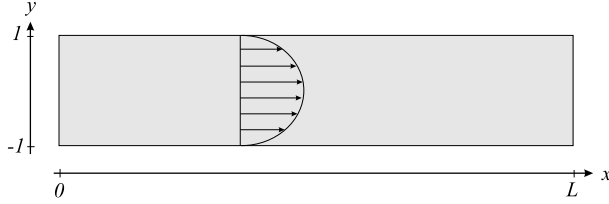
Figure 2.5: Geometry of the 2D channel flow.

Choosing the pipe radius (which is 1) as the characteristic length, and the center velocity (which is 1) as the characteristic velocity, the Reynolds number is simply $Re = \rho/\mu$.

2.6.3   2D Channel/Pipe Flow

In 2D, channel and pipe flows have the same domain, which is shown in Figure 2.5. The domain is in this case $\Omega = \{(x, y) \in [0, L) \times (-1, 1)\}$, and periodic boundary conditions are employed in the streamwise (x) direction. With no-slip boundary conditions at the wall, we have the steady-state solution

$$\left(\tilde{U}, \tilde{V}, \tilde{P}\right) = \left(1 - y^2, 0, -\frac{2}{Re}x\right) \tag{2.72}$$

and the perturbation equations become

$$\frac{\partial u}{\partial x} + \frac{\partial v}{\partial y} = 0 \tag{2.73}$$

$$\frac{\partial u}{\partial t} + u\frac{\partial u}{\partial x} + \tilde{U}\frac{\partial u}{\partial x} + v\frac{\partial u}{\partial y} + v\frac{\partial \tilde{U}}{\partial y} \quad = \quad -\frac{\partial p}{\partial x} + \frac{1}{Re}\left(\frac{\partial^2 u}{\partial x^2} + \frac{\partial^2 u}{\partial y^2}\right) \tag{2.74}$$

$$\frac{\partial v}{\partial t} + u\frac{\partial v}{\partial x} + \tilde{U}\frac{\partial v}{\partial x} + v\frac{\partial v}{\partial y} \quad = \quad -\frac{\partial p}{\partial y} + \frac{1}{Re}\left(\frac{\partial^2 v}{\partial x^2} + \frac{\partial^2 v}{\partial y^2}\right). \tag{2.75}$$

The linearized equations are

$$\frac{\partial u}{\partial x} + \frac{\partial v}{\partial y} = 0 \tag{2.76}$$

$$\frac{\partial u}{\partial t} + \tilde{U}\frac{\partial u}{\partial x} + v\frac{\partial \tilde{U}}{\partial y} \quad = \quad -\frac{\partial p}{\partial x} + \frac{1}{Re}\left(\frac{\partial^2 u}{\partial x^2} + \frac{\partial^2 u}{\partial y^2}\right) \tag{2.77}$$

$$\frac{\partial v}{\partial t} + \tilde{U}\frac{\partial v}{\partial x} \quad = \quad -\frac{\partial p}{\partial y} + \frac{1}{Re}\left(\frac{\partial^2 v}{\partial x^2} + \frac{\partial^2 v}{\partial y^2}\right). \tag{2.78}$$

Choosing the channel half width (which is 1) as the characteristic length, and the center velocity (which is 1) as the characteristic velocity, the Reynolds number is simply $Re = \rho/\mu$.
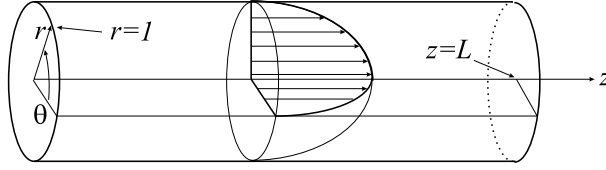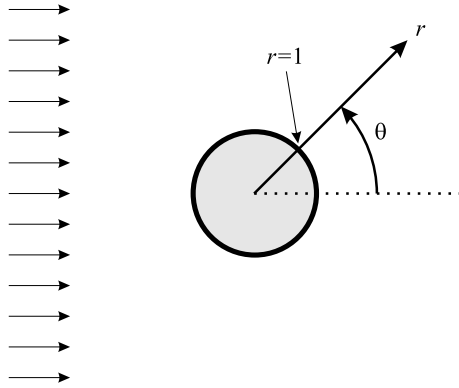
Figure 2.6: Geometry of the 2D cylinder flow.

2.6.4   2D Cylinder Flow

For the 2D cylinder flow, the domain is the entire plane, except for the unit disc (see Figure 2.6). That is, $\Omega = \{(r, \theta) \in (1, \infty) \times [0, 2\pi)\}$. In the angular ($\theta$) direction the boundary conditions are periodic, and in the radial (r) direction we impose no-slip at the wall ($r = 1$), and uniform flow with unit amplitude at $r = \infty$, that is, $V_r(\infty, \theta) = cos(\theta)$ and $V_\theta(\infty, \theta) = -sin(\theta)$. Choosing the disc diameter (which is 2) as the characteristic length, and the velocity at infinity (which is 1) as the characteristic velocity, the Reynolds number is simply $Re = 2\rho/\mu$. In great contrast to the previous cases, we are unable to solve for a steady-state solution of the cylinder flow. Consequently, in what follows, this case is treated numerically, only. However, a simplified model of vortex shedding, the Ginzburg-Landau model, is presented and analyzed with respect to stability in Section 4.4.

2.7   Spatial Discretization

For simulation purposes, as well as some approaches to control design, one needs to discretize the equations of motion both spatially and temporally. A general treatment of discretization methods for the Navier-Stokes equation is given in [42]. In this section, the treatment of this subject is restricted to the methods used in the design of controllers in the next chapter. These are so-called spectral methods, which lend themselves particularly well suited for the prototype flows that were described in the previous section. In [31], an in-depth treatment of spectral methods applied to partial differential equations, including the two methods outlined below, is given.

2.7.1 Spectral Methods

Consider the evolution equation

$$\frac{\partial u}{\partial t} = A(u) \qquad (2.79)$$

with the initial condition

$$u(x, 0) = u_0(x),$$

where $u \in \mathcal{X}$ is the solution sought, and A is an operator containing the spatial derivatives of u. The equation is defined on the spatial domain Ω, which we will assume is one-dimensional for simplicity, that is, $x \in \Omega \subset \mathbb{R}$. $\mathcal{X}$ is a Hilbert space with scalar product

$$(u, v)_{\mathcal{X}} = \int\limits_{\Omega} u\bar{v}d\Omega$$

and norm

$$\|u\|_{\mathcal{X}} = (u, u)^{\frac{1}{2}}.$$

The bar ($\bar{v}$) denotes complex conjugation. In order to complete the problem, appropriate boundary conditions must be supplied. Now, consider a series expansion for the solution u, that is

$$u^*(x, t) = \sum_k a_k(t)\phi_k(x) \qquad (2.80)$$

where the ϕ_k are called the *trial functions*, and the a_k are called the *expansion coefficients*. The ϕ_k are assumed to constitute a complete basis for $\mathcal{X}$, so that the series (2.80) converges to u in $\mathcal{X}$ as $k \to \infty$. The approximation of (2.80), of order N, is defined as the truncated series

$$u^N(x, t) = \sum_{k \in I} a_k(t)\phi_k(x),$$

where I is a finite set of indices. Thus, $u^N \in \mathcal{X}^N = span\{\phi_k \,|k \in I\,\} \subset \mathcal{X}$. Since u^N is an approximate solution of (2.79), the residual

$$R\left(u^N\right) = \frac{\partial u^N}{\partial t} - A\left(u^N\right)$$

will in general not vanish everywhere, but its projection onto the span of a set of *test functions*, $\mathcal{Y}^N = span\{\psi_j \,|j \in I\,\}$, is required to be zero. That is,

$$\left(\frac{\partial u^N}{\partial t} - A(u^N), \psi_j\right)_{\mathcal{X}} = \int\limits_{\Omega} \left(\frac{\partial u^N}{\partial t} - A(u^N)\right) \bar{\psi}_j \, d\Omega = 0, \ j \in I. \qquad (2.81)$$

Equation (2.81) results in N ordinary differential equation for the determination of the expansion coefficients a_k.

2.7.2   The Fourier-Galerkin Method

The Galerkin method is characterized by the fact that the trial functions and the test functions are the same, and that each test function satisfies the boundary conditions. When the boundary conditions are periodic with period L, that is $\Omega = [0, L)$, a natural choice for the trial functions is

$$\phi_k = \psi_k = e^{ik\frac{2\pi}{L}x}, \ \ k = -N/2, ..., N/2.$$

With this choice of test and trial functions, equation (2.81) is called the Fourier-Galerkin method. The ϕ_k constitute an orthogonal basis for $\mathcal{X}^N$, since

$$(\phi_j, \phi_k)_{\mathcal{X}} = \int_0^L \phi_j \bar{\phi}_k \, dx = \int_0^L e^{i(j-k)\frac{2\pi}{L}x} \, dx = \left\{ \begin{array}{l} L, \ j = k \\ 0, \ j \neq k \end{array} \right. .$$

The main advantage of using trigonometric polynomials is the simplicity and accuracy in calculating the derivatives

$$\frac{d^m}{dx^m}\phi_k = \left(\frac{2\pi ik}{L} \right)^m \phi_k. \tag{2.82}$$

As an example, assume that the operator A is linear, and contains spatial derivatives up to order M. In view of (2.82), the operator A acting on ϕ_k can be represented as the finite sum

$$A(\phi_k) = \sum_{m=0}^M c_{mk} \phi_k$$

where the c_{mk} are complex constants. From (2.81), keeping in mind that A is linear and that the scalar product is bilinear, we get

$$\left(\frac{\partial}{\partial t} \left(\sum_{k=-N/2}^{N/2} a_k(t)\phi_k \right) - A \left(\sum_{k=-N/2}^{N/2} a_k(t)\phi_k \right), \phi_j \right)_{\mathcal{X}} =$$
$$\sum_{k=-N/2}^{N/2} \left(\frac{\partial a_k(t)}{\partial t} - a_k(t) \sum_{m=0}^M c_{mk} \right) (\phi_k, \phi_j)_{\mathcal{X}} = L \left(\frac{\partial a_j(t)}{\partial t} - a_j(t) \sum_{m=0}^M c_{mj} \right).$$

Thus, the finite set of ordinary differential equations

$$\frac{da_k(t)}{dt} - a_k(t) \sum_{m=0}^M c_{mk} = 0, \ \text{for } k = -N/2, ..., N/2$$

determines the expansion coefficients a_k. The initial condition is obtained by the usual relation (Fourier transform)

$$a_k(0) = \frac{1}{L} \int_0^L u_0(x) \, e^{-ik\frac{2\pi}{L}x} \, dx, \ \ k = -N/2, ..., N/2.$$

2.7.3 The Chebyshev Collocation Method

The collocation method is characterized by the fact that the test functions are shifted *Dirac* functions, $\psi_j(x) = \delta(x - x_j)$, which are defined by

$$\int_\Omega \delta(x - x_j) f dx = f(x_j).$$

Thus, (2.81) reduces to

$$\left(\frac{\partial u^N}{\partial t} - A(u^N), \psi_j\right)_\chi = \int_\Omega \left(\frac{\partial u^N}{\partial t} - A(u^N)\right) \bar\psi_j d\Omega =$$

$$\left(\frac{\partial u^N(x_j)}{\partial t} - A(u^N(x_j))\right) = 0, \ \ j = 1, 2, 3, ..., N - 1. \quad (2.83)$$

The boundary conditions are taken to be $u^N(-1, t) = u^N(x_0, t)$, and $u^N(1, t) = u^N(x_N, t)$, and the initial condition is $u^N(x_j, 0) = u(x_j, 0)$, for $j = 0, 1, 2, ..., N$. Unlike the Galerkin method, which is implemented in terms of the expansion coefficients, a_k, the collocation method is implemented in terms of u at the collocation points, x_j. The expansion coefficients are used in the differentiation of u^N. In the Chebyshev collocation method, the trial functions are Chebyshev polynomials (or a linear combination of Chebyshev polynomials), which are defined on $\Omega = [-1, 1]$ as

$$\phi_k(x) = \cos(k\theta), \ \ \theta = \cos^{-1}(x) \ \text{ for } k = 0, 1, 2, 3, ...$$

The Chebyshev expansion of u is

$$u^*(x) = \sum_{k=0}^\infty a_k \phi_k(x), \ \ a_k = \frac{2}{\pi c_k} \int_{-1}^1 u(x) \phi_k(x) w(x) dx \quad (2.84)$$

where

$$c_k = \begin{cases} 2, k = 0 \\ 1, k > 0 \end{cases}$$

$$w(x) = \frac{1}{\sqrt{1 - x^2}}.$$

The derivative of (2.84) is

$$\frac{du(x)}{dx} = \sum_{k=0}^\infty a_k \frac{d\phi_k(x)}{dx}$$

which is computed most efficiently by deriving a recursive formula. For $k \geq 1$, we have that

$$\frac{d\phi_{k-1}(x)}{dx} = -(k-1)\sin((k-1)\theta)\frac{d\theta}{dx}$$

$$\frac{d\phi_{k+1}(x)}{dx} = -(k+1)\sin((k+1)\theta)\frac{d\theta}{dx}$$

which, by standard trigonometric relationships, gives

$$\frac{1}{k+1}\frac{d\phi_{k+1}(x)}{dx} - \frac{1}{k-1}\frac{d\phi_{k-1}(x)}{dx} = -2\cos(k\theta)\sin(\theta)\frac{d\theta}{dx}.$$

Since

$$\frac{d\theta}{dx} = -\frac{1}{\sqrt{1-x^2}} = -\frac{1}{\sin(\theta)}$$

we obtain

$$\frac{1}{k+1}\frac{d\phi_{k+1}(x)}{dx} - \frac{1}{k-1}\frac{d\phi_{k-1}(x)}{dx} = 2\phi_k(x).$$

Thus, the derivative of the trial functions obeys the recursive formula

$$\frac{d\phi_k(x)}{dx} = \frac{k}{k-2}\frac{d\phi_{k-2}(x)}{dx} + 2k\phi_{k-1}(x), \ \ k \geq 2. \tag{2.85}$$

Repeated use of (2.85) yields

$$\frac{d\phi_k(x)}{dx} = 2k\left(\phi_{k-1}(x) + \phi_{k-3}(x) + \phi_{k-5}(x) + \cdots + \frac{1}{2-l}\phi_l(x)\right)$$
$$k \geq 2, \ l = \left\{ \begin{array}{l} 0 \text{ for } k \text{ odd} \\ 1 \text{ for } k \text{ even} \end{array} \right. . \tag{2.86}$$

From $d\phi_0(x)/dx = 0$, $d\phi_1(x)/dx = \phi_0(x)$, we see that (2.86) is valid for all $k \geq 0$. It follows from (2.86) that the expansion coefficients for du/dx, denoted a_k^d, are given as

$$a_0^d = \sum_{\substack{m=1 \\ m \text{ odd}}}^{\infty} m a_m \tag{2.87}$$

$$a_k^d = 2 \sum_{\substack{m=k+1 \\ m+k \text{ odd}}}^{\infty} m a_m, \ \ k \geq 1. \tag{2.88}$$

The accuracy of the approximation is highly dependent on the choice of collocation points, and a common choice is (Chebyshev-Gauss-Lobatto)

$$x_j = -\cos\frac{\pi j}{N}, \ \ j = 0, 1, 2, ..., N. \tag{2.89}$$

In the discrete case, the expansion of the approximation is the truncated series

$$u(x) = \sum_{k=0}^{N} a_k \phi_k(x)$$

with the discrete expansion coefficients

$$a_k = \frac{1}{\gamma_k}\sum_{j=0}^{N} u(x_j)\phi_k(x_j)w_j$$

where

$$\gamma_k = \begin{cases} \pi, & \text{for } k = 0, N \\ \frac{\pi}{2}, & \text{for } 0 < k < N \end{cases}, \text{ and } w_j = \begin{cases} \frac{\pi}{2N}, & \text{for } j = 0, N \\ \frac{\pi}{N}, & \text{for } 0 < j < N \end{cases}.$$

Equations (2.87)–(2.88) provide a recursive formula for the calculation of the derivatives in Chebyshev space

$$a^d_{k \geq N} = 0$$

$$a^d_k = 2 \sum_{\substack{m=k+1 \\ m+k \text{ odd}}}^{N} m a_m = 2(k+1) a_{k+1} + a^d_{k+2}, \ k \geq 1$$

$$a^d_0 = a_1 + \sum_{\substack{m=3 \\ m \text{ odd}}}^{\infty} m a_m = a_1 + \frac{1}{2} a^d_2.$$

As for the Fourier-Galerkin method, the result is a finite set of ordinary differential equations, which are difficult to write in this case. The discrete derivative may also be expressed as a matrix multiplication, that is

$$\frac{du^N(x_k)}{dx} = \sum_{j=0}^{N} (\mathcal{D}_N)_{kj} u^N(x_j)$$

where $\mathcal{D}_N$ is the $N+1 \times N+1$ matrix

$$(\mathcal{D}_N)_{kj} \triangleq d_{kj} = \begin{cases} \frac{\bar{c}_k}{\bar{c}_j} \frac{(-1)^{k+j}}{x_k - x_j} & k \neq j \\ -\frac{x_j}{2(1-x_j^2)} & 1 \leq k = j \leq N-1 \\ \frac{2N^2+1}{6} & k = j = 1 \\ -\frac{2N^2+1}{6} & k = j = N \end{cases}. \qquad (2.90)$$

Computationally, the Chebyshev transform is superior to matrix multiplication for computing the derivative when $N > \sim 20$.

Chapter 3

Control Theoretic Preliminaries

The following control theoretic preliminaries are based on the books [9, 45, 49, 119, 106].

3.1 Linear Time-Invariant Systems

Consider the following linear time-invariant system

$$\dot{x} = Ax + Bu \qquad (3.1)$$
$$y = Cx + Du \qquad (3.2)$$

with initial condition $x(t_0) = x_0$. The system transfer function for this system is

$$G(s) = C(sI - A)^{-1}B + D.$$

The fact that $G(s)$ has the state-space realization (3.1)–(3.2) is denoted

$$G(s) = \left[\begin{array}{c|c} A & B \\ \hline C & D \end{array} \right].$$

3.1.1 Classical Control

Here we will review one result from classical control theory, namely the *Nyquist stability criterion*, which is based on the argument principle of complex analysis. In short, the Nyquist stability criterion relates the open-loop frequency response to the number of poles of the system in the right half of the complex plane. We study the feedback configuration shown schematically in Figure 3.1, and for simplicity, we assume that the controller is a simple proportional controller with constant feedback gain. To determine stability of the closed loop system
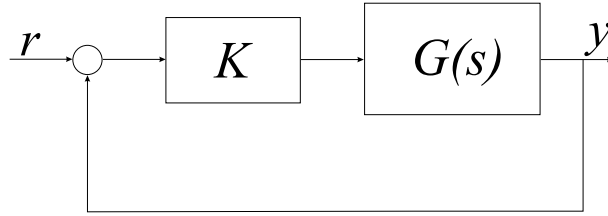
Figure 3.1: Feedback configuration for application of the Nyquist criterion.

$$G_c\left(s\right) = \frac{KG(s)}{1 + KG(s)}$$

where $G(s)$ is the plant transfer function, and K is the feedback gain, the Nyquist stability criterion can be used in the following three-step procedure

1. Determine the number of unstable poles of $G(s)$ and call that number P.

2. Plot the Nyquist plot of $G(s)$ (which is simply the curve $(real(G(j\omega), imag(G(j\omega)))$ for $\omega \in \mathbb{R}$), and evaluate the number of times the curve encircles $-1/K$ in the clockwise direction. Call that number N.

3. The number of unstable closed-loop roots is $Z = N + P$.

3.1.2   LQG Control

In LQG control (linear-quadratic-gaussian), the system (3.1)–(3.2) is assumed to be subjected to disturbances entering additively in both equations. Thus, we have

$$\dot{x} = Ax + Bu + w_d \qquad\qquad (3.3)$$
$$y = Cx + Du + w_n \qquad\qquad (3.4)$$

where w_d is a disturbance and w_n is measurement noise. w_d and w_n are assumed to be uncorrelated Gaussian stochastic processes with zero means and covariances

$$E\left\{w_d\left(t\right) w_d^T\left(\tau\right)\right\} = W\delta\left(t - \tau\right), \text{ and}$$
$$E\left\{w_n\left(t\right) w_n^T\left(\tau\right)\right\} = V\delta\left(t - \tau\right),$$

respectively, where W and V are constant matrices. E denotes the expectation operator, and δ denotes the delta function. The LQG control problem is to find the controller K that minimizes the cost functional

$$J = E\left\{\lim_{T \to \infty} \frac{1}{T}\int_{t_0}^{T}\left(x^T Q x + u^T R u\right) dt\right\}$$

where Q and R are constant weighting matrices satisfying $Q = Q^T \geq 0$ and $R = R^T > 0$. This problem is solved by a three step procedure: 1) find the optimal state feedback when the noise is ignored; 2) find the optimal state estimator; and 3) replace the state in 1) with its estimate. The fact that the state feedback law and the estimator can be designed independently is referred to as the *separation theorem* (or the *certainty equivalence principle*). The optimal state feedback is the feedback u that minimizes the cost functional

$$J_s = \lim_{T \to \infty} \int_{t_0}^{T} \left(x^T Q x + u^T R u \right) dt.$$

If (A, B) is stabilizable, the problem has a unique solution given by

$$u(t) = -F x(t),$$

where $F = R^{-1} B^T X$ and $X = X^T \geq 0$ uniquely solves the algebraic Riccati equation

$$A^T X + X A - X B R^{-1} B^T X + Q = 0.$$

The optimal state estimator, or the *Kalman filter*, having the structure

$$\dot{\hat{x}} = A\hat{x} + Bu + L\left(y - C\hat{x}\right) \tag{3.5}$$

is the one that minimizes the covariance of the estimation error

$$E\left\{ (x - \hat{x})^T (x - \hat{x}) \right\}.$$

If (A, C) is detectable, the problem has a unique solution given by

$$L = YC^T V^{-1}$$

where $Y = Y^T \geq 0$ uniquely solves the algebraic Riccati equation

$$YA^T + AY - YC^T V^{-1} CY + W = 0.$$

In summary, the controller K is given as

$$K(s) = \left[\begin{array}{c|c} A - BF - LC & L \\ \hline -F & 0 \end{array} \right]. \tag{3.6}$$

3.1.3 $\mathcal{H}_2$ Control

The standard $\mathcal{H}_2$ problem considers the system shown in Figure 3.2, which can be described by

$$\begin{align} \left[\begin{array}{c} z \\ y \end{array} \right] &= G(s) \left[\begin{array}{c} w \\ u \end{array} \right] = \left[\begin{array}{cc} G_{11}(s) & G_{12}(s) \\ G_{21}(s) & G_{22}(s) \end{array} \right] \left[\begin{array}{c} w \\ u \end{array} \right] \\ u &= K(s)y \end{align} \tag{3.7}$$
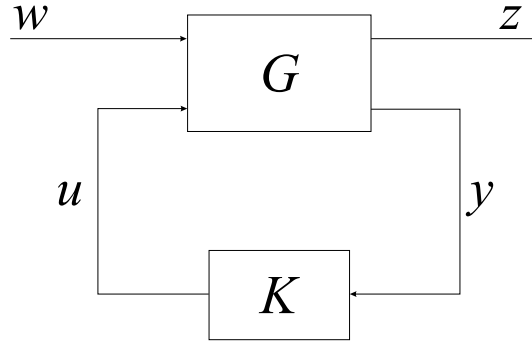
Figure 3.2: Standard control system configuration.

with the state-space realization

$$
G\left(s\right) = \left[\begin{array}{c|c} A & \left[\begin{array}{cc} B_1 & B_2 \end{array} \right] \\ \hline \left[\begin{array}{c} C_1 \\ C_2 \end{array} \right] & \left[\begin{array}{cc} 0 & D_{12} \\ D_{21} & 0 \end{array} \right] \end{array} \right],
\tag{3.8}
$$

that is

$$
\begin{aligned}
\dot{x} &= Ax + B_1 w + B_2 u & (3.9) \\
z &= C_1 x + D_{12} u & (3.10) \\
y &= C_2 x + D_{21} w & (3.11)
\end{aligned}
$$

where x is the n-dimensional state vector, u is an m-vector of control inputs, w is an l-vector of external disturbance inputs, z is a p-vector of objectives, and y is a q-vector of measurements. We wish to find the proper, real-rational controller K, which stabilizes G internally, and minimizes

$$
\|T_{zw}\left(s\right)\|_2 \triangleq \sqrt{\frac{1}{2\pi} \int\limits_{-\infty}^{\infty} Trace\left\{T_{zw}^*\left(i\omega\right) T_{zw}\left(i\omega\right)\right\} d\omega},
$$

which is referred to as the $\mathcal{H}_2$-norm of T_{zw}. The transfer function T_{zw}, which is the transfer function from the external disturbances to the objectives, is given by

$$
T_{zw}\left(s\right) = G_{11}\left(s\right) + G_{12}\left(s\right) K\left(s\right) \left(I - G_{22}\left(s\right) K\left(s\right)\right)^{-1} G_{21}\left(s\right).
\tag{3.12}
$$

The problem has a unique solution provided that

1. (A, B_2) is stabilizable and (C_2, A) is detectable;

2. D_{12} and D_{21} have full rank;

3. $\begin{bmatrix} A - i\omega I & B_2 \\ C_1 & D_{12} \end{bmatrix}$ has full column rank for all ω;

4. $\begin{bmatrix} A - i\omega I & B_1 \\ C_2 & D_{21} \end{bmatrix}$ has full row rank for all ω.

The optimal controller is given by

$$K_{opt}(s) = \left[\begin{array}{c|c} A_2 & -L_2 \\ \hline F_2 & 0 \end{array} \right]$$

where

$$
\begin{aligned}
F_2 &= -\left(B_2^* X_2 + D_{12}^* C_1\right) \\
L_2 &= -\left(Y_2 C_2^* + B_1 D_{21}^*\right) \\
A_2 &= A + B_2 F_2 + L_2 C_2
\end{aligned}
$$

and X_2 and Y_2 uniquely solve the algebraic Riccati equations

$$
\begin{aligned}
\left(A - B_2 D_{12}^* C_1\right)^* X_2 + X_2 \left(A - B_2 D_{12}^* C_1\right) & \\
- X_2 B_2 B_2^* X_2 + C_1^* C_1 - C_1^* D_{12} D_{12}^* C_1 = 0, & \text{ and}
\end{aligned}
$$

$$
\begin{aligned}
\left(A - B_1 D_{21}^* C_2\right)^* Y_2 + Y_2 \left(A^* - C_2^* D_{21} B_1^*\right) & \\
- Y_2 C_2^* C_2 Y_2 + B_1 B_1^* - B_1 D_{21}^* D_{21} B_1^* = 0, &
\end{aligned}
$$

respectively. Note that the LQG control design of the previous section fits into this framework by setting

$$
z = \begin{bmatrix} Q^{\frac{1}{2}} & 0 \\ 0 & R^{\frac{1}{2}} \end{bmatrix} \begin{bmatrix} x \\ u \end{bmatrix}
$$

$$
\begin{bmatrix} w_d \\ w_n \end{bmatrix} = \begin{bmatrix} W^{\frac{1}{2}} & 0 \\ 0 & V^{\frac{1}{2}} \end{bmatrix} w
$$

where w is a white noise process of unit intensity. For this reason, the terms LQG and $\mathcal{H}_2$ control are used interchangeably in the literature.

3.1.4 $\mathcal{H}_\infty$ Control

Again, we consider the standard system (3.7) with the state-space realization (3.8) (sketched in Figure 3.2). The sub-optimal $\mathcal{H}_\infty$ control problem is to find all proper, real-rational controllers K, which stabilize (3.8) internally, and satisfy

$$\|T_{zw}(s)\|_\infty \triangleq \sup_\omega \sigma_{\max}\left(T_{zw}(j\omega)\right) < \gamma \tag{3.13}$$

for some prescribed γ, where $\sigma_{\max}(\cdot)$ denotes the maximum singular value of its argument. $\|T_{zw}(s)\|_\infty$ is referred to as the $\mathcal{H}_\infty$-norm of T_{zw}, and T_{zw} is given

in (3.12). There is an optimal γ, denoted γ_0, which is simply the infimum of all γ for which the sub-optimal problem is solvable. Unlike the $\mathcal{H}_2$ control case, where we were able to explicitly write the unique optimal controller, the optimal γ must in this case be found iteratively. Returning to the sub-optimal problem, it is solvable provided Assumptions 1-4 in the previous section hold, and in addition, the following assumptions hold

5. X_∞ solves the algebraic Riccati equation

$$A^T X_\infty + X_\infty A - X_\infty \left(B_2 B_2^T - \frac{1}{\gamma^2} B_1 B_1^T \right) X_\infty + C_1^T C_1 = 0$$

and $X_\infty \geq 0$.

6. Y_∞ solves the algebraic Riccati equation

$$AY_\infty + Y_\infty A^T - Y_\infty \left(C_2^T C_2 - \frac{1}{\gamma^2} C_1^T C_1 \right) Y_\infty + B_1 B_1^T = 0$$

and $Y_\infty \geq 0$.

7. $\rho(X_\infty Y_\infty) < \gamma^2$ (ρ denotes spectral radius).

Under these conditions, one admissible controller is given by

$$K_{sub}(s) = \left[\begin{array}{c|c} A_\infty & -Z_\infty L_\infty \\ \hline F_\infty & 0 \end{array} \right] \tag{3.14}$$

where

$$A_\infty = A + \frac{1}{\gamma^2} B_1 B_1^T X_\infty + B_2 F_\infty + Z_\infty L_\infty C_2$$

$$F_\infty = -B_2^T X_\infty, \;\; L_\infty = -Y_\infty C_2^T, \;\; Z_\infty = \left(I - \frac{1}{\gamma^2} Y_\infty X_\infty \right)^{-1}.$$

Note that in the limit $\gamma \to \infty$, the controller (3.14) approaches the optimal $\mathcal{H}_2$ controller of the previous section.

3.2   Nonlinear Systems

3.2.1   Stability in the Sense of Lyapunov

Consider the system

$$\dot{x} = f(t, x). \tag{3.15}$$

The following definitions are taken from [76, 79, 80].

Definition 3.1 *A continuous function $\alpha : \mathbb{R}_+ \to \mathbb{R}_+$ is said to be a class $\mathcal{K}$ function if it is strictly increasing and $\alpha(0) = 0$. If, in addition, $\alpha(r) \to \infty$ as $r \to \infty$ it is said to be a class $\mathcal{K}_\infty$ function. A continuous function $\beta : \mathbb{R}_+ \times \mathbb{R}_+ \to \mathbb{R}_+$ is said to be a class $\mathcal{KL}$ function if, for each fixed s, the mapping $\beta(r,s)$ is a class $\mathcal{K}$ function with respect to r and, for each fixed r, the mapping $\beta(r,s)$ is decreasing with respect to s and $\beta(r,s) \to 0$ as $s \to \infty$.*

Definition 3.2 *The solution $x(t; x_0, t_0)$ of (3.15) is uniformly globally bounded (UGB) if for each $x_0 \in \mathbb{R}^n$ there exists a constant b (independent of t_0), such that*

$$\|x(t)\| \leq b(x_0)$$

Definition 3.3 *The equilibrium point $x = 0$ of (3.15) is uniformly globally asymptotically stable (UGAS) if*

1. *it is uniformly globally stable (UGS), that is, there exists $\gamma \in \mathcal{K}_\infty$ such that, for each $(t_0, x_0) \in \mathbb{R}_+ \times \mathbb{R}^n$ and all $t \geq t_0$, we have*

$$\|x(t)\| \leq \gamma(\|x_0\|) ;$$

2. *for each pair of strictly positive real numbers ϵ and r, there exists a positive real number T such that*

$$\|x(t)\| \leq \epsilon, \quad \forall t \geq t_0 + T(\epsilon, r), \ \forall \|x(t_0)\| < r \tag{3.16}$$

Definition 3.4 *The equilibrium point $x = 0$ of (3.15) is uniformly locally exponentially stable (ULES) if there exist positive constants k, γ and c such that*

$$\|x(t)\| \leq k \|x(t_0)\| e^{-\gamma(t-t_0)}, \quad \forall t \geq t_0, \ \forall \|x(t_0)\| < c \tag{3.17}$$

If (3.17) is satisfied for any initial state $x(t_0)$, then the equilibrium point is uniformly globally exponentially stable (UGES).

Definition 3.5 *The system $\dot{x} = f(t, x, u)$ is input-to-state stable (ISS) if there exist a class $\mathcal{KL}$ function β, and a class $\mathcal{K}$ function γ, such that for any initial state $x(t_0)$, and any bounded input $u(t)$, the solution $x(t)$ exists and satisfies*

$$\|x(t)\| \leq \beta(\|x(t_0)\|, t - t_0) + \gamma\left(\sup_{t_0 \leq \tau \leq t} u(\tau)\right).$$

Definition 3.6 *The system $\dot{x} = f(t, x, u)$ with output $y = h(x)$ is input-output-to-state stable (IOSS) if there exist a class $\mathcal{KL}$ function β, and class $\mathcal{K}$ functions γ_1 and γ_2, such that for any initial state $x(t_0)$, and any bounded input $u(t)$, the solution $x(t)$ exists and satisfies*

$$\|x(t)\| \leq \max\left\{\beta(\|x(t_0)\|, t - t_0), \gamma_1\left(\sup_{t_0 \leq \tau \leq t} u(\tau)\right), \gamma_2\left(\sup_{t_0 \leq \tau \leq t} y(\tau)\right)\right\}.$$

Stability of solutions of system (3.15) is analyzed using Lyapunov stability theory [76, Theorem 3.8, Corollary 3.3, and Corollary 3.4].

Theorem 3.1 *Let $x = 0$ be an equilibrium point for the system $\dot{x} = f(t, x)$ and $D \subset \mathbb{R}^n$ be a domain containing $x = 0$. Let $V : [0, \infty) \times D \rightarrow \mathbb{R}$ be a continuously differentiable function such that*

$$
\begin{aligned}
W_1(x) &\leq V(t, x) \leq W_2(x) \\
\frac{\partial V}{\partial t} + \frac{\partial V}{\partial x} f(t, x) &\leq -W_3(x)
\end{aligned}
$$

for all $t \geq 0$ and for all $x \in D$ where $W_1(x)$, $W_2(x)$, and $W_3(x)$ are continuous positive definite functions on D. Then, $x = 0$ is uniformly asymptotically stable. Moreover, if

$$
W_1(x) \geq k_1 \|x\|^c, \ W_2(x) \leq k_2 \|x\|^c, \ W_3(x) \geq k_3 \|x\|^c
$$

for some positive constants k_1, k_2, k_3, and c, then $x = 0$ is exponentially stable. If $D = \mathbb{R}^n$, then $x = 0$ is globally uniformly asymptotically stable (respectively globally exponentially stable).

The function V in Theorem 3.1 is called a *Lyapunov function*, and is in general not easy to find. A systematic method that in many cases simplifies the task of finding a Lyapunov function, called *backstepping*, is now presented in its simplest form (integrator backstepping).

3.2.2   Integrator Backstepping

Consider the system [80]

$$
\begin{aligned}
\dot{x} &= f(x) + g(x)\xi, \ f(0) = 0 & (3.18) \\
\dot{\xi} &= u, & (3.19)
\end{aligned}
$$

where $x \in \mathbb{R}^n$ and $\xi, u \in \mathbb{R}$, and suppose there exist a continuously differentiable function $\alpha : \mathbb{R}^n \rightarrow \mathbb{R}$ with $\alpha(0) = 0$, and a smooth, positive definite, radially unbounded function $V : \mathbb{R}^n \rightarrow \mathbb{R}$, such that

$$
\frac{\partial V}{\partial x}(x)[f(x) + g(x)\alpha(x)] \leq -W(x) \leq 0
$$

where $W : \mathbb{R}^n \rightarrow \mathbb{R}$ is positive definite. In other words, if ξ is taken as the control input in (3.18), called the *virtual control*, then the control $\xi = \alpha(x)$ renders the equilibrium point $x = 0$ globally asymptotically stable. α is thus called a *stabilizing function*. We now define the *error variable* z to be the deviation of ξ from its desired value $\alpha(x)$, that is

$$
z = \xi - \alpha(x).
$$

Augmenting V with a quadratic term in z, we get the Lyapunov function candidate

$$V_a = V + \frac{1}{2} z^2$$

whose time derivative along solutions of system (3.18)–(3.19) is

$$
\begin{aligned}
\dot{V}_a &= \frac{\partial V}{\partial x}(x)\left[f(x) + g(x)\xi\right] + z\dot{z} \\
&= \frac{\partial V}{\partial x}(x)\left[f(x) + g(x)(z + \alpha(x))\right] + z\left(\dot{\xi} - \frac{\partial \alpha}{\partial x}(x)\left[f(x) + g(x)\xi\right]\right) \\
&= \frac{\partial V}{\partial x}(x)\left[f(x) + g(x)\alpha(x)\right] \\
&\quad + z\left[\frac{\partial V}{\partial x}(x)g(x) + u - \frac{\partial \alpha}{\partial x}(x)\left[f(x) + g(x)\xi\right]\right] \\
&\leq -W(x) + z\left[\frac{\partial V}{\partial x}(x)g(x) + u - \frac{\partial \alpha}{\partial x}(x)\left[f(x) + g(x)\xi\right]\right]. \qquad (3.20)
\end{aligned}
$$

We are now in a position to select the control u in such a fashion that $\dot{V}_a \leq -W_a(x, z)$, with $W_a(x, z)$ positive definite. The most straight forward choice is simply to cancel all terms in the bracket in (3.20), and add a term that ensures positive definiteness of W_a. So, defining the control

$$u(x) = -c(\xi - \alpha(x)) - \frac{\partial V}{\partial x}(x)g(x) + \frac{\partial \alpha}{\partial x}(x)\left[f(x) + g(x)\xi\right] \qquad (3.21)$$

we get $W_a(x, z) = W(x) + cz^2$, which proves that the control (3.21) renders $(x, z) = (0, 0)$ globally asymptotically stable, which in turn implies that $(x, \xi) = (0, 0)$ is globally asymptotically stable. If system (3.18)–(3.19) were augmented with more integrators, the backstepping procedure demonstrated above may be applied repeatedly, defining new virtual controls, stabilizing functions and error variables at each step. Such recursive designs are treated in detail in [80].

Chapter 4

Stabilization

The steady-state solutions, or equilibrium velocity profiles, obtained for the prototype flows of Section 2.6, are parabolic in shape in the streamwise direction, and zero in the other directions. Thus, the flows consist of parallel layers of fluid moving in a very regular and deterministic way. These are examples of so-called *laminar* flows. For wall-bounded laminar flows, wall friction, or *drag*, is favorably low, and these flows are therefore target flows in drag reduction applications. Unfortunately, they are rarely stable. In fact, stability is assured at small Reynolds number, only. An unstable flow is characterized by the fact that small perturbations from the equilibrium velocity profile will grow, and eventually cause the flow to transition to *turbulent* flow. Turbulent flow is characterized by small scale, apparently stochastic, velocity components, which lead to substantially higher drag than what is present in laminar flow. Being able to relaminarize a turbulent flow is therefore of great importance, and can be achieved in the prototype flows studied here, by stabilizing the parabolic equilibrium profile using boundary control. Boundary control implies specifying the flow field dynamically on the boundary of the domain, in this case on the channel or pipe walls, possibly based on values of flow variables taken at the boundary (boundary feedback). In this work, we assume that there exist sensors that provide distributed flow information at the wall, and actuators that can set prescribed distributed velocities. Chapter 6 reviews a selection of sensors and actuators that accomplish this task.

The problem of stabilizing the parabolic equilibrium profile of the channel flow has been attacked from several different angles by a number of authors. Approaches range from discretizing the linearized Navier-Stokes equation and using the tools available for stabilizing finite-dimensional linear time invariant systems, to Lyapunov stability analysis of the full, nonlinear Navier-Stokes equation. In the following sections, these efforts are summarized. Recent results on stabilization of pipe flows and cylinder flows are also presented.
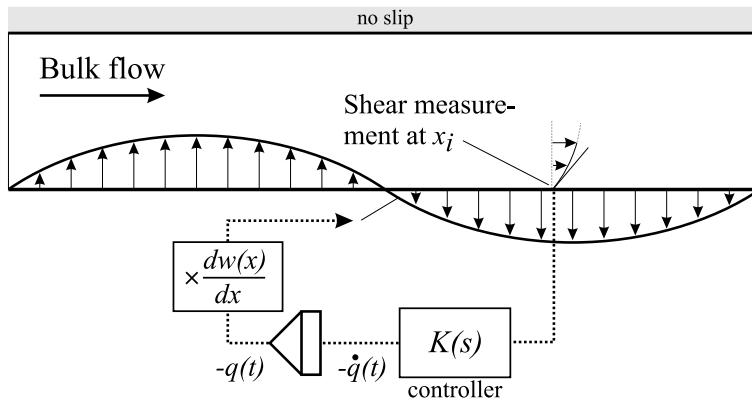
Figure 4.1: Control system configuration for controlling 2D channel flow by wall transpiration at the lower wall.

4.1 Linearization and Reduced Order Methods

This section summarizes the efforts on stabilization of the discretized, linearized Navier-Stokes equations. Bringing the linearized Navier-Stokes equations on the form of a linear time invariant system constitute a major part of the work involved in these methods. Once the state-space model is constructed, any tool from linear control theory can be applied in a fairly straight forward manner.

4.1.1 2D Channel Flow

In a series of papers [36, 37, 70, 71], stabilization of a reduced order model of 2D channel flow by classical and optimal control techniques is considered. The shear ($\partial U/\partial y$) at a single point on the lower wall is taken as measurement, and the rate of change in the intensity of fluid transpiration on the lower wall is the control input. The actuator applies blowing and suction of fluid distributed as a prescribed function of x along the lower wall. The control system setup is shown schematically in Figure 4.1.

Reduced Order Model

The point of departure for obtaining a reduced order model on state space form is the linearized Navier-Stokes equation for 2D channel flow, (2.76) and (2.77)–(2.78). Due to (2.76) there exists a single valued function $\psi(x, y, t)$ such that

$$u(x, y, t) \quad = \quad \frac{\partial \psi}{\partial y}(x, y, t) \tag{4.1}$$

$$v(x, y, t) \quad = \quad -\frac{\partial \psi}{\partial x}(x, y, t). \tag{4.2}$$

The function ψ is unique up to a constant, and is called the *stream function* due to the fact that contours of constant ψ define streamlines of the flow. Inserting (4.1)–(4.2) into (2.77)–(2.78) yields

$$\frac{\partial^2 \psi}{\partial t \partial y} + \tilde{U} \frac{\partial^2 \psi}{\partial y \partial x} - \frac{\partial \tilde{U}}{\partial y} \frac{\partial \psi}{\partial x} + \frac{\partial p}{\partial x} - \frac{1}{Re} \left(\frac{\partial^3 \psi}{\partial y \partial x^2} + \frac{\partial^3 \psi}{\partial y^3} \right) = 0 \qquad (4.3)$$

$$-\frac{\partial^2 \psi}{\partial t \partial x} - \tilde{U} \frac{\partial^2 \psi}{\partial x^2} + \frac{\partial p}{\partial y} + \frac{1}{Re} \left(\frac{\partial^3 \psi}{\partial x^3} + \frac{\partial^3 \psi}{\partial x \partial y^2} \right) = 0. \qquad (4.4)$$

Taking the partial derivative of (4.3) with respect to y and subtracting the partial derivative of (4.4) with respect to x yield

$$\frac{\partial^3 \psi}{\partial t \partial y^2} + \frac{\partial^3 \psi}{\partial t \partial x^2} + \tilde{U} \frac{\partial^3 \psi}{\partial x \partial y^2} - \frac{\partial^2 \tilde{U}}{\partial y^2} \frac{\partial \psi}{\partial x} + \tilde{U} \frac{\partial^3 \psi}{\partial x^3}$$
$$- \frac{1}{Re} \left(\frac{\partial^4 \psi}{\partial x^4} + 2 \frac{\partial^4 \psi}{\partial x^2 \partial y^2} + \frac{\partial^4 \psi}{\partial y^4} \right) = 0. \quad (4.5)$$

Suppose boundary control is applied by imposing a boundary condition on the lower wall of the form

$$\psi(x, y = -1, t) = q(t) w(x) f(y = -1) \qquad (4.6)$$

while keeping no slip boundary conditions on the upper wall, that is

$$\frac{\partial \psi}{\partial y}(x, y = 1, t) = \frac{\partial \psi}{\partial x}(x, y = 1, t) = 0.$$

Restricting the boundary control to blowing and suction of fluid through the wall at normal angle to the wall, that is $u(x, y = -1, t) = \frac{\partial \psi}{\partial y}(x, y = -1, t) = 0$, along with the no slip condition on the upper wall, restrict the function $f(y)$ in the following manner

$$\frac{\partial f}{\partial y}(y = \pm 1) = 0 \qquad (4.7)$$

$$f(y = 1) = 0. \qquad (4.8)$$

As in [70], we will use

$$f(y) = \frac{1}{2} y^4 + \frac{1}{4} y^3 - y^2 - \frac{3}{4} y + 1$$

although there are many other choices satisfying (4.7)–(4.8). When implementing the boundary control law (4.6) in practice, the physical flow variables, U and V, must be set such that the resulting stream function satisfies (4.6). In terms of the physical flow variables U and V, the boundary control law is

$$U(x, y = \pm 1, t) = 0, \ V(x, y = 1, t) = 0,$$

$$V(x, y = -1, t) = v(x, y = -1, t) =$$
$$-\frac{\partial \psi}{\partial x}(x, y = -1, t) = -q(t)\frac{\partial w}{\partial x}(x) f(y = -1).$$

In order to obtain homogeneous boundary conditions, we introduce the change of variables

$$\phi(x, y, t) \triangleq \psi(x, y, t) - q(t)w(x)f(y)$$

which substituted into (4.5) yields

$$\frac{\partial^3 \phi}{\partial t \partial y^2} + \frac{dq}{dt}w\frac{d^2 f}{dy^2} + \frac{\partial^3 \phi}{\partial t \partial x^2} + \frac{dq}{dt}\frac{d^2 w}{dx^2}f + \tilde{U}\left(\frac{\partial^3 \phi}{\partial x \partial y^2} + q\frac{dw}{dx}\frac{d^2 f}{dy^2}\right)$$
$$- \frac{d^2 \tilde{U}}{dy^2}\left(\frac{\partial \phi}{\partial x} + q\frac{dw}{dx}f\right) + \tilde{U}\left(\frac{\partial^3 \phi}{\partial x^3} + q\frac{d^3 w}{dx^3}f\right)$$
$$-\frac{1}{Re}\left(\left(\frac{\partial^4 \phi}{\partial x^4} + q\frac{d^4 w}{dx^4}f\right) + 2\left(\frac{\partial^4 \phi}{\partial x^2 \partial y^2} + q\frac{d^2 w}{dx^2}\frac{d^2 f}{dy^2}\right) + \left(\frac{\partial^4 \phi}{\partial y^4} + qw\frac{d^4 f}{dy^4}\right)\right) = 0.$$
$$(4.9)$$

The boundary conditions in terms of ϕ are

$$\phi(x, y = \pm 1, t) = 0$$

$$\frac{\partial \phi}{\partial y}(x, y = \pm 1, t) = 0.$$

The streamwise component of shear at a single point at the lower wall is used as a measurement, that is

$$z(t) = \frac{\partial u}{\partial y}(x_i, y = -1, t).$$

In terms of ϕ, we have

$$z(t) = \frac{\partial^2 \psi}{\partial y^2}(x_i, y = -1, t) = \frac{\partial^2 \phi}{\partial y^2}(x_i, y = -1, t) + q(t)w(x_i)\frac{d^2 f}{dy^2}(y = -1). \quad (4.10)$$

A standard Fourier-Galerkin procedure is used to discretize the partial differential equation in the streamwise direction, and a Chebyshev collocation method is used in the wall-normal direction. Starting with the streamwise direction, we set

$$\phi(x, y, t) = \sum_{n=-N}^{N} a_n(y, t)P_n(x) \qquad (4.11)$$

$$w(x) = \sum_{n=-N}^{N} w_n P_n(x) \qquad (4.12)$$

where

$$P_n(x) = e^{in\frac{2\pi}{L}x}. \qquad (4.13)$$

The partial derivatives of ϕ and w with respect to x up to order four are

$$\frac{\partial \phi}{\partial x}(x,y,t) = \sum_{n=-N}^{N} \alpha_n i a_n(y,t) P_n(x) \quad \frac{dw}{dx}(x) = \sum_{n=-N}^{N} \alpha_n i w_n P_n(x) \qquad (4.14)$$

$$\frac{\partial^2 \phi}{\partial x^2}(x,y,t) = -\sum_{n=-N}^{N} \alpha_n^2 a_n(y,t) P_n(x) \quad \frac{d^2 w}{dx^2}(x) = -\sum_{n=-N}^{N} \alpha_n^2 w_n P_n(x) \quad (4.15)$$

$$\frac{\partial^3 \phi}{\partial x^3}(x,y,t) = -\sum_{n=-N}^{N} \alpha_n^3 i a_n(y,t) P_n(x) \quad \frac{d^3 w}{dx^3}(x) = -\sum_{n=-N}^{N} \alpha_n^3 i w_n P_n(x)$$

$$(4.16)$$

$$\frac{\partial^4 \phi}{\partial x^4}(x,y,t) = \sum_{n=-N}^{N} \alpha_n^4 a_n(y,t) P_n(x) \quad \frac{d^4 w}{dx^4}(x) = \sum_{n=-N}^{N} \alpha_n^4 w_n P_n(x) \qquad (4.17)$$

where $\alpha_n = 2\pi n/L$. The Gelerkin method provides the set of equations

$$\int_0^L \left\{ \frac{\partial^3 \phi}{\partial t \partial y^2} + \frac{dq}{dt} w \frac{d^2 f}{dy^2} + \frac{\partial^3 \phi}{\partial t \partial x^2} + \frac{dq}{dt}\frac{d^2 w}{dx^2} f + \tilde{U}\left(\frac{\partial^3 \phi}{\partial x \partial y^2} + q\frac{dw}{dx}\frac{d^2 f}{dy^2} \right) \right.$$

$$- \frac{\partial^2 \tilde{U}}{\partial y^2}\left(\frac{\partial \phi}{\partial x} + q\frac{dw}{dx}f \right) + \tilde{U}\left(\frac{\partial^3 \phi}{\partial x^3} + q\frac{d^3 w}{dx^3}f \right) - \frac{1}{Re}\left(\frac{\partial^4 \phi}{\partial x^4} + q\frac{d^4 w}{dx^4}f \right)$$

$$\left. + 2\left(\frac{\partial^4 \phi}{\partial x^2 \partial y^2} + q\frac{d^2 w}{dx^2}\frac{d^2 f}{dy^2} \right) + \frac{\partial^4 \phi}{\partial y^4} + qw\frac{d^4 f}{dy^4} \right\} \bar{P}_k(x)\,dx = 0. \quad (4.18)$$

Inserting (4.11)–(4.12) and (4.14)–(4.17) into (4.18) yields

$$\int_0^L \sum_{n=-N}^{N} \left\{ \left[\frac{\partial^3 a_n}{\partial t \partial y^2} + \frac{dq}{dt}\frac{d^2 f}{dy^2}w_n - \alpha_n^2 \frac{\partial a_n}{\partial t} - \frac{dq}{dt}f\alpha_n^2 w_n \right. \right.$$

$$+ \tilde{U}\left(\alpha_n i \frac{\partial^2 a_n}{\partial y^2} + q\frac{d^2 f}{dy^2}\alpha_n i w_n \right) - \frac{d^2 \tilde{U}}{dy^2}\left(\alpha_n i a_n + q f \alpha_n i w_n \right) - \tilde{U}\left(\alpha_n^3 i a_n + q f \alpha_n^3 i w_n \right)$$

$$- \frac{1}{Re}\left[\alpha_n^4 a_n + q f \alpha_n^4 w_n - 2\left(\alpha_n^2 \frac{\partial^2 a_n}{\partial y^2} + q\frac{d^2 f}{dy^2}\alpha_n^2 w_n \right) \right.$$

$$\left. \left. \left. + \frac{\partial^4 a_n}{\partial y^4} + q\frac{d^4 f}{dy^4}w_n \right] \right] P_n \bar{P}_k \right\} dx = 0.$$

By the orthogonality of the P_n functions, that is

$$\int_0^L P_n(x)\bar{P}_k(x)\,dx = \int_0^L e^{in\frac{2\pi}{L}x}e^{-ik\frac{2\pi}{L}x}\,dx = \int_0^L e^{i(n-k)\frac{2\pi}{L}x}\,dx = \begin{cases} L, \ n = k \\ 0, \ n \neq k \end{cases}$$

we get

$$
\frac{\partial^3 a_k}{\partial t \partial y^2} + \frac{dq}{dt}\frac{d^2 f}{dy^2}w_k - \alpha_k^2\frac{\partial a_k}{\partial t} - \frac{dq}{dt}f\alpha_k^2 w_k + \tilde{U}\left(\alpha_k i\frac{\partial^2 a_k}{\partial y^2} + q\frac{d^2 f}{dy^2}\alpha_k i w_k\right)
$$

$$
- \frac{\partial^2 \tilde{U}}{\partial y^2}\left(\alpha_k i a_k + qf\alpha_k i w_k\right) - \tilde{U}\left(\alpha_k^3 i a_k + qf\alpha_k^3 i w_k\right) - \frac{1}{Re}\left[\alpha_k^4 a_k + qf\alpha_k^4 w_k\right.
$$

$$
\left. -2\left(\alpha_k^2\frac{\partial^2 a_k}{\partial y^2} + q\frac{d^2 f}{dy^2}\alpha_k^2 w_k\right) + \frac{\partial^4 a_k}{\partial y^4} + q\frac{d^4 f}{dy^4}w_k\right] = 0 \triangleq E, \text{ for } k = -N, ..., N.
$$

$$\tag{4.19}$$

For the measurement (4.10), the Galerkin method yields

$$
z(t) = \sum_{k=-N}^{N}\frac{\partial^2 a_k}{\partial y^2}\left(y = -1, t\right)P_k(x_i) + \frac{5}{2}w(x_i)q. \tag{4.20}
$$

An interesting property of the set of equations (4.19) is that the equations are decoupled in terms of the wavenumber α_k. This fact lets us study each wavenumber individually. We now rewrite equation (4.19) in terms of a_k^R and a_k^I, where a_k^R and a_k^I are the real and imaginary parts of a_k, respectively. Since $real(a) = (a + \bar{a})/2$ and $imag(a) = (a - \bar{a})/2i$, the equations for a_k^R and a_k^I are obtained by

$$
\frac{1}{2}\left(E + \bar{E}\right) = 0
$$

and

$$
\frac{1}{2i}\left(E - \bar{E}\right) = 0,
$$

respectively. We have that

$$
\bar{E} = \frac{\partial^3 \bar{a}_k}{\partial t \partial y^2} + \frac{dq}{dt}\frac{d^2 f}{dy^2}\bar{w}_k - \alpha^2\frac{\partial \bar{a}_k}{\partial t} - \frac{dq}{dt}f\alpha_k^2 \bar{w}_k - \tilde{U}\left(\alpha_k i\frac{\partial^2 \bar{a}_k}{\partial y^2} + q\frac{d^2 f}{dy^2}\alpha_k i \bar{w}_k\right)
$$

$$
+ \frac{d^2 \tilde{U}}{dy^2}\left(\alpha_k i\bar{a}_k + qf\alpha_k i\bar{w}_k\right) + \tilde{U}\left(\alpha_k^3 i\bar{a}_k + qf\alpha_k^3 i\bar{w}_k\right) - \frac{1}{Re}\left[\alpha_k^4 \bar{a}_k + qf\alpha_k^4 \bar{w}_k\right.
$$

$$
\left. -2\left(\alpha_k^2\frac{\partial^2 \bar{a}_k}{\partial y^2} + q\frac{d^2 f}{dy^2}\alpha_k^2 \bar{w}_k\right) + \frac{\partial^4 \bar{a}_k}{\partial y^4} + q\frac{d^4 f}{dy^4}\bar{w}_k\right]
$$

so that

$$
\frac{1}{2}\left(E + \bar{E}\right) = \frac{\partial^3 a_k^R}{\partial t \partial y^2} + \frac{dq}{dt}\frac{d^2 f}{dy^2}w_k^R - \alpha_k^2\frac{\partial a_k^R}{\partial t} - \frac{dq}{dt}f\alpha_k^2 w_k^R
$$

$$
- \tilde{U}\left(\alpha_k\frac{\partial^2 a_k^I}{\partial y^2} + q\frac{d^2 f}{dy^2}\alpha_k w_k^I\right) + \frac{d^2 \tilde{U}}{dy^2}\left(\alpha_k a_k^I + qf\alpha_k w_k^I\right) + \tilde{U}\left(\alpha_k^3 a_k^I + qf\alpha_k^3 w_k^I\right)
$$

$$
- \frac{1}{Re}\left[\alpha_k^4 a_k^R + qf\alpha_k^4 w_k^R - 2\left(\alpha_k^2\frac{\partial^2 a_k^R}{\partial y^2} + q\frac{d^2 f}{dy^2}\alpha_k^2 w_k^R\right) + \frac{\partial^4 a_k^R}{\partial y^4} + q\frac{d^4 f}{dy^4}w_k^R\right] = 0
$$

$$\tag{4.21}$$

and

$$\frac{1}{2i}\left(E - \bar{E}\right) = \frac{\partial^3 a_k^I}{\partial t \partial y^2} + \frac{dq}{dt}\frac{d^2 f}{dy^2}w_k^I - \alpha_k^2\frac{\partial a_k^I}{\partial t} - \frac{dq}{dt}f\alpha_k^2 w_k^I$$

$$+ \tilde{U}\left(\alpha_k\frac{\partial^2 a_k^R}{\partial y^2} + q\frac{d^2 f}{dy^2}\alpha_k w_k^R\right) - \frac{d^2\tilde{U}}{dy^2}\left(\alpha_k a_k^R + qf\alpha_k w_k^R\right) - \tilde{U}\left(\alpha_k^3 a_k^R + qf\alpha_k^3 w_k^R\right)$$

$$- \frac{1}{Re}\left[\alpha_k^4 a_k^I + qf\alpha_k^4 w_k^I - 2\left(\alpha_k^2\frac{\partial^2 a_k^I}{\partial y^2} + q\frac{d^2 f}{dy^2}\alpha_k^2 w_k^I\right) + \frac{\partial^4 a_k^I}{\partial y^4} + q\frac{d^4 f}{dy^4}w_k^I\right] = 0.$$

$$(4.22)$$

Next, we discretize the equation in the y-direction. For this, we use the Chebyshev collocation method described in Section 2.7.3 on $N+1$ Chebyshev-Gauss-Labotto points as defined in (2.89). Applying the differentiation matrix $\mathcal{D}_N$, treating f and $\tilde{U}$ and their derivatives as known functions, yields

$$\mathcal{D}_N^2\frac{d\mathbf{a}_k^R}{dt} - \alpha_k^2\frac{d\mathbf{a}_k^R}{dt} = \frac{dq}{dt}\mathbf{f}_N^{(0)}\alpha_k^2 w_k^R - \frac{dq}{dt}\mathbf{f}_N^{(2)}w_k^R + \tilde{U}_N\left(\alpha_k\mathcal{D}_N^2\mathbf{a}_k^I + q\mathbf{f}_N^{(2)}\alpha_k w_k^I\right)$$

$$- \tilde{U}_N^{(2)}\left(\alpha_k\mathbf{a}_k^I + q\mathbf{f}_N^{(0)}\alpha_k w_k^I\right) - \tilde{U}_N\left(\alpha_k^3\mathbf{a}_k^I + q\mathbf{f}_N^{(0)}\alpha_k^3 w_k^I\right) + \frac{1}{Re}\left[\alpha_k^4\mathbf{a}_k^R + q\mathbf{f}_N^{(0)}\alpha_k^4 w_k^R\right.$$

$$\left. -2\left(\alpha_k^2\mathcal{D}_N^2\mathbf{a}_k^R + q\mathbf{f}_N^{(2)}\alpha_k^2 w_k^R\right) + \mathcal{D}_N^4\mathbf{a}_k^R + q\mathbf{f}_N^{(4)}w_k^R\right] \quad (4.23)$$

$$\mathcal{D}_N^2\frac{d\mathbf{a}_k^I}{dt} - \alpha_k^2\frac{d\mathbf{a}_k^I}{dt} = \frac{dq}{dt}\mathbf{f}_N^{(0)}\alpha_k^2 w_k^I - \frac{dq}{dt}\mathbf{f}_N^{(2)}w_k^I - \tilde{U}_N\left(\alpha_k\mathcal{D}_N^2\mathbf{a}_k^R + q\mathbf{f}_N^{(2)}\alpha_k w_k^R\right)$$

$$+ \tilde{U}_N^{(2)}\left(\alpha_k\mathbf{a}_k^R + q\mathbf{f}_N^{(0)}\alpha_k w_k^R\right) + \tilde{U}_N\left(\alpha_k^3\mathbf{a}_k^R + q\mathbf{f}_N^{(0)}\alpha_k^3 w_k^R\right) + \frac{1}{Re}\left[\alpha_k^4\mathbf{a}_k^I + q\mathbf{f}_N^{(0)}\alpha_k^4 w_k^I\right.$$

$$\left. -2\left(\alpha_k^2\mathcal{D}_N^2\mathbf{a}_k^I + q\mathbf{f}_N^{(2)}\alpha_k^2 w_k^I\right) + \mathcal{D}_N^4\mathbf{a}_k^I + q\mathbf{f}_N^{(4)}w_k^I\right] \quad (4.24)$$

where $\mathbf{a}_k^R$ and $\mathbf{a}_k^I$ denote the vectors

$$\mathbf{a}_k^R = \begin{bmatrix} a_k^R(y_0) & a_k^R(y_1) & \cdots & a_k^R(y_N) \end{bmatrix}^T$$

$$\mathbf{a}_k^I = \begin{bmatrix} a_k^I(y_0) & a_k^I(y_1) & \cdots & a_k^I(y_N) \end{bmatrix}^T$$

and

$$\tilde{U}_N^{(m)} = \begin{bmatrix} \frac{d^m\tilde{U}}{dy^m}(y_0) & 0 & 0 & 0 \\ 0 & \frac{d^m\tilde{U}}{dy^m}(y_1) & 0 & 0 \\ 0 & 0 & \ddots & 0 \\ 0 & 0 & 0 & \frac{d^m\tilde{U}}{dy^m}(y_N) \end{bmatrix}, \quad m = 0, 1, 2... \quad (4.25)$$

$$\mathbf{f}_N^{(m)} = \begin{bmatrix} \frac{d^m f}{dy^m}(y_0) & \frac{d^m f}{dy^m}(y_1) & \cdots & \frac{d^m f}{dy^m}(y_N) \end{bmatrix}^T, \quad m = 0, 1, 2, ...$$

Above, (m) denotes the mth order derivative with respect to y. It remains to implement the boundary conditions. The Dirichlet boundary conditions are satisfied by simply setting $a_k^R(y_0) = a_k^I(y_0) = a_k^R(y_N) = a_k^I(y_N) = 0$, and omitting

the differential equations for these variables. Satisfying the Neumann boundary conditions is more involved. We start by noticing that the Neumann boundary conditions imply that

$$\sum_{j=0}^{N} d_{0j} a_k(y_j) = 0, \text{ and } \sum_{j=0}^{N} d_{Nj} a_k(y_j) = 0 \tag{4.26}$$

where the superscripts I and R are omitted since the following derivation is valid for either one. The d_{jk} constants in (4.26) are the elements of $\mathcal{D}_N$ as defined in (2.90). From (4.26), we can solve for $a_k(y_1)$ and $a_k(y_{N-1})$ to obtain

$$\begin{aligned} a_k(y_1) &= \mathbf{l}_1^T \mathbf{a} \\ a_k(y_{N-1}) &= \mathbf{l}_2^T \mathbf{a} \end{aligned}$$

where we have defined

$$\left[\begin{array}{c} \mathbf{l}_1^T \\ \mathbf{l}_2^T \end{array} \right] = - \left[\begin{array}{cc} d_{01} & d_{0(N-1)} \\ d_{N1} & d_{N(N-1)} \end{array} \right]^{-1} \left[\begin{array}{cccc} d_{02} & d_{03} & \cdots & d_{0(N-2)} \\ d_{N2} & d_{N3} & \cdots & d_{N(N-2)} \end{array} \right]$$

and

$$\mathbf{a} = \left[\begin{array}{cccc} a_k(y_2) & a_k(y_3) & \cdots & a_k(y_{N-2}) \end{array} \right]^T.$$

Thus, we have that

$$\mathbf{a}_k = \left[\begin{array}{c} \mathbf{0}^T \\ \mathbf{l}_1^T \\ \mathcal{I}_{N-3} \\ \mathbf{l}_2^T \\ \mathbf{0}^T \end{array} \right] \mathbf{a} \triangleq \mathcal{I}_a \mathbf{a}. \tag{4.27}$$

Inserting (4.27) into (4.23)–(4.24), and keeping in mind that the equations for $a_k(y_0)$, $a_k(y_1)$, $a_k(y_{N-1})$, and $a_k(y_N)$ should be omitted since these variables are determined by the boundary conditions, we obtain

$$\begin{aligned} R \left(\mathcal{D}_N^2 - \alpha_k^2 \mathcal{I} \right) \mathcal{I}_a \dot{\mathbf{a}}^R &= \frac{1}{Re} R \left(\mathcal{D}_N^4 \mathcal{I}_a - 2\alpha_k^2 \mathcal{D}_N^2 \mathcal{I}_a + \alpha_k^4 \mathcal{I}_a \right) \mathbf{a}^R \\ &\quad + R \left(\alpha_k \tilde{U}_N \mathcal{D}_N^2 \mathcal{I}_a - \left(\alpha_k \tilde{U}_N^{(2)} + \alpha_k^3 \tilde{U}_N \right) \mathcal{I}_a \right) \mathbf{a}^I \\ &\quad + w_k^I R \left(\alpha_k \tilde{U}_N \mathbf{f}_N^{(2)} - \left(\alpha_k \tilde{U}_N^{(2)} + \alpha_k^3 \tilde{U}_N \right) \mathbf{f}_N^{(0)} \right) q \\ &\quad + \frac{w_k^R}{Re} R \left(\alpha_k^4 \mathbf{f}_N^{(0)} - 2\alpha_k^2 \mathbf{f}_N^{(2)} + \mathbf{f}_N^{(4)} \right) q - w_k^R R \left(\mathbf{f}_N^{(2)} - \alpha_k^2 \mathbf{f}_N^{(0)} \right) \dot{q} \end{aligned}$$

$$\begin{aligned} R \left(\mathcal{D}_N^2 - \alpha_k^2 \mathcal{I} \right) \mathcal{I}_a \dot{\mathbf{a}}^I &= -R \left(\alpha_k \tilde{U}_N \mathcal{D}_N^2 \mathcal{I}_a - \left(\alpha_k \tilde{U}_N^{(2)} + \alpha_k^3 \tilde{U}_N \right) \mathcal{I}_a \right) \mathbf{a}^R \\ &\quad + \frac{1}{Re} R \left(\mathcal{D}_N^4 \mathcal{I}_a - 2\alpha_k^2 \mathcal{D}_N^2 \mathcal{I}_a + \alpha_k^4 \mathcal{I}_a \right) \mathbf{a}^I \\ &\quad - w_k^R R \left(\alpha_k \tilde{U}_N \mathbf{f}_N^{(2)} - \left(\alpha_k \tilde{U}_N^{(2)} + \alpha_k^3 \tilde{U}_N \right) \mathbf{f}_N^{(0)} \right) q \\ &\quad + \frac{w_k^I}{Re} R \left(\alpha_k^4 \mathbf{f}_N^{(0)} - 2\alpha_k^2 \mathbf{f}_N^{(2)} + \mathbf{f}_N^{(4)} \right) q - w_k^I R \left(\mathbf{f}_N^{(2)} - \alpha_k^2 \mathbf{f}_N^{(0)} \right) \dot{q} \end{aligned}$$

where R is a matrix that selects appropriate rows, defined as

$$R = \begin{bmatrix} \mathbf{0}_{(N-3)\times 2} & \mathcal{I}_{N-3} & \mathbf{0}_{(N-3)\times 2} \end{bmatrix}.$$

Assuming the measurement is real, we redefine z as the real part of (4.20), so we get

$$z(t) = \sum_{k=-M}^{M} \left\{ \cos\left(\alpha_k x_i\right) \mathbf{s}_1^T \mathcal{D}_N^2 \mathcal{I}_a \mathbf{a}^R - \sin\left(\alpha_k x_i\right) \mathbf{s}_1^T \mathcal{D}_N^2 \mathcal{I}_a \mathbf{a}^I \right\} + \frac{5}{2} w(x_i) q \quad (4.28)$$

where $\mathbf{s}_j$ is a vector of compatible dimension with a 1 at the jth position being the only nonzero entry. It is clear that the measurement (4.28) is not decoupled in terms of the wavenumber α_k, but if we choose w appropriately, we may omit all terms but one in (4.28). The reason for this will be discussed in the next section. Finally we get the system on state space form

$$\dot{\mathbf{x}} = A\mathbf{x} + Bu \quad (4.29)$$
$$z = C\mathbf{x} + Du \quad (4.30)$$

where

$$\mathbf{x} = \begin{bmatrix} a_k^R\left(y_2\right) & \cdots & a_k^R\left(y_{N-2}\right) & a_k^I\left(y_2\right) & \cdots & a_k^I\left(y_{N-2}\right) & q \end{bmatrix}^T, \; u = \dot{q}$$

$$A = \begin{bmatrix} M^{-1}A_R^R & M^{-1}A_R^I & M^{-1}\left(w_k^I \mathbf{q}_1 + w_k^R \mathbf{q}_2\right) \\ M^{-1}A_I^R & M^{-1}A_I^I & M^{-1}\left(-w_k^R \mathbf{q}_1 + w_k^I \mathbf{q}_2\right) \\ 0 & 0 & 0 \end{bmatrix}, \; B = \begin{bmatrix} -w_k^R M^{-1}\mathbf{b} \\ -w_k^I M^{-1}\mathbf{b} \\ 1 \end{bmatrix}$$

$$C = \begin{bmatrix} \cos\left(\alpha_k x_i\right) \mathbf{s}_N^T \mathcal{D}_N^2 \mathcal{I}_a & -\sin\left(\alpha_k x_i\right) \mathbf{s}_N^T \mathcal{D}_N^2 \mathcal{I}_a & \frac{5}{2} w(x_i) \end{bmatrix}, \; D = 0$$

$$M = R\left(\mathcal{D}_N^2 - \alpha_k^2 \mathcal{I}\right)\mathcal{I}_a$$
$$A_R^R = A_I^I = \frac{1}{Re} R\left(\mathcal{D}_N^4 \mathcal{I}_a - 2\alpha_k^2 \mathcal{D}_N^2 \mathcal{I}_a + \alpha_k^4 \mathcal{I}_a\right)$$
$$A_R^I = -A_I^R = R\left(\alpha_k \tilde{U}_N \mathcal{D}_N^2 \mathcal{I}_a - \left(\alpha_k \tilde{U}_N^{(2)} + \alpha_k^3 \tilde{U}_N\right)\mathcal{I}_a\right)$$

$$\mathbf{q}_1 = R\left(\alpha_k \tilde{U}_N \mathbf{f}_N^{(2)} - \left(\alpha_k \tilde{U}_N^{(2)} + \alpha_k^3 \tilde{U}_N\right)\mathbf{f}_N^{(0)}\right)$$
$$\mathbf{q}_2 = \frac{1}{Re} R\left(\alpha_k^4 \mathbf{f}_N^{(0)} - 2\alpha_k^2 \mathbf{f}_N^{(2)} + \mathbf{f}_N^{(4)}\right)$$
$$\mathbf{b} = R\left(\mathbf{f}_N^{(2)} - \alpha_k^2 \mathbf{f}_N^{(0)}\right), \; R = \begin{bmatrix} \mathbf{0}_{(N-3)\times 2} & \mathcal{I}_{N-3} & \mathbf{0}_{(N-3)\times 2} \end{bmatrix}.$$
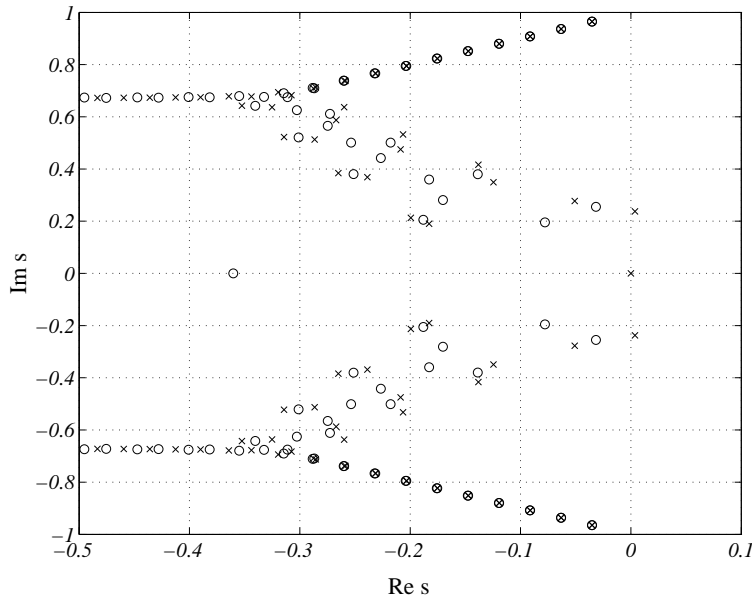
Figure 4.2: Poles ($\times$) and zeros ($\circ$) for the system.

Classical Control

In the previous section we developed a state space representation of the discretized 2D linearized channel flow equations. Apart from the measurement equation, the resulting system is decoupled in terms of the wave number. It turns out that the system has one complex conjugate pair of eigenvalues in the right half of the complex plane for $k = 2$. All other poles of the system are in the left half of the complex plane (except for the pole at the origin, due to the boundary control input configuration). Figure 4.2 shows poles and zeros for $k = 2$ at Reynolds number 10000 and $N = 150$ (i.e. 151 collocation points), and with the shear measurement taken at $x_i = \pi$, $w(x) = sin(\frac{2\pi k}{L}x)$, and $L = 4\pi$. With this choice of $w(x)$, (A, B) is rendered uncontrollable for all wave numbers with $k \neq 2$. Therefore, the fact that the measurement does not decouple in terms of the wavenumber does not present a problem, since the control will be unable to destabilize any pole of sub-systems with $k \neq 2$. Figure 4.3 shows the Nyquist plot. The Nyquist stability criterion indicates that when $-1/K \in (-105, 0)$ (approximately), no poles of the closed loop system lie in the right half plane, which corresponds to $K > 0.0095$. This result is confirmed by Figure 4.4, which shows the real component of the system's least stable eigenvalue as a function of feedback gain K.

Figure 4.3: Nyquist plot.

Figure 4.4: Real component of the least stable eigenvalue as a function of feedback gain K.
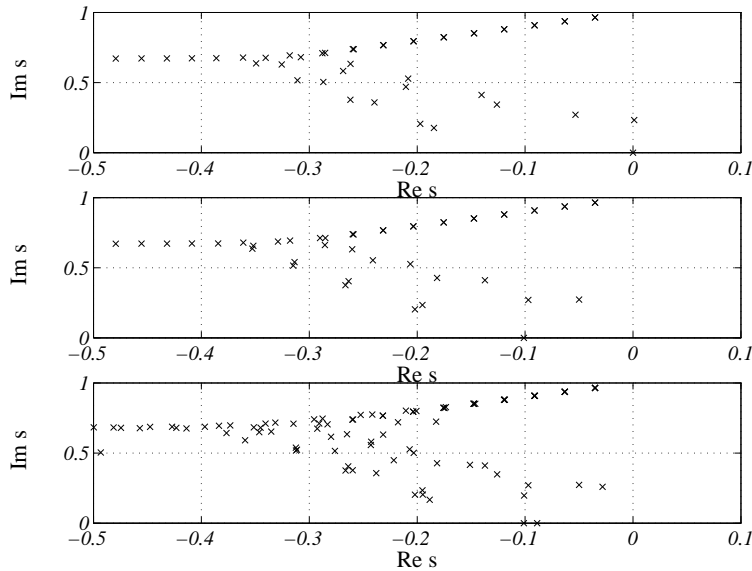
Figure 4.5: LQG synthesis: system poles for the open-loop system (top), the state feedback closed-loop system (middle), and the output feedback closed-loop system (bottom).

LQG Control

Assuming that (4.29)–(4.30) are subjected to additive disturbances, w_d and w_n, that are uncorrelated Gaussian stochastic processes with zero means and covariances W, and V, respectively, it is straight forward to apply LQG control theory. For illustration, we select $W = I$ and $V = 1$, and $Q = I$ and $R = 1$, and construct the controller according to (3.6). Figure 4.5 shows the result in terms of the system poles for the open-loop system, the state feedback closed-loop system, and the output feedback closed-loop system. Clearly, the open-loop unstable poles are moved into the left half of the complex plane by the control.

Implementation

Although the state space model (4.29)–(4.30) takes the form of a single-input-single-output (SISO) system, with input $u = \dot{q}(t)$ and output $z = \partial u/\partial y\,(x_i, -1, t)$, the realization of the control system is distributed. This follows from the fact that the actuation is blowing and suction of fluid distributed along the wall as a *cosine* in x $(dw/dx$, where w is a sine in $x)$, whose amplitude is altered with a speed given by the control input $u = \dot{q}(t)$. The control law is centralized since the control signal must reach all actuators on the wall. Centralized versus decentralized control schemes are discussed in more detail in Section 4.2.

4.1.2 3D Channel Flow

Reduced Order Model

In [20] linear control is applied to the 3D channel flow. In this case, shear measurements in two directions ($\partial U/\partial y$ and $\partial W/\partial y$) are taken at every point on both walls, and actuation is applied in the form of wall transpiration on both walls. The point of departure is the linearized Navier-Stokes equations for 3D channel flow (2.55)–(2.58), which may be rewritten in terms of the wall-normal velocity component v, and the wall-normal vorticity component, denoted ω (vorticity is defined as $\omega = curl(\mathbf{W})$). Taking the Laplacian of (2.57) yields

$$
\frac{\partial}{\partial t}\left(\frac{\partial^2 v}{\partial x^2} + \frac{\partial^2 v}{\partial y^2} + \frac{\partial^2 v}{\partial z^2}\right) + \tilde{U}\frac{\partial}{\partial x}\left(\frac{\partial^2 v}{\partial x^2} + \frac{\partial^2 v}{\partial y^2} + \frac{\partial^2 v}{\partial z^2}\right)
$$
$$
+ \frac{\partial^2 \tilde{U}}{\partial y^2}\frac{\partial v}{\partial x} + 2\frac{\partial \tilde{U}}{\partial y}\frac{\partial^2 v}{\partial x \partial y} = -\frac{\partial}{\partial y}\left(\frac{\partial^2 p}{\partial x^2} + \frac{\partial^2 p}{\partial y^2} + \frac{\partial^2 p}{\partial z^2}\right)
$$
$$
+ \frac{1}{Re}\left(\frac{\partial^4 v}{\partial x^4} + \frac{\partial^4 v}{\partial y^4} + \frac{\partial^4 v}{\partial z^4} + 2\frac{\partial^4 v}{\partial x^2 \partial y^2} + 2\frac{\partial^4 v}{\partial x^2 \partial z^2} + 2\frac{\partial^4 v}{\partial y^2 \partial z^2}\right). \quad (4.31)
$$

Taking the divergence of (2.56)–(2.58) yields

$$
\frac{\partial}{\partial t}\left(\frac{\partial u}{\partial x} + \frac{\partial v}{\partial y} + \frac{\partial w}{\partial z}\right) + \tilde{U}\frac{\partial}{\partial x}\left(\frac{\partial u}{\partial x} + \frac{\partial v}{\partial y} + \frac{\partial w}{\partial z}\right) + 2\frac{d\tilde{U}}{dy}\frac{\partial v}{\partial x} =
$$
$$
-\frac{\partial^2 p}{\partial x^2} - \frac{\partial^2 p}{\partial y^2} - \frac{\partial^2 p}{\partial z^2} + \frac{1}{Re}\left(\frac{\partial^2}{\partial x^2}\left(\frac{\partial u}{\partial x} + \frac{\partial v}{\partial y} + \frac{\partial w}{\partial z}\right)\right.
$$
$$
\left. + \frac{\partial^2}{\partial y^2}\left(\frac{\partial u}{\partial x} + \frac{\partial v}{\partial y} + \frac{\partial w}{\partial z}\right) + \frac{\partial^2}{\partial z^2}\left(\frac{\partial u}{\partial x} + \frac{\partial v}{\partial y} + \frac{\partial w}{\partial z}\right)\right)
$$

and using continuity (2.55), we obtain

$$
2\frac{d\tilde{U}}{dy}\frac{\partial v}{\partial x} = -\frac{\partial^2 p}{\partial x^2} - \frac{\partial^2 p}{\partial y^2} - \frac{\partial^2 p}{\partial z^2}. \quad (4.32)
$$

Inserting (4.32) into (4.31) yields the equation for the wall-normal velocity component, v, as

$$
\frac{\partial}{\partial t}\left(\frac{\partial^2 v}{\partial x^2} + \frac{\partial^2 v}{\partial y^2} + \frac{\partial^2 v}{\partial z^2}\right) = -\tilde{U}\frac{\partial}{\partial x}\left(\frac{\partial^2 v}{\partial x^2} + \frac{\partial^2 v}{\partial y^2} + \frac{\partial^2 v}{\partial z^2}\right) + \frac{d^2 \tilde{U}}{dy^2}\frac{\partial v}{\partial x}
$$
$$
+ \frac{1}{Re}\left(\frac{\partial^4 v}{\partial x^4} + \frac{\partial^4 v}{\partial y^4} + \frac{\partial^4 v}{\partial z^4} + 2\frac{\partial^4 v}{\partial x^2 \partial y^2} + 2\frac{\partial^4 v}{\partial x^2 \partial z^2} + 2\frac{\partial^4 v}{\partial y^2 \partial z^2}\right). \quad (4.33)
$$

The wall-normal component of vorticity is $\omega = \partial u/\partial z - \partial w/\partial x$. Thus, taking the partial derivative of (2.56) with respect to z and subtracting the partial derivative of (2.58) with respect to x, yields

$$
\frac{\partial \omega}{\partial t} = -\frac{d\tilde{U}}{dy}\frac{\partial v}{\partial z} - \tilde{U}\frac{\partial \omega}{\partial x} + \frac{1}{Re}\left(\frac{\partial^2 \omega}{\partial x^2} + \frac{\partial^2 \omega}{\partial y^2} + \frac{\partial^2 \omega}{\partial z^2}\right). \quad (4.34)
$$

The control is applied as an unsteady boundary condition on the wall-normal velocity component v, and the no-slip condition in the x and z directions leads to homogeneous Dirichlet boundary conditions for ω, that is

$$\omega\left(x, y = \pm 1, z, t\right) = 0.$$

By continuity, $\partial v / \partial y = 0$ at the wall, so (4.33) is also subject to homogeneous Neumann boundary conditions. Expanding v and ω as

$$
\begin{aligned}
v(x, y, z, t) &= \sum_{k_x, k_z} \hat{v}\left(k_x, y, k_z, t\right) e^{i\left(\frac{2\pi k_x}{L_x} x + \frac{2\pi k_z}{L_z} z\right)} \\
\omega(x, y, z, t) &= \sum_{k_x, k_z} \hat{\omega}\left(k_x, y, k_z, t\right) e^{i\left(\frac{2\pi k_x}{L_x} x + \frac{2\pi k_z}{L_z} z\right)},
\end{aligned}
$$

the Fourier-Galerkin method yields

$$
\begin{aligned}
\frac{\partial}{\partial t}\left(-\alpha_x^2 \hat{v} + \frac{\partial^2 \hat{v}}{\partial y^2} - \alpha_z^2 \hat{v}\right) &= \tilde{U}\left(i\alpha_x^3 \hat{v} - i\alpha_x \frac{\partial^2 \hat{v}}{\partial y^2} + i\alpha_x \alpha_z^2 \hat{v}\right) \\
&+ \frac{\partial^2 \tilde{U}}{\partial y^2} i\alpha_x \hat{v} + \frac{1}{Re}\left(\alpha_x^4 \hat{v} + \frac{\partial^4 \hat{v}}{\partial y^4} + \alpha_z^4 \hat{v} - 2\alpha_x^2 \frac{\partial^2 \hat{v}}{\partial y^2} + 2\alpha_x^2 \alpha_z^2 \hat{v} - 2\alpha_z^2 \frac{\partial^2 \hat{v}}{\partial y^2}\right)
\end{aligned}
$$

$$
\frac{\partial \hat{\omega}}{\partial t} = -\frac{\partial \tilde{U}}{\partial y} i\alpha_z \hat{v} - \tilde{U} i\alpha_x \hat{\omega} + \frac{1}{Re}\left(-\alpha_x^2 \hat{\omega} + \frac{\partial^2 \hat{\omega}}{\partial y^2} - \alpha_z^2 \hat{\omega}\right)
$$

where

$$
\begin{aligned}
\alpha_x &= \frac{2\pi k_x}{L_x} \\
\alpha_z &= \frac{2\pi k_z}{L_x}.
\end{aligned}
$$

As in Section 4.1.1 we discretize the wall-normal direction on $N + 1$ Chebyshev-Gauss-Lobatto (2.89) points using the Chebyshev-collocation method. Applying the differentiation matrix $\mathcal{D}_N$, treating $\tilde{U}$ and its derivatives as known functions, yields

$$
\begin{aligned}
\left(\mathcal{D}_N^2 - \left(\alpha_x^2 + \alpha_z^2\right)\mathcal{I}\right)\frac{d\hat{\mathbf{v}}_a}{dt} &= \left(\tilde{U}_N^{(0)}\left(-i\alpha_x \mathcal{D}_N^2 + \left(i\alpha_x^3 + i\alpha_x \alpha_z^2\right)\mathcal{I}\right)\right. \\
&\left.+ \tilde{U}_N^{(2)} i\alpha_x + \frac{1}{Re}\left(\mathcal{D}_N^4 - 2\left(\alpha_x^2 + \alpha_z^2\right)\mathcal{D}_N^2 + \left(\alpha_x^2 + \alpha_z^2\right)^2 \mathcal{I}\right)\right)\hat{\mathbf{v}}_a \quad (4.35)
\end{aligned}
$$

$$
\frac{d\hat{\omega}_a}{dt} = -\tilde{U}_N^{(1)} i\alpha_z \hat{\mathbf{v}}_a + \left(-\tilde{U}_N^{(0)} i\alpha_x + \frac{1}{Re}\left(\mathcal{D}_N^2 - \left(\alpha_x^2 + \alpha_z^2\right)\mathcal{I}\right)\right)\hat{\omega}_a \qquad (4.36)
$$

where

$$
\begin{aligned}
\hat{\mathbf{v}}_a &= \left[\begin{array}{cccc} \hat{v}(y_0) & \hat{v}(y_1) & \cdots & \hat{v}(y_N) \end{array}\right]^T \\
\hat{\omega}_a &= \left[\begin{array}{cccc} \hat{\omega}(y_0) & \hat{\omega}(y_1) & \cdots & \hat{\omega}(y_N) \end{array}\right]^T
\end{aligned}
$$

and $\tilde{U}_N^{(m)}$ is defined as in (4.25). Since the time derivative of $\hat{v}(y_0)$ and $\hat{v}(y_N)$ occur in (4.35)–(4.36), we let the time derivative of $\hat{v}(y_0)$ and $\hat{v}(y_N)$ be the control input. The Neumann boundary conditions on v imply that

$$\sum_{j=0}^{N} d_{0j}\hat{v}(y_j) = 0, \text{ and } \sum_{j=0}^{N} d_{Nj}\hat{v}(y_j) = 0. \tag{4.37}$$

Solving (4.37) for $\hat{v}(y_1)$ and $\hat{v}(y_{N-1})$, yields

$$\hat{v}(y_1) = \mathbf{l}_1^T \hat{\mathbf{v}} \tag{4.38}$$

$$\hat{v}(y_{N-1}) = \mathbf{l}_2^T \hat{\mathbf{v}} \tag{4.39}$$

where we have defined

$$\left[\begin{array}{c} \mathbf{l}_1^T \\ \mathbf{l}_2^T \end{array}\right] = -\left[\begin{array}{cc} d_{01} & d_{0(N-1)} \\ d_{N1} & d_{N(N-1)} \end{array}\right]^{-1} \left[\begin{array}{ccccc} d_{00} & d_{02} & \cdots & d_{0(N-2)} & d_{0N} \\ d_{N0} & d_{N2} & \cdots & d_{N(N-2)} & d_{NN} \end{array}\right], \text{ and}$$

$$\hat{\mathbf{v}} = \left[\begin{array}{ccccc} \hat{v}(y_0) & \hat{v}(y_2) & \cdots & \hat{v}(y_{N-2}) & \hat{v}(y_N) \end{array}\right]^T.$$

Thus, we get

$$\hat{\mathbf{v}}_a = \left[\begin{array}{c} \mathbf{s}_1^T \\ \mathbf{l}_1^T \\ \mathcal{I}_{N-3} \\ \mathbf{l}_2^T \\ \mathbf{s}_{N-3}^T \end{array}\right] \hat{\mathbf{v}} \triangleq \mathcal{I}_v \hat{\mathbf{v}} \tag{4.40}$$

and, defining $\hat{\omega} \triangleq \left[\begin{array}{cccc} \hat{\omega}(y_1) & \hat{\omega}(y_2) & \cdots & \hat{\omega}(y_{N-1}) \end{array}\right]^T$, the homogeneous Dirichlet boundary conditions on ω yields

$$\hat{\omega}_a = \left[\begin{array}{c} \mathbf{0}^T \\ \mathcal{I}_{N-1} \\ \mathbf{0}^T \end{array}\right] \hat{\omega} \triangleq \mathcal{I}_\omega \hat{\omega}. \tag{4.41}$$

Inserting (4.40) and (4.41) into (4.35)–(4.36), omitting the equations for $\hat{v}(y_1)$, and $\hat{v}(y_{N-1})$ (since they are determined by the homogeneous Neumann boundary conditions), and omitting the equations for $\hat{\omega}(y_0)$ and $\hat{\omega}(y_N)$ (since they are zero due to the homogeneous Dirichlet boundary conditions), we get

$$\frac{d\hat{\mathbf{v}}}{dt} = M_1^{-1} R_1 \left(\tilde{U}_N^{(0)} \left(-i\alpha_x \mathcal{D}_N^2 + i\alpha_x \alpha \mathcal{I} \right) + \tilde{U}_N^{(2)} i\alpha_x \right.$$
$$\left. + \frac{1}{Re} \left(\mathcal{D}_N^4 - 2\alpha \mathcal{D}_N^2 + \alpha^2 \mathcal{I} \right) \right) \mathcal{I}_v \hat{\mathbf{v}} \quad (4.42)$$

$$\frac{d\hat{\omega}}{dt} = -M_2^{-1} R_2 \tilde{U}_N^{(1)} i\alpha_z \mathcal{I}_v \hat{\mathbf{v}} + M_2^{-1} R_2 \left(-\tilde{U}_N^{(0)} i\alpha_x + \frac{1}{Re} \left(\mathcal{D}_N^2 - \alpha \mathcal{I} \right) \right) \mathcal{I}_\omega \hat{\omega} \quad (4.43)$$

where $\alpha = \alpha_x^2 + \alpha_z^2$, and

$$
\begin{aligned}
M_1 &= R_1 \left(\mathcal{D}_N^2 - \left(\alpha_x^2 + \alpha_z^2 \right) \mathcal{I} \right) \mathcal{I}_v \\
M_2 &= R_2 \mathcal{I}_\omega \\
R_1 &= \begin{bmatrix} 1 & 0 & \cdots & 0 & 0 \\ \mathbf{0} & \mathbf{0} & \mathcal{I}_{N-3} & \mathbf{0} & \mathbf{0} \\ 0 & 0 & \cdots & 0 & 1 \end{bmatrix} \\
R_2 &= \begin{bmatrix} \mathbf{0} & \mathcal{I}_{N-1} & \mathbf{0} \end{bmatrix} .
\end{aligned}
$$

The measurement $\hat{z}$ is the following

$$
\hat{z}(\alpha_x, \alpha_z, t) = \frac{1}{Re} \begin{bmatrix} -\frac{\partial \hat{u}}{\partial y} \left(\alpha_x, y = 1, \alpha_z, t \right) \\ \frac{\partial \hat{u}}{\partial y} \left(\alpha_x, y = -1, \alpha_z, t \right) \\ -\frac{\partial \hat{w}}{\partial y} \left(\alpha_x, y = 1, \alpha_z, t \right) \\ \frac{\partial \hat{w}}{\partial y} \left(\alpha_x, y = -1, \alpha_z, t \right) \end{bmatrix} ,
$$

which is obtained physically by measuring the shear in two directions ($\partial U / \partial y$ and $\partial W / \partial y$) on the entire wall. From continuity (2.55) we have that

$$
i \alpha_x \hat{u} + \frac{\partial \hat{v}}{\partial y} + i \alpha_z \hat{w} = 0
$$

which, along with $\hat{\omega} = i \alpha_z \hat{u} - i \alpha_x \hat{w}$, yield

$$
\begin{aligned}
\hat{u} &= \frac{i}{\alpha} \left(\alpha_x \frac{\partial \hat{v}}{\partial y} - \alpha_z \hat{\omega} \right) \\
\hat{w} &= \frac{i}{\alpha} \left(\alpha_z \frac{\partial \hat{v}}{\partial y} + \alpha_x \hat{\omega} \right) .
\end{aligned}
$$

So the measurement is

$$
\hat{z}(\alpha_x, \alpha_z, t) = \frac{i}{\alpha Re} \begin{bmatrix} -\alpha_x \mathbf{s}_{N+1}^T \mathcal{D}_N^2 \mathcal{I}_v \hat{\mathbf{v}} + \alpha_z \mathbf{s}_{N+1}^T \mathcal{D}_N^1 \mathcal{I}_\omega \hat{\omega} \\ \alpha_x \mathbf{s}_1^T \mathcal{D}_N^{(2)} \mathcal{I}_v \hat{\mathbf{v}} - \alpha_z \mathbf{s}_1^T \mathcal{D}_N^1 \mathcal{I}_\omega \hat{\omega} \\ -\alpha_z \mathbf{s}_{N+1}^T \mathcal{D}_N^{(2)} \mathcal{I}_v \hat{\mathbf{v}} - \alpha_x \mathbf{s}_{N+1}^T \mathcal{D}_N^1 \mathcal{I}_\omega \hat{\omega} \\ \alpha_z \mathbf{s}_1^T \mathcal{D}_N^{(2)} \mathcal{I}_v \hat{\mathbf{v}} + \alpha_x \mathbf{s}_1^T \mathcal{D}_N^1 \mathcal{I}_\omega \hat{\omega} \end{bmatrix} .
$$

Finally, replacing the equations for $\hat{v}(y_0)$ and $\hat{v}(y_N)$ in (4.42) by the control input, we get the system on state space form

$$
\begin{aligned}
\dot{\mathbf{x}} &= A\mathbf{x} + B\mathbf{u} & (4.44) \\
z &= C\mathbf{x} + D\mathbf{u} & (4.45)
\end{aligned}
$$

where

$$
\mathbf{x} = \begin{bmatrix} \hat{\mathbf{v}}^T & \hat{\omega}^T \end{bmatrix}^T , \quad \mathbf{u} = \begin{bmatrix} \dot{\hat{v}}(y_0) & \dot{\hat{v}}(y_N) \end{bmatrix}^T
$$

$$
A = \begin{bmatrix} A_{11} & \mathbf{0} \\ A_{21} & A_{22} \end{bmatrix} , \quad B = \begin{bmatrix} \mathcal{I}_b \\ \mathbf{0} \end{bmatrix}
$$

$$C = \frac{i}{Re\left(\alpha_z^2 + \alpha_x^2\right)} \begin{bmatrix} -\alpha_x \mathbf{s}_{N+1}^T \mathcal{D}_N^2 \mathcal{I}_v & \alpha_z \mathbf{s}_{N+1}^T \mathcal{D}_N^1 \mathcal{I}_\omega \\ \alpha_x \mathbf{s}_1^T \mathcal{D}_N^{(2)} \mathcal{I}_v & -\alpha_z \mathbf{s}_1^T \mathcal{D}_N^1 \mathcal{I}_\omega \\ -\alpha_z \mathbf{s}_{N+1}^T \mathcal{D}_N^{(2)} \mathcal{I}_v & -\alpha_x \mathbf{s}_{N+1}^T \mathcal{D}_N^1 \mathcal{I}_\omega \\ \alpha_z \mathbf{s}_1^T \mathcal{D}_N^{(2)} \mathcal{I}_v & \alpha_x \mathbf{s}_1^T \mathcal{D}_N^1 \mathcal{I}_\omega \end{bmatrix}, \; D = \mathbf{0}_{4 \times 2}$$

$$A_{11} = R_3 M_1^{-1} R_1 \left(\tilde{U}_N^{(0)} \left(-i\alpha_x \mathcal{D}_N^2 + \left(i\alpha_x^3 + i\alpha_x \alpha_z^2 \right) \mathcal{I} \right) + \tilde{U}_N^{(2)} i\alpha_x \right.$$
$$\left. + \frac{1}{Re} \left(\mathcal{D}_N^4 - 2 \left(\alpha_x^2 + \alpha_z^2 \right) \mathcal{D}_N^2 + \left(\alpha_x^2 + \alpha_z^2 \right)^2 \mathcal{I} \right) \right) \mathcal{I}_v$$

$$A_{21} = -M_2^{-1} R_2 \tilde{U}_N^{(1)} i\alpha_z \mathcal{I}_v$$
$$A_{22} = M_2^{-1} R_2 \left(-\tilde{U}_N^{(0)} i\alpha_x + \frac{1}{Re} \left(\mathcal{D}_N^2 - \left(\alpha_x^2 + \alpha_z^2 \right) \mathcal{I} \right) \right) \mathcal{I}_\omega$$

$$\mathcal{I}_b = \begin{bmatrix} 1 & 0 & \cdots & 0 & 0 \\ 0 & 0 & \cdots & 0 & 1 \end{bmatrix}^T_{2 \times (N-1)}$$

$$R_3 = \begin{bmatrix} 0 & \cdots & 0 \\ \vdots & \mathcal{I}_{N-3} & \vdots \\ 0 & \cdots & 0 \end{bmatrix}.$$

Note that the rigorous derivation of the homogeneous Neumann boundary conditions on v removes the spurious eigenvalues reported in [20], and thus removes the need for redesigning the matrix A to damp out these modes, which is done in that reference.

Control Strategies: A Comparative Study

In [20], two cases are studied in detail: 1) Reynolds number 10000, $\alpha_x = 2$, and $\alpha_z = 0$; and 2) Reynolds number 5000, $\alpha_x = 0$, and $\alpha_z = 2.044$. In case 1, where $\alpha_z = 0$, the equations for ω decouples from the equation for v as well as from the control input, and the problem becomes the same as that studied in the previous sections. Case 2) is a different problem in that it is subcritical, which means that there are no unstable modes. The control problem is nevertheless interesting because perturbations in laminar subcritical flows may lead to transition to turbulence. Therefore, it is of interest to apply control in order to delay, or maybe even prevent, transition to turbulence. The particular case chosen here is the pair (α_x, α_z) that gives the maximum transient energy growth, as shown in [29]. The "worst-case" transient energy growth is defined as

$$\mathcal{E}(t) = \sup_{x_0} \frac{\|x(t)\|_2}{\|x_0\|_2}.$$

The state space model developed in the previous section is subjected to state disturbances, w_1, and measurement noise, w_2, such that it can be written

$$\begin{aligned} \dot{x} &= Ax + B_1 w + B_2 u \\ y &= C_2 x + D_{21} w \end{aligned}$$

where

$$w = \left[\begin{array}{c} w_1 \\ w_2 \end{array} \right], B_1 = \left[\begin{array}{cc} I & 0 \end{array} \right], B_2 = B, C_2 = C, \text{ and } D_{21} = \left[\begin{array}{cc} 0 & \alpha I \end{array} \right].$$

The performance variable, z, is defined as

$$z = C_1 x + D_{12} u$$

where

$$C_1 = \left[\begin{array}{c} Q^{1/2} \\ 0 \end{array} \right], D_{12} = \left[\begin{array}{c} 0 \\ lI \end{array} \right].$$

The system is now on the standard form (3.9)–(3.11), needed for application of the $\mathcal{H}_2$ and $\mathcal{H}_\infty$ control strategies. Q, which shapes the dependence of the performance upon the states, is chosen such that $x^* Q x$ is related to the energy of the flow perturbations, which appears to be the best choice for delaying transition to turbulence [21]. In [20], an extensive parametric study is carried out, quantifying the performance of $\mathcal{H}_2$, $\mathcal{H}_\infty$ and proportional control strategies in terms of the system norms $\|T_{xw}\|_2$, $\|T_{xw}\|_\infty$ and $\|T_{uw}\|_2$, where T_{xw} is the transfer matrix from the disturbance input w to the state x, and T_{uw} is the transfer matrix from the disturbance input w to the control u. Thus, the norms are measures of the state response to Gaussian disturbances, the state response to worst-case disturbances, and the control used in response to Gaussian disturbances, respectively. For case 1, the results show that the proportional controllers are not nearly as effective as the $\mathcal{H}_2$ and $\mathcal{H}_\infty$ controllers. The best $\mathcal{H}_\infty$ controller tested, is reported to perform better than all proportional controllers tested with respect to the response of the state to both white noise disturbances and worst case disturbances, and use significantly less control energy than the proportional controllers.

Turning now to case 2, Figure 4.6 shows the eleven least stable poles for this case. Clearly, they are all in the left half plane. Figure 4.7 shows the eigenvectors corresponding to the eleven least stable eigenvalues. The eigenvectors appear pairwise quite similar (except for the first eigenvector), implying that they are highly non-orthogonal. The problem of large transient energy growth is connected with this non-orthogonality, along with the magnitude of the corresponding eigenvalues. This can be illustrated by the following example, involving the second order time invariant system

$$\dot{x} = Ax = \left[\begin{array}{cc} -1 & 0 \\ a & -11 \end{array} \right] x,$$

with initial condition $x(0) = x_0$. The eigenvalues of A are $\lambda_1 = -1$ and $\lambda_2 = -11$, that is, they are independent of a by the triangular structure of A. The
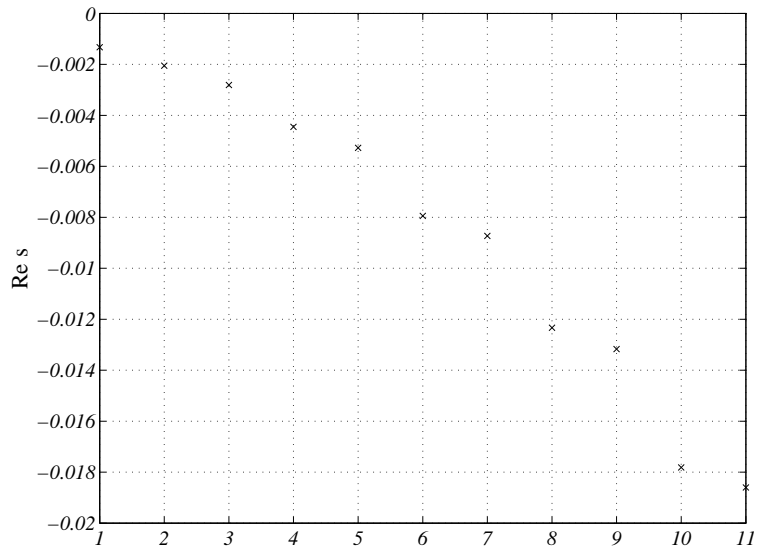
Figure 4.6: The eleven least stable eigenvalues in case 2. All eigenvalues are real.
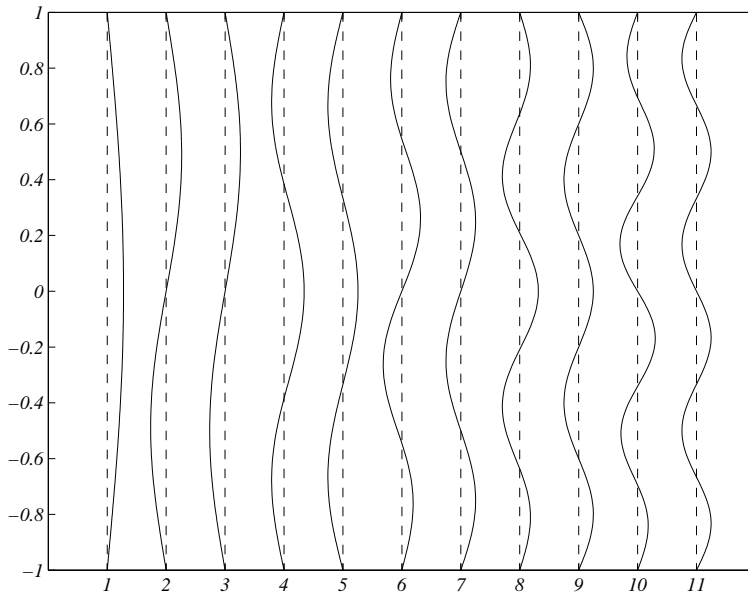
Figure 4.7: Eigenvectors corresponding to the eleven least stable eigenvalues.
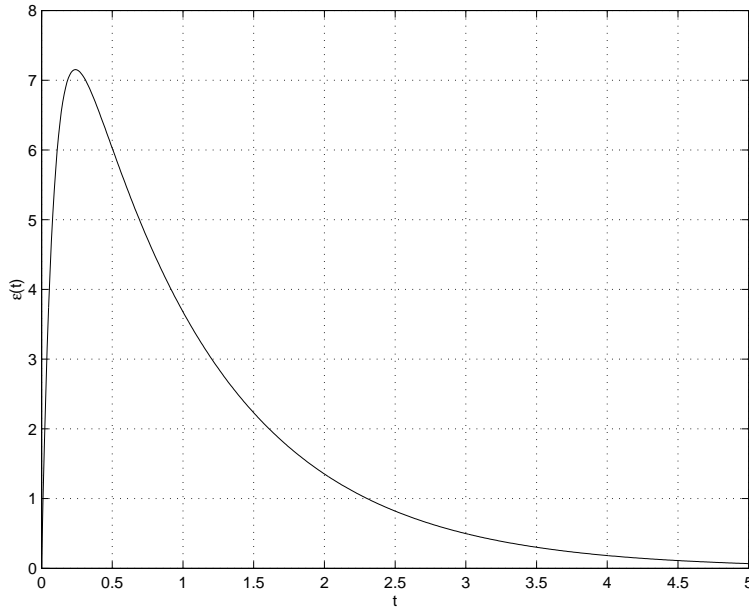
Figure 4.8: Energy growth in second order example system.

associated normalized eigenvectors of A are $v_1 = \begin{bmatrix} 1 & a/10 \end{bmatrix}^T / \sqrt{a^2/100 + 1}$ and $v_2 = \begin{bmatrix} 0 & 1 \end{bmatrix}^T$, respectively. The scalar product of the two eigenvectors is

$$v_1 \cdot v_2 = \frac{a}{\sqrt{a^2 + 100}}$$

which is maximized as $a \to \infty$. When $a = 0$ the eigenvectors are orthogonal, and the energy decreases monotonically for all initial conditions, since the solution is simply given by

$$x(t) = \begin{bmatrix} e^{-t} & 0 \\ 0 & e^{-11t} \end{bmatrix} x_0$$

in this case. However, if $a = 100$, for instance, the solution is given by

$$x(t) = \begin{bmatrix} e^{-t} & 0 \\ 10 \left(e^{-t} - e^{-11t} \right) & e^{-11t} \end{bmatrix} x_0$$

so the (worst case) transient energy growth is

$$\mathcal{E}(t) = \sup_{x_0} \frac{\|x(t)\|_2}{\|x_0\|_2} = \left\| \begin{bmatrix} e^{-t} & 0 \\ 10 \left(e^{-t} - e^{-11t} \right) & e^{-11t} \end{bmatrix} \right\|_2 = 10 \left(e^{-t} - e^{-11t} \right),$$

which is plotted in Figure 4.8. When this phenomenon occurs in a channel flow, transition to turbulence is likely to occur, because the nonlinear terms in the

Navier-Stokes equation come into play. Thus, it is an important property of any control law for (4.44)–(4.45), that the transient energy growth is suppressed. This is the main point in [20] regarding case 2. The parametric study carried out in [20], indicate that the $\mathcal{H}_2$ and $\mathcal{H}_\infty$ controllers act to make the set of eigenvectors more orthogonal. The maximum transient energy growth of the system is reported to be reduced effectively.

4.2   Spatial Invariance Yields Localized Control

In [37], an implementation of the control system for stabilizing the 2D channel flow was suggested. Figure 4.9 shows schematically the setup, involving arrays of sensors and actuators, and a central computing unit. Data from the entire sensor array is fed into the computer, Fourier transformed, and then fed to the control algorithm. The resulting control signal is inverse Fourier transformed and output to the actuator array. The communication needs are tremendous, and so is the computational load. It would be desirable to have localized control, that is, actuation at a certain spatial position should depend on sensing in a neighborhood of that location. Intuitively, flow variables far away from a certain actuation point should be less important than flow variables that are closer. And indeed, this is the case, as shown in [17]. The results are based on the notion of spatial invariance. Loosely put, the system is spatially invariant with respect to the spatial variable x if the system looks the same looking up and down the x-axis, regardless of the point of reference. It is clear that the prototype flows studied here have this property in the streamwise (and spanwise, in the 3D case) direction. In this case, the optimal controllers derived above also are spatially invariant. Moreover, the optimal state feedback $u = K\psi$ at a location x can be written as

$$u(x,t) = \int_{\mathbb{R}} k_s(x - \zeta)\psi(\zeta)\,d\zeta \tag{4.46}$$

where the convolution kernel k_s decays exponentially, that is

$$|k_s(x)| \leq Me^{-\alpha|x|}$$

for some positive constants M and α. Similarly, an exponentially decaying convolution kernel, k_e, can be found for the estimation problem. Thus, one can approximate the integral (4.46) to any desired degree of accuracy by truncating it at some appropriate $\varepsilon > 0$, to obtain

$$u(x,t) = \int_{\mathbb{R}} k_s(x - \zeta)\psi(\zeta)\,d\zeta \approx \int_{-\varepsilon}^{\varepsilon} k_s(x - \zeta)\psi(\zeta)\,d\zeta.$$

It follows that one can design decentralized controllers that are arbitrarily close to optimal. For the linearized Navier-Stokes equations for 3D channel flow, these kernels have been calculated in [64]. Implementation of the control can be done in terms of a lattice of identical tiles incorporating sensors, actuators and computation logic, as shown schematically in Figure 4.10. Each tile estimates the state
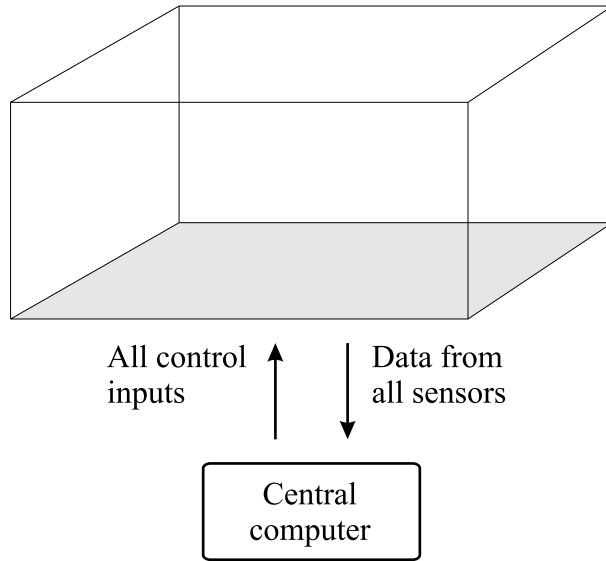
Figure 4.9: Centralized control. Actuators and sensors are distributed over the shaded face. All sensor data is sent to a central computer which calculates and issues control signals to all actuators.

above itself, and the information is communicated to its neighbors. Based on gathered information, each tile calculates its control. The choice of ε determines the distance over which sensor information must be communicated.

The implications of the results presented in this section is that the optimal control laws designed for channel flow in the previous sections, which require huge amounts of wiring and a powerful central computer, can be approximated by localized controllers.

4.3   Lyapunov Stability Approach

In this section, we use Lyapunov stability analysis to show stability of the parabolic equilibrium profiles (2.72) and (2.63), for 2D channel flow and 3D pipe flow, respectively. The results extend easily to 3D channel flow as well. The Navier-Stokes equations are nonlinear, and the only way we can assure global stability of the feedback system is by nonlinear analysis. Note, though, that this does not necessarily mean that the stabilizing feedback control law has to be nonlinear. Indeed, the result of the analysis below, turns out to give astonishingly simple control laws, that are linear and completely decentralized.
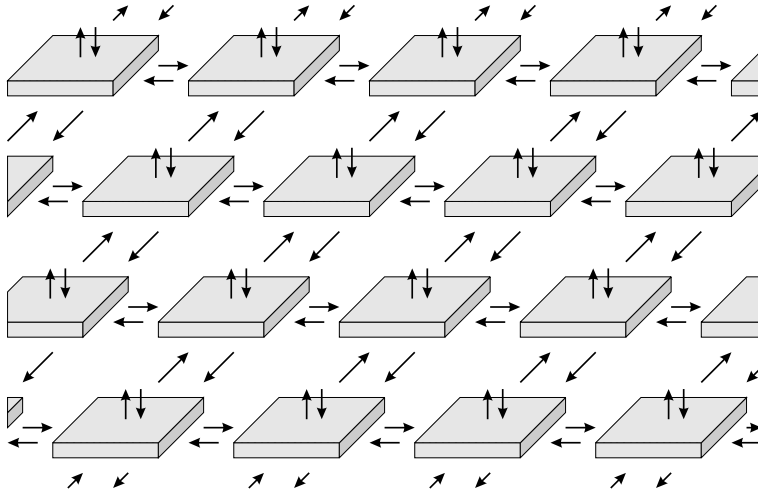
Figure 4.10: Decentralized control. A lattice of identical tiles incorporating sensors and actuators, and computation logic. Sensor information is communicated between neighboring tiles, and each tile computes the control above itself.

4.3.1 2D Channel Flow

Lyapunov Stability Analysis

Boundary control laws for stabilization are sought such that the kinetic energy of the system decays as a function of time. This is a standard Lyapunov-based approach, in which the Lyapunov function is chosen as

$$E(\mathbf{w}) = \|\mathbf{w}\|_{L_2}^2 = \int\limits_{-1}^{1} \int\limits_{0}^{L} \left(u^2 + v^2\right) dxdy. \tag{4.47}$$

The Lyapunov analysis is performed in the perturbation variables, since the parabolic equilibrium profile is moved to the origin in these variables. Moving the equilibrium point that is to be stabilized to the origin by means of a coordinate transformation is standard procedure in Lyapunov analysis. The time derivative of $E(\mathbf{w})$ along the trajectories of (2.74)–(2.75) is

$$\dot{E}(\mathbf{w}) = 2 \int\limits_{-1}^{1} \int\limits_{0}^{L} \left(u\frac{\partial u}{\partial t} + v\frac{\partial v}{\partial t} \right) dxdy$$

$$= 2 \int\limits_{-1}^{1} \int\limits_{0}^{L} u \left(\frac{1}{Re}\left(\frac{\partial^2 u}{\partial x^2} + \frac{\partial^2 u}{\partial y^2} \right) - u\frac{\partial u}{\partial x} - \tilde{U}\frac{\partial u}{\partial x} - v\frac{\partial u}{\partial y} - v\frac{d\tilde{U}}{dy} - \frac{\partial p}{\partial x} \right) dxdy$$

$$+ 2 \int\limits_{-1}^{1} \int\limits_{0}^{L} v \left(\frac{1}{Re} \left(\frac{\partial^2 v}{\partial x^2} + \frac{\partial^2 v}{\partial y^2} \right) - u \frac{\partial v}{\partial x} - \tilde{U} \frac{\partial v}{\partial x} - v \frac{\partial v}{\partial y} - \frac{\partial p}{\partial y} \right) dx\, dy. \quad (4.48)$$

Integration by parts, noticing that $u^2 \frac{\partial u}{\partial x} = \frac{1}{2} u \frac{\partial (u^2)}{\partial x}$ and $v^2 \frac{\partial v}{\partial y} = \frac{1}{2} v \frac{\partial (v^2)}{\partial y}$, and keeping in mind that all the variables are periodic in x, yields

$$\dot{E}(\mathbf{w}) = \frac{2}{Re} \int\limits_{0}^{L} \left[\frac{\partial u}{\partial y} u + \frac{\partial v}{\partial y} v \right]_{y=-1}^{1} dx$$

$$- \frac{2}{Re} \int\limits_{-1}^{1} \int\limits_{0}^{L} \left(\left(\frac{\partial u}{\partial x} \right)^2 + \left(\frac{\partial u}{\partial y} \right)^2 + \left(\frac{\partial v}{\partial x} \right)^2 + \left(\frac{\partial v}{\partial y} \right)^2 \right) dx\, dy + \int\limits_{-1}^{1} \int\limits_{0}^{L} u^2 \frac{\partial u}{\partial x} dx\, dy$$

$$\underbrace{- 2 \int\limits_{-1}^{1} \int\limits_{0}^{L} \tilde{U} \frac{\partial u}{\partial x} u\, dx\, dy}_{=0^{1}} - \int\limits_{0}^{L} \left[u^2 v \right]_{y=-1}^{1} dx + \int\limits_{-1}^{1} \int\limits_{0}^{L} u^2 \frac{\partial v}{\partial y} dx\, dy$$

$$- 2 \int\limits_{-1}^{1} \int\limits_{0}^{L} v u \frac{d\tilde{U}}{dy} dx\, dy - 2 \int\limits_{-1}^{1} \int\limits_{0}^{L} \frac{\partial u}{\partial x} p\, dx\, dy + \int\limits_{-1}^{1} \int\limits_{0}^{L} v^2 \frac{\partial u}{\partial x} dx\, dy$$

$$\underbrace{- 2 \int\limits_{-1}^{1} \int\limits_{0}^{L} \tilde{U} \frac{\partial v}{\partial x} v\, dx\, dy}_{=0^{1}} - \int\limits_{0}^{L} \left[v^3 \right]_{y=-1}^{1} dx + \int\limits_{-1}^{1} \int\limits_{0}^{L} v^2 \frac{\partial v}{\partial y} dx\, dy$$

$$- 2 \int\limits_{0}^{L} \left[v p \right]_{y=-1}^{1} dx + 2 \int\limits_{-1}^{1} \int\limits_{0}^{L} \frac{\partial v}{\partial y} p\, dx\, dy$$

$$= - \frac{2}{Re} \int\limits_{-1}^{1} \int\limits_{0}^{L} \left(\left(\frac{\partial u}{\partial x} \right)^2 + \left(\frac{\partial u}{\partial y} \right)^2 + \left(\frac{\partial v}{\partial x} \right)^2 + \left(\frac{\partial v}{\partial y} \right)^2 \right) dx\, dy$$

$$- 2 \int\limits_{-1}^{1} \int\limits_{0}^{L} v u \frac{d\tilde{U}}{dy} dx\, dy + \int\limits_{-1}^{1} \int\limits_{0}^{L} u^2 \left(\frac{\partial u}{\partial x} + \frac{\partial v}{\partial y} \right) dx\, dy - 2 \int\limits_{-1}^{1} \int\limits_{0}^{L} p \left(\frac{\partial u}{\partial x} + \frac{\partial v}{\partial y} \right) dx\, dy$$

$$+ \int\limits_{-1}^{1} \int\limits_{0}^{L} v^2 \left(\frac{\partial u}{\partial x} + \frac{\partial v}{\partial y} \right) dx\, dy + \frac{2}{R} \int\limits_{0}^{L} \left[\frac{\partial u}{\partial y} u \right]_{y=-1}^{1} dx$$

---

[1] Due to periodic boundary conditions in the streamwise direction: $\int\limits_{0}^{L} \tilde{U} \frac{\partial u}{\partial x} u\, dx = \frac{\tilde{U}}{2} \int\limits_{0}^{L} \frac{\partial (u^2)}{\partial x} dx = \frac{\tilde{U}}{2} \left[u^2 \right]_{0}^{L} = 0.$

$$+ \frac{2}{Re} \int_0^L \left[\left(\frac{\partial v}{\partial y} - Rp \right) v \right]_{y=-1}^1 dx - \int_0^L \left[\left(u^2 + v^2 \right) v \right]_{y=-1}^1 dx. \quad (4.49)$$

Using continuity (2.73), we get

$$\dot{E}(\mathbf{w}) = -\frac{2}{Re} \int_{-1}^1 \int_0^L \int_0^L \left(\left(\frac{\partial u}{\partial x} \right)^2 + \left(\frac{\partial u}{\partial y} \right)^2 + \left(\frac{\partial v}{\partial x} \right)^2 + \left(\frac{\partial v}{\partial y} \right)^2 \right) dx dy$$

$$- 2 \int_{-1}^1 \int_0^L uv \frac{d\tilde{U}}{dy} dx dy + \frac{2}{Re} \int_0^L \left[\frac{\partial u}{\partial y} u \right]_{y=-1}^1 dx$$

$$+ \frac{2}{Re} \int_0^L \left[\left(\frac{\partial v}{\partial y} - Rp \right) v \right]_{y=-1}^1 dx - \int_0^L \left[\left(u^2 + v^2 \right) v \right]_{y=-1}^1 dx. \quad (4.50)$$

Following [15, Lemma 6.2] (also in [14, Lemma 3.2]), we set

$$u(x, y, t) = u(x, -1, t) + \int_{-1}^y \frac{\partial u}{\partial y}(x, \gamma, t) d\gamma \quad (4.51)$$

where the integration variable is denoted γ for notational clarity. Squaring (4.51) yields

$$u^2(x, y, t) = \left(u(x, -1, t) + \int_{-1}^y \frac{\partial u}{\partial y}(x, \gamma, t) d\gamma \right)^2 \leq$$

$$2u^2(x, -1, t) + 2 \left(\int_{-1}^y \frac{\partial u}{\partial y}(x, \gamma, t) d\gamma \right)^2 .$$

By the Schwartz inequality,

$$\left(\int_{-1}^y 1 \frac{\partial u}{\partial y}(x, \gamma, t) d\gamma \right)^2 \leq (y + 1) \left(\int_{-1}^y \left(\frac{\partial u}{\partial y}(x, \gamma, t) \right)^2 d\gamma \right) \quad (4.52)$$

so we have that

$$u^2(x, y, t) \leq 2u^2(x, -1, t) + 2(y + 1) \int_{-1}^1 \left(\frac{\partial u}{\partial y}(x, y, t) \right)^2 dy \quad (4.53)$$

where we have set $y = 1$ in the integral. Therefore, we get

$$\int_{-1}^{1} \int_{0}^{L} u^2 dxdy \leq 4 \int_{0}^{L} u^2(x, -1, t)dxdy$$

$$+ 2 \int_{-1}^{1} \int_{0}^{L} (y+1) \left(\int_{-1}^{1} \left(\frac{\partial u}{\partial y}(x, y, t) \right)^2 dy \right) dxdy$$

$$= 4 \int_{0}^{L} u^2(x, -1, t)dxdy + 2 \int_{0}^{L} \left(\int_{-1}^{1} (y+1) \, dy \right) \left(\int_{-1}^{1} \left(\frac{\partial u}{\partial y}(x, y, t) \right)^2 dy \right) dx$$

$$= 4 \int_{0}^{L} u^2(x, -1, t)dxdy + 4 \int_{-1}^{1} \int_{0}^{L} \left(\frac{\partial u}{\partial y}(x, y, t) \right)^2 dxdy. \quad (4.54)$$

An analogous derivation for $\frac{\partial v}{\partial y}$ now gives

$$- \int_{-1}^{1} \int_{0}^{L} \left(\left(\frac{\partial u}{\partial y} \right)^2 + \left(\frac{\partial v}{\partial y} \right)^2 \right) dxdy \leq - \frac{E(\mathbf{w})}{4}$$

$$+ \int_{0}^{L} \left(u^2(x, -1, t) + v^2(x, -1, t) \right) dx. \quad (4.55)$$

Inserting (4.55) into (4.50) we get

$$\dot{E}(\mathbf{w}) \leq - \frac{1}{2Re} E(\mathbf{w}) + \frac{2}{Re} \int_{0}^{L} \left(u^2(x, -1, t) + v^2(x, -1, t) \right) dx$$

$$- \frac{2}{Re} \int_{-1}^{1} \int_{0}^{L} \left(\left(\frac{\partial u}{\partial x} \right)^2 + \left(\frac{\partial v}{\partial x} \right)^2 \right) dxdy - 2 \int_{-1}^{1} \int_{0}^{L} uv \frac{d\tilde{U}}{dy} dxdy + \frac{2}{Re} \int_{0}^{L} \left[\frac{\partial u}{\partial y} u \right]_{y=-1}^{1} dx$$

$$+ \frac{2}{Re} \int_{0}^{L} \left[\left(\frac{\partial v}{\partial y} - Rp \right) v \right]_{y=-1}^{1} dx - \int_{0}^{L} \left[(u^2 + v^2) v \right]_{y=-1}^{1} dx. \quad (4.56)$$

Since

$$-2 \int_{-1}^{1} \int_{0}^{L} uv \frac{d\tilde{U}}{dy} dxdy \leq 2 \int_{-1}^{1} \int_{0}^{L} 2 |u| |v| \, dxdy \leq 2 \int_{-1}^{1} \int_{0}^{L} \left(u^2 + v^2 \right) dxdy = 2E(\mathbf{w})$$

$$(4.57)$$

we finally get

$$\dot{E}(\mathbf{w}) \le -\frac{1}{2}\left(\frac{1}{Re} - 4\right) E(\mathbf{w}) + \frac{2}{Re} \int_0^L \left(u^2(x, -1, t) + v^2(x, -1, t)\right) dx$$

$$+\frac{2}{Re} \int_0^L \left[\frac{\partial u}{\partial y} u\right]_{y=-1}^1 dx + 2 \int_0^L \left[\left(\frac{1}{Re}\frac{\partial v}{\partial y} - p\right) v\right]_{y=-1}^1 dx - \int_0^L \left[\left(u^2 + v^2\right) v\right]_{y=-1}^1 dx.$$

$$(4.58)$$

Notice that for $Re < 1/4$, $E(\mathbf{w})$ decays exponentially with time even in the uncontrolled case ($u(x, \pm 1, t) = v(x, \pm 1, t) \equiv 0$). In other words, the fixed point $(\tilde{U}, \tilde{V})$ is globally exponentially stable (in L_2) in this case, and the goal of applying boundary control is to enhance stability. The four last terms in (4.58) are evaluated on the boundary, and are the means by which boundary control laws are designed. Below, two control laws are presented: the first uses wall-tangential actuation; and the second uses wall-normal actuation.

Wall-Tangential Distributed Actuation

The following boundary control was suggested in [15]:

$$u(x, -1, t) = k_u \frac{\partial u}{\partial y}(x, -1, t), \quad u(x, 1, t) = -k_u \frac{\partial u}{\partial y}(x, 1, t) \qquad (4.59)$$

$$v(x, -1, t) = v(x, 1, t) = 0. \qquad (4.60)$$

Inserting (4.59)–(4.60) into (4.58) gives

$$\dot{E}(\mathbf{w}) \le -\frac{1}{2}\left(\frac{1}{Re} - 4\right) E(\mathbf{w}) - \frac{2}{Re}\left(\frac{1}{k_u} - 1\right) \int_0^L u^2(x, -1, t) dx. \qquad (4.61)$$

Thus, for $Re < 1/4$ and $k_u \in [0, 1]$, $E(\mathbf{w})$ decays exponentially with time.

Wall-Normal Distributed Actuation

Actuation normal to the wall is another strategy of active interest. The inequality (4.58) also suggests a control law structure for wall-normal control [1] (also in [2]). Setting $u(x, -1, t) = u(x, 1, t) = 0$, $\frac{\partial v}{\partial y}$ is zero at the wall by continuity (2.73), so we have

$$\dot{E}(\mathbf{w}) \le -\frac{1}{2}\left(\frac{1}{Re} - 4\right) E(\mathbf{w}) + \frac{2}{Re} \int_0^L v^2(x, -1, t) dx$$

$$-2 \int_0^L [pv]_{y=-1}^1 dx - \int_0^L [v^3]_{y=-1}^1 dx. \qquad (4.62)$$

Now, by imposing $v(x, -1, t) = v(x, 1, t)$, the last term in (4.62) vanishes. Thus, we propose the following control law

$$u(x, -1, t) = u(x, 1, t) = 0 \tag{4.63}$$

$$v(x, -1, t) = v(x, 1, t) = k_v \left(p(x, 1, t) - p(x, -1, t) \right). \tag{4.64}$$

Inserting (4.63)–(4.64) into (4.62) gives

$$\dot{E}(\mathbf{w}) \leq -\frac{1}{2} \left(\frac{1}{Re} - 4 \right) E(\mathbf{w}) - 2 \left(\frac{1}{k_v} - \frac{1}{Re} \right) \int_0^L v^2(x, -1, t) dx. \tag{4.65}$$

Thus, for $Re < 1/4$ and $k_v \in [0, Re]$, $E(\mathbf{w})$ decays exponentially with time. Furthermore, note that (4.64) ensures that the net mass flux through the walls be zero.

Implementation

In order to implement the above controllers we have to express them in terms of the actual flow variables, U, V and P. For the wall-tangential case, we get

$$U(x, -1, t) = k_u \left(\frac{\partial U}{\partial y}(x, -1, t) - \frac{d\tilde{U}}{dy}(x, -1, t) \right)$$
$$U(x, 1, t) = -k_u \left(\frac{\partial U}{\partial y}(x, 1, t) - \frac{d\tilde{U}}{dy}(x, 1, t) \right) \tag{4.66}$$

$$V(x, -1, t) = V(x, 1, t) = 0, \tag{4.67}$$

and for the wall-normal case we get

$$U(x, -1, t) = U(x, 1, t) = 0 \tag{4.68}$$

$$V(x, -1, t) = V(x, 1, t) = k_v \left(P(x, 1, t) - P(x, -1, t) \right). \tag{4.69}$$

It is interesting to notice that the wall-normal control is independent of the physical parameters of the flow. This is an important property, since the physical parameters of any real flow are subject to inaccuracy. In contrast, $\frac{d\tilde{U}}{dy}(x, \pm 1, t)$ must be known for wall-tangential control.

It is also worth noting that the above control laws are of the Jurdjevic-Quinn [72] type, with respect to the Lyapunov function $E(\mathbf{w})$. This endows these control laws with inverse optimality with respect to a meaningful cost functional, which is in these cases complicated to write.

Numerical Demonstration

The theoretical results in this section are only valid for Reynolds numbers less than $1/4$, for which the parabolic equilibrium profile is globally exponentially stable in the uncontrolled case. Thus, the analysis only tells us that the proposed control laws maintain stability, and not necessarily enhance it. In fact, for wall-normal control, simulations at $Re = 0.1$ show that for $k_v = 0.1$, $E(\mathbf{w})$ converges

more slowly to 0 than in the uncontrolled case, whereas for $k_v = -0.1$, stability is enhanced. Although this result was unexpected, it does not contradict the theoretical results.

Being valid for small Reynolds numbers only, the theoretical results are of limited practical value. However, they do suggest controller structures worth testing on flows having higher Reynolds numbers. In [15], results from numerical simulations with wall-tangential control were presented that show stabilization of channel flow at $Re = 15000$. Here, we do a comparison of the performance of the two control laws for flows at $Re = 7500$ and $L = 4\pi$.

The simulations are performed using a hybrid Fourier pseudospectral-finite difference discretization and the fractional step technique based on a hybrid Runge-Kutta/Crank-Nicolson time discretization using the numerical method of [22]. This method is particularly well suited even for the cases with wall-normal actuation because of its implicit treatment of the wall-normal convective terms. The wall-parallel direction is discretized using 128 Fourier-modes, while the wall-normal direction is discretized using energy-conserving central finite differences on a stretched staggered grid with 100 gridpoints. The gridpoints have hyperbolic tangent distribution in the wall-normal direction in order to adequately resolve the high-shear regions near the walls. A fixed flow-rate formulation is used, rather than fixed average pressure gradient, since observations suggest that the approach to equilibrium is faster in this case [69]. The difference between the two formulations is discussed briefly in [104]. The time step is in the range $0.05 - 0.07$ for all simulations. In addition to reporting the time evolution of the energy, $E(\mathbf{w})$, we also consider the instantaneous control effort and drag force as measures of performance. The control effort is defined as

$$C(\mathbf{w}) = \sqrt{\int_0^L \left(|\mathbf{w}(x, -1, t)|^2 + |\mathbf{w}(x, 1, t)|^2 \right) dx} \qquad (4.70)$$

and the drag force as

$$D(\mathbf{w}) = \frac{1}{L} \int_0^L \left(\frac{\partial U}{\partial y}(x, -1, t) - \frac{\partial U}{\partial y}(x, 1, t) \right) dx \qquad (4.71)$$

(Notice that (4.71) is really the mean wall shear, which is related to the drag force by the factor μL). For selected time instants, vorticity maps are also provided. The vorticity, ω, is defined using the actual flow variables (rather than the perturbation variables) as

$$\omega(x, y, t) = \frac{\partial V}{\partial x}(x, y, t) - \frac{\partial U}{\partial y}(x, y, t). \qquad (4.72)$$

A total of six simulations are performed: wall-tangential control with $k_u \in [0.05, 0.1, 0.2]$; and wall-normal control with $k_v \in [-0.125, -0.08, -0.05]$. The parabolic equilibrium profile is unstable for $Re = 7500$, so infinitesimal disturbances will
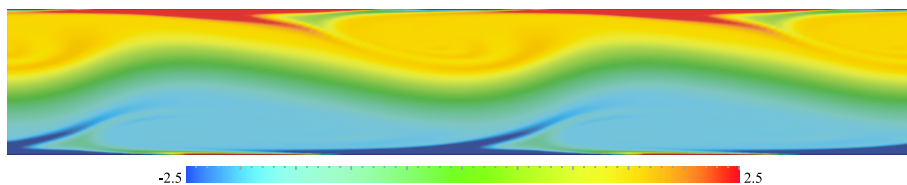
Figure 4.11: Vorticity map for the fully established 2D channel flow (uncontrolled).

grow, but the flow eventually reaches a statistically steady state, which we call *fully established flow*. For all simulations, the fully established flow, for which $E(\mathbf{w}) \approx 1.3$, is chosen as the initial data. Figure 4.11 shows a vorticity map for the fully established uncontrolled flow. It is similar to vorticity maps presented in [69], and clearly shows the ejection of vorticity from the walls into the core of the channel as described in [69].

Figure 4.12 compares wall-tangential and wall-normal control. It is clear that stabilization is obtained for both controllers, in terms of the energy $E(\mathbf{w})$. Figure 4.12 shows that $E(\mathbf{w})$ decays faster for wall-normal control, and at much less control effort (notice the different scales for $C(\mathbf{w})$ for the two cases in Figure 4.12). The ratio of the peak kinetic energy of the control flow (wall-normal), versus the perturbation kinetic energy in the uncontrolled case (drained out by the control), $C(\mathbf{w})^2/E(\mathbf{w})$, is less than 0.25%. Also, reduction of drag is more efficient in the wall-normal control case.[1]

Figure 4.13 shows vorticity maps at three different time instances for wall-normal control with $k_v = -0.125$. The removal of vortical structures is evident already at $t = 30$ (top graph), and at $t = 120$ (bottom graph) the flow is nearly uniform. Figure 4.14 shows the pressure field immediately after onset of wall-normal control ($k_v = -0.125$). Regions of low pressure coincide with regions of circulation cells, as the velocity vectors in the intermediate zoom show. In the most detailed zoom, we see that the controller applies suction in this region.

4.3.2   3D Channel Flow

It is recognized that channel flow instability mechanisms are inherently 3D. Efforts that study the stabilization problem only in 2D are thus inconclusive about physical flows, for which 3D effects are quite significant. However, the "model problem" of 2D channel flow stabilization is a useful testbed for techniques that can eventually be extended to 3D flows. The Lyapunov stability analysis presented in the previous section can be extended to the 3D channel flow in a straight forward manner, and similar boundary control laws can be derived. Balogh (private

---

[1] It is interesting to note (see Figure 4.12) that, when the control is applied to the 2D flow, a transient ensues in which the drag dips below the laminar level and then asymptotes towards the laminar state. This transient, however, is dependent on the initial flow state being that of the fully established 2D flow, which has a drag which is significantly higher than laminar. Thus, this transient result does not disprove the conjecture stated in [21], as discussed in Section 4.3.4.
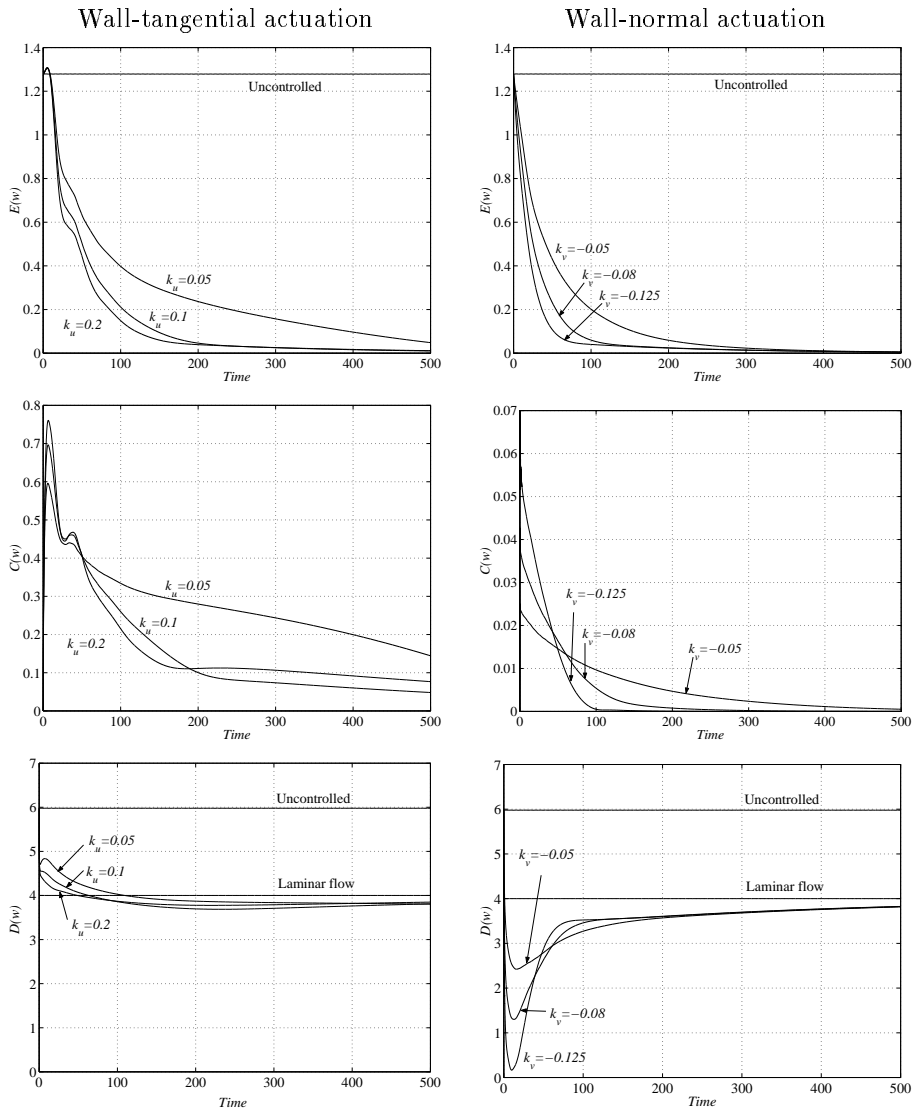
Figure 4.12: Energy $E(\mathbf{w})$ (top row), control effort $C(\mathbf{w})$, and drag $D(\mathbf{w})$ (bottom row), as functions of time for wall-tangential actuation (left column) and wall-normal actuation (right column).
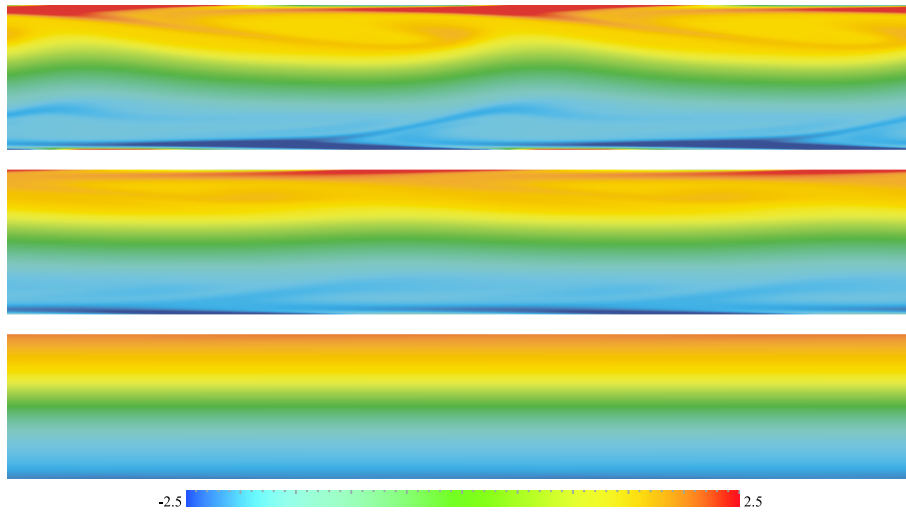
Figure 4.13: Vorticity maps for wall-normal actuation at $t = 30$ (top figure), $t = 60$, and $t = 120$ (bottom figure). The feedback gain is $k_v = -0.125$.
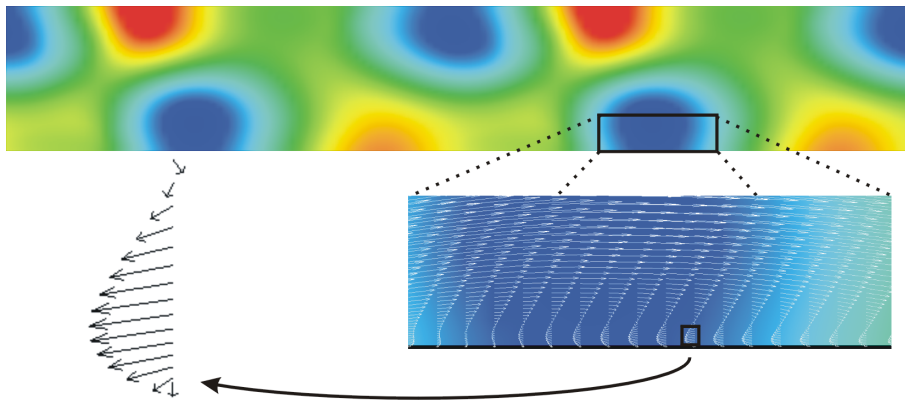
Figure 4.14: Pressure (perturbation only, i.e. p) immediately after onset of wall-normal actuation. Zoom shows velocity vectors in a region with low pressure.
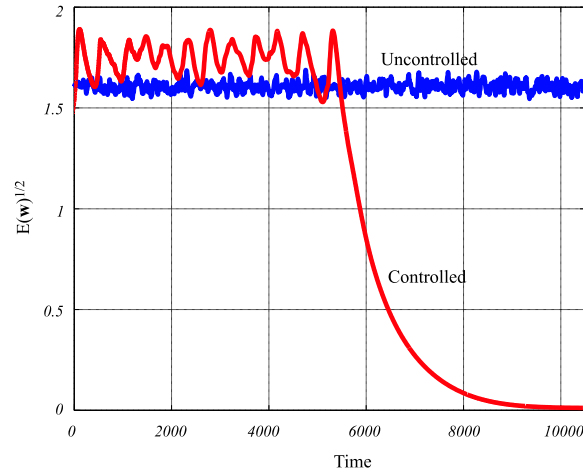
Figure 4.15: Perturbation energy (square root of) as a function of time for uncontrolled and controlled 3D channel flow at $Re = 4000$.

communication) reports that, in numerical simulations, the very simple, and fully decentralized boundary control law

$$
\begin{aligned}
U(x, -1, z, t) &= k\left(\frac{\partial U}{\partial y}(x, -1, z, t) - \frac{\partial \tilde{U}}{\partial y}(-1)\right) \\
U(x, 1, z, t) &= -k\left(\frac{\partial U}{\partial y}(x, 1, z, t) - \frac{\partial \tilde{U}}{\partial y}(1)\right) \\
V(x, -1, z, t) &= V(x, 1, z, t) = 0 \\
W(x, -1, z, t) &= W(x, 1, z, t) = 0
\end{aligned}
$$

with $k > 0$, relaminarizes a turbulent 3D channel flow at $Re = 4000$. Figure 4.15 shows the perturbation energy as a function of time. The perturbation energy is in this case

$$
E(\mathbf{w}) = \int_0^{L_z} \int_{-1}^1 \int_0^{L_x} \left(u^2 + v^2 + w^2\right) dx\,dy\,dz
$$

and the channel dimensions are $L_x = 6\pi$ and $L_z = 3\pi$. The plots in Figure 4.16 show places where the discriminant[2] has values larger than 0.9 at $t = 4000$, indicating locations of vortical structures, and the plots in Figure 4.17 show the

---

[2] The discriminant of the velocity gradient tensor is a scalar quantity that is commonly used in visualizations to pinpoint vortex-type motions in the flow. The following definition of the discrimant is taken from [23]: $D = (27/4)\,R^2 - Q^3$, where Q and R are the second and third invariants of the velocity gradient tensor A, defined by $Q = \frac{1}{2}\left\{trace(A)^2 - trace(A^2)\right\}$, and $R = -det(A)$, respectively.
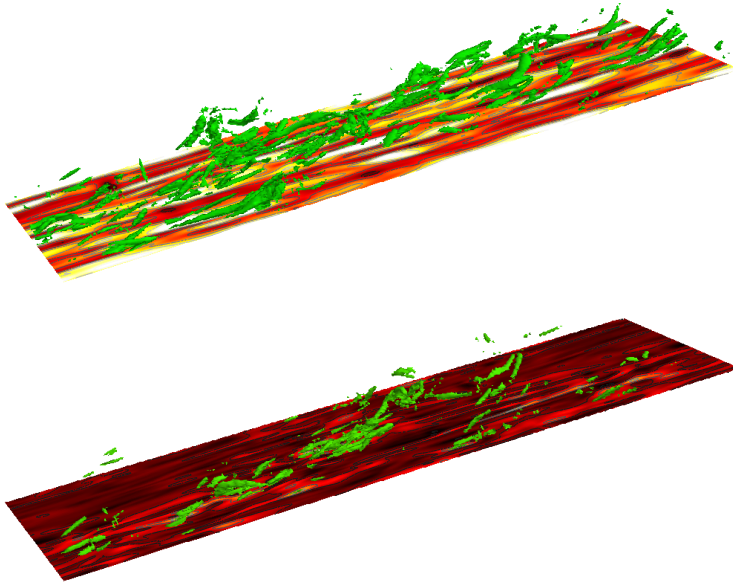
Figure 4.16: Places where the discriminant has values larger than 0.9 at $t = 4000$, for uncontrolled (upper) and controlled (lower) 3D channel flow at $Re = 4000$.

spanwise vorticity at $t = 5000$. It is interesting to notice that the perturbation energy is still large at these points in time (see Figure 4.15), but the control has clearly influenced the vortical structures in the flow. Figure 4.18 shows drag as a function of time. Drag is reduced to below laminar level (which is 4) almost instantly, and then gradually approaches the laminar level. This is the same result as obtained in the 2D case. Notice that drag reduction is not explicitly the objective of the control, stabilization of the parabolic equilibrium profile is. Reduction of drag to laminar level is therefore expected in the limit as $t \to \infty$, but the striking result of immediate drag reduction is obtained!

4.3.3   3D Pipe Flow

In this section we show that the Lyapunov analysis that was developed for 2D and 3D channel flow, can be modified to apply for the 3D pipe flow as well.

Lyapunov Stability Analysis

Consider the following Lyapunov function candidate

$$E(\mathbf{w}) \triangleq \lim_{\varepsilon \to 0} E_\varepsilon(\mathbf{w}) \triangleq \lim_{\varepsilon \to 0} \frac{1}{2} \int\limits_0^L \int\limits_0^{2\pi} \int\limits_\varepsilon^1 \left(v_r^2 + v_\theta^2 + v_z^2 \right) r dr d\theta dz$$
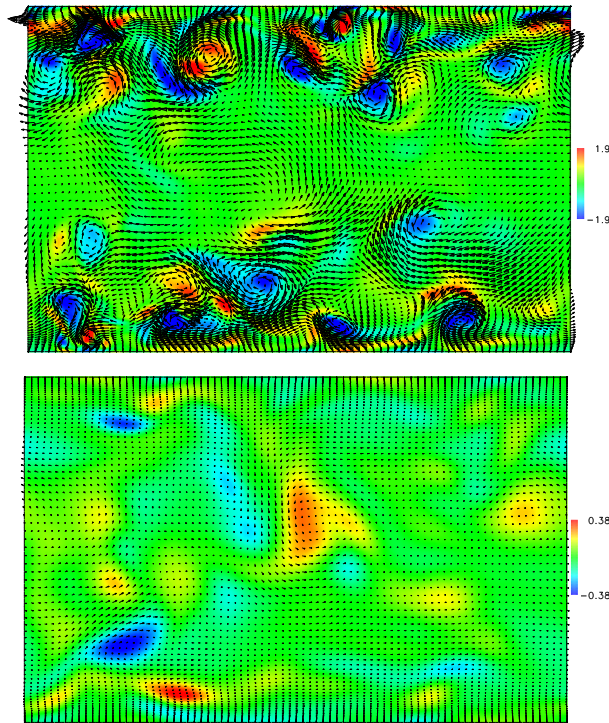
Figure 4.17: Spanwise vorticity at $t = 5000$ for uncontrolled (upper) and controlled (lower) 3D channel flow at $Re = 4000$.
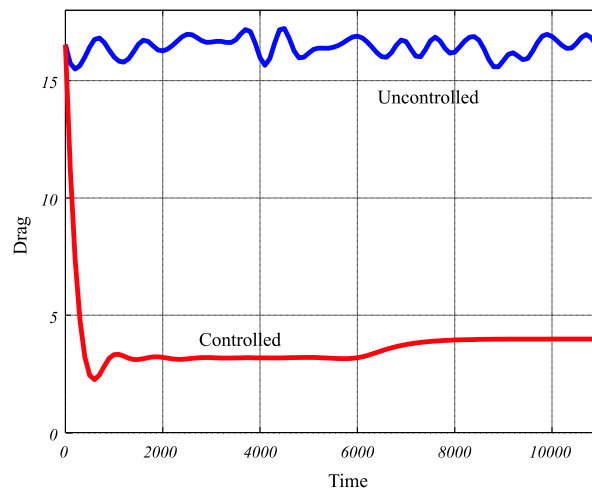
Figure 4.18: Drag as a function of time for uncontrolled and controlled 3D channel flow at $Re = 4000$.

which is simply the perturbation energy of the flow. Its time derivative along trajectories of (2.65)–(2.67) is

$$
\dot{E}_\varepsilon(\mathbf{w}) = \int_0^L \int_0^{2\pi} \int_\varepsilon^1 \left(v_r \dot{v}_r + v_\theta \dot{v}_\theta + v_z \dot{v}_z \right) r \, dr \, d\theta \, dz =
$$

$$
\int_0^L \int_0^{2\pi} \int_\varepsilon^1 \left[-\left(v_r^2 r \frac{\partial v_r}{\partial r} + v_r v_\theta \frac{\partial v_r}{\partial \theta} - v_r v_\theta^2 + r v_r \left(v_z + \tilde{V}_z \right) \frac{\partial v_r}{\partial z} \right) \right.
$$

$$
\left. -r v_r \frac{\partial p}{\partial r} + \frac{1}{Re} \left(r v_r \frac{\partial}{\partial r} \left(\frac{1}{r} \frac{\partial}{\partial r} (r v_r) \right) + \frac{v_r}{r} \frac{\partial^2 v_r}{\partial \theta^2} - \frac{2 v_r}{r} \frac{\partial v_\theta}{\partial \theta} + r v_r \frac{\partial^2 v_r}{\partial z^2} \right) \right] dr \, d\theta \, dz
$$

$$
+ \int_0^L \int_0^{2\pi} \int_\varepsilon^1 \left[-\left(r v_\theta v_r \frac{\partial v_\theta}{\partial r} + v_\theta^2 \frac{\partial v_\theta}{\partial \theta} + v_r v_\theta^2 + r v_\theta \left(v_z + \tilde{V}_z \right) \frac{\partial v_\theta}{\partial z} \right) \right.
$$

$$
\left. -v_\theta \frac{\partial p}{\partial \theta} + \frac{1}{Re} \left(r v_\theta \frac{\partial}{\partial r} \left(\frac{1}{r} \frac{\partial}{\partial r} (r v_\theta) \right) + \frac{v_\theta}{r} \frac{\partial^2 v_\theta}{\partial \theta^2} + \frac{2 v_\theta}{r} \frac{\partial v_r}{\partial \theta} + r v_\theta \frac{\partial^2 v_\theta}{\partial z^2} \right) \right] dr \, d\theta \, dz
$$

$$
+ \int_0^L \int_0^{2\pi} \int_\varepsilon^1 \left[-\left(r v_z v_r \frac{\partial \left(v_z + \bar{V}_z \right)}{\partial r} + v_z v_\theta \frac{\partial v_z}{\partial \theta} + r v_z \left(v_z + \tilde{V}_z \right) \frac{\partial v_z}{\partial z} \right) \right.
$$

$$
\left. -r v_z \frac{\partial p}{\partial z} + \frac{1}{Re} \left(v_z \frac{\partial}{\partial r} \left(r \frac{\partial v_z}{\partial r} \right) + v_z \frac{1}{r} \frac{\partial^2 v_z}{\partial \theta^2} + r v_z \frac{\partial^2 v_z}{\partial z^2} \right) \right] dr \, d\theta \, dz. \quad (4.73)
$$

Integration by parts of the first integral in (4.73) yields

$$
\int_0^L \int_0^{2\pi} \int_\varepsilon^1 \left[-\left(r v_r^2 \frac{\partial v_r}{\partial r} + v_r v_\theta \frac{\partial v_r}{\partial \theta} - v_r v_\theta^2 + r v_r \left(v_z + \tilde{V}_z \right) \frac{\partial v_r}{\partial z} \right) - r v_r \frac{\partial p}{\partial r} \right.
$$

$$
\left. + \frac{1}{Re} \left(r v_r \frac{\partial}{\partial r} \left(\frac{1}{r} \frac{\partial}{\partial r} (r v_r) \right) + \frac{v_r}{r} \frac{\partial^2 v_r}{\partial \theta^2} - \frac{2 v_r}{r} \frac{\partial v_\theta}{\partial \theta} + r v_r \frac{\partial^2 v_r}{\partial z^2} \right) \right] dr \, d\theta \, dz
$$

$$
= \int_0^L \int_0^{2\pi} \left[-\frac{1}{2} r v_r^3 \right]_\varepsilon^1 d\theta \, dz + \frac{1}{2} \int_0^L \int_0^{2\pi} \int_\varepsilon^1 v_r^2 \frac{\partial (r v_r)}{\partial r} \, dr \, d\theta \, dz
$$

$$
+ \frac{1}{2} \int_0^L \int_0^{2\pi} \int_\varepsilon^1 v_r^2 \frac{\partial v_\theta}{\partial \theta} \, dr \, d\theta \, dz + \int_0^L \int_0^{2\pi} \int_\varepsilon^1 v_r v_\theta^2 \, dr \, d\theta \, dz
$$

$$
+ \frac{1}{2} \int_0^L \int_0^{2\pi} \int_\varepsilon^1 r v_r^2 \frac{\partial v_z}{\partial z} \, dr \, d\theta \, dz + \int_0^L \int_0^{2\pi} \left[-r v_r p \right]_\varepsilon^1 d\theta \, dz
$$

$$
+ \int_0^L \int_0^{2\pi} \int_\varepsilon^1 \frac{\partial (r v_r)}{\partial r} p \, dr \, d\theta \, dz + \frac{1}{Re} \int_0^L \int_0^{2\pi} \left[v_r \frac{\partial}{\partial r} (r v_r) \right]_\varepsilon^1 d\theta \, dz
$$

$$-\frac{1}{Re}\int\limits_0^L\int\limits_0^{2\pi}\int\limits_\varepsilon^1\frac{1}{r}\left(\frac{\partial}{\partial r}\left(rv_r\right)\right)^2drd\theta dz-\frac{1}{Re}\int\limits_0^L\int\limits_0^{2\pi}\int\limits_\varepsilon^1\frac{1}{r}\left(\frac{\partial v_r}{\partial\theta}\right)^2drd\theta dz$$

$$-\frac{1}{Re}\int\limits_0^L\int\limits_0^{2\pi}\int\limits_\varepsilon^1\frac{2}{r}v_r\frac{\partial v_\theta}{\partial\theta}drd\theta dz-\frac{1}{Re}\int\limits_0^L\int\limits_0^{2\pi}\int\limits_\varepsilon^1 r\left(\frac{\partial v_r}{\partial z}\right)^2drd\theta dz.$$

Integration by parts of the second integral in (4.73) yields

$$\int\limits_0^L\int\limits_0^{2\pi}\int\limits_\varepsilon^1\left[-\left(rv_\theta v_r\frac{\partial v_\theta}{\partial r}+v_\theta^2\frac{\partial v_\theta}{\partial\theta}+v_r v_\theta^2+rv_\theta\left(v_z+\tilde{V}_z\right)\frac{\partial v_\theta}{\partial z}\right)-v_\theta\frac{\partial p}{\partial\theta}\right.$$

$$\left.+\frac{1}{Re}\left(rv_\theta\frac{\partial}{\partial r}\left(\frac{1}{r}\frac{\partial}{\partial r}\left(rv_\theta\right)\right)+\frac{v_\theta}{r}\frac{\partial^2 v_\theta}{\partial\theta^2}+\frac{2v_\theta}{r}\frac{\partial v_r}{\partial\theta}+rv_\theta\frac{\partial^2 v_\theta}{\partial z^2}\right)\right]drd\theta dz$$

$$=\frac{1}{2}\int\limits_0^L\int\limits_0^{2\pi}\left[-rv_r v_\theta^2\right]_\varepsilon^1 d\theta dz+\frac{1}{2}\int\limits_0^L\int\limits_0^{2\pi}\int\limits_\varepsilon^1 v_\theta^2\frac{\partial\left(rv_r\right)}{\partial r}drd\theta dz$$

$$+\frac{1}{2}\int\limits_0^L\int\limits_0^{2\pi}\int\limits_\varepsilon^1 v_\theta^2\frac{\partial v_\theta}{\partial\theta}drd\theta dz-\int\limits_0^L\int\limits_0^{2\pi}\int\limits_\varepsilon^1 v_r v_\theta^2 drd\theta dz$$

$$+\frac{1}{2}\int\limits_0^L\int\limits_0^{2\pi}\int\limits_\varepsilon^1 rv_\theta^2\frac{\partial v_z}{\partial z}drd\theta dz+\int\limits_0^L\int\limits_0^{2\pi}\int\limits_\varepsilon^1\frac{\partial v_\theta}{\partial\theta}pdrd\theta dz$$

$$+\frac{1}{Re}\int\limits_0^L\int\limits_0^{2\pi}\left[v_\theta\frac{\partial}{\partial r}\left(rv_\theta\right)\right]_\varepsilon^1 d\theta dz-\frac{1}{Re}\int\limits_0^L\int\limits_0^{2\pi}\int\limits_\varepsilon^1\frac{1}{r}\left(\frac{\partial}{\partial r}\left(rv_\theta\right)\right)^2drd\theta dz$$

$$-\frac{1}{Re}\int\limits_0^L\int\limits_0^{2\pi}\int\limits_\varepsilon^1\frac{1}{r}\left(\frac{\partial v_\theta}{\partial\theta}\right)^2drd\theta dz+\frac{1}{Re}\int\limits_0^L\int\limits_0^{2\pi}\int\limits_\varepsilon^1\frac{2}{r}v_\theta\frac{\partial v_r}{\partial\theta}drd\theta dz$$

$$-\frac{1}{Re}\int\limits_0^L\int\limits_0^{2\pi}\int\limits_\varepsilon^1 r\left(\frac{\partial v_\theta}{\partial z}\right)^2drd\theta dz.$$

Integration by parts of the third integral in (4.73) yields

$$\int\limits_0^L\int\limits_0^{2\pi}\int\limits_\varepsilon^1\left[-\left(rv_z v_r\frac{\partial\left(v_z+\tilde{V}_z\right)}{\partial r}+v_z v_\theta\frac{\partial v_z}{\partial\theta}+rv_z\left(v_z+\tilde{V}_z\right)\frac{\partial v_z}{\partial z}\right)-rv_z\frac{\partial p}{\partial z}\right.$$

$$\left.+\frac{1}{Re}\left(v_z\frac{\partial}{\partial r}\left(r\frac{\partial v_z}{\partial r}\right)+v_z\frac{1}{r}\frac{\partial^2 v_z}{\partial\theta^2}+rv_z\frac{\partial^2 v_z}{\partial z^2}\right)\right]drd\theta dz$$

$$=\frac{1}{2}\int\limits_0^L\int\limits_0^{2\pi}\left[-rv_z^2 v_r\right]_\varepsilon^1 d\theta dz+\frac{1}{2}\int\limits_0^L\int\limits_0^{2\pi}\int\limits_\varepsilon^1 v_z^2\frac{\partial\left(rv_r\right)}{\partial r}drd\theta dz$$

$$
- \int\limits_0^L \int\limits_0^{2\pi} \int\limits_\varepsilon^1 r v_z v_r \frac{\partial \tilde{V}_z}{\partial r} dr d\theta dz + \frac{1}{2} \int\limits_0^L \int\limits_0^{2\pi} \int\limits_\varepsilon^1 v_z^2 \frac{\partial v_\theta}{\partial \theta} dr d\theta dz
$$

$$
+ \frac{1}{2} \int\limits_0^L \int\limits_0^{2\pi} \int\limits_\varepsilon^1 r v_z^2 \frac{\partial v_z}{\partial z} dr d\theta dz + \int\limits_0^L \int\limits_0^{2\pi} \int\limits_\varepsilon^1 r \frac{\partial v_z}{\partial z} p \, dr d\theta dz
$$

$$
+ \frac{1}{Re} \int\limits_0^L \int\limits_0^{2\pi} \left[r v_z \frac{\partial v_z}{\partial r} \right]_\varepsilon^1 d\theta dz - \frac{1}{Re} \int\limits_0^L \int\limits_0^{2\pi} \int\limits_\varepsilon^1 r \left(\frac{\partial v_z}{\partial r} \right)^2 dr d\theta dz
$$

$$
- \frac{1}{Re} \int\limits_0^L \int\limits_0^{2\pi} \int\limits_\varepsilon^1 \frac{1}{r} \left(\frac{\partial v_z}{\partial \theta} \right)^2 dr d\theta dz - \frac{1}{Re} \int\limits_0^L \int\limits_0^{2\pi} \int\limits_\varepsilon^1 r \left(\frac{\partial v_z}{\partial z} \right)^2 dr d\theta dz.
$$

Inserting the results into (4.73) yields

$$
\dot{E}_\varepsilon(\mathbf{w}) = \frac{1}{2} \int\limits_0^L \int\limits_0^{2\pi} \int\limits_\varepsilon^1 \left(v_r^2 + v_\theta^2 + v_z^2 + \frac{2}{\rho} p \right) \underbrace{\left(\frac{1}{r} \frac{\partial(r v_r)}{\partial r} + \frac{1}{r} \frac{\partial v_\theta}{\partial \theta} + \frac{\partial v_z}{\partial z} \right)}_{=0 \text{ by incompressibility}} r \, dr d\theta dz
$$

$$
+ \int\limits_0^L \int\limits_0^{2\pi} \left[-\frac{1}{2} r v_r^3 \right]_\varepsilon^1 d\theta dz + \int\limits_0^L \int\limits_0^{2\pi} \left[-r v_r p \right]_\varepsilon^1 d\theta dz + \frac{1}{Re} \int\limits_0^L \int\limits_0^{2\pi} \left[v_r \frac{\partial}{\partial r}(r v_r) \right]_\varepsilon^1 d\theta dz
$$

$$
+ \frac{1}{2} \int\limits_0^L \int\limits_0^{2\pi} \left[-r v_r v_\theta^2 \right]_\varepsilon^1 d\theta dz + \frac{1}{Re} \int\limits_0^L \int\limits_0^{2\pi} \left[v_\theta \frac{\partial}{\partial r}(r v_\theta) \right]_\varepsilon^1 d\theta dz + \frac{1}{2} \int\limits_0^L \int\limits_0^{2\pi} \left[-r v_z^2 v_r \right]_\varepsilon^1 d\theta dz
$$

$$
+ \frac{1}{Re} \int\limits_0^L \int\limits_0^{2\pi} \left[r v_z \frac{\partial v_z}{\partial r} \right]_\varepsilon^1 d\theta dz - \int\limits_0^L \int\limits_0^{2\pi} \int\limits_\varepsilon^1 r v_z v_r \frac{\partial \tilde{V}_z}{\partial r} dr d\theta dz - \frac{1}{Re} \int\limits_0^L \int\limits_0^{2\pi} \int\limits_\varepsilon^1 \frac{2}{r} v_r \frac{\partial v_\theta}{\partial \theta} dr d\theta dz
$$

$$
+ \frac{1}{Re} \int\limits_0^L \int\limits_0^{2\pi} \int\limits_\varepsilon^1 \frac{2}{r} v_\theta \frac{\partial v_r}{\partial \theta} dr d\theta dz - \frac{1}{Re} \int\limits_0^L \int\limits_0^{2\pi} \int\limits_\varepsilon^1 \frac{1}{r} \left(\frac{\partial}{\partial r}(r v_r) \right)^2 dr d\theta dz
$$

$$
- \frac{1}{Re} \int\limits_0^L \int\limits_0^{2\pi} \int\limits_\varepsilon^1 \frac{1}{r} \left(\frac{\partial v_r}{\partial \theta} \right)^2 dr d\theta dz - \frac{1}{Re} \int\limits_0^L \int\limits_0^{2\pi} \int\limits_\varepsilon^1 r \left(\frac{\partial v_r}{\partial z} \right)^2 dr d\theta dz
$$

$$
- \frac{1}{Re} \int\limits_0^L \int\limits_0^{2\pi} \int\limits_\varepsilon^1 \frac{1}{r} \left(\frac{\partial}{\partial r}(r v_\theta) \right)^2 dr d\theta dz - \frac{1}{Re} \int\limits_0^L \int\limits_0^{2\pi} \int\limits_\varepsilon^1 \frac{1}{r} \left(\frac{\partial v_\theta}{\partial \theta} \right)^2 dr d\theta dz
$$

$$
- \frac{1}{Re} \int\limits_0^L \int\limits_0^{2\pi} \int\limits_\varepsilon^1 r \left(\frac{\partial v_\theta}{\partial z} \right)^2 dr d\theta dz - \frac{1}{Re} \int\limits_0^L \int\limits_0^{2\pi} \int\limits_\varepsilon^1 r \left(\frac{\partial v_z}{\partial r} \right)^2 dr d\theta dz
$$

$$
- \frac{1}{Re} \int\limits_0^L \int\limits_0^{2\pi} \int\limits_\varepsilon^1 \frac{1}{r} \left(\frac{\partial v_z}{\partial \theta} \right)^2 dr d\theta dz - \frac{1}{Re} \int\limits_0^L \int\limits_0^{2\pi} \int\limits_\varepsilon^1 r \left(\frac{\partial v_z}{\partial z} \right)^2 dr d\theta dz.
$$

Since

$$\int\limits_0^L \int\limits_0^{2\pi} \int\limits_\varepsilon^1 v_r \frac{\partial v_r}{\partial r} dr d\theta dz \;\; = \;\; \frac{1}{2} \int\limits_0^L \int\limits_0^{2\pi} \left[v_r^2\right]_{r=\varepsilon}^1 d\theta dz$$

$$\int\limits_0^L \int\limits_0^{2\pi} \int\limits_\varepsilon^1 v_\theta \frac{\partial v_\theta}{\partial r} dr d\theta dz \;\; = \;\; \frac{1}{2} \int\limits_0^L \int\limits_0^{2\pi} \left[v_\theta^2\right]_{r=\varepsilon}^1 d\theta dz$$

we have that

$$-\frac{1}{Re} \int\limits_0^L \int\limits_0^{2\pi} \int\limits_\varepsilon^1 \frac{1}{r} \left(\frac{\partial}{\partial r}\left(r v_r\right)\right)^2 dr d\theta dz - \frac{1}{Re} \int\limits_0^L \int\limits_0^{2\pi} \int\limits_\varepsilon^1 \frac{1}{r} \left(\frac{\partial}{\partial r}\left(r v_\theta\right)\right)^2 dr d\theta dz$$

$$-\frac{1}{Re} \int\limits_0^L \int\limits_0^{2\pi} \int\limits_\varepsilon^1 \frac{1}{r} \left(\frac{\partial v_r}{\partial \theta}\right)^2 dr d\theta dz - \frac{1}{Re} \int\limits_0^L \int\limits_0^{2\pi} \int\limits_\varepsilon^1 \frac{1}{r} \left(\frac{\partial v_\theta}{\partial \theta}\right)^2 dr d\theta dz$$

$$+\frac{1}{Re} \int\limits_0^L \int\limits_0^{2\pi} \int\limits_\varepsilon^1 \frac{2}{r} v_\theta \frac{\partial v_r}{\partial \theta} dr d\theta dz - \frac{1}{Re} \int\limits_0^L \int\limits_0^{2\pi} \int\limits_\varepsilon^1 \frac{2}{r} v_r \frac{\partial v_\theta}{\partial \theta} dr d\theta dz$$

$$= -\frac{1}{Re} \int\limits_0^L \int\limits_0^{2\pi} \int\limits_\varepsilon^1 \frac{1}{r} \left(v_r^2 + 2 r v_r \frac{\partial v_r}{\partial r} + r^2 \left(\frac{\partial v_r}{\partial r}\right)^2 \right) dr d\theta dz$$

$$-\frac{1}{Re} \int\limits_0^L \int\limits_0^{2\pi} \int\limits_\varepsilon^1 \frac{1}{r} \left(v_\theta^2 + 2 r v_\theta \frac{\partial v_\theta}{\partial r} + r^2 \left(\frac{\partial v_\theta}{\partial r}\right)^2 \right) dr d\theta dz$$

$$-\frac{1}{Re} \int\limits_0^L \int\limits_0^{2\pi} \int\limits_\varepsilon^1 \frac{1}{r} \left(\frac{\partial v_r}{\partial \theta}\right)^2 dr d\theta dz - \frac{1}{Re} \int\limits_0^L \int\limits_0^{2\pi} \int\limits_\varepsilon^1 \frac{1}{r} \left(\frac{\partial v_\theta}{\partial \theta}\right)^2 dr d\theta dz$$

$$+\frac{1}{Re} \int\limits_0^L \int\limits_0^{2\pi} \int\limits_\varepsilon^1 \frac{2}{r} v_\theta \frac{\partial v_r}{\partial \theta} dr d\theta dz - \frac{1}{Re} \int\limits_0^L \int\limits_0^{2\pi} \int\limits_\varepsilon^1 \frac{2}{r} v_r \frac{\partial v_\theta}{\partial \theta} dr d\theta dz$$

$$= -\frac{1}{Re} \int\limits_0^L \int\limits_0^{2\pi} \left[v_r^2 + v_\theta^2\right]_{r=\varepsilon}^1 d\theta dz - \frac{1}{Re} \int\limits_0^L \int\limits_0^{2\pi} \int\limits_\varepsilon^1 \frac{1}{r} \left(v_r^2 + r^2 \left(\frac{\partial v_r}{\partial r}\right)^2 \right) dr d\theta dz$$

$$-\frac{1}{Re} \int\limits_0^L \int\limits_0^{2\pi} \int\limits_\varepsilon^1 \frac{1}{r} \left(v_\theta^2 + r^2 \left(\frac{\partial v_\theta}{\partial r}\right)^2 \right) dr d\theta dz - \frac{1}{Re} \int\limits_0^L \int\limits_0^{2\pi} \int\limits_\varepsilon^1 \frac{1}{r} \left(\frac{\partial v_r}{\partial \theta}\right)^2 dr d\theta dz$$

$$-\frac{1}{Re} \int\limits_0^L \int\limits_0^{2\pi} \int\limits_\varepsilon^1 \frac{1}{r} \left(\frac{\partial v_\theta}{\partial \theta}\right)^2 dr d\theta dz + \frac{1}{Re} \int\limits_0^L \int\limits_0^{2\pi} \int\limits_\varepsilon^1 \frac{2}{r} v_\theta \frac{\partial v_r}{\partial \theta} dr d\theta dz$$

$$-\frac{1}{Re} \int\limits_0^L \int\limits_0^{2\pi} \int\limits_\varepsilon^1 \frac{2}{r} v_r \frac{\partial v_\theta}{\partial \theta} dr d\theta dz$$

$$= -\frac{1}{Re} \int\limits_0^L \int\limits_0^{2\pi} \left[v_r^2 + v_\theta^2\right]_{r=\varepsilon}^1 d\theta dz - \frac{1}{Re} \int\limits_0^L \int\limits_0^{2\pi} \int\limits_\varepsilon^1 r \left(\frac{\partial v_r}{\partial r}\right)^2 dr d\theta dz$$

$$-\frac{1}{Re} \int\limits_0^L \int\limits_0^{2\pi} \int\limits_\varepsilon^1 r \left(\frac{\partial v_\theta}{\partial r}\right)^2 dr d\theta dz - \frac{1}{Re} \int\limits_0^L \int\limits_0^{2\pi} \int\limits_\varepsilon^1 \frac{1}{r} \left(v_r + \frac{\partial v_\theta}{\partial \theta}\right)^2 dr d\theta dz$$

$$-\frac{1}{Re} \int\limits_0^L \int\limits_0^{2\pi} \int\limits_\varepsilon^1 \frac{1}{r} \left(v_\theta - \frac{\partial v_r}{\partial \theta}\right)^2 dr d\theta dz.$$

Therefore, we get

$$\dot{E}_\varepsilon(\mathbf{w}) = \int\limits_0^L \int\limits_0^{2\pi} \left[-\frac{1}{2} r v_r^3\right]_\varepsilon^1 d\theta dz + \int\limits_0^L \int\limits_0^{2\pi} \left[-r v_r p\right]_\varepsilon^1 d\theta dz$$

$$+ \frac{1}{Re} \int\limits_0^L \int\limits_0^{2\pi} \left[v_r \frac{\partial}{\partial r}(r v_r)\right]_\varepsilon^1 d\theta dz + \frac{1}{2} \int\limits_0^L \int\limits_0^{2\pi} \left[-r v_r v_\theta^2\right]_\varepsilon^1 d\theta dz$$

$$+ \frac{1}{Re} \int\limits_0^L \int\limits_0^{2\pi} \left[v_\theta \frac{\partial}{\partial r}(r v_\theta)\right]_\varepsilon^1 d\theta dz + \frac{1}{2} \int\limits_0^L \int\limits_0^{2\pi} \left[-r v_z^2 v_r\right]_\varepsilon^1 d\theta dz$$

$$+ \frac{1}{Re} \int\limits_0^L \int\limits_0^{2\pi} \left[r v_z \frac{\partial v_z}{\partial r}\right]_\varepsilon^1 d\theta dz - \frac{1}{Re} \int\limits_0^L \int\limits_0^{2\pi} \left[v_r^2 + v_\theta^2\right]_{r=\varepsilon}^1 d\theta dz$$

$$- \int\limits_0^L \int\limits_0^{2\pi} \int\limits_\varepsilon^1 r v_z v_r \frac{\partial \bar{V}_z}{\partial r} dr d\theta dz - \frac{1}{Re} \int\limits_0^L \int\limits_0^{2\pi} \int\limits_\varepsilon^1 r \left(\frac{\partial v_r}{\partial z}\right)^2 dr d\theta dz$$

$$- \frac{1}{Re} \int\limits_0^L \int\limits_0^{2\pi} \int\limits_\varepsilon^1 r \left(\frac{\partial v_\theta}{\partial z}\right)^2 dr d\theta dz - \frac{1}{Re} \int\limits_0^L \int\limits_0^{2\pi} \int\limits_\varepsilon^1 r \left(\frac{\partial v_z}{\partial r}\right)^2 dr d\theta dz$$

$$- \frac{1}{Re} \int\limits_0^L \int\limits_0^{2\pi} \int\limits_\varepsilon^1 \frac{1}{r} \left(\frac{\partial v_z}{\partial \theta}\right)^2 dr d\theta dz - \frac{1}{Re} \int\limits_0^L \int\limits_0^{2\pi} \int\limits_\varepsilon^1 r \left(\frac{\partial v_z}{\partial z}\right)^2 dr d\theta dz$$

$$- \frac{1}{Re} \int\limits_0^L \int\limits_0^{2\pi} \int\limits_\varepsilon^1 r \left(\frac{\partial v_r}{\partial r}\right)^2 dr d\theta dz - \frac{1}{Re} \int\limits_0^L \int\limits_0^{2\pi} \int\limits_\varepsilon^1 r \left(\frac{\partial v_\theta}{\partial r}\right)^2 dr d\theta dz$$

$$- \frac{1}{Re} \int\limits_0^L \int\limits_0^{2\pi} \int\limits_\varepsilon^1 \frac{1}{r} \left(v_r + \frac{\partial v_\theta}{\partial \theta}\right)^2 dr d\theta dz - \frac{1}{Re} \int\limits_0^L \int\limits_0^{2\pi} \int\limits_\varepsilon^1 \frac{1}{r} \left(v_\theta - \frac{\partial v_r}{\partial \theta}\right)^2 dr d\theta dz.$$

$$(4.74)$$

Now, we write

$$v_r \left(r, \theta, z, t \right) = v_r \left(1, \theta, z, t \right) - \int\limits_r^1 \frac{\partial v_r}{\partial r} dr$$

so that

$$v_r^2 \left(r, \theta, z, t \right) = \left(v_r \left(1, \theta, z, t \right) - \int\limits_r^1 \frac{\partial v_r}{\partial r} dr \right)^2 \leq 2 v_r^2 \left(1, \theta, z, t \right) + 2 \left(\int\limits_r^1 \frac{\partial v_r}{\partial r} dr \right)^2.$$

By the Schwartz inequality,

$$\left(\int\limits_r^1 \frac{1}{\sqrt{r}} \sqrt{r} \frac{\partial v_r}{\partial r} dr \right)^2 \leq -\ln r \int\limits_r^1 r \left(\frac{\partial v_r}{\partial r} \right)^2 dr$$

so we have that

$$r v_r^2 \left(r, \theta, z, t \right) \leq 2 r v_r^2 \left(1, \theta, z, t \right) - 2 r \ln r \int\limits_\varepsilon^1 r \left(\frac{\partial v_r}{\partial r} \right)^2 dr$$

where we have set $r = \varepsilon$ in the lower integral limit. We now get

$$\int\limits_0^L \int\limits_0^{2\pi} \int\limits_\varepsilon^1 v_r^2 r \, dr d\theta dz \leq \int\limits_0^L \int\limits_0^{2\pi} \int\limits_\varepsilon^1 \left(2 r v_r^2 \left(1, \theta, z, t \right) - 2 r \ln r \int\limits_\varepsilon^1 r \left(\frac{\partial v_r}{\partial r} \right)^2 dr \right) dr d\theta dz$$

$$= \left(1 - \varepsilon^2 \right) \int\limits_0^L \int\limits_0^{2\pi} v_r^2 \left(1, \theta, z, t \right) d\theta dz + \frac{1}{2} \left(1 - \varepsilon^2 + 2\varepsilon^2 \ln \varepsilon \right) \int\limits_0^L \int\limits_0^{2\pi} \int\limits_\varepsilon^1 r \left(\frac{\partial v_r}{\partial r} \right)^2 dr d\theta dz.$$

Analogous derivations for v_θ, and v_z, yield

$$-\frac{1}{Re} \int\limits_0^L \int\limits_0^{2\pi} \int\limits_\varepsilon^1 \left(\left(\frac{\partial v_r}{\partial r} \right)^2 + \left(\frac{\partial v_\theta}{\partial r} \right)^2 + \left(\frac{\partial v_z}{\partial r} \right)^2 \right) r \, dr d\theta dz \leq$$

$$-\frac{4}{Re \left(1 - \varepsilon^2 + 2\varepsilon^2 \ln \varepsilon \right)} E(\mathbf{w})$$

$$+ \frac{2 \left(1 - \varepsilon^2 \right)}{Re \left(1 - \varepsilon^2 + 2\varepsilon^2 \ln \varepsilon \right)} \int\limits_0^L \int\limits_0^{2\pi} \left(v_r^2 \left(1, \theta, z, t \right) + v_\theta^2 \left(1, \theta, z, t \right) + v_z^2 \left(1, \theta, z, t \right) \right) d\theta dz.$$

Inserting this result into (4.74), and letting $\varepsilon \to 0$, gives

$$\dot{E}(\mathbf{w}) \leq -2\left(\frac{2}{Re}-1\right)E(\mathbf{w}) + \frac{2}{Re}\int_0^L\int_0^{2\pi}[v_r^2+v_\theta^2+v_z^2]_{r=1}\,d\theta dz$$

$$-\frac{1}{2}\int_0^L\int_0^{2\pi}[v_r^3]_{r=1}\,d\theta dz - \int_0^L\int_0^{2\pi}[v_rp]_{r=1}\,d\theta dz - \frac{1}{2}\int_0^L\int_0^{2\pi}[v_rv_\theta^2]_{r=1}\,d\theta dz$$

$$-\frac{1}{2}\int_0^L\int_0^{2\pi}[v_z^2v_r]_{r=1}\,d\theta dz + \frac{1}{Re}\int_0^L\int_0^{2\pi}\left[v_r\frac{\partial v_r}{\partial r}\right]_{r=1}\,d\theta dz$$

$$+\frac{1}{Re}\int_0^L\int_0^{2\pi}\left[v_\theta\frac{\partial v_\theta}{\partial r}\right]_{r=1}\,d\theta dz + \frac{1}{Re}\int_0^L\int_0^{2\pi}\left[v_z\frac{\partial v_z}{\partial r}\right]_{r=1}\,d\theta dz \quad (4.75)$$

where we have used

$$-\int_0^L\int_0^{2\pi}\int_\varepsilon^1 rv_zv_r\frac{\partial \tilde{V}_z}{\partial r}drd\theta dz \leq \int_0^L\int_0^{2\pi}\int_\varepsilon^1 r\,|v_z|\,|v_r|\left|\frac{\partial \tilde{V}_z}{\partial r}\right|drd\theta dz$$

$$\leq \int_0^L\int_0^{2\pi}\int_0^1 \left(v_r^2+v_\theta^2+v_z^2\right)rdrd\theta dz = 2E(\mathbf{w})$$

and

$$\frac{1}{Re}\int_0^L\int_0^{2\pi}\left[v_r\frac{\partial}{\partial r}(rv_r)\right]_\varepsilon^1\,d\theta dz + \frac{1}{Re}\int_0^L\int_0^{2\pi}\left[v_\theta\frac{\partial}{\partial r}(rv_\theta)\right]_\varepsilon^1\,d\theta dz$$

$$-\frac{1}{Re}\int_0^L\int_0^{2\pi}[v_r^2+v_\theta^2]_\varepsilon^1\,d\theta dz$$

$$=\frac{1}{Re}\int_0^L\int_0^{2\pi}\left[v_r\frac{\partial v_r}{\partial r}\right]_{r=1}\,d\theta dz + \frac{1}{Re}\int_0^L\int_0^{2\pi}\left[v_\theta\frac{\partial v_\theta}{\partial r}\right]_{r=1}\,d\theta dz.$$

In (4.75), all but the first term on the right hand side of the inequality are evaluated on the boundary. These are the terms by which boundary control laws are designed. Below, a pressure-based control law is presented.

Boundary Control

We propose the following control law

$$v_r(1,\theta,z,t) = k(p(1,\theta,z,t) - p(1,\theta+\pi,z,t))$$
$$v_\theta(1,\theta,z,t) = 0 \qquad\qquad (4.76)$$
$$v_z(1,\theta,z,t) = 0.$$

Inserting into (4.75), yields

$$\dot{E}(\mathbf{w}) \le -2 \left(\frac{2}{Re} - 1 \right) E(\mathbf{w}) + \frac{1}{Re} \int_0^L \int_0^{2\pi} v_r^2 \left(1, \theta, z, t \right) d\theta dz$$

$$- \frac{1}{2} \int_0^L \int_0^{2\pi} v_r^3 \left(1, \theta, z, t \right) d\theta dz - \int_0^L \int_0^{2\pi} v_r \left(1, \theta, z, t \right) p \left(1, \theta, z, t \right) d\theta dz \quad (4.77)$$

For n odd, we get

$$\int_0^{2\pi} v_r^n (1, \theta, z, t) d\theta = \int_{-\pi}^0 v_r^n \left(1, \theta, z, t \right) d\theta + \int_0^{\pi} v_r^n \left(1, \theta, z, t \right) d\theta$$

$$= -\int_{-\pi}^0 v_r^n \left(1, -\theta, z, t \right) d\theta + \int_0^{\pi} v_r^n \left(1, \theta, z, t \right) d\theta$$

and by a change of variables in the first integral ($\theta^* = -\theta$), we get

$$\int_0^{2\pi} v_r^n (1, \theta, z) d\theta = -\int_0^{\pi} v_r^n \left(1, \theta^*, z, t \right) d\theta^* + \int_0^{\pi} v_r^n \left(1, \theta, z, t \right) d\theta = 0$$

which proves that the net mass flow through the wall is zero, and that

$$\int_0^{2\pi} \left[v_r^3 \right]_{r=1} d\theta = 0$$

by setting $n = 1$ and $n = 3$, respectively. Since

$$\int_0^{2\pi} v_r \left(1, \theta, z, t \right) p \left(1, \theta, z, t \right) d\theta$$

$$= \int_{-\pi}^0 v_r \left(1, \theta, z, t \right) p \left(1, \theta, z, t \right) d\theta + \int_0^{\pi} v_r \left(1, \theta, z, t \right) p \left(1, \theta, z, t \right) d\theta$$

$$= -\int_{\pi}^0 v_r \left(1, -\theta^*, z, t \right) p \left(1, -\theta^*, z, t \right) d\theta^* + \int_0^{\pi} v_r \left(1, \theta, z, t \right) p \left(1, \theta, z, t \right) d\theta$$

$$= -\int_0^{\pi} v_r \left(1, \theta^*, z, t \right) p \left(1, -\theta^*, z, t \right) d\theta^* + \int_0^{\pi} v_r \left(1, \theta, z, t \right) p \left(1, \theta, z, t \right) d\theta$$

$$= \int_0^{\pi} v_r \left(1, \theta, z, t \right) \left(p \left(1, \theta, z, t \right) - p \left(1, -\theta, z, t \right) \right) d\theta$$

$$= \frac{1}{k} \int_0^\pi v_r^2 \left(1, \theta, z, t\right) d\theta = \frac{1}{2k} \int_0^{2\pi} v_r^2 \left(1, \theta, z, t\right) d\theta$$

we obtain

$$\dot{E}(\mathbf{w}) \leq -2 \left(\frac{2}{Re} - 1 \right) E(\mathbf{w}) - \left(\frac{1}{2k} - \frac{1}{Re} \right) \int_0^L \int_0^{2\pi} v_r^2 \left(1, \theta, z, t\right) d\theta dz. \qquad (4.78)$$

Thus, we have shown that the equilibrium profile is globally exponentially stable in L_2 for sufficiently small Re and for appropriately selected feedback gain k. Note that the control law is decentralized and has a symmetrical structure similar to that of the pressure-based control designed for the 2D channel flow case (see equations (4.63)–(4.64)).

4.3.4   Drag Reduction Below Laminar Flow

The simple pressure-based feedback control strategy for wall-transpiration control of incompressible unsteady 2D channel flow proposed in Section 4.3.1, leads to flow transients with instantaneous drag far lower than that of the corresponding laminar flow (see lower right graph in Figure 4.12). This touches at the common belief that the laminar flow constitutes a fundamental limit to the drag reduction that is possible to obtain, which is stated in [21] as the following conjecture

Conjecture 4.1 *The lowest sustainable drag of an incompressible constant mass-flux channel flow in either 2D or 3D, when controlled via a distribution of zero-net mass-flux blowing/suction over the channel walls, is exactly that of the laminar flow.*

We denote the drag of the laminar flow D_L. By sustainable drag, D_∞, we mean the time average (denoted $\bar{D}(t)$) of the instantaneous drag, $D(t)$, as the averaging time T approaches infinity, i.e.,

$$D_\infty \triangleq \lim_{T \to \infty} \bar{D}(T) \triangleq \lim_{T \to \infty} \frac{1}{T} \int_0^T D(t) dt$$

with the instantaneous drag given as in (4.71), multiplied by the factor μL. In [25] the mechanisms that initiate the $D(t) < D_L$ transient are investigated, and an attempt at sustaining the drag below that of laminar flow is made. A simulation of a constant mass-flux 2D channel flow at $Re = 7500$, using a box length 60 times the channel half width serves as an illustration. The flow at $t = 0^-$ in Figure 4.19, a fully established unsteady flow in a 2D channel (see, e.g., [69]), has extensive regions of backflow near the walls. This appears to be the key to initiating a $D(t) < D_L$ transient. A scatter plot of the local control ϕ as a function of the local value of $(-\mu \partial U / \partial n)$ at $t = 5$ (shortly after the control is turned on)
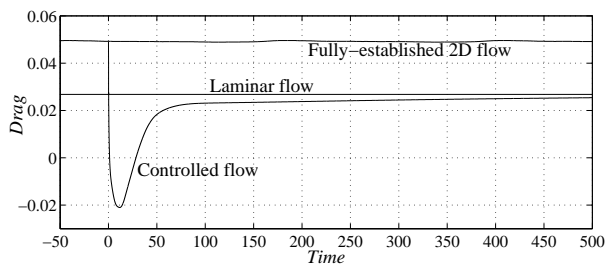
Figure 4.19: History of drag. Simulation initiated from fully established unsteady 2D flow at $Re = 7500$. Stabilizing pressure-based feedback control strategy with $k = -0.125$ turned on at $t = 0$.
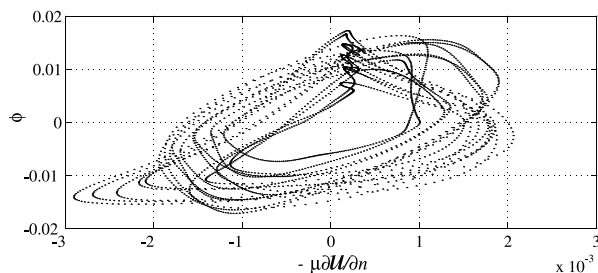
Figure 4.20: Scatterplot of ϕ versus $(-\mu \partial U / \partial n)$ at $t = 5$.

is shown in Figure 4.20, demonstrating correlation of blowing with local regions of positive drag and suction with local regions of negative drag using the present strategy (76% of the samples are in the first and third quadrants). By generally applying suction at the walls in regions of negative drag, and applying blowing in regions of large positive drag, the negative drag regions are intensified (locally, more negative drag) and the high positive drag regions are moderated (locally, less positive drag), as illustrated in Figure 4.21. In terms of reducing the total instantaneous drag $D(t)$ integrated over the walls at time $t = 5$, both effects are beneficial, and thus the control application results, for a brief amount of time, in a "win-win" situation, facilitating a drastic transient reduction in skin-friction drag to well below laminar levels. Unfortunately, the wall suction quickly acts to remove the backflow from the flow domain entirely, after which the instantaneous drag $D(t)$ asymptotes back to the laminar level, D_L.

A metric which quantifies the degree of backflow present at any instant in a particular flow is given by

$$b_p = \left[\frac{1}{A} \int_{\Omega^-} |U|^p d\Omega \right]^{1/p}$$

where Ω^- is the subset of the channel flow domain Ω which is characterized by
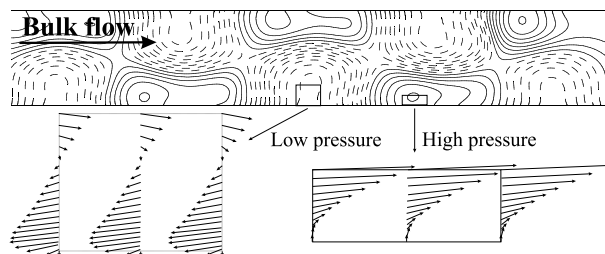
Figure 4.21: Win-win mechanism at $t = 5$: intensification of local regions of negative drag by suction in low pressure regions and moderation of positive drag by blowing in high pressure regions. Shown are contours of pressure in 1/6 of the computational domain (top) and selected velocity profiles (bottom)
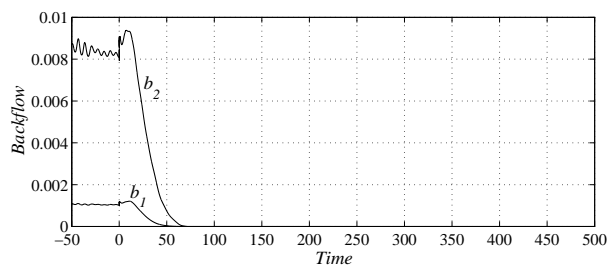
Figure 4.22: Elimination of backflow after control is turned on, as measured by $b_1(t)$ and $b_2(t)$.

regions of flow with negative streamwise velocity, $i.e.$, $\Omega^- = \{\Omega(x, y)|U(x, y) < 0\}$, and A is the volume of the entire channel domain Ω. For the simulation depicted in Figures 4.19–4.21, plots of the history of b_1 and b_2 are shown in Figure 4.22. Note that, by both measures, the backflow is quickly eliminated after the control is initiated; flow visualizations such as Figure 4.21 demonstrate clearly that the backflowing fluid in Ω^- is simply removed from the channel by the control suction.

As a "standard" problem to test the utility of a given control strategy for reducing time-averaged drag to below laminar levels, a series of controlled 2D channel flow simulations at $Re = 7500$ were initialized from small (random) perturbations to a laminar flow profile. The control producing the $D(t) < D_L$ transients was cycled off and on periodically, with the "running average" of the drag, $\overline{D}(t) = \int_0^t D(t')\,dt'$, computed as the flow evolved to quantify progress towards sustained drag reduction. A large variety of different periods, duty cycles, and control amplitudes were explored; Table 1 summarizes specific cases examined in detail.

Cases 1-5 reported in Table 4.1 were executed at a cycle time of $T_{cycle} = 3000$ for a variety of duty cycles with relatively strong stabilizing feedback applied during the second segment of each cycle. Cases 6-8 were similar, but applied relatively

Case	T_{cycle}	T_1	T_2	k_1	k_2
1	3000	2600	400	0	0.125
2	3000	2700	300	0	0.125
3	3000	2800	200	0	0.125
4	3000	2900	100	0	0.125
5	3000	2950	50	0	0.125
6	3000	2000	1000	0	0.031
7	3000	2500	500	0	0.031
8	3000	2800	200	0	0.031
9	2000	1600	400	0	0.125
10	2000	1700	300	0	0.125
11	2000	1800	200	0	0.125
12	2000	1900	100	0	0.125
13	2000	1950	50	0	0.125
14	1000	250	750	−0.031	0.031
15	1000	350	650	−0.031	0.031
16	1000	500	500	−0.031	0.031

Table 4.1: Forcing schedules explored during parametric study: T_{cycle} indicates the period of the cycle used, T_1 denotes the duration of the first segment of the cycle, T_2 denotes the duration of the second segment, k_1 denotes the feedback coefficient used during the first segment, and k_2 denotes the feedback coefficient during the second segment.

weak stabilizing feedback. Cases 9-13 returned to the relatively strong stabilizing feedback, but investigated a shorter cycle time. Finally, cases 14-16 were executed with destabilizing feedback applied during the first segment of each cycle, and stabilizing feedback applied during the second segment of each cycle; this was done to accelerate the formation of the backflow regions. Histories of the L_2 energy, the instantaneous and "running time-averaged" drag $D(t)$ and $\overline{D}(t)$, and the backflow measures b_1 and b_2 are illustrated in Figure 4.23 for four representative cases.

It was found in cases 1, 2, 9, 10, and 14, with T_2 relatively *large*, that the stabilization provided by the control during the second segment of each cycle was sufficient to stabilize the entire channel flow back to the parabolic profile; to illustrate, case 14 is plotted in Figure 4.23c. These cases imply that T_2 must be a sufficiently small fraction of T_{cycle} in order to allow a quasi-periodic behavior to establish.

It was found in cases 5, 8, 13, and 16, with T_2 relatively *small*, that the uncontrolled (or, in case 16, destabilized) evolution of the flow during the first segment of each cycle was sufficient to drive the time-averaged drag to heightened levels.

A trade-off is thus identified: decrease T_2 and there will be more backflow to exploit during each cycle (so the transient will be more effective at reducing drag), but by allowing the 2D unsteady flow to evolve for a longer time uncontrolled or destabilized, the mean drag is pulled up higher above the laminar level. Intermediate values of T_2 were sought for a variety of cycle times and forcing amplitudes over a
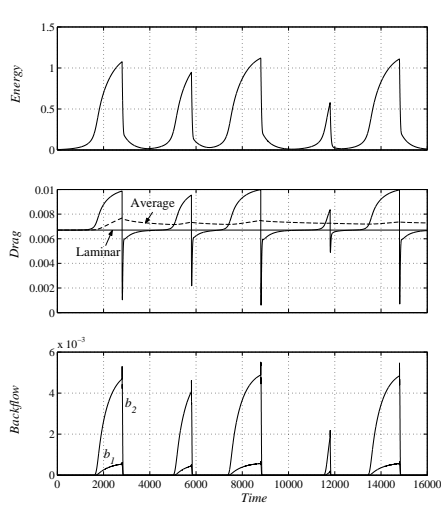
Figure 4.23a: Case 3: $T_{cycle} = 3000$, no feedback for $T_1 = 2600$, relatively strong stabilizing feedback for $T_2 = 400$.
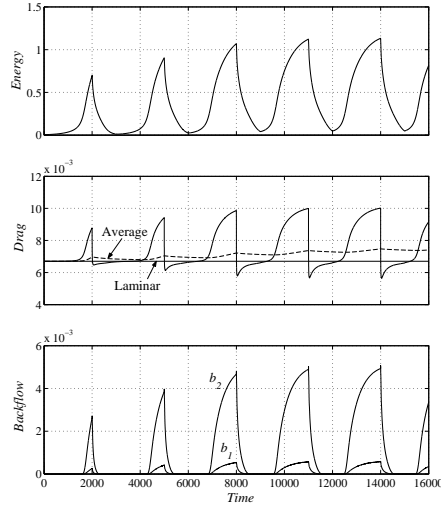
Figure 4.23b: Case 6: $T_{cycle} = 3000$, no feedback for $T_1 = 2000$, relatively weak stabilizing feedback for $T_2 = 1000$.
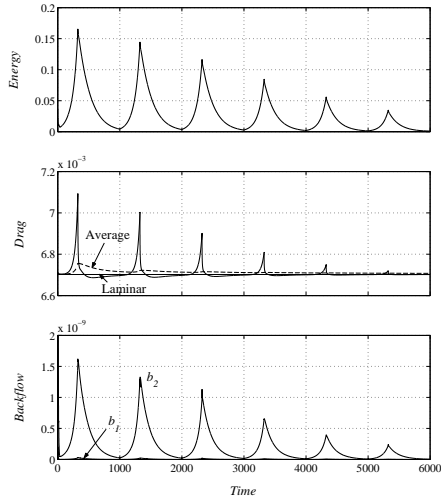
Figure 4.23c: Case 14: $T_{cycle} = 1000$, destabilizing feedback for $T_1 = 325$, stabilizing feedback for $T_2 = 675$.
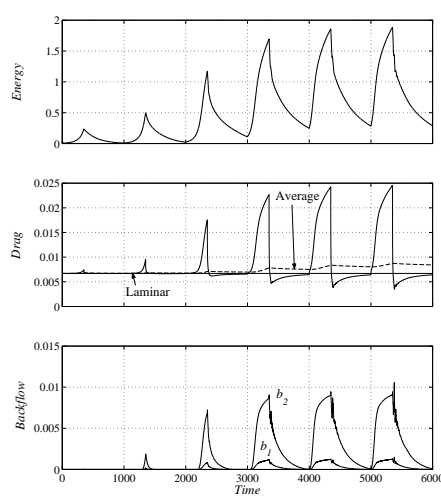
Figure 4.23d: Case 15: $T_{cycle} = 1000$, destabilizing feedback for $T_1 = 350$, stabilizing feedback for $T_2 = 650$.

Figure 4.23: Energy, drag and backflow for cases 3, 6, 14 and 15.

parametric study of several simulations, some of which are reported here. Over all these simulations, this trade-off was evident, and *not once did the running average,* $\overline{D}(t)$, *dip below the laminar value* when the simulations were initiated from the perturbed laminar state. These results indicate that it is always necessary to pay a more expensive price (in terms of the time-averaged drag) to obtain the backflow than the benefit (in terms of the time-averaged drag) that can be obtained by applying suction to the backflow regions. Therefore, it appears that the parabolic equilibrium profile represents a fundamental limit to the drag reduction possible when applying control based on wall transpiration with zero-net mass flow.

The objective of the control strategies above has been to stabilize the parabolic equilibrium profile. Although not explicitly stated in the objective, drag reduction is obtained indirectly using this strategy. For wall normal actuation, with zero-net mass flow, the objective of stabilizing the parabolic profile is equivalent to minimizing drag, due to Conjecture 4.1. However, it is clear that drag can be reduced further if actuation is directed in the streamwise direction, and in particular if it is allowed a steady-state offset. This calls for new actuators that allow slip boundary conditions at rigid walls. Advancements in this direction based on conveyer belts as actuators, allowing slip boundary conditions, are currently being pursued [26].

4.4 Suppression of Vortex Shedding

4.4.1 Simulations of the Controlled Navier-Stokes Equation

The flow past a 2D circular cylinder has been a popular model flow for studying vortex shedding suppression by means of open-loop or feedback control. For Reynolds numbers slightly larger than the critical value for onset of vortex shedding (which is approximately $Re_c = 47$), several authors have successfully suppressed vortex shedding in numerical simulations using various simple feedback control configurations. In [99], a pair of suction/blowing slots positioned on the cylinder wall were used for actuation, and shedding was suppressed for $Re = 60$, using proportional feedback from a single velocity measurement taken some distance downstream of the cylinder.

Using FLUENT[3], this result has been reproduced on a grid of approximately 4000 nodes shown in Figure 4.24. The initial condition for the simulations is obtained by starting from a perturbed velocity field and running the simulation for 500 time units. The result is a periodic steady state, as indicated in Figure 4.25 in terms of the lift coefficient, which is the normalized force acting on the cylinder in the vertical direction. The vorticity field at the end of this initial run is shown in Figure 4.26, where the von Kármán vortex street is clearly visible.

For the controlled flow, starting from the initial data from Figure 4.26, the time evolutions of the lift coefficient is shown in Figure 4.27, and the control effort is shown in Figure 4.28. They indicate that the vortex shedding is weakened, which

---

[3] FLUENT is a commercial computational fluid dynamics (CFD) package available from Fluent Inc.
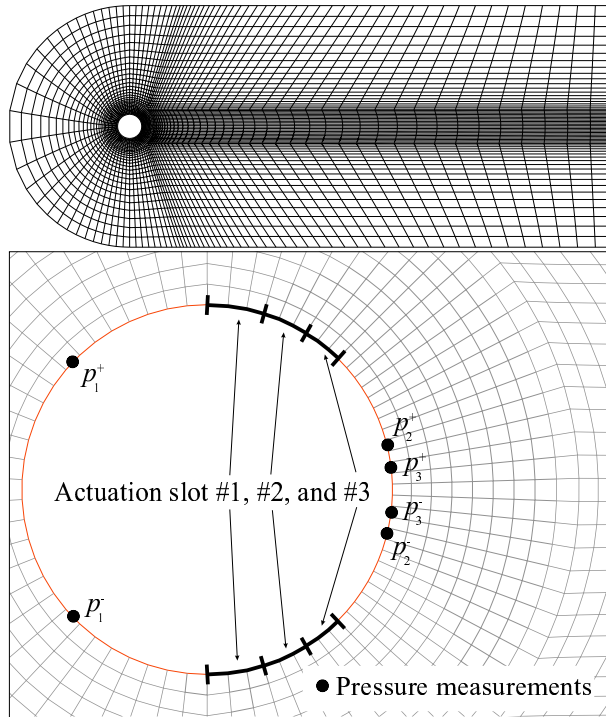
Figure 4.24: Computational grid, and zoom showing slots for blowing and suction, and locations at which pressure measurements are taken.

is confirmed by the nearly symmetric (about the streamwise axis) vorticity map at $t = 750$ shown in Figure 4.29. The controlled velocity field continues to oscillate a little, though. In terms of the lift coefficient, it continues to vary between $\approx \pm 0.02$ beyond the time interval shown in Figure 4.27, which is about 10% of its amplitude in the uncontrolled case.

For $Re = 80$, vortex shedding was reduced, but substantially less than for the $Re = 60$ case. In [53], the same actuation configuration was tried for $Re = 60$, using feedback from a pair of pressure sensors located on the cylinder wall. This attempt was unsuccessful, but by adding a third actuation slot, shedding was reduced considerably, even at $Re = 80$. In [6], simulations showed that stabilization at $Re = 60$ is also possible by adding more pressure sensors instead of adding an additional actuation slot.

Although some success in controlling vortex shedding has been achieved in numerical simulations, rigorous control designs are scarce due to the complexity of designing controllers based on the Navier-Stokes equation. A much simpler model, the Ginzburg-Landau equation with appropriate coefficients, has been found to model well the dynamics of vortex shedding near the critical value of the Reynolds number [63]. In [103], it was shown numerically that the Ginzburg-Landau model
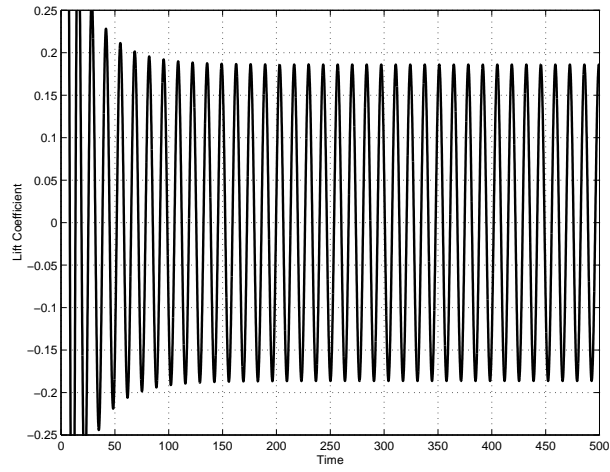
Figure 4.25: Lift coefficient for initial simulation at $Re = 60$.
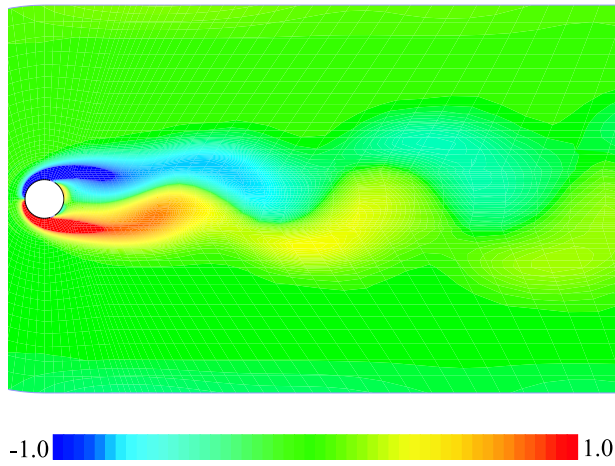
Figure 4.26: Vorticity field at $t = 500$ for $Re = 60$.
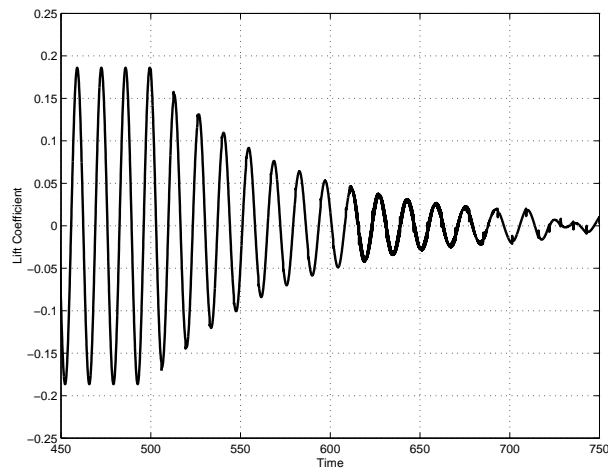
Figure 4.27: Lift coefficient for stabilizing control at $Re = 60$. Feedback from velocity measurement.
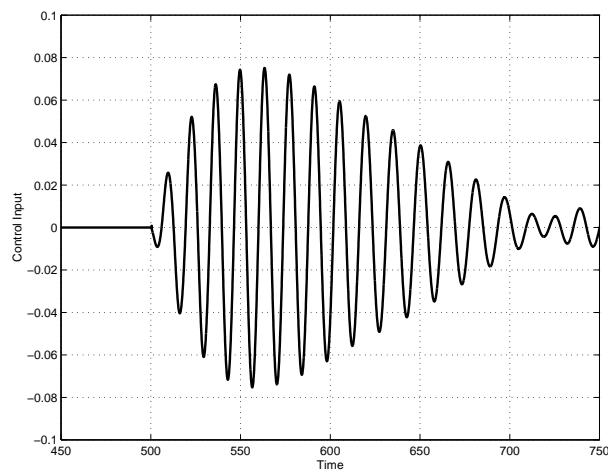
Figure 4.28: Control input for stabilizing control at $Re = 60$. Feedback from velocity measurement.
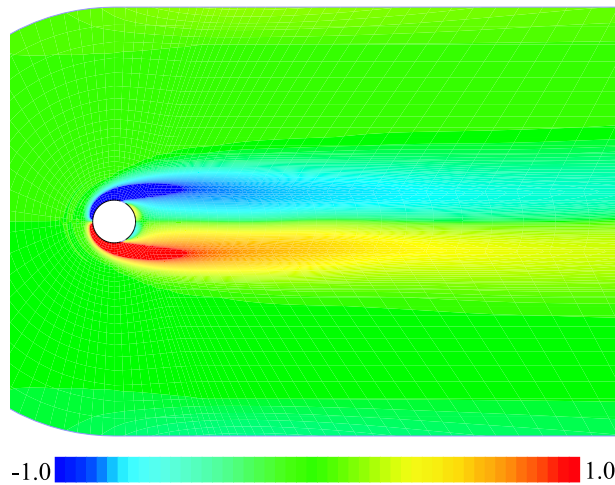
Figure 4.29: Vorticity field at $t = 750$ for stabilizing control at $Re = 60$. Feedback from velocity measurement.

for Reynolds numbers close to Re_c can be stabilized using proportional feedback from a single measurement downstream of the cylinder, to local forcing at the location of the cylinder. In [83], using the model from [103], stabilization was obtained in numerical simulations for $Re = 100$, with an LQG controller designed for the linearized Ginzburg-Landau equation.

In the following sections, we present a controller designed using backstepping, that is shown to globally stabilize the equilibrium at zero of a finite difference discretization of any order of the nonlinear Ginzburg-Landau model presented in [103]. These sections are based on [4] (also in [5]), and the method is similar to the work presented in [28]. The design is valid for any Reynolds number. Numerical simulations are provided in order to demonstrate the performance of the controller, along with the potential of using low order discretizations for the control design, and thereby reducing the number of sensors needed for implementation.

4.4.2 The Ginzburg-Landau Equation

The Ginzburg-Landau equation in the notation of [103] is given by

$$\frac{\partial A}{\partial t} = -a_1(x)\frac{\partial A}{\partial x} - a_2\frac{\partial^2 A}{\partial x^2} - a_4(x)A + a_5|A|^2 A + \delta(x - x_a)u \qquad (4.79)$$

where $x \in \mathbb{R}$, $A : \mathbb{R} \times \mathbb{R}_+ \to \mathbb{C}$, $a_1, a_4 : \mathbb{R} \to \mathbb{C}$, and $a_2, a_5 \in \mathbb{C}$. δ denotes the Dirac distribution and $u : \mathbb{R}_+ \to \mathbb{C}$ is the control input. Thus, control input is in the form of local forcing at x_a. The boundary conditions are $A(x \to \pm\infty, t) = 0$, that is, homogeneous Dirichlet boundary conditions. We now rewrite the equation to

obtain two coupled partial differential equations in real variables and coefficients by defining

$$\rho \triangleq \frac{1}{2}\left(A + \bar{A}\right), \ \iota \triangleq \frac{1}{2i}\left(A - \bar{A}\right) \tag{4.80}$$

$$a_{R_j} \triangleq \frac{1}{2}\left(a_j + \bar{a}_j\right), \ a_{I_j} \triangleq \frac{1}{2i}\left(a_j - \bar{a}_j\right), \ j = 1, 2, 4, 5 \tag{4.81}$$

$$u_R \triangleq \frac{1}{2}\left(u + \bar{u}\right), \ u_I \triangleq \frac{1}{2i}\left(u - \bar{u}\right) \tag{4.82}$$

where i denotes the imaginary unit and $^-$ denotes complex conjugation. With these definitions we obtain

$$
\begin{aligned}
\frac{\partial \rho}{\partial t} &= \frac{1}{2}\left(\frac{\partial A}{\partial t} + \frac{\partial \bar{A}}{\partial t}\right) \\
&= \frac{1}{2}\left(-\left(a_{R_1} + ia_{I_1}\right)\left(\frac{\partial \rho}{\partial x} + i\frac{\partial \iota}{\partial x}\right) - \left(a_{R_2} + ia_{I_2}\right)\left(\frac{\partial^2 \rho}{\partial x^2} + i\frac{\partial^2 \iota}{\partial x^2}\right)\right. \\
&\quad -\left(a_{R_4} + ia_{I_4}\right)\left(\rho + i\iota\right) + \left(a_{R_5} + ia_{I_5}\right)|A|^2\left(\rho + i\iota\right) \\
&\quad +\delta\left(x - x_a\right)\left(u_R + iu_I\right) \\
&\quad -\left(a_{R_1} - ia_{I_1}\right)\left(\frac{\partial \rho}{\partial x} - i\frac{\partial \iota}{\partial x}\right) - \left(a_{R_2} - ia_{I_2}\right)\left(\frac{\partial^2 \rho}{\partial x^2} - i\frac{\partial^2 \iota}{\partial x^2}\right) \\
&\quad -\left(a_{R_4} - ia_{I_4}\right)\left(\rho - i\iota\right) + \left(a_{R_5} - ia_{I_5}\right)|A|^2\left(\rho - i\iota\right) \\
&\quad \left.+ \delta\left(x - x_a\right)\left(u_R - iu_I\right)\right) \\
&= -a_{R_1}\left(x\right)\frac{\partial \rho}{\partial x} + a_{I_1}\left(x\right)\frac{\partial \iota}{\partial x} - a_{R_2}\frac{\partial^2 \rho}{\partial x^2} + a_{I_2}\frac{\partial^2 \iota}{\partial x^2} \\
&\quad -a_{R_4}\left(x\right)\rho + a_{I_4}\left(x\right)\iota + |A|^2 a_{R_5}\rho - |A|^2 a_{I_5}\iota + \delta\left(x - x_a\right)u_R \quad (4.83)
\end{aligned}
$$

and

$$
\begin{aligned}
\frac{\partial \iota}{\partial t} &= \frac{1}{2i}\left(\frac{\partial A}{\partial t} - \frac{\partial \bar{A}}{\partial t}\right) \\
&= \frac{1}{2i}\left(-\left(a_{R_1} + ia_{I_1}\right)\left(\frac{\partial \rho}{\partial x} + i\frac{\partial \iota}{\partial x}\right) - \left(a_{R_2} + ia_{I_2}\right)\left(\frac{\partial^2 \rho}{\partial x^2} + i\frac{\partial^2 \iota}{\partial x^2}\right)\right. \\
&\quad -\left(a_{R_4} + ia_{I_4}\right)\left(\rho + i\iota\right) + \left(a_{R_5} + ia_{I_5}\right)|A|^2\left(\rho + i\iota\right) \\
&\quad +\delta\left(x - x_a\right)\left(u_R + iu_I\right) \tag{4.84} \\
&\quad +\left(a_{R_1} - ia_{I_1}\right)\left(\frac{\partial \rho}{\partial x} - i\frac{\partial \iota}{\partial x}\right) + \left(a_{R_2} - ia_{I_2}\right)\left(\frac{\partial^2 \rho}{\partial x^2} - i\frac{\partial^2 \iota}{\partial x^2}\right) \\
&\quad +\left(a_{R_4} - ia_{I_4}\right)\left(\rho - i\iota\right) - \left(a_{R_5} - ia_{I_5}\right)|A|^2\left(\rho - i\iota\right) \tag{4.85} \\
&\quad \left.- \delta\left(x - x_a\right)\left(u_R - iu_I\right)\right) \\
&= -a_{R_1}\left(x\right)\frac{\partial \iota}{\partial x} - a_{I_1}\left(x\right)\frac{\partial \rho}{\partial x} - a_{R_2}\frac{\partial^2 \iota}{\partial x^2} - a_{I_2}\frac{\partial^2 \rho}{\partial x^2} \\
&\quad -a_{R_4}\left(x\right)\iota - a_{I_4}\left(x\right)\rho + |A|^2 a_{R_5}\iota + |A|^2 a_{I_5}\rho + \delta\left(x - x_a\right)u_I. \quad (4.86)
\end{aligned}
$$

Uniform incoming flow
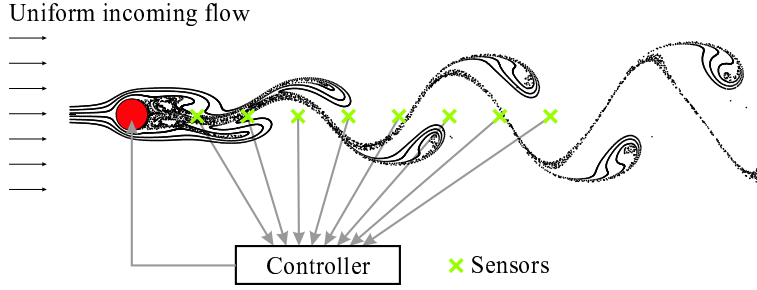
Figure 4.30: Vortex shedding from a cylinder visualized by passive tracer particles. The figure also shows the proposed control system configuration for suppression of vortex shedding.

Rearranging the terms, the equations become

$$
\frac{\partial \rho}{\partial t} = - \left(a_{R_1}(x) \frac{\partial}{\partial x} + a_{R_2} \frac{\partial^2}{\partial x^2} + a_{R_4}(x) - a_{R_5} \left(\rho^2 + \iota^2 \right) \right) \rho
$$
$$
+ \left(a_{I_1}(x) \frac{\partial}{\partial x} + a_{I_2} \frac{\partial^2}{\partial x^2} + a_{I_4}(x) - a_{I_5} \left(\rho^2 + \iota^2 \right) \right) \iota + \delta \left(x - x_a \right) u_R \quad (4.87)
$$

$$
\frac{\partial \iota}{\partial t} = - \left(a_{I_1}(x) \frac{\partial}{\partial x} + a_{I_2} \frac{\partial^2}{\partial x^2} + a_{I_4}(x) - a_{I_5} \left(\rho^2 + \iota^2 \right) \right) \rho
$$
$$
- \left(a_{R_1}(x) \frac{\partial}{\partial x} + a_{R_2} \frac{\partial^2}{\partial x^2} + a_{R_4}(x) - a_{R_5} \left(\rho^2 + \iota^2 \right) \right) \iota + \delta \left(x - x_a \right) u_I \quad (4.88)
$$

with boundary conditions $\rho \left(x \to \pm\infty, t \right) = 0$ and $\iota \left(x \to \pm\infty, t \right) = 0$.

Equations (4.87)–(4.88), with numerical values as given in [103, Appendix A] (reproduced in Appendix A), have been found to model well the dynamics of vortex shedding from a circular cylinder at Reynolds numbers near the critical Reynolds number, Re_c. Our objective is to design a state feedback controller that stabilizes the equilibrium $(\rho, \iota) = 0$ of (4.87)–(4.88). Figure 4.30 shows a sketch of the control system, superimposed on a visualization of vortex shedding. Based on the numerical values given in [103, Appendix A] (reproduced in Appendix A), we state the following assumptions which are assumed to hold throughout the analysis that follows.

Assumption 4.1 $a_2 \in (-\infty, 0)$ and $\mathfrak{Re}(a_5) \in (0, \infty)$, that is, $a_{R_2} < 0$, $a_{I_2} = 0$, and $a_{R_5} > 0$.

Assumption 4.2 For $|x| \gg 0$,

$$
\frac{1}{4 a_{R_2}} a_{I_1}^2(x) + a_{R_4}(x) \sim x^2. \tag{4.89}
$$

The basic idea of the control design is to divide the domain into three separate parts; the upstream subsystem, the core, and the downstream subsystem, for which the following two facts are shown:

1. The upstream and downstream subsystems are input-to-state stable (in L_2 norm) with respect to certain boundary input terms.

2. A finite-difference approximation of any order of the core can be stabilized by state feedback, driving all the states to zero, including the boundary input terms of the upstream and downstream subsystems.

These two facts are treated in detail in Sections 4.4.3 and 4.4.4, respectively.

4.4.3   Energy Analysis

Lemma 4.1 *There exist real constants $x_u < 0$ and $x_d > 0$ such that solutions of system (4.87)–(4.88) satisfy*

$$\frac{d}{dt}\left(\|(\rho,\iota)\|^2_{L_2(-\infty,x_u)} \right) \le -c \,\|(\rho,\iota)\|^2_{L_2(-\infty,x_u)}$$
$$-\left(a_{R_1}(x)\left(\rho^2+\iota^2\right) + 2a_{R_2}\left(\frac{\partial\rho}{\partial x}\rho + \frac{\partial\iota}{\partial x}\iota\right)\right)\Bigg|_{x=x_u} \qquad (4.90)$$

$$\frac{d}{dt}\left(\|(\rho,\iota)\|^2_{L_2(x_d,\infty)} \right) \le -c \,\|(\rho,\iota)\|^2_{L_2(x_d,\infty)}$$
$$+\left(a_{R_1}(x)\left(\rho^2+\iota^2\right) + 2a_{R_2}\left(\frac{\partial\rho}{\partial x}\rho + \frac{\partial\iota}{\partial x}\iota\right)\right)\Bigg|_{x=x_d} \qquad (4.91)$$

for some positive constant c.

Proof. The time derivative of $\|(\rho,\iota)\|^2_{L_2(a,b)}$ along solutions of (4.87)–(4.88) is

$$\frac{d}{dt}\left(\|(\rho,\iota)\|^2_{L_2(a,b)} \right) = 2\int_a^b (\rho\dot\rho + \iota\dot\iota)\,dx$$

$$= 2\int_a^b\Bigg[-\left(a_{R_1}(x)\frac{\partial\rho}{\partial x} + a_{R_2}\frac{\partial^2\rho}{\partial x^2} + a_{R_4}(x)\rho - |A|^2 a_{R_5}\rho\right)\rho$$
$$+\left(a_{I_1}(x)\frac{\partial\iota}{\partial x} + a_{I_2}\frac{\partial^2\iota}{\partial x^2}\right)\rho - \left(a_{I_1}(x)\frac{\partial\rho}{\partial x} + a_{I_2}\frac{\partial^2\rho}{\partial x^2}\right)\iota$$
$$-\left(a_{R_1}(x)\frac{\partial\iota}{\partial x} + a_{R_2}\frac{\partial^2\iota}{\partial x^2} + a_{R_4}(x)\iota - |A|^2 a_{R_5}\iota\right)\iota\Bigg]\,dx, \qquad (4.92)$$

where $a < b$ are arbitrary constants. Integration by parts yields

$$-2\int_a^b a_{R_1}(x)\frac{\partial\rho}{\partial x}\rho\,dx \;=\; -\left[a_{R_1}(x)\rho^2\right]_a^b + \int_a^b \frac{\partial a_{R_1}}{\partial x}\rho^2\,dx \qquad (4.93)$$

$$-2\int_a^b a_{R_1}(x)\frac{\partial\iota}{\partial x}\iota\,dx \;=\; -\left[a_{R_1}(x)\iota^2\right]_a^b + \int_a^b \frac{\partial a_{R_1}}{\partial x}\iota^2\,dx \qquad (4.94)$$

$$-2\int_a^b a_{R_2}\frac{\partial^2\rho}{\partial x^2}\rho\,dx \;=\; -2\left[a_{R_2}\frac{\partial\rho}{\partial x}\rho\right]_a^b + 2\int_a^b a_{R_2}\left(\frac{\partial\rho}{\partial x}\right)^2 dx \qquad (4.95)$$

$$-2\int_a^b a_{R_2}\frac{\partial^2\iota}{\partial x^2}\iota\,dx \;=\; -2\left[a_{R_2}\frac{\partial\iota}{\partial x}\iota\right]_a^b + 2\int_a^b a_{R_2}\left(\frac{\partial\iota}{\partial x}\right)^2 dx. \qquad (4.96)$$

Inserting (4.93)–(4.96) into (4.92), keeping in mind that $a_{I_2} = 0$ and $a_{R_5} < 0$ (Assumption 4.1), yields

$$\frac{d}{dt}\left(\|(\rho,\iota)\|^2_{L_2(a,b)}\right) \leq \left[-a_{R_1}(x)\left(\rho^2 + \iota^2\right) - 2a_{R_2}\left(\frac{\partial\rho}{\partial x}\rho + \frac{\partial\iota}{\partial x}\iota\right)\right]_a^b$$

$$+ 2\int_a^b \left[a_{R_2}\left(\frac{\partial\iota}{\partial x}\right)^2 + a_{I_1}(x)\frac{\partial\iota}{\partial x}\rho - \left(-\frac{\partial a_{R_1}}{\partial x} + a_{R_4}(x)\right)\rho^2\right.$$

$$\left. + a_{R_2}\left(\frac{\partial\rho}{\partial x}\right)^2 - a_{I_1}(x)\frac{\partial\rho}{\partial x}\iota - \left(-\frac{\partial a_{R_1}}{\partial x} + a_{R_4}(x)\right)\iota^2\right] dx. \qquad (4.97)$$

Now, consider the integrand in (4.97). We have that

$$a_{R_2}\left(\frac{\partial\iota}{\partial x}\right)^2 + a_{I_1}(x)\frac{\partial\iota}{\partial x}\rho - \left(-\frac{\partial a_{R_1}}{\partial x} + a_{R_4}(x)\right)\rho^2$$

$$+ a_{R_2}\left(\frac{\partial\rho}{\partial x}\right)^2 - a_{I_1}(x)\frac{\partial\rho}{\partial x}\iota - \left(-\frac{\partial a_{R_1}}{\partial x} + a_{R_4}(x)\right)\iota^2$$

$$\leq \;\; a_{R_2}\left|\frac{\partial\iota}{\partial x}\right|^2 + |a_{I_1}(x)|\left|\frac{\partial\iota}{\partial x}\right||\rho| - \left(-\frac{\partial a_{R_1}}{\partial x} + a_{R_4}(x)\right)\rho^2$$

$$+ a_{R_2}\left|\frac{\partial\rho}{\partial x}\right|^2 + |a_{I_1}(x)|\left|\frac{\partial\rho}{\partial x}\right||\iota| - \left(-\frac{\partial a_{R_1}}{\partial x} + a_{R_4}(x)\right)\iota^2$$

$$= \;\; a_{R_2}\left(\left|\frac{\partial\iota}{\partial x}\right| + \frac{1}{2a_{R_2}}|a_{I_1}(x)||\rho|\right)^2 - \left(\frac{1}{4a_{R_2}}a_{I_1}^2(x) - \frac{\partial a_{R_1}}{\partial x} + a_{R_4}(x)\right)\rho^2$$

$$a_{R_2}\left(\left|\frac{\partial\rho}{\partial x}\right| + \frac{1}{2a_{R_2}}|a_{I_1}(x)||\iota|\right)^2 - \left(\frac{1}{4a_{R_2}}a_{I_1}^2(x) - \frac{\partial a_{R_1}}{\partial x} + a_{R_4}(x)\right)\iota^2$$

$$\leq \;\; -\left(\frac{1}{4a_{R_2}}a_{I_1}^2(x) - \frac{\partial a_{R_1}}{\partial x} + a_{R_4}(x)\right)\left(\rho^2 + \iota^2\right) \qquad (4.98)$$
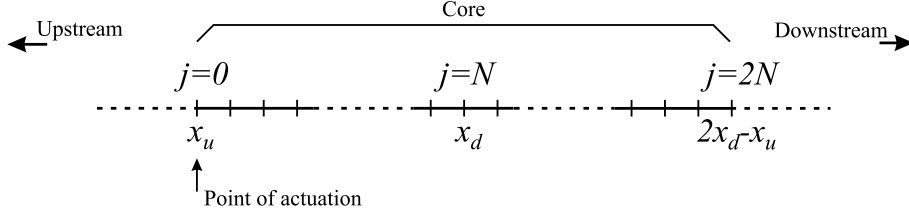
Figure 4.31: The system is discretized only in the core, which is the interval $[x_u, 2x_d - x_u]$, using a uniform grid with cell size h.

where we have used the fact that $a_{R_2} < 0$ (Assumption 4.1). Inserting (4.98) into (4.97) we obtain

$$\frac{d}{dt}\left(\|(\rho, \iota)\|^2_{L_2(a,b)}\right) \leq \left[-a_{R_1}(x)\left(\rho^2 + \iota^2\right) - 2a_{R_2}\left(\frac{\partial \rho}{\partial x}\rho + \frac{\partial \iota}{\partial x}\iota\right)\right]_a^b$$
$$- 2\int_a^b \left(\frac{1}{4a_{R_2}}a_{I_1}^2(x) - \frac{\partial a_{R_1}}{\partial x} + a_{R_4}(x)\right)\left(\rho^2 + \iota^2\right) dx. \quad (4.99)$$

By Assumption 4.2 there exist positive constants $x_u < 0$ and $x_d > 0$ such that

$$\frac{1}{4a_{R_2}}a_{I_1}^2(x) - \frac{\partial a_{R_1}}{\partial x} + a_{R_4}(x) > 0, \text{ for } x \in (-\infty, x_u) \cup (x_d, \infty), \quad (4.100)$$

and consequently, there exists a positive constant c, such that

$$\left(\frac{1}{4a_{R_2}}a_{I_1}^2(x) - \frac{\partial a_{R_1}}{\partial x} + a_{R_4}(x)\right) > \frac{1}{2}c, \text{ for } x \in (-\infty, x_u) \cup (x_d, \infty). \quad (4.101)$$

Inserting (4.101) into (4.99), (4.90) and (4.91) now follow by picking $(a, b) = (-\infty, x_u)$ and $(a, b) = (x_d, \infty)$, respectively, and applying the boundary conditions at $x = \pm\infty$.

■

4.4.4 Stabilization by State Feedback

Discretization

Having determined the two constants x_u and x_d, which exist by Lemma 4.1, we discretize (4.87)–(4.88) using finite difference approximations on the interval $[x_u, 2x_d - x_u]$ as shown schematically in Figure 4.31. We define the finite difference

approximations

$$\frac{\partial \rho}{\partial x}(jh) \approx \frac{\rho((j+1)h) - \rho(jh)}{h} \triangleq \frac{1}{h}\rho_{j+1} - \frac{1}{h}\rho_j \tag{4.102}$$

$$\frac{\partial^2 \rho}{\partial x^2} \approx \frac{\rho((j+1)h) - 2\rho(jh) + \rho((j-1)h)}{h^2}$$

$$\triangleq \frac{\rho_{j+1}}{h^2} - 2\frac{\rho_j}{h^2} + \frac{\rho_{j-1}}{h^2} \tag{4.103}$$

$$\frac{\partial \iota}{\partial x}(jh) \approx \frac{\iota((j+1)h) - \iota(jh)}{h} \triangleq \frac{1}{h}\iota_{j+1} - \frac{1}{h}\iota_j \tag{4.104}$$

$$\frac{\partial^2 \iota}{\partial x^2} \approx \frac{\iota((j+1)h) - 2\iota(jh) + \iota((j-1)h)}{h^2}$$

$$\triangleq \frac{\iota_{j+1}}{h^2} - 2\frac{\iota_j}{h^2} + \frac{\iota_{j-1}}{h^2} \tag{4.105}$$

where h is the grid cell size, and to simplify notation we set

$$r_{1,j} = a_{R_1}(x_j) \tag{4.106}$$

$$i_{1,j} = a_{I_1}(x_j) \tag{4.107}$$

$$r_2 = \frac{a_{R_2}}{h} \tag{4.108}$$

$$r_{3,j} = ha_{R_4}(x_j) \tag{4.109}$$

$$i_{3,j} = ha_{I_4}(x_j) \tag{4.110}$$

$$r_4 = ha_{R_5} \tag{4.111}$$

$$i_4 = ha_{I_5}. \tag{4.112}$$

Inserting (4.102)–(4.112) into (4.87)–(4.88) we obtain the set of ordinary differential equations

$$h\dot{\rho}_j = -r_2\rho_{j-1} + \left(r_{1,j} + 2r_2 - r_{3,j} + r_4\left(\rho_j^2 + \iota_j^2\right)\right)\rho_j - \left(r_{1,j} + r_2\right)\rho_{j+1}$$
$$+ \left(-i_{1,j} + i_{3,j} - i_4\left(\rho_j^2 + \iota_j^2\right)\right)\iota_j + i_{1,j}\iota_{j+1} + \delta_{0,j}u_R \tag{4.113}$$

$$h\dot{\iota}_j = \left(i_{1,j} - i_{3,j} + i_4\left(\rho_j^2 + \iota_j^2\right)\right)\rho_j - i_{1,j}\rho_{j+1} - r_2\iota_{j-1}$$
$$+ \left(r_{1,j} + 2r_2 - r_{3,j} + r_4\left(\rho_j^2 + \iota_j^2\right)\right)\iota_j - \left(r_{1,j} + r_2\right)\iota_{j+1} + \delta_{0,j}u_I \tag{4.114}$$

for $j = 0, 1, 2, ..., 2N+2$, where $x_j \triangleq hj + x_u$ and $\delta_{i,j}$ denotes the Kronecker delta function. In (4.113)–(4.114) we have set the point of actuation to $x_a = x_u$, and used the fact that $a_{I_2} = 0$. Inserting (4.102)–(4.112) into (4.90) and (4.91) we obtain

$$\frac{d}{dt}\left(\|(\rho, \iota)\|^2_{L_2(-\infty, x_u)}\right) \leq -c\|(\rho, \iota)\|^2_{L_2(-\infty, x_u)}$$
$$- r_{1,0}\left(\rho_0^2 + \iota_0^2\right) - 2r_2\left((\rho_1 - \rho_0)\rho_0 + (\iota_1 - \iota_0)\iota_0\right) \tag{4.115}$$

and

$$\frac{d}{dt}\left(\|(\rho, \iota)\|^2_{L_2(x_d, \infty)}\right) \leq -c\|(\rho, \iota)\|^2_{L_2(x_d, \infty)}$$
$$+ r_{1,N}\left(\rho_N^2 + \iota_N^2\right) + 2r_2\left((\rho_{N+1} - \rho_N)\rho_N + (\iota_{N+1} - \iota_N)\iota_N\right), \tag{4.116}$$

which are the semi-discrete versions of (4.90)–(4.91).

Control design

The following Theorem summarizes our control design.

Theorem 4.1 *The control law defined recursively by the scheme*

$$\alpha_N \equiv \beta_N \equiv 0 \tag{4.117}$$

$$\alpha_{N-1}\left(\rho_N, \rho_{N+1}, \iota_{N+1}\right)$$
$$= \frac{1}{r_2}\left[\left(\frac{3}{2}r_{1,N} - r_{3,N} + c_N\right)\rho_N - r_{1,N}\rho_{N+1} + i_{1,N}\iota_{N+1}\right] \tag{4.118}$$

$$\beta_{N-1}\left(\rho_{N+1}, \iota_N, \iota_{N+1}\right)$$
$$= \frac{1}{r_2}\left[-i_{1,N}\rho_{N+1} + \left(\frac{3}{2}r_{1,N} - r_{3,N} + c_N\right)\iota_N - r_{1,N}\iota_{N+1}\right] \tag{4.119}$$

$$\alpha_{N-k}\left(\rho_j, \iota_j : j \in [N-k+1, N+k]\right) = \frac{1}{r_2}\Big[c_{N-(k-1)}\left(\rho_{N-(k-1)} - \alpha_{N-(k-1)}\right)$$
$$+ \left(r_{1,N-(k-1)} + 2r_2 - r_{3,N-(k-1)} + r_4\left(\rho_{N-(k-1)}^2 + \iota_{N-(k-1)}^2\right)\right)\rho_{N-(k-1)}$$
$$- \left(r_{1,N-(k-1)} + 2r_2\right)\rho_{N-(k-2)}$$
$$+ \left(-i_{1,N-(k-1)} + i_{3,N-(k-1)} - i_4\left(\rho_{N-(k-1)}^2 + \iota_{N-(k-1)}^2\right)\right)\iota_{N-(k-1)}$$
$$+ i_{1,N-(k-1)}\iota_{N-(k-2)} + r_2\alpha_{N-(k-2)}$$
$$- \sum_{j=N-k+2}^{N+k-1} \frac{\partial \alpha_{N-(k-1)}}{\partial \rho_j}\left(-r_2\rho_{j-1} + \left(r_{1,j} + 2r_2 - r_{3,j} + r_4\left(\rho_j^2 + \iota_j^2\right)\right)\rho_j\right.$$
$$\left. - \left(r_{1,j} + r_2\right)\rho_{j+1} + \left(-i_{1,j} + i_{3,j} - i_4\left(\rho_j^2 + \iota_j^2\right)\right)\iota_j + i_{1,j}\iota_{j+1}\right)$$
$$- \sum_{j=N-k+2}^{N+k-1} \frac{\partial \alpha_{N-(k-1)}}{\partial \iota_j}\left(\left(i_{1,j} - i_{3,j} + i_4\left(\rho_j^2 + \iota_j^2\right)\right)\rho_j - i_{1,j}\rho_{j+1} - r_2\iota_{j-1}\right.$$
$$\left. + \left(r_{1,j} + 2r_2 - r_{3,j} + r_4\left(\rho_j^2 + \iota_j^2\right)\right)\iota_j - \left(r_{1,j} + r_2\right)\iota_{j+1}\right] \tag{4.120}$$

$$\beta_{N-k}\left(\rho_j, \iota_j : j \in [N-k+1, N+k]\right) = \frac{1}{r_2}\Big[c_{N-(k-1)}\left(\iota_{N-(k-1)} - \beta_{N-(k-1)}\right)$$
$$+ \left(i_{1,N-(k-1)} - i_{3,N-(k-1)} + i_4\left(\rho_{N-(k-1)}^2 + \iota_{N-(k-1)}^2\right)\right)\rho_{N-(k-1)}$$
$$- i_{1,N-(k-1)}\rho_{N-(k-2)}$$
$$+ \left(r_{1,N-(k-1)} + 2r_2 - r_{3,N-(k-1)} + r_4\left(\rho_{N-(k-1)}^2 + \iota_{N-(k-1)}^2\right)\right)\iota_{N-(k-1)}$$
$$- \left(r_{1,N-(k-1)} + 2r_2\right)\iota_{N-(k-2)} + r_2\beta_{N-(k-2)}$$

$$- \sum_{j=N-k+2}^{N+k-1} \frac{\partial \beta_{N-(k-1)}}{\partial \rho_j} \left(-r_2 \rho_{j-1} + \left(r_{1,j} + 2r_2 - r_{3,j} + r_4 \left(\rho_j^2 + \iota_j^2 \right) \right) \rho_j \right.$$

$$\left. - \left(r_{1,j} + r_2 \right) \rho_{j+1} + \left(-i_{1,j} + i_{3,j} - i_4 \left(\rho_j^2 + \iota_j^2 \right) \right) \iota_j + i_{1,j} \iota_{j+1} \right)$$

$$- \sum_{j=N-k+2}^{N+k-1} \frac{\partial \beta_{N-(k-1)}}{\partial \iota_j} \left(\left(i_{1,j} - i_{3,j} + i_4 \left(\rho_j^2 + \iota_j^2 \right) \right) \rho_j - i_{1,j} \rho_{j+1} - r_2 \iota_{j-1} \right.$$

$$\left. + \left(r_{1,j} + 2r_2 - r_{3,j} + r_4 \left(\rho_j^2 + \iota_j^2 \right) \right) \iota_j - \left(r_{1,j} + r_2 \right) \iota_{j+1} \right], \quad (4.121)$$

for $k = 2, 3, 4, ..., N,$ *and*

$$u_R \left(\rho_j, \iota_j : j \in [-1, 2N+1] \right)$$

$$= - \left[c_0 \left(\rho_0 - \alpha_0 \right) - r_2 \rho_{-1} + \left(r_{1,0} + 2r_2 - r_{3,0} + r_4 \left(\rho_0^2 + \iota_0^2 \right) \right) \rho_0 \right.$$

$$- \left(r_{1,0} + 2r_2 \right) \rho_1 + \left(-i_{1,0} + i_{3,0} - i_4 \left(\rho_0^2 + \iota_0^2 \right) \right) \iota_0 + i_{1,0} \iota_1 + r_2 \alpha_1$$

$$- \sum_{j=1}^{2N} \frac{\partial \alpha_0}{\partial \rho_j} \left(-r_2 \rho_{j-1} + \left(r_{1,j} + 2r_2 - r_{3,j} + r_4 \left(\rho_j^2 + \iota_j^2 \right) \right) \rho_j \right.$$

$$\left. - \left(r_{1,j} + r_2 \right) \rho_{j+1} + \left(-i_{1,j} + i_{3,j} - i_4 \left(\rho_j^2 + \iota_j^2 \right) \right) \iota_j + i_{1,j} \iota_{j+1} \right)$$

$$- \sum_{j=1}^{2N} \frac{\partial \alpha_0}{\partial \iota_j} \left(\left(i_{1,j} - i_{3,j} + i_4 \left(\rho_j^2 + \iota_j^2 \right) \right) \rho_j - i_{1,j} \rho_{j+1} - r_2 \iota_{j-1} \right.$$

$$\left. + \left(r_{1,j} + 2r_2 - r_{3,j} + r_4 \left(\rho_j^2 + \iota_j^2 \right) \right) \iota_j - \left(r_{1,j} + r_2 \right) \iota_{j+1} \right] \quad (4.122)$$

$$u_I \left(\rho_j, \iota_j : j \in [-1, 2N+1] \right)$$

$$= - \left[c_0 \left(\iota_0 - \beta_0 \right) + \left(i_{1,0} - i_{3,0} + i_4 \left(\rho_0^2 + \iota_0^2 \right) \right) \rho_0 - i_{1,0} \rho_1 \right.$$

$$- r_2 \iota_{-1} + \left(r_{1,0} + 2r_2 - r_{3,0} + r_4 \left(\rho_0^2 + \iota_0^2 \right) \right) \iota_0 - \left(r_{1,0} + 2r_2 \right) \iota_1 + r_2 \beta_1$$

$$- \sum_{j=1}^{2N} \frac{\partial \beta_0}{\partial \rho_j} \left(-r_2 \rho_{j-1} + \left(r_{1,j} + 2r_2 - r_{3,j} + r_4 \left(\rho_j^2 + \iota_j^2 \right) \right) \rho_j \right.$$

$$\left. - \left(r_{1,j} + r_2 \right) \rho_{j+1} + \left(-i_{1,j} + i_{3,j} - i_4 \left(\rho_j^2 + \iota_j^2 \right) \right) \iota_j + i_{1,j} \iota_{j+1} \right)$$

$$- \sum_{j=1}^{2N} \frac{\partial \beta_0}{\partial \iota_j} \left(\left(i_{1,j} - i_{3,j} + i_4 \left(\rho_j^2 + \iota_j^2 \right) \right) \rho_j - i_{1,j} \rho_{j+1} - r_2 \iota_{j-1} \right.$$

$$\left. + \left(r_{1,j} + 2r_2 - r_{3,j} + r_4 \left(\rho_j^2 + \iota_j^2 \right) \right) \iota_j - \left(r_{1,j} + r_2 \right) \iota_{j+1} \right] \quad (4.123)$$

renders $\left(\rho_0, \iota_0, \rho_1, \iota_1, ..., \rho_N, \iota_N \right) = 0$ *globally asymptotically stable. Moreover, solutions of system (4.87)–(4.88) satisfy*

$$\| (\rho, \iota) \|_{L_2(-\infty, x_u)}^2 \to 0 \qquad (4.124)$$

$$\| (\rho, \iota) \|_{L_2(x_d, \infty)}^2 \to 0 \qquad (4.125)$$

as $t \to \infty.$

Proof. Consider the Lyapunov function candidate

$$V = \frac{h}{2} \sum_{j=0}^{N} \left[(\rho_j - \alpha_j)^2 + (\iota_j - \beta_j)^2 \right] + \frac{1}{2} \| (\rho, \iota) \|_{L_2(x_d, \infty)}^2 . \tag{4.126}$$

The time derivative of (4.126) along solutions of the system is

$$\begin{aligned}
\dot{V} &= \sum_{j=0}^{N-1} \left[(\rho_j - \alpha_j)(h\dot{\rho}_j - h\dot{\alpha}_j) + (\iota_j - \beta_j)\left(h\dot{\iota}_j - h\dot{\beta}_j \right) \right] \\
&\quad + (\rho_N h \dot{\rho}_N + \iota_N h \dot{\iota}_N) + \frac{1}{2} \frac{d}{dt} \left[\| (\rho, \iota) \|_{L_2(x_d, \infty)}^2 \right] ,
\end{aligned} \tag{4.127}$$

where we have used the fact that $\alpha_N = \beta_N = 0$. Inserting (4.118)–(4.119) into (4.127), yields

$$\begin{aligned}
\dot{V} &\leq \sum_{j=0}^{N-1} \left[(\rho_j - \alpha_j)(h\dot{\rho}_j - h\dot{\alpha}_j) + (\iota_j - \beta_j)\left(h\dot{\iota}_j - h\dot{\beta}_j \right) \right] \\
&\quad - r_2 \rho_N (\rho_{N-1} - \alpha_{N-1}) - r_2 \iota_N (\iota_{N-1} - r_2 \beta_{N-1}) \\
&\quad - (c_N - r_2)(\rho_N^2 + \iota_N^2) \\
&\quad + r_4 (\rho_N^2 + \iota_N^2)^2 - \frac{c}{2} \| (\rho, \iota) \|_{L_2(x_d, \infty)}^2 \\
&\leq \sum_{j=0}^{N-1} \left[(\rho_j - \alpha_j)(h\dot{\rho}_j - h\dot{\alpha}_j) + (\iota_j - \beta_j)\left(h\dot{\iota}_j - h\dot{\beta}_j \right) \right] \\
&\quad - r_2 \rho_N (\rho_{N-1} - \alpha_{N-1}) - r_2 \iota_N (\iota_{N-1} - \beta_{N-1}) - (c_N - r_2)(\rho_N^2 + \iota_N^2) \\
&\quad - \frac{c}{2} \| (\rho, \iota) \|_{L_2(x_d, \infty)}^2
\end{aligned} \tag{4.128}$$

where we have used the fact that $r_4 < 0$ (Assumption 4.1) in the last step. Next, we insert (4.113)–(4.114) into (4.128), and obtain

$$\begin{aligned}
\dot{V} &\leq (\rho_0 - \alpha_0) \Big[-r_2 \rho_{-1} + \left(r_{1,0} + 2r_2 - r_{3,0} + r_4 (\rho_0^2 + \iota_0^2) \right) \rho_0 - (r_{1,0} + r_2) \rho_1 \\
&\quad + \left(-i_{1,0} + i_{3,0} - i_4 (\rho_0^2 + \iota_0^2) \right) \iota_0 + i_{1,0} \iota_1 + u_R - h\dot{\alpha}_0 \Big] \\
&\quad + (\iota_0 - \beta_0) \Big[\left(i_{1,0} - i_{3,0} + i_4 (\rho_0^2 + \iota_0^2) \right) \rho_0 - i_{1,0} \rho_1 - r_2 \iota_{-1} \\
&\quad + \left(r_{1,0} + 2r_2 - r_{3,0} + r_4 (\rho_0^2 + \iota_0^2) \right) \iota_0 - (r_{1,0} + r_2) \iota_1 + u_I - h\dot{\beta}_0 \Big] \\
&\quad + \sum_{j=1}^{N-1} \Big[(\rho_j - \alpha_j) \left(-r_2 \rho_{j-1} + \left(r_{1,j} + 2r_2 - r_{3,j} + r_4 (\rho_j^2 + \iota_j^2) \right) \rho_j \right. \\
&\quad - (r_{1,j} + r_2) \rho_{j+1} + \left(-i_{1,j} + i_{3,j} - i_4 (\rho_j^2 + \iota_j^2) \right) \iota_j + i_{1,j} \iota_{j+1} - h\dot{\alpha}_j) \\
&\quad + (\iota_j - \beta_j) \left(\left(i_{1,j} - i_{3,j} + i_4 (\rho_j^2 + \iota_j^2) \right) \rho_j - i_{1,j} \rho_{j+1} - r_2 \iota_{j-1} \right. \\
&\quad + \left(r_{1,j} + 2r_2 - r_{3,j} + r_4 (\rho_j^2 + \iota_j^2) \right) \iota_j - (r_{1,j} + r_2) \iota_{j+1} - h\dot{\beta}_j) \Big] \\
&\quad - r_2 \rho_N (\rho_{N-1} - \alpha_{N-1}) - r_2 \iota_N (\iota_{N-1} - \beta_{N-1}) - (c_N - r_2)(\rho_N^2 + \iota_N^2) \\
&\quad - \frac{c}{2} \| (\rho, \iota) \|_{L_2(x_d, \infty)}^2 .
\end{aligned} \tag{4.129}$$

At this point, we observe that the two summations in (4.120) in fact equal the time derivative of the previous α multiplied by h, that is $h\dot{\alpha}_{N-(k-1)}$. Similarly, the two summations in (4.121) equal the time derivative of the previous β multiplied by h, that is $h\dot{\beta}_{N-(k-1)}$. Therefore, from (4.120)–(4.121) we have

$$
\begin{aligned}
h\dot{\alpha}_j &= c_j\left(\rho_j - \alpha_j\right) - r_2\alpha_{j-1} + \left(r_{1,j} + 2r_2 - r_{3,j} + r_4\left(\rho_j^2 + \iota_j^2\right)\right)\rho_j \\
&\quad - \left(r_{1,j} + 2r_2\right)\rho_{j+1} + \left(-i_{1,j} + i_{3,j} - i_4\left(\rho_j^2 + \iota_j^2\right)\right)\iota_j \\
&\quad + i_{1,j}\iota_{j+1} + r_2\alpha_{j+1}, \quad\quad\quad\quad\quad\quad\quad\quad\quad\quad\quad\quad (4.130) \\
h\dot{\beta}_j &= c_j\left(\iota_j - \beta_j\right) - r_2\beta_{j-1} + \left(i_{1,j} - i_{3,j} + i_4\left(\rho_j^2 + \iota_j^2\right)\right)\rho_j \\
&\quad - i_{1,j}\rho_{j+1} + \left(r_{1,j} + 2r_2 - r_{3,j} + r_4\left(\rho_j^2 + \iota_j^2\right)\right)\iota_j \\
&\quad - \left(r_{1,j} + 2r_2\right)\iota_{j+1} + r_2\beta_{j+1}, \quad\quad\quad\quad\quad\quad\quad\quad\quad (4.131)
\end{aligned}
$$

for $j = 1, ..., N - 1$. Furthermore, the two summations in (4.122) equal $h\dot{\alpha}_0$, and the two summations in (4.123) equal $h\dot{\beta}_0$. Keeping this in mind, and inserting (4.130)–(4.131) and (4.122)–(4.123) into (4.129), we get

$$
\begin{aligned}
\dot{V} \leq\ & \left(\rho_0 - \alpha_0\right)\left(-c_0\left(\rho_0 - \alpha_0\right) + r_2\rho_1 - r_2\alpha_1\right) \\
& + \left(\iota_0 - \beta_0\right)\left(-c_0\left(\iota_0 - \beta_0\right) + r_2\iota_1 - r_2\beta_1\right) \\
& + \sum_{j=1}^{N-1}\left[\left(\rho_j - \alpha_j\right)\left(-r_2\rho_{j-1} - c_j\left(\rho_j - \alpha_j\right) + r_2\alpha_{j-1} + r_2\rho_{j+1} - r_2\alpha_{j+1}\right)\right. \\
& \left. + \left(\iota_j - \beta_j\right)\left(-r_2\iota_{j-1} - c_j\left(\iota_j - \beta_j\right) + r_2\beta_{j-1} + r_2\iota_{j+1} - r_2\beta_{j+1}\right)\right] \\
& - r_2\rho_N\left(\rho_{N-1} - \alpha_{N-1}\right) - r_2\iota_N\left(\iota_{N-1} - \beta_{N-1}\right) - \left(c_N - r_2\right)\left(\rho_N^2 + \iota_N^2\right) \\
& - \frac{c}{2}\left\|(\rho, \iota)\right\|_{L_2(x_d, \infty)}^2. \quad\quad\quad\quad\quad\quad\quad\quad\quad\quad (4.132)
\end{aligned}
$$

After rearranging the terms, we get

$$
\begin{aligned}
\dot{V} \leq\ & -\sum_{j=0}^{N-1} c_j\left(\left(\rho_j - \alpha_j\right)^2 + \left(\iota_j - \beta_j\right)^2\right) \\
& + r_2\left(\rho_0 - \alpha_0\right)\left(\rho_1 - \alpha_1\right) + r_2\left(\iota_0 - \beta_0\right)\left(\iota_1 - \beta_1\right) \\
& + \sum_{j=1}^{N-1}\left[\left(\rho_j - \alpha_j\right)\left(-r_2\rho_{j-1} + r_2\alpha_{j-1} + r_2\rho_{j+1} - r_2\alpha_{j+1}\right)\right. \\
& \left. + \left(\iota_j - \beta_j\right)\left(-r_2\iota_{j-1} + r_2\beta_{j-1} + r_2\iota_{j+1} - r_2\beta_{j+1}\right)\right] \\
& - r_2\rho_N\left(\rho_{N-1} - \alpha_{N-1}\right) - r_2\iota_N\left(\iota_{N-1} - \beta_{N-1}\right) \\
& - \left(c_N - r_2\right)\left(\rho_N^2 + \iota_N^2\right) - \frac{c}{2}\left\|(\rho, \iota)\right\|_{L_2(x_d, \infty)}^2. \quad\quad\quad (4.133)
\end{aligned}
$$

By splitting up the summation and changing summation indices, we obtain

$$
\begin{aligned}
\dot{V} \leq\ & -\sum_{j=0}^{N-1} c_j\left(\left(\rho_j - \alpha_j\right)^2 + \left(\iota_j - \beta_j\right)^2\right) \\
& + r_2\left(\rho_0 - \alpha_0\right)\left(\rho_1 - \alpha_1\right) + r_2\left(\iota_0 - \beta_0\right)\left(\iota_1 - \beta_1\right)
\end{aligned}
$$

$$-r_2 \left(\rho_1 - \alpha_1 \right) \left(\rho_0 - \alpha_0 \right) - r_2 \sum_{j=1}^{N-2} \left(\rho_{j+1} - \alpha_{j+1} \right) \left(\rho_j - \alpha_j \right)$$

$$+r_2 \left(\rho_{N-1} - \alpha_{N-1} \right) \left(\rho_N - \alpha_N \right) + r_2 \sum_{j=1}^{N-2} \left(\rho_j - \alpha_j \right) \left(\rho_{j+1} - \alpha_{j+1} \right)$$

$$-r_2 \left(\iota_1 - \beta_1 \right) \left(\iota_0 - \beta_0 \right) - r_2 \sum_{j=1}^{N-2} \left(\iota_{j+1} - \beta_{j+1} \right) \left(\iota_j - \beta_j \right)$$

$$+r_2 \left(\iota_{N-1} - \beta_{N-1} \right) \left(\iota_N - \beta_N \right) + r_2 \sum_{j=1}^{N-2} \left(\iota_j - \beta_j \right) \left(\iota_{j+1} - \beta_{j+1} \right)$$

$$-r_2 \rho_N \left(\rho_{N-1} - \alpha_{N-1} \right) - r_2 \iota_N \left(\iota_{N-1} - \beta_{N-1} \right)$$

$$- \left(c_N - r_2 \right) \left(\rho_N^2 + \iota_N^2 \right) - \frac{c}{2} \left\| \left(\rho, \iota \right) \right\|_{L_2(x_d, \infty)}^2 , \tag{4.134}$$

and after cancellation of terms, we have

$$\dot{V} \leq - \sum_{j=0}^{N-1} c_j \left(\left(\rho_j - \alpha_j \right)^2 + \left(\iota_j - \beta_j \right)^2 \right)$$

$$- \left(c_N - r_2 \right) \left(\rho_N^2 + \iota_N^2 \right) - \frac{c}{2} \left\| \left(\rho, \iota \right) \right\|_{L_2(x_d, \infty)}^2 . \tag{4.135}$$

In the last step we used the fact that $\alpha_N = \beta_N = 0$. It now follows from standard results [80], that the equilibrium point $\left(\rho_0, \iota_0, \rho_1, \iota_1, \ldots, \rho_N, \iota_N \right) = 0$ is globally asymptotically stable, and that

$$\left\| \left(\rho, \iota \right) \right\|_{L_2(x_d, \infty)}^2 \to 0 \text{ as } t \to \infty. \tag{4.136}$$

Having established that $\rho_0, \iota_0, \rho_1, \iota_1 \to 0$ as $t \to \infty$, it follows from (4.90) in Lemma 4.1, and its semi-discrete version (4.115), that

$$\left\| \left(\rho, \iota \right) \right\|_{L_2(-\infty, x_u)}^2 \to 0 \text{ as } t \to \infty. \tag{4.137}$$

$\blacksquare$

4.4.5 Simulation Study

In order to demonstrate the performance of our backstepping controller, we present a simulation example. We set the Reynolds number to $Re = 50$, and discretize (4.87)–(4.88) on the domain $x \in [-5, 15]$ using 21 nodes. Homogeneous Dirichlet boundary conditions are enforced at $x = -5$ and $x = 15$. Next, we plot the expression (4.101), that is

$$\frac{1}{4a_{R_2}} a_{I_1}^2 \left(x \right) - \frac{\partial a_{R_1}}{\partial x} + a_{R_4} \left(x \right), \tag{4.138}$$

on our chosen domain. The result is shown in Figure 4.32. By inspection of the
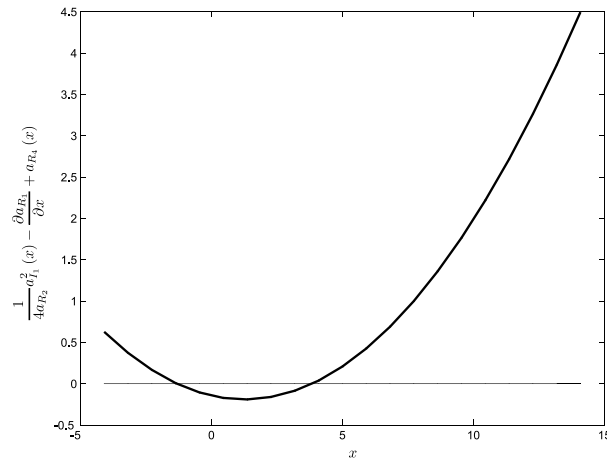
Figure 4.32: Graphical determination of the constants x_u and x_d for $R = 50$ using the numerical coefficients in [103].
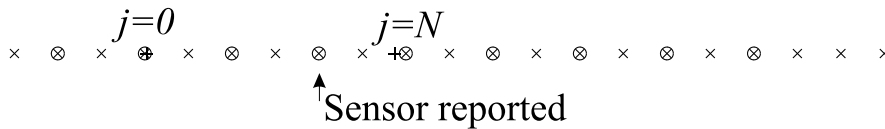
Figure 4.33: Locations of the grid points ($\times$), sensors ($\circ$), and $[x_u, x_d]$ ($+$). Only every second node is used for feedback, requiring three steps of backstepping in this case.

graph, we pick $x_u = -1.32$ and $x_d = 3.85$. The nodes of the discretization, along with x_u and x_d, are plotted in Figure 4.33. As the Figure shows, applying Theorem 4.1 at this point requires six backstepping steps. Instead, we use a discretization that is coarser for the control design, removing every other node. The remaining nodes, which are sensors, are shown in Figure 4.33 as circles. Now, only three steps of backstepping are required. The controller is generated using the symbolic toolbox in MATLAB, and is too complicated to write here. Figure 4.34 shows the values of (ρ, ι), represented by a vector originating at every node, for three time instances: $t = 200$, which is just before control is turned on, $t = 250$ and $t = 300$. As the Figure shows, the vectors alternate in direction and length indicating spatial unsteadiness reminiscent of vortex shedding. As time passes, the vectors become shorter, and eventually, all the states are driven to zero. Figure 4.35 shows the performance of the controller in terms of the output (ρ, ι) from one of the sensors (identified in Figure 4.33). As the Figure shows, the system is in the state of natural shedding for a couple of cycles, and then, at $t = 200$, the control is turned on. The measured state is effectively driven to zero.
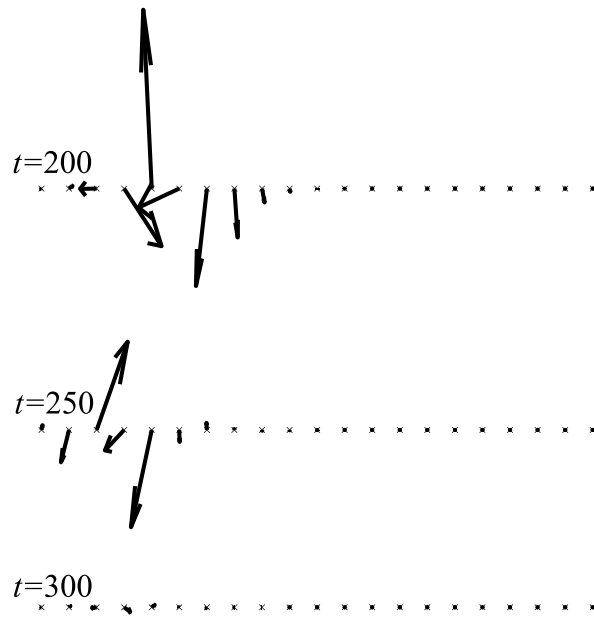
Figure 4.34: Nodal values of (ρ, ι) at three time instances: $t = 200$ (just before control is turned on), $t = 250$, and $t = 300$.
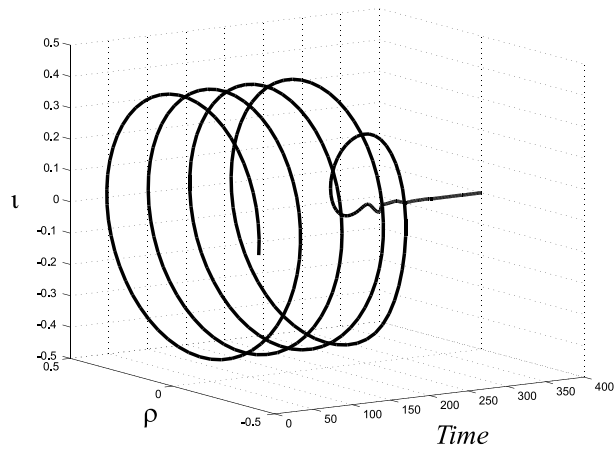
Figure 4.35: Time evolution of (ρ, ι) at sensor location number 4. Feedback is turned on at $t = 200$.

Chapter 5

Mixing

A number of inherently different processes constitute what is called mixing. Ottino [96] distinguishes between three sub-problems of mixing: (i) mixing of a single fluid (or similar fluids) governed by the stretching and folding of material elements; (ii) mixing governed by diffusion or chemical reactions; and (iii) mixing of different fluids governed by the breakup and coalescence of material elements. Of course, all processes may be present simultaneously. In the first sub-problem, the interfaces between the fluids are passive [12], and the mixing may be determined by studying the movement of a passive tracer, or dye, in a homogeneous fluid flow. This is the problem we are interested in here.

In the following sections, we will review selected results on diagnostics of mixing based on dynamical systems theory, and then present new results on mixing enhancement using feedback control.

5.1 Dynamical Systems Approach

5.1.1 Chaotic Advection in the Blinking Vortex Flow

The application of dynamical systems theory to problems in mixing was initiated by Aref [11], who studied advection of passive tracer particles in the setting of an incompressible, inviscid fluid, contained in a 2D circular domain. It was shown in that reference, that a simple-looking, deterministic Eulerian velocity field may produce an essentially stochastic response in the Lagrangian advection characteristics of a passive tracer. This behavior is referred to as *chaotic advection*. The flow is driven by a point vortex, whose motion in a circular domain of radius a, is denoted $z(t)$, and it's strength is denoted Γ. The function $z(t)$ is referred to as the *stirring protocol*. A point in the domain is denoted ζ, so that $\zeta = x + iy$. The flow is represented by a complex valued function $f(\zeta)$, such that

$$w = f(\zeta) = \phi + i\psi$$
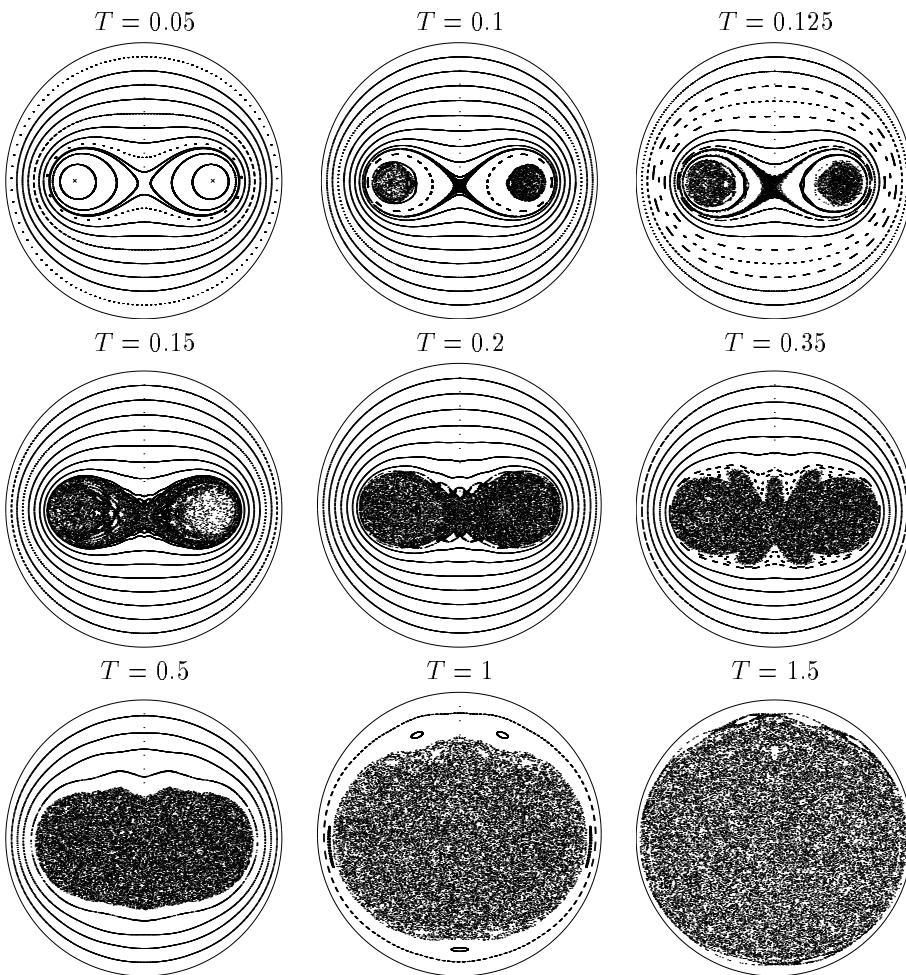
Figure 5.1: Iterated-map results ($\mathcal{P}_{2000}$) for $T \in [0.05, 0.1, 0.125, 0.15, 0.2, 0.35, 0.5, 1, 1.5]$.

where ϕ is the potential function and ψ is the stream function. A point vortex at the origin with strength Γ is given by

$$w = \frac{\Gamma}{2\pi i} \ln \zeta.$$

If the point vortex is allowed to move according to $z(t)$, we get

$$w = \frac{\Gamma}{2\pi i} \ln \left(\zeta - z\right).$$

For a circular domain with radius a, we superpose the image of the point vortex at $z(t)$ to obtain

$$w = \frac{\Gamma}{2\pi i} \ln \left(\zeta - z\right) + \left(-\frac{\Gamma}{2\pi i} \ln \left(\zeta - \frac{a^2}{\bar{z}}\right)\right) = \frac{\Gamma}{2\pi i} \ln \left(\frac{\zeta - z}{\zeta - \frac{a^2}{\bar{z}}}\right).$$

Consider a particle p, placed into the domain. We denote it's position by

$$\zeta_p = x + iy.$$

The velocity of the particle is given by

$$\dot{\bar{\zeta}}_p = u - iv = \frac{\partial \phi}{\partial x} + i \frac{\partial \psi}{\partial x} = \frac{\partial w}{\partial x} = \frac{\Gamma}{2\pi i} \left(\frac{1}{\zeta_p - z} - \frac{1}{\zeta_p - \frac{a^2}{\bar{z}}}\right). \tag{5.1}$$

By solving (5.1) for an array of particles, we can now visualize the mixing properties of the flow for various stirring protocols. In [11], the particular case when

$$z(t) = \begin{cases} b & \text{for } nT \leq t < \left(n + \frac{1}{2}\right) T \\ -b & \text{for } \left(n + \frac{1}{2}\right) T \leq t < (n+1) T \end{cases}, \quad n = 0, 1, 2, 3, \ldots \tag{5.2}$$

is studied in detail. b is a constant (possibly complex) contained in the domain, and T is a positive real constant specifying the period of $z(t)$. The flow resulting from the stirring protocol (5.2) is called the blinking vortex flow. The evolution governed by (5.1) induces a mapping of the disk $|\zeta| \leq a$ onto itself, defined by $M : \zeta(t) \to \zeta(t + T)$. The mapping M is referred to as a Poincaré map. Denoting an initial set of points as P_0, and applying the map iteratively to obtain the sets

$$P_n = M(P_{n-1}), \ n = 1, 2, 3, \ldots$$

we define the set of visited points after N iterations as

$$\mathcal{P}_N = \bigcup_{0 \leq n \leq N} P_n.$$

Figure 5.1 shows $\mathcal{P}_{2000}$ for $b = 0.5$, $P_0 = [-0.35, -0.2, -0.05, 0.1i, 0.2i, \ldots, 0.8i, 0.9i, 0.05, 0.2, 0.35]$, and for 9 different periods ($T \in [0.05, 0.1, 0.125, 0.15, 0.20, 0.35, 0.5, 1, 1.5]$). For $T = 0.05$, $\mathcal{P}_{2000}$ appears very regular, and the points visit a very small area of the total domain. This suggests that a blob of tracer material put into this flow, would be contained in a limited area given by the lines in the
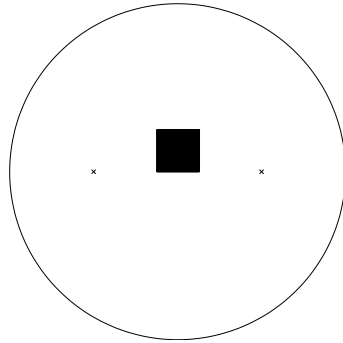
Figure 5.2: Initial configuration of particles for studying the mixing properties of the blinking vortex flow. The position of the point vortex is indicated by the two crosses ($\times$).

figure. As T is increased, regions of chaotic behavior appear, and the size of these regions increase with increasing T. When $T = 1.5$, no trace of regularity can be seen.

Next, we consider the kind of stirring experiment which would be carried out in a real device. This is done by introducing a blob of tracer material into the fluid at $t = 0$, and watch it evolve with time. Figure 5.2 shows the initial configuration of particles representing a square blob for the study of the mixing properties of (5.2). 10000 particles are evenly distributed in the box $[-0.125, 0.125] \times [0, 0.25]$. The position of the point vortex is again chosen as $b = 0.5$. Figure 5.3 shows the configuration of particles for 4 different time instances ($t \in [3, 6, 9, 12]$) for 3 different periods ($T \in [0.1, 1, 3]$). As anticipated in Figure 5.1, the blob is contained in a very limited area for $T = 0.1$, and the shape of the area is easily recognized to be formed by the lines appearing in Figure 5.1. Thus, it is shown how the study of a dynamical system can be reduced to the study of a map, for which redundant dynamics are filtered out so that emphasis is put on the underlying structures that govern mixing and transport.

5.1.2   Particle Transport in the Mixing Region of the Oscillating Vortex Pair Flow

The Oscillating Vortex Pair Flow

In [102] dynamical systems theory is applied in a mathematically rigorous manner in order to study the mixing properties in a 2D model flow governed by a vortex pair in the presence of an oscillating external strain-rate field. The vortices have strength $\pm\Gamma$, and are initially separated by a distance $2d$ in the y direction. The stream function for the flow in a frame moving with the average velocity of the
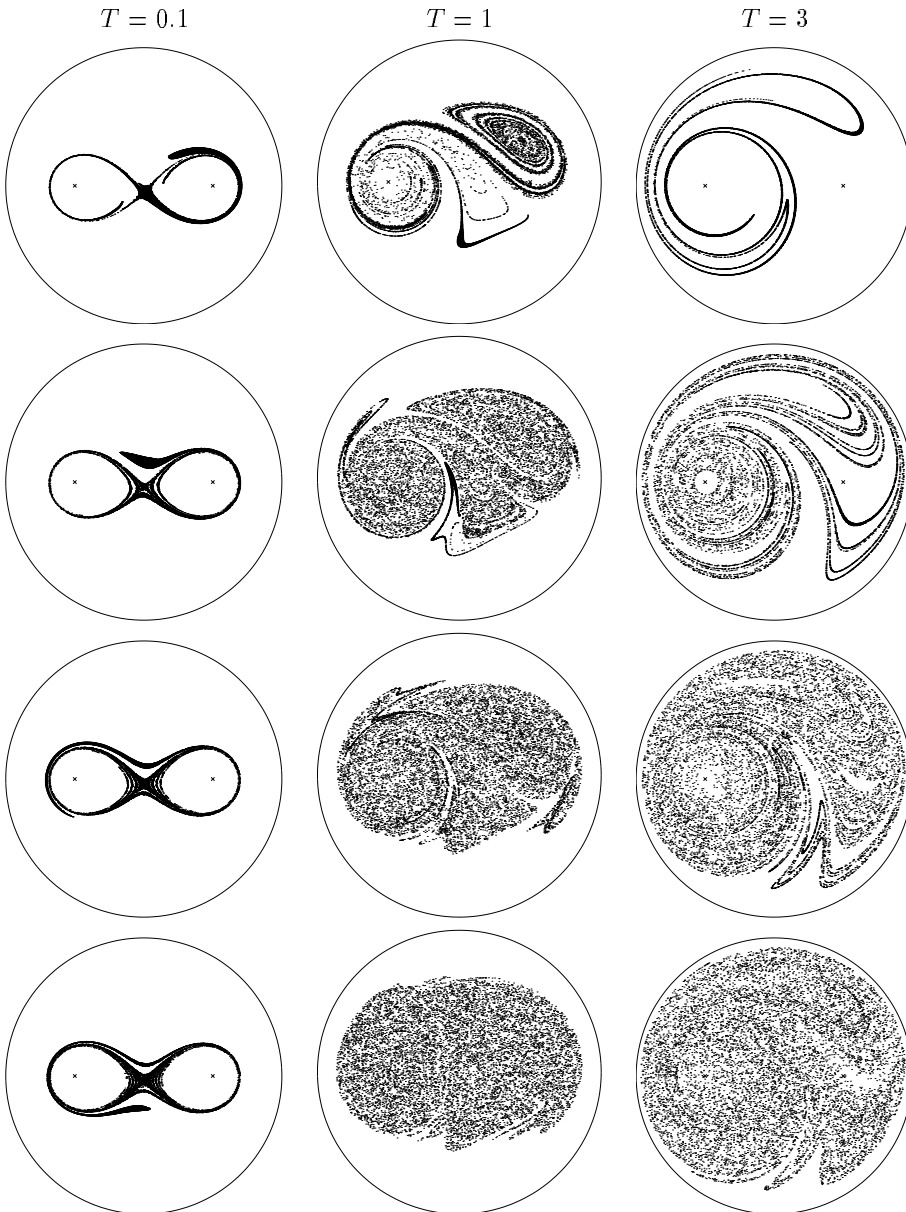
Figure 5.3: Configuration of particles in the blinking vortex flow for 4 different time instances ($t \in [3, 6, 9, 12]$) for 3 different periods ($T \in [0.1, 1, 3]$).

vortices is

$$\Psi = -\frac{\Gamma}{4\pi} \log \left\{ \frac{(x - x_v)^2 + (y - y_v)^2}{(x - x_v)^2 + (y + y_v)^2} \right\} - V_v y + \epsilon x y \sin(\omega t),$$

where $(x_v(t), y_v(t))$ and $(x_v(t), -y_v(t))$ are the vortex positions, ϵ is the strain rate and V_v is the average velocity of the vortex pair. For $\epsilon = 0$, $x_v(t) = 0$, $y_v(t) = d$ and $V_v = \Gamma/4\pi d$. Introducing appropriate scaling of the variables, and defining $\gamma = \Gamma/2\pi\omega d^2$ and $\nu_v = 2\pi d V_v/\Gamma$, we obtain the dimensionless equations for particle motion

$$\frac{dx}{dt} = -\left(\frac{y - y_v}{(x - x_v)^2 + (y - y_v)^2} - \frac{y + y_v}{(x - x_v)^2 + (y + y_v)^2} \right)$$
$$- \nu_v + \frac{\epsilon x}{\gamma} \sin(t/\gamma) \quad (5.3)$$

$$\frac{dy}{dt} = (x - x_v) \left(\frac{1}{(x - x_v)^2 + (y - y_v)^2} - \frac{1}{(x - x_v)^2 + (y + y_v)^2} \right)$$
$$- \frac{\epsilon y}{\gamma} \sin(t/\gamma). \quad (5.4)$$

The vortex positions are governed by

$$\frac{dx_v}{dt} = \frac{1}{2y_v} - \nu_v + \frac{\epsilon x_v}{\gamma} \sin(t/\gamma)$$
$$\frac{dy_v}{dt} = -\frac{\epsilon y_v}{\gamma} \sin(t/\gamma).$$

This flow approximates the motion in the vicinity of a vortex pair moving in a wavy-walled channel. In the perturbation analysis that follows, ϵ is assumed to be small. The right hand side of (5.3)–(5.4) can be expanded in powers of ϵ to obtain

$$\dot{x} = f_1(x, y) + \epsilon g_1(x, y, t/\gamma; \gamma) + O(\epsilon^2) \quad (5.5)$$
$$\dot{y} = f_2(x, y) + \epsilon g_2(x, y, t/\gamma; \gamma) + O(\epsilon^2) \quad (5.6)$$

where

$$f_1(x, y) = -\frac{y - 1}{I_-} + \frac{y + 1}{I_+} - \frac{1}{2}, \quad f_2(x, y) = x \left(\frac{1}{I_-} - \frac{1}{I_+} \right)$$

$$g_1(x, y, t/\gamma; \gamma) = (\cos(t/\gamma) - 1) \left(\frac{1}{I_-} + \frac{1}{I_+} - \frac{2(y + 1)^2}{I_+^2} \right)$$
$$+ \frac{x}{\gamma} \sin(t/\gamma) \left(\gamma^2 \left(\frac{y - 1}{I_-^2} - \frac{y + 1}{I_+^2} \right) + 1 \right) - \frac{1}{2}$$
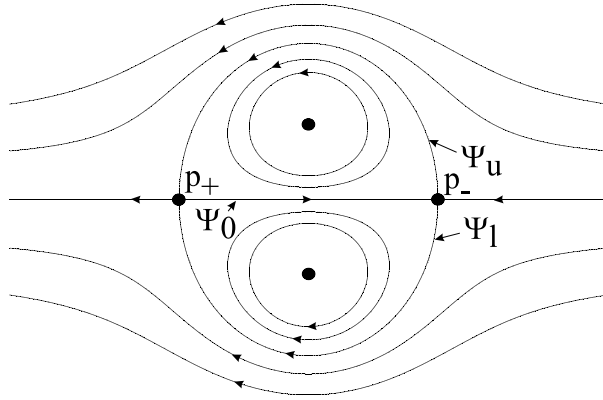
Figure 5.4: Streamlines of the unperturbed vortex pair flow.

$$g_2\left(x,y,t/\gamma;\gamma\right) = 2x\left(cos\left(t/\gamma\right)-1\right)\left(\frac{y-1}{I_-^2}+\frac{y+1}{I_+^2}\right)$$

$$+\frac{1}{\gamma}sin\left(t/\gamma\right)\left(\frac{\gamma^2}{2}\left(\frac{1}{I_-}-\frac{1}{I_+}\right)-x^2y^2\left(\frac{1}{I_-^2}-\frac{1}{I_+^2}\right)-y\right)$$

$$I_+ = x^2+\left(y+1\right)^2,\ \ I_- = x^2+\left(y-1\right)^2.$$

The streamlines of the unperturbed flow ($\epsilon = 0$) are shown in Figure 5.4. For this case, there are two hyperbolic fixed points, p_- and p_+, connected by the limiting streamlines defined by

$$\Psi_l\quad:\quad \Psi\left(x,y\right)|_{\epsilon=0} = 0,\ \ |x| < \sqrt{3},\ y < 0$$

$$\Psi_0\quad:\quad \Psi\left(x,y\right)|_{\epsilon=0} = 0,\ \ |x| < \sqrt{3},\ y = 0$$

$$\Psi_u\quad:\quad \Psi\left(x,y\right)|_{\epsilon=0} = 0,\ \ |x| < \sqrt{3},\ y > 0.$$

The particle motions on the interior of the limiting streamlines $\Psi_l\cup\Psi_u\cup p_-\cup p_+$ are qualitatively different from those on the exterior. Also, since streamlines cannot cross (for $\epsilon = 0$), there is no transport between the interior and the exterior of the limiting streamlines. We are interested in analyzing how this picture changes when the strain rate field is applied ($\epsilon \neq 0$).

The Poincaré Map

We may rewrite the time-varying system (5.5)–(5.6) as an equivalent time-invariant system by introducing the state $\theta = t/\gamma$ mod 2π. Thus, the system (5.5)–(5.6) can be written as

$$\dot{x} \quad = \quad f_1\left(x,y\right)+\epsilon g_1\left(x,y,\theta;\gamma\right)+O\left(\epsilon^2\right) \qquad (5.7)$$

$$\dot{y} \quad = \quad f_2\left(x,y\right)+\epsilon g_2\left(x,y,\theta;\gamma\right)+O\left(\epsilon^2\right) \qquad (5.8)$$

$$\dot{\theta} \quad = \quad 1/\gamma \qquad (5.9)$$

which is now a three-dimensional time-invariant system. A two-dimensional global cross section of the three-dimensional state space of (5.7)–(5.9) can be defined by

$$\Sigma_{\tilde{\theta}} = \left\{ (x, y, \theta) | \, \theta = \tilde{\theta} \in [0, 2\pi) \right\}$$

on which we define the Poincaré map

$$T_{\tilde{\theta}} : \Sigma_{\tilde{\theta}} \to \Sigma_{\tilde{\theta}}$$
$$\left(x \left(\tilde{\theta} \right), y \left(\tilde{\theta} \right) \right) \mapsto \left(x \left(\tilde{\theta} + 2\pi \right), y \left(\tilde{\theta} + 2\pi \right) \right). \tag{5.10}$$

In the unperturbed case, the orbits of the Poincaré map are sequences of discrete points lying on the streamlines shown in Figure 5.4. Thus, the streamlines are invariant manifolds of the map. Orbits starting on Ψ_l, Ψ_0 and Ψ_u are heteroclinic orbits, and the points p_- and p_+ are fixed points of the map. Orbits on Ψ_l and Ψ_u approach p_+ in positive time, and $\Psi_l \cup \Psi_u \cup p_+$ is therefore the stable manifold of p_+, denoted W_+^s. Similarly, $\Psi_l \cup \Psi_u \cup p_-$ is the unstable manifold of p_-, denoted W_-^u. The unstable manifold of p_+, denoted W_+^u, is $\left\{ (x, y) | \, x < \sqrt{3}, \, y = 0 \right\}$, and the stable manifold of p_-, denoted W_-^s, is $\left\{ (x, y) | \, x > -\sqrt{3}, \, y = 0 \right\}$. Clearly, W_+^s and W_-^u intersect along Ψ_l and Ψ_u, creating a barrier to transport between the interior and exterior of the limiting streamlines. For sufficiently small ϵ, p_+ and p_- persist as fixed points of the Poincaré map (5.10), denoted $p_{+,\epsilon}$ and $p_{-,\epsilon}$, respectively. Their stable and unstable manifolds, W_+^s, W_-^s, W_+^u, and W_-^u also persist to become the stable and unstable manifolds of $p_{+,\epsilon}$ and $p_{-,\epsilon}$. They are denoted $W_{+,\epsilon}^s$, $W_{-,\epsilon}^s$, $W_{+,\epsilon}^u$, and $W_{-,\epsilon}^u$, respectively. Due to symmetry about the x-axis, $y = 0$ is an invariant manifold for all ϵ, which implies that the stable manifold of $p_{-,\epsilon}$ and the unstable manifold of $p_{+,\epsilon}$ always coincide on the line connecting the two fixed points. $W_{+,\epsilon}^s$ and $W_{-,\epsilon}^u$, on the other hand, may not coincide in the perturbed case. It is possible for $W_{+,\epsilon}^s$ and $W_{-,\epsilon}^u$ to intersect at an isolated point, which implies, by invariance of $W_{+,\epsilon}^s$ and $W_{-,\epsilon}^u$, that they must also intersect at every iterate of the Poincaré map and it's inverse. Thus, $W_{+,\epsilon}^s$ and $W_{-,\epsilon}^u$ may intersect at infinitely many discrete points, leading to a geometry like the one shown in Figure 5.5. If this is the case, the barrier that is present in the unperturbed case splits open, and transport of fluid across it becomes possible. This behavior of the stable and unstable manifolds is also reminiscent of chaotic particle motion.

Melnikov's Method

The existence of an isolated point of intersection of $W_{+,\epsilon}^s$ and $W_{-,\epsilon}^u$ can be established by Melnikov's method [116], which relates the signed distance between the two manifolds to the so-called Melnikov function according to

$$d(t_0, \epsilon) = \epsilon \frac{M(t_0)}{\|f(q_u(-t_0))\|} + O\left(\epsilon^2\right),$$

where $q_u(t)$ is the heteroclinic particle trajectory of the unperturbed velocity field, coinciding with Ψ_u of Figure 5.4, t_0 parametrizes distance along Ψ_u, and

$$\|f(q_u(-t_0))\| = \sqrt{f_1(q_u(-t_0))^2 + f_2(q_u(-t_0))^2}.$$
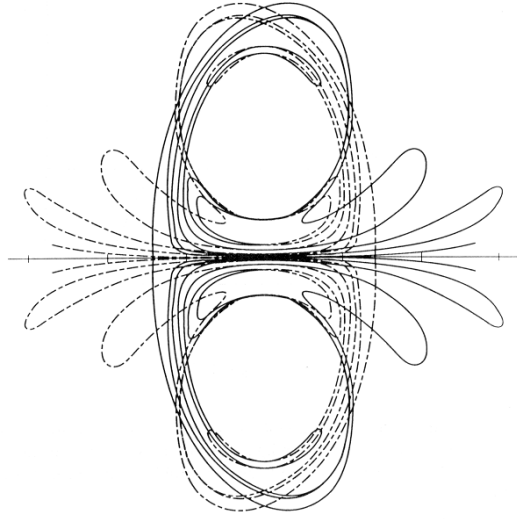
Figure 5.5: A Poincaré section of the oscillating vortex pair flow, showing the unstable (solid line) and stable (dashed line) manifolds of the two hyperbolic fixed points. Due to the tangling of the manifolds, this image is also referred to as the *homoclinic tangle*.

$M(t_0)$ is the Melnikov function defined as

$$M(t_0) = \int\limits_{-\infty}^{\infty} \{f_1(q_u(t))g_2(q_u(t), t+t_0) - f_2(q_u(t))g_1(q_u(t), t+t_0)\}\, dt.$$

The result of Melnikov states that simple zeros of $M(t_0)$ imply simple zeros of $d(t_0, \epsilon)$ (for sufficiently small ϵ). In [102], the Melnikov function for the system at hand is computed numerically to obtain

$$M(t_0) = \frac{F(\gamma)}{\gamma} sin(t_0/\gamma)$$

with $F(\gamma)$ plotted in Figure 5.6. For any fixed $\gamma \neq \gamma^*$, $M(t_0)$ has an infinite number of simple zeros, corresponding to transverse intersections of $W^s_{+,\epsilon}$ and $W^u_{-,\epsilon}$. This confirms the geometry shown in Figure 5.5. Studying the dynamics associated with the tangling of the stable and unstable manifolds of $p_{+,\epsilon}$ and $p_{-,\epsilon}$, can further quantify the particle transport taking place. This involves the motion of so-called *lobes*, and the area of these lobes quantifies transport. Again, for sufficiently small ϵ, the Melnikov function is a measure of the area of the lobes. We will not pursue this here, but refer the reader to [102] for further details.
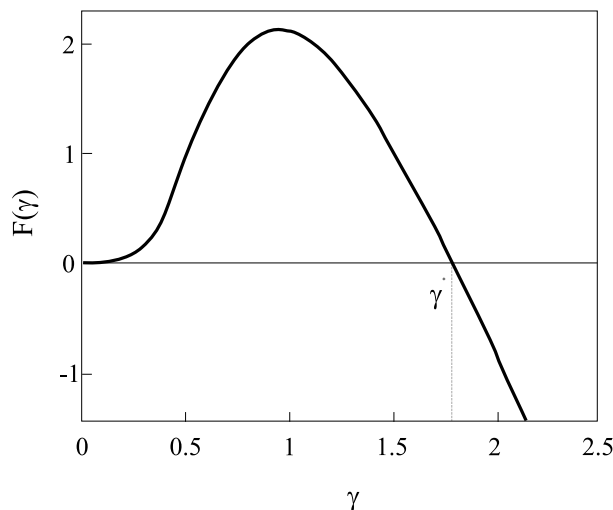
Figure 5.6: Graph of $F(\gamma)$ appearing in the Melnikov function.

5.1.3   Diagnostic Tools for Finite-Time Mixing

In time-periodic advection models, it is enough to know the velocity for finite times (e.g. for one period) to reproduce its infinite-time history. As a result, transport can be studied through the lobe dynamics of stable and unstable manifolds of appropriate Poincaré maps, as was demonstrated in the previous sections. However, for real flows, which in general are not periodic, one would have to know the velocity field for infinite times in order to define stable and unstable manifolds. This fact rules out the study of experimental datasets, both those consisting of measurements of actual flows, as well as those produced in a computer simulation. In a series of papers [55, 100, 101, 56, 57, 58], Haller and coworkers introduced and applied the notions of finite-time stable and unstable manifolds. The essentials of this new theory are outlined below.

Coherent Structures

A real flow will contain regions having different dynamical behavior. These regions are referred to as *Lagrangian coherent structures*. In Section 5.1.2 we encountered two fundamentally different dynamical behaviors in the oscillating vortex pair flow. One was the rotational motion occurring in the interior of the separating streamlines Ψ_l and Ψ_u, and the other was the translational motion occurring in the exterior of the separating streamlines. Thus, the regions in the interior and exterior of the separating streamlines are examples of coherent structures. The stable and unstable manifolds of the two fixed points coincided on the separating streamlines in the unperturbed case. In the perturbed case, however, they did not coincide, but intersected transversely at an infinite number of discrete points, leading to the
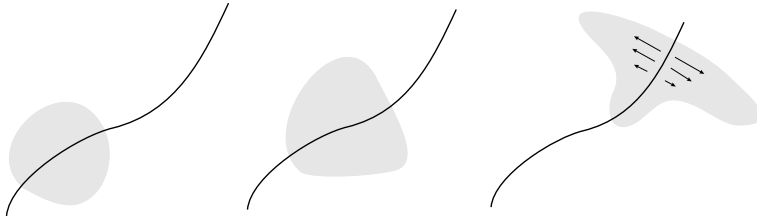
Figure 5.7: Stretching across a coherent structure boundary.
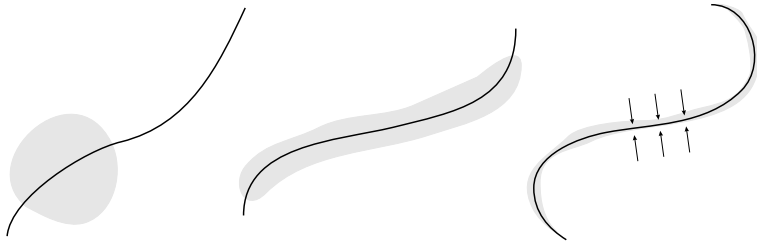
Figure 5.8: Stretching along a coherent structure boundary leading to folding.

formation of lobes whose dynamics is the mechanism by which transport between the interior and the exterior of the boundaries occurs. Such boundaries between coherent structures in the flow appear to be the locations in the flow where material blobs are stretched and folded most extensively. Extensive stretching and folding are reminiscent of effective mixing. Blobs of particles that travel together in the vicinity of coherent structure boundaries will in certain cases suddenly depart in opposite directions leading to local stretching *across* the boundary, as illustrated in Figure 5.7. In other cases the blob will become thinner and thinner as it is stretched *along* the coherent structure boundary leading, eventually, to folding due to the global geometry of the boundary, as illustrated in Figure 5.8. For these reasons, it is of interest to be able to localize the boundaries of coherent structures in a given finite-time dataset. A method that achieves this is presented next.

Material Lines and Surfaces

Consider the two-dimensional velocity field, $u(x, t)$, with the corresponding particle motion

$$\dot{x} = u(x, t) \tag{5.11}$$

on some *finite-time* interval $[t_{-1}, t_1]$. Given a curve of initial conditions, Γ_{t_0}, on the state space, later images of Γ_{t_0} under the motion (5.11), denoted Γ_t, are called *material lines*. Augmenting the state space with the time variable, the evolving curve, Γ_t, spans a two-dimensional surface in the extended state space (x, t). This surface is called a *material surface*, denoted M, and sketched in Figure 5.9. In
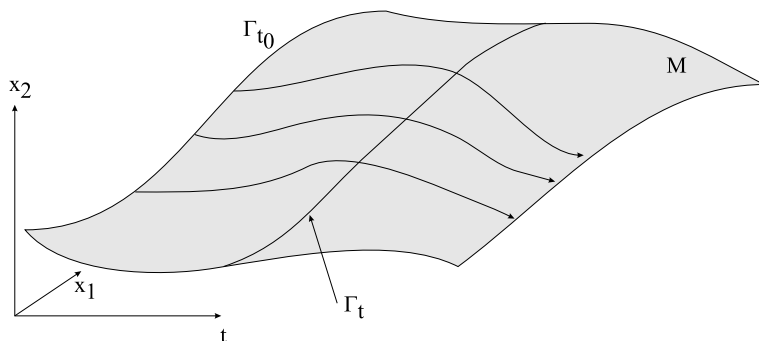
Figure 5.9: A material surface M spanned out by the material line Γ_t.

order to study the stability of M, we need to linearize the extended flow map, $\mathcal{F}^\tau$, along M. The extended flow map is given by

$$\mathcal{F}^\tau : \left(\begin{array}{c} x_0 \\ t_0 \end{array} \right) \longmapsto \left(\begin{array}{c} x(t_0 + \tau; t_0, x_0) \\ t_0 + \tau \end{array} \right).$$

We denote the linearized extended flow map by $D\mathcal{F}^\tau$.

Stability Properties of Material Surfaces

M is called an unstable material surface on the time interval I_u if there is a positive exponent λ_u such that for any sufficiently close initial condition $p(\tau) = (x(\tau), \tau)$ and for any small time step $h > 0$, with $\tau \in I_u$ and $\tau + h \in I_u$, we have

$$dist(p(\tau + h), M) \geq dist(p(\tau), M) e^{\lambda_u h}.$$

So, if $\mathcal{N}(p, t)$ is a unit normal to M at the point (p, t) in the extended state space, then M is an unstable material surface over I_u if for all $\tau, \tau + h \in I_u$ and for all initial conditions $(x_0, \tau) \in M$, we have

$$\left| \mathcal{N}(x(\tau + h), t + h) \cdot D\mathcal{F}^h(x_0)\mathcal{N}(x_0, \tau) \right| \geq e^{\lambda_u h}, \tag{5.12}$$

where $(x(\tau + h), \tau + h)$ is the trajectory passing through (x_0, τ) in the extended state space. Figure 5.10 shows a sketch of an unstable material surface over the time interval I_u. N is called a stable material surface if it is an unstable material surface in the sense of (5.12) backwards in time. An unstable (respectively, stable) material line with instability interval I_u (respectively, stability interval I_s) is a curve Γ_t which generates an unstable (respectively, stable) material surface in the extended state space. Unstable and stable material lines and surfaces are referred to as *hyperbolic material lines* and *hyperbolic material surfaces*, respectively. Their associated intervals I_u and I_s are referred to as *hyperbolicity intervals*. Hyperbolic material surfaces are never unique on a finite-time interval. However, if they are unstable for a sufficiently long time interval, they will appear unique up to
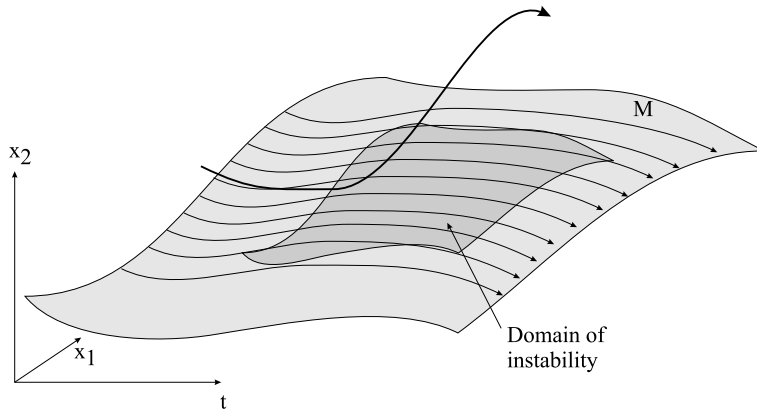
Figure 5.10: An unstable material surface repelling nearby trajectories..

numerically unresolvable errors. Thus, stable and unstable material surfaces will be used in the definition of coherent structure boundaries given below. The results outlined above have also been extended to the 3D setting [58].

Detecting Coherent Structure Boundaries

For any initial condition x_0 at time $t_0 \in [t_{-1}, t_1]$, consider the maximal open set, $\mathcal{I}_u(x_0)$, within $[t_0, t_1]$ on which the instability condition (5.12) is satisfied. The instability time $T_u(x_0, t_0)$ associated with x_0 over the time interval $[t_0, t_1]$ is defined as

$$T_u(x_0, t_0) = \frac{1}{t_1 - t_0} \int_{\mathcal{I}_u(x_0)} dt.$$

That is, T_u is the fraction of the time $t_1 - t_0$, for which the instability condition (5.12) holds. Similarly, the maximal open set, $\mathcal{I}_s(x_0)$, within $[t_0, t_{-1}]$, on which the instability condition (5.12) is satisfied in backward time, defines the stability time $T_s(x_0, t_0)$ associated with x_0 over the backward time interval $[t_0, t_{-1}]$ as

$$T_s(x_0, t_0) = \frac{1}{t_0 - t_{-1}} \int_{\mathcal{I}_s(x_0)} dt.$$

$T_u(x_0, t_0)$ and $T_s(x_0, t_0)$ are called the *hyperbolicity times* associated with x_0 at t_0. With these definitions, coherent structure boundaries at $t = t_0$ are given by stable and unstable material lines along which T_s or T_u attains local extrema. In the next section, the fields T_s and T_u are plotted for studying mixing properties in controlled 2D channel flow. It is interesting to note, that for time periodic velocity fields, the coherent structure boundaries defined above coincide with the stable and unstable manifolds of hyperbolic fixed points of the corresponding Poincaré map.

5.2   Destabilization of 2D Channel Flow

5.2.1   Numerical Simulations

Mixing is commonly induced by means of open loop methods such as mechanical stirring, jet injection or mixing valves. These methods may use excessive amounts of energy, which in certain cases is undesirable. In [1], it is proposed to use active feedback control on the boundary of a 2D channel flow, in order to exploit the natural tendency in the flow to mix. The results of Section 4.3.1 show that the control law (4.63)–(4.64) has a significant stabilizing influence on the 2D channel flow. In this section, we explore the behavior of the flow when k_v is chosen such that this feedback destabilizes the flow rather than stabilizes it. The conjecture is that the flow will develop a complicated pattern in which mixing will occur. 2D simulations are performed at $R = 6000$, for which the parabolic equilibrium profile is unstable. The vorticity map for the fully established flow (uncontrolled) at this Reynolds number is shown in the topmost graph in Figure 5.11. This is the initial data for the simulations. Some mixing might be expected in this flow, as it periodically ejects vorticity into the core of the channel. The objective, however, is to enhance the mixing process by boundary control, which we impose by setting $k_v = 0.1$ in (4.64). The vorticity maps in Figure 5.11 suggest that the flow pattern becomes considerably more complicated as a result of the control. The upper-left and upper-right graphs in Figure 5.12 show the perturbation energy, $E(\mathbf{w})$, and enstrophy as functions of time. The former increases by a factor of 5, while the latter is doubled. It is interesting to notice that the control leading to such an agitated flow is small (see lower-left graph in Figure 5.12). The maximum value of the control flow kinetic energy is less than 0.7% of the perturbation kinetic energy of the uncontrolled flow, and only about 0.1% of the fully developed, mixed (controlled) flow! Next, we will quantify the mixing in a more rigorous way, by studying the movement of passive tracer particles, representing dye blobs.

The location of the dye as a function of time completely describes the mixing, but in a flow that mixes well, the length of the interface between the dye and the fluid increases exponentially with time. Thus, calculating the location of the dye for large times is not feasible within the restrictions of modest computer resources [44]. We do, nevertheless, attempt this for small times, and supplement the results with less accurate, but computationally feasible, calculations for larger times. A particle-line method, loosely based on [112] and [78], is used to track the dye interface. In short, this method represents the interface as a number of particles connected by straight lines. The positions of the particles are governed by the equation $dX/dt = (U(X,t), V(X,t))$, where X is a vector of particle positions. At the beginning of each time step, new particles are added such that at the end of the time step, a prescribed resolution, given in terms of the maximum length between neighboring particles, is maintained. The fact that we are working with a single fluid representing multiple miscible fluids, ensures that dye surfaces remain connected [97]. At $t = 50$, when the perturbation energy is about tripled in the controlled case (Figure 5.12), eighteen blobs are distributed along the centerline of the channel as shown in Figure 5.13. They cover 25% of the total domain.
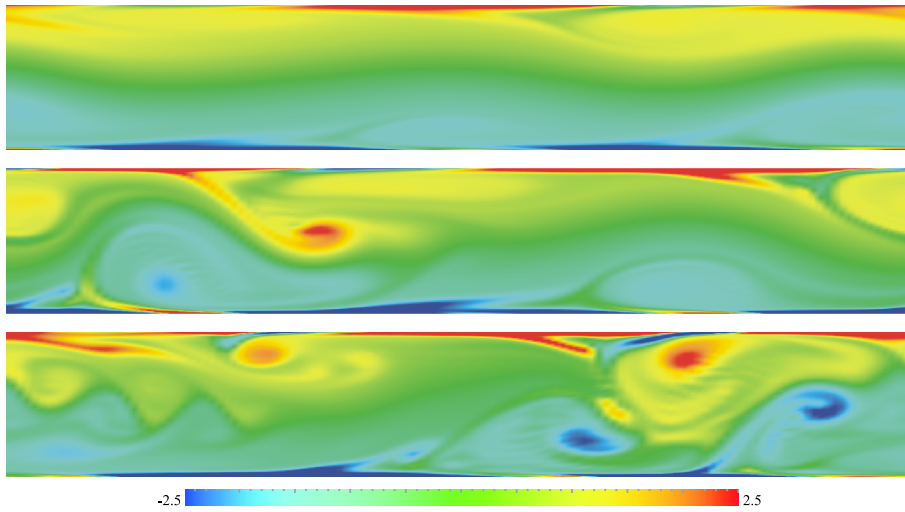
Figure 5.11: Vorticity map for the fully established, uncontrolled, channel flow at $Re = 6000$ (top), and for the controlled case at $t = 50$ (middle) and $t = 80$ (bottom).
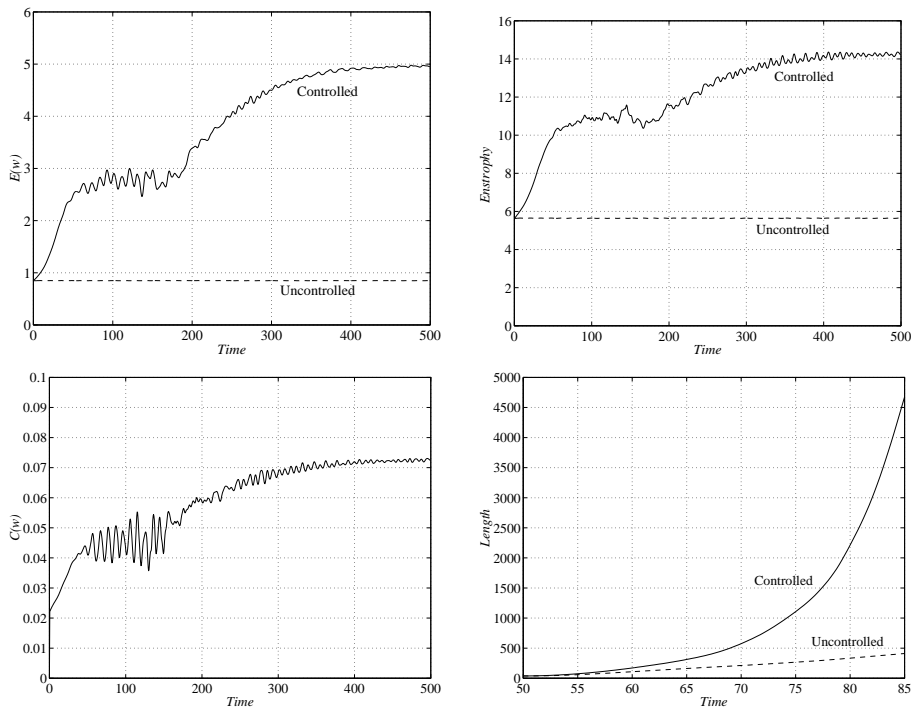
Figure 5.12: Energy $E(\mathbf{w})$ (top left), enstropy (top right), control effort $C(\mathbf{w})$ (bottom left), and dye surface length (bottom right), as functions of time.
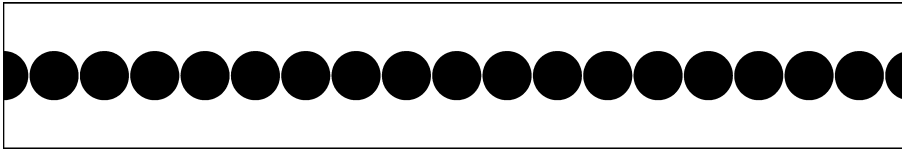
Figure 5.13: Initial distribution of dye blobs (at $t = 50$).
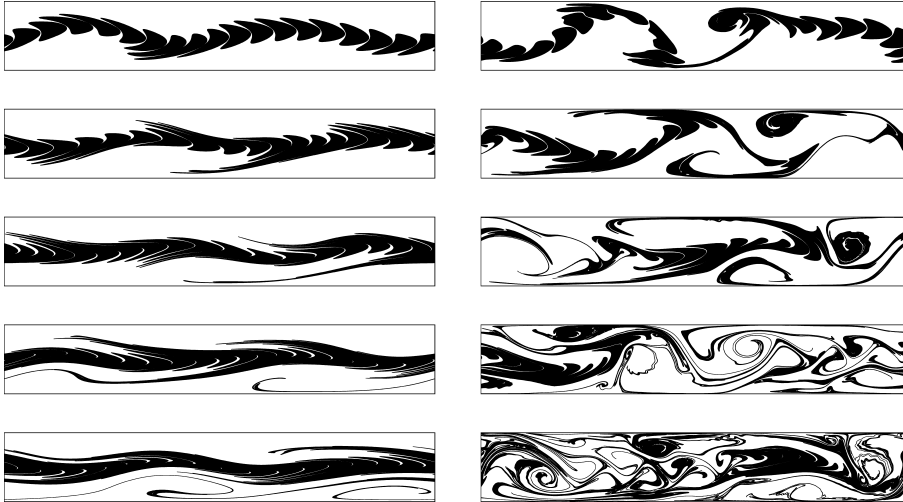
Figure 5.14: Dye distribution for uncontrolled flow (left column) versus controlled flow (right column) at $t = 55$, 60, 65, 75 and 85 (from top towards bottom).

Figure 5.14 compares the configuration of the dye in the uncontrolled and controlled cases for 5 time instances. The difference in complexity is clear, however, large regions are poorly mixed even at $t = 85$. The lower-right graph in Figure 5.12 shows the total length of the surface of the dye. The length appears to grow linearly with time in the uncontrolled case, whereas for the controlled case, it grows much faster, reaching values an order of magnitude larger than in the uncontrolled case. In order to approximate the dye distribution for large time, a fixed number of particles are uniformly distributed throughout the domain, distinguishing between particles placed on the inside (*black* particles) and on the outside (*white* particles) of regions occupied by dye. Figure 5.15 shows the distribution of black particles at $t = 85$ (for comparison with Figure 5.14), 100, 125 and 150. The particle distribution becomes increasingly uniform.

In order to quantify the mixing further, we ask the following question: given a box of size ε, what is the probability, P, of the fluid inside being *well mixed*? An appropriate choice of ε, and what is considered well mixed, are application specific parameters, and are usually given by requirements of some downstream process. In our case, the blobs initially cover 25% of the domain, so we will define *well*
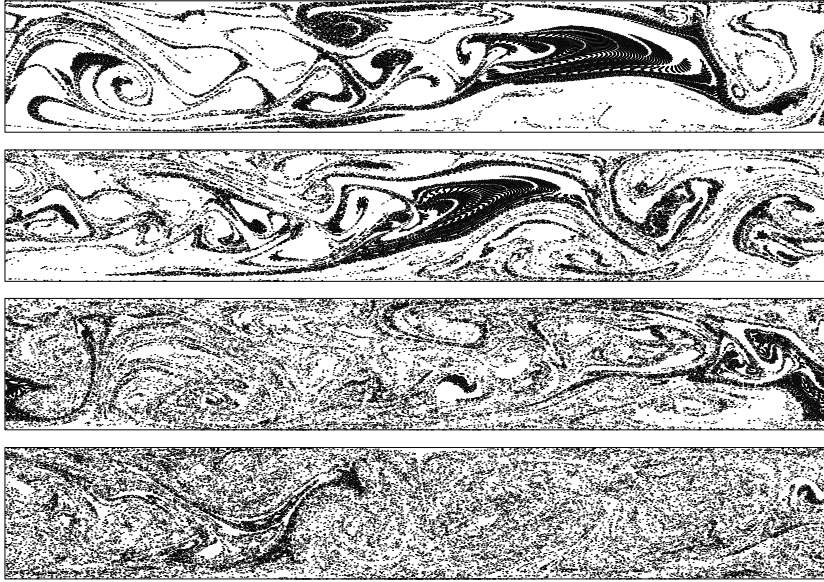
Figure 5.15: Particle distribution for controlled flow at $t = 85$, 100, 125 and 150 (from top towards bottom).

mixed to mean that the dye covers between 20% and 30% of the area of the box. The size ε of the boxes will be given in terms of pixels along one side of the box, so that the box covers ε^2 pixels out of a total of 2415 × 419 pixels for the entire domain. On this canvas, the box may be placed in $(419 - (\varepsilon - 1)) \times 2415$ different locations. The fraction of area covered by dye inside box i of size ε, is for small times calculated according to

$$c_\varepsilon^i = \frac{n_p}{\varepsilon^2} \tag{5.13}$$

where n_p is the number of pixels covered by dye, and for large times according to

$$c_\varepsilon^i = \frac{n_b}{n_w + n_b} \tag{5.14}$$

where n_b and n_w denote the number of black and white particles, respectively, contained in the box. P , which depends on ε, is calculated as follows

$$P_\varepsilon = \frac{1}{n} \sum_{i=1}^{n} eval(0.2 < c_\varepsilon^i < 0.3) \tag{5.15}$$

where n is the total number of boxes. The expression in the summation evaluates to 1 when $0.2 < c_\varepsilon^i < 0.3$ and 0 otherwise. For small times $n = (419 - (\varepsilon - 1)) \times 2415$, whereas for large times n may be smaller as we choose to ignore boxes containing less than 25 particles. Figures 5.16 and 5.17 show P_ε as a function of time for
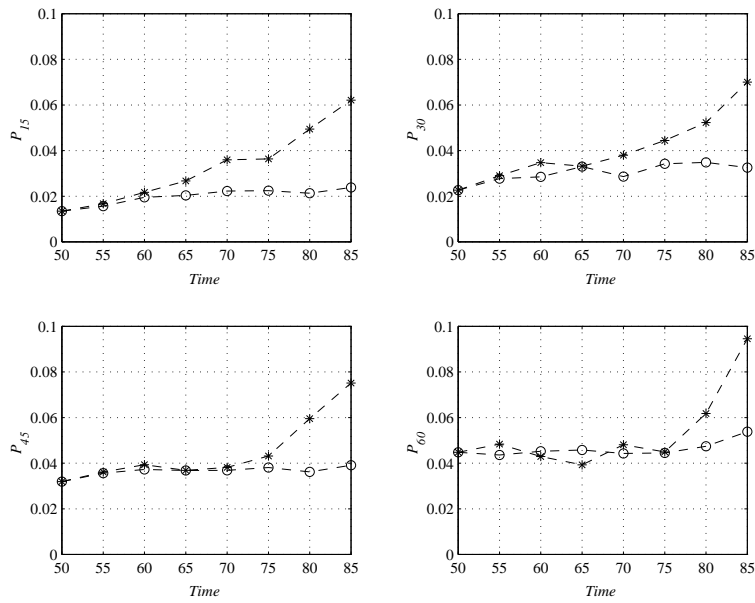
Figure 5.16: Probability of well mixedness for the uncontrolled case (o) and controlled case (*).
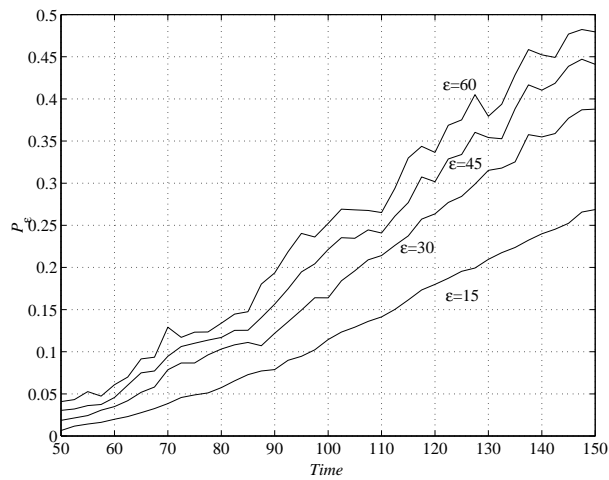
Figure 5.17: Probability of well mixedness for the controlled case based on uniform particle distribution.

Uncontrolled flow, forward time $(T_u(x_0, t_0))$

Uncontrolled flow, backward time $(T_s(x_0, t_0))$

Controlled flow, forward time $(T_u(x_0, t_0))$

Controlled flow, backward time $(T_s(x_0, t_0))$
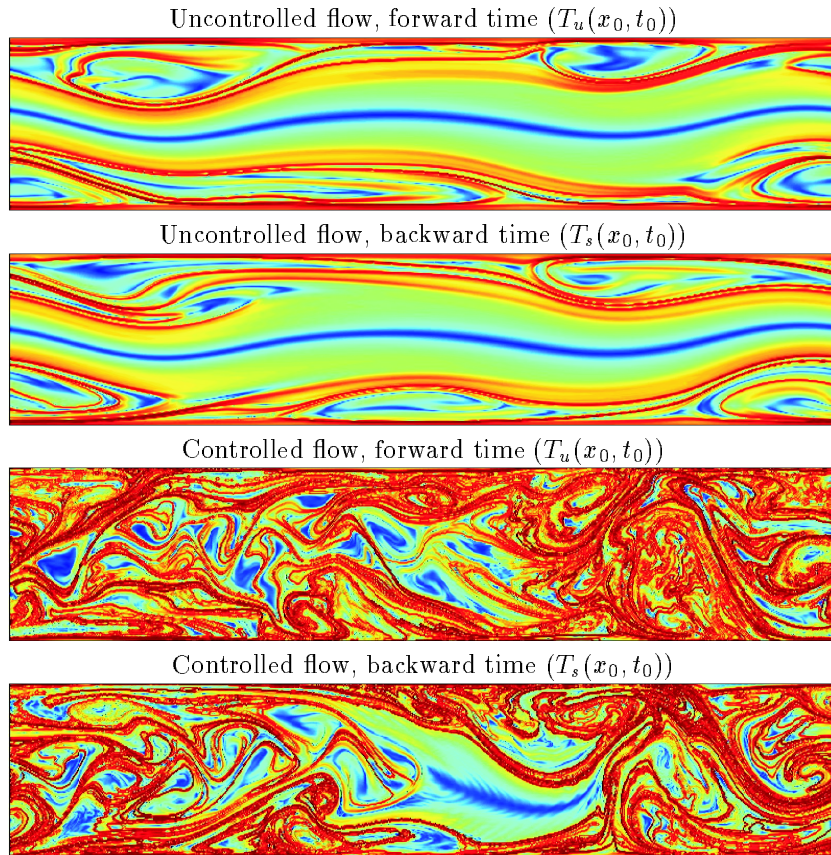
Figure 5.18: Hyperboliticy times for uncontrolled (upper two graphs) and controlled (lower two graphs) channel flow at $t_0 = 100$.

$\varepsilon \in [15, 30, 45, 60]$. For all cases, the probability of the contents of the box being well mixed increases with time. In Figure 5.18, the hyperbolicity times of a grid of uniformly distributed initial conditions at $t_0 = 100$ are shown (see Section 5.1.3 for the definition of hyperbolicity time). The geometry of the coherent structure boundaries become considerable more complex in the controlled case, indicating extensive stretching and folding of material elements in the flow.

In conclusion, we have achieved substantial mixing enhancement using relatively small control effort, by exploiting instability mechanisms inherent in the flow.

5.3 Optimal Mixing in 3D Pipe Flow

Recently, the results of the previous section have been generalized to 3D pipe flow [16] (also in [3]). Using a control law similar to that designed for the stabilizing
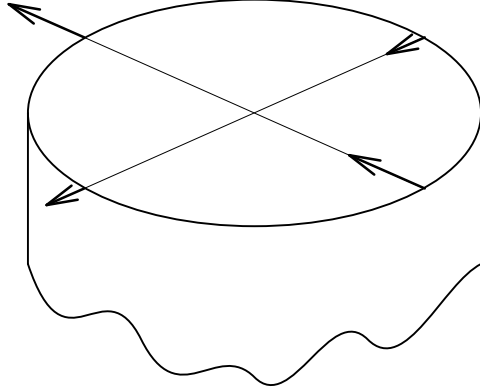
Figure 5.19: Actuation is symmetric about the pipe centerline.

case in (4.76), enhanced instability of the parabolic equilibrium profile is achieved, and the control law is shown to exhibit optimality properties. This will be made clear in the following derivations, originating from the Navier-Stokes equation for 3D pipe flow stated in (2.64) and (2.65)–(2.67).

5.3.1   Sensing and Actuation

As mentioned in the previous section, the boundary conditions on the wall of the pipe incorporate our actuation. The fluid velocity at the wall is restricted to be normal to the wall, that is, we take v_{r-w} as the control input, and set $v_{\theta-w} = v_{z-w} = 0$, where we have defined, for notational convenience, the variables on the wall as

$$
\begin{aligned}
v_{r-w}\left(\theta, z, t\right) &\triangleq v_r\left(1, \theta, z, t\right), \; v_{\theta-w}\left(\theta, z, t\right) \triangleq v_\theta\left(1, \theta, z, t\right), \; \text{and} \\
v_{z-w}\left(\theta, z, t\right) &\triangleq v_z\left(1, \theta, z, t\right).
\end{aligned}
$$

We also impose on the control input that it satisfies

$$
v_{r-w}\left(\theta, z, t\right) = -v_{r-w}\left(\theta + \pi, z, t\right), \tag{5.16}
$$

which states that if suction is applied at a point (θ, z) on the pipe wall, then an equal amount of blowing is applied at the opposite point $(\theta + \pi, z)$. This is illustrated in Figure 5.19. It is clear that condition (5.16) ensures a zero net mass flux across the pipe wall, and therefore it is a natural condition to impose from a mass balance point of view. The measurement available is the pressure drop, denoted Δp, from any point (θ, z) on the pipe wall to the opposite point $(\theta + \pi, z)$. That is,

$$
\Delta p(\theta, z, t) \triangleq p\left(1, \theta, z, t\right) - p\left(1, \theta + \pi, z, t\right). \tag{5.17}
$$

5.3.2 Measures of Mixing

There are two key ingredients to effective mixing. The fluid flow field must inflict extensive stretching to material elements, and the stretching should be accompanied by folding. In this work, we define two measures of the fluid flow field that are instrumental to our development below. One is the kinetic energy of the perturbation, defined as

$$E\left(\mathbf{w}\right) \triangleq \lim_{\varepsilon \to 0} E_\varepsilon\left(\mathbf{w}\right) \triangleq \lim_{\varepsilon \to 0} \frac{1}{2} \int_0^L \int_0^{2\pi} \int_\varepsilon^1 \left(v_r^2 + v_\theta^2 + v_z^2\right) r \, dr \, d\theta \, dz, \qquad (5.18)$$

and the other is a measure of spatial velocity gradients, defined as

$$m\left(\mathbf{w}\right) \triangleq \int_0^L \int_0^{2\pi} \int_0^1 \left[\left(\frac{\partial v_r}{\partial z}\right)^2 + \left(\frac{\partial v_\theta}{\partial z}\right)^2 + \left(\frac{\partial v_z}{\partial r}\right)^2 + \left(\frac{1}{r}\frac{\partial v_z}{\partial \theta}\right)^2 + \left(\frac{\partial v_z}{\partial z}\right)^2 \right.$$
$$\left. + \left(\frac{\partial v_r}{\partial r}\right)^2 + \left(\frac{\partial v_\theta}{\partial r}\right)^2 + \left(\frac{v_r}{r} + \frac{1}{r}\frac{\partial v_\theta}{\partial \theta}\right)^2 + \left(\frac{v_\theta}{r} - \frac{1}{r}\frac{\partial v_r}{\partial \theta}\right)^2 \right] r \, dr \, d\theta \, dz. \quad (5.19)$$

The latter measure, (5.19), appears to be stronger connected to mixing. While it is clear that stretching of material elements is explicit in a measure of spatial gradients of the flow field, folding is implicit in the measure due to the boundedness of the flow domain, and the fact that $\mathbf{w}$ satisfies the Navier-Stokes equation. Thus, our objective becomes that of designing a feedback control law, in terms of suction and blowing of fluid normally to the pipe wall, that is optimal with respect to some meaningful cost functional related to $m(\mathbf{w})$.

5.3.3 Energy Analysis

Before giving the main result on controller design and optimality, we state two key lemmas that are needed frequently in what follows. The first lemma is a Lyapunov type result and it relates the time derivative of $E\left(\mathbf{w}\left(t\right)\right)$ to $m\left(\mathbf{w}\left(t\right)\right)$. The second lemma provides a bound on a crossterm in the streamwise (v_z) and radial (v_r) velocities, originating from the nonlinear convective terms in the Navier-Stokes equations.

Lemma 5.1 *If $v_{\theta-w}$ and v_{z-w} are zero, and v_{r-w} satisfies (5.16), then*

$$\dot{E}(\mathbf{w}) = -\frac{1}{2} \int_0^L \int_0^{2\pi} v_{r-w} \Delta p \, d\theta \, dz - \frac{1}{Re} \int_0^L \int_0^{2\pi} v_{r-w}^2 \, d\theta \, dz$$
$$- \frac{1}{Re} m\left(\mathbf{w}\right) - \int_0^L \int_0^{2\pi} \int_0^1 r v_z v_r \frac{\partial \tilde{V}_z}{\partial r} dr \, d\theta \, dz \quad (5.20)$$

along solutions of system (2.64)–(2.67).

Proof. The time derivative of $E_\varepsilon(\mathbf{w})$ along trajectories of (2.64)–(2.67) was calculated in Section 4.3.3 and the result was

$$
\dot{E}_\varepsilon(\mathbf{w}) = \int_0^L \int_0^{2\pi} \left[-\frac{1}{2} r v_r^3 \right]_\varepsilon^1 d\theta dz + \int_0^L \int_0^{2\pi} \left[-r v_r p \right]_\varepsilon^1 d\theta dz + \frac{1}{Re} \int_0^L \int_0^{2\pi} \left[r v_r \frac{\partial v_r}{\partial r} \right]_\varepsilon^1 d\theta dz
$$

$$
+ \frac{1}{2} \int_0^L \int_0^{2\pi} \left[-r v_r v_\theta^2 \right]_\varepsilon^1 d\theta dz + \frac{1}{Re} \int_0^L \int_0^{2\pi} \left[r v_\theta \frac{\partial v_\theta}{\partial r} \right]_\varepsilon^1 d\theta dz + \frac{1}{2} \int_0^L \int_0^{2\pi} \left[-r v_z^2 v_r \right]_\varepsilon^1 d\theta dz
$$

$$
+ \frac{1}{Re} \int_0^L \int_0^{2\pi} \left[r v_z \frac{\partial v_z}{\partial r} \right]_\varepsilon^1 d\theta dz - \int_0^L \int_0^{2\pi} \int_\varepsilon^1 r v_z v_r \frac{\partial \tilde{V}_z}{\partial r} dr d\theta dz
$$

$$
- \frac{1}{Re} \int_0^L \int_0^{2\pi} \int_\varepsilon^1 r \left(\frac{\partial v_r}{\partial z} \right)^2 dr d\theta dz - \frac{1}{Re} \int_0^L \int_0^{2\pi} \int_\varepsilon^1 r \left(\frac{\partial v_\theta}{\partial z} \right)^2 dr d\theta dz
$$

$$
- \frac{1}{Re} \int_0^L \int_0^{2\pi} \int_\varepsilon^1 r \left(\frac{\partial v_z}{\partial r} \right)^2 dr d\theta dz - \frac{1}{Re} \int_0^L \int_0^{2\pi} \int_\varepsilon^1 \frac{1}{r} \left(\frac{\partial v_z}{\partial \theta} \right)^2 dr d\theta dz
$$

$$
- \frac{1}{Re} \int_0^L \int_0^{2\pi} \int_\varepsilon^1 r \left(\frac{\partial v_z}{\partial z} \right)^2 dr d\theta dz - \frac{1}{Re} \int_0^L \int_0^{2\pi} \int_\varepsilon^1 r \left(\frac{\partial v_r}{\partial r} \right)^2 dr d\theta dz
$$

$$
- \frac{1}{Re} \int_0^L \int_0^{2\pi} \int_\varepsilon^1 r \left(\frac{\partial v_\theta}{\partial r} \right)^2 dr d\theta dz - \frac{1}{Re} \int_0^L \int_0^{2\pi} \int_\varepsilon^1 \frac{1}{r} \left(v_r + \frac{\partial v_\theta}{\partial \theta} \right)^2 dr d\theta dz
$$

$$
- \frac{1}{Re} \int_0^L \int_0^{2\pi} \int_\varepsilon^1 \frac{1}{r} \left(v_\theta - \frac{\partial v_r}{\partial \theta} \right)^2 dr d\theta dz. \quad (5.21)
$$

Since v_{r-w} has the form (5.16), we have for odd n

$$
\int_0^{2\pi} v_{r-w}^n d\theta = \int_{-\pi}^0 v_{r-w}^n d\theta + \int_0^{\pi} v_{r-w}^n d\theta
$$

$$
= -\int_{-\pi}^0 v_{r-w}^n (-\theta, z, t) d\theta + \int_0^{\pi} v_{r-w}^n (\theta, z, t) d\theta
$$

and by a change of variables in the first integral ($\theta^* = -\theta$), we get

$$
\int_0^{2\pi} v_{r-w}^n d\theta = -\int_0^{\pi} v_{r-w}^n (\theta^*, z, t) d\theta^* + \int_0^{\pi} v_{r-w}^n (\theta, z, t) d\theta = 0.
$$

This proves that the net mass flow through the wall is zero, and that

$$\int_0^{2\pi} v_{r-w}^3 \, d\theta = 0 \tag{5.22}$$

by setting $n = 1$ and $n = 3$, respectively. Furthermore, we have

$$\int_0^{2\pi} [v_r p]_{r=1} \, d\theta = \int_0^{\pi} [v_r p]_{r=1} \, d\theta + \int_{\pi}^{2\pi} [v_r p]_{r=1} \, d\theta$$

$$= \int_0^{\pi} [v_r p]_{r=1} \, d\theta - \int_0^{\pi} v_{r-w} \left(\theta, z, t\right) p \left(1, \theta + \pi, z, t\right) d\theta$$

$$= \int_0^{\pi} v_{r-w} \left(\theta, z, t\right) \Delta p d\theta = \frac{1}{2} \int_0^{2\pi} v_{r-w} \left(\theta, z, t\right) \Delta p d\theta \tag{5.23}$$

and, since $v_{\theta-w}$ and v_{z-w} are zero, (2.64) yields

$$\frac{\partial v_r}{\partial r} \left(1, \theta, z, t\right) = -v_r \left(1, \theta, z, t\right). \tag{5.24}$$

By inserting $v_{\theta-w} \left(\theta, z, t\right) = v_{z-w} \left(\theta, z, t\right) = 0$ and (5.22)–(5.24) into (5.21), and letting $\varepsilon \to 0$, we obtain (5.20). ∎

Lemma 5.2 *If v_{z-w} is zero, then solutions of system (2.64)–(2.67) satisfy*

$$\int_0^L \int_0^{2\pi} \int_0^1 v_z v_r \frac{\partial \tilde{V}_z}{\partial r} r dr d\theta dz \leq \frac{a}{2} (1 + b) \int_0^L \int_0^{2\pi} v_{r-w}^2 \, d\theta dz$$

$$+ \frac{a}{4} \left(1 + \frac{1}{b}\right) \int_0^L \int_0^{2\pi} \int_0^1 \left(\frac{\partial v_r}{\partial r}\right)^2 r dr d\theta dz + \frac{1}{4a} \int_0^L \int_0^{2\pi} \int_0^1 \left(\frac{\partial v_z}{\partial r}\right)^2 r dr d\theta dz \tag{5.25}$$

for arbitrary positive constants a and b.

Proof. Since $\sup_\Omega \left| \frac{\partial \tilde{V}_z}{\partial r} \right| = 2$, we have

$$\int_0^L \int_0^{2\pi} \int_\varepsilon^1 v_z v_r \frac{\partial \tilde{V}_z}{\partial r} r dr d\theta dz \leq 2 \int_0^L \int_0^{2\pi} \int_\varepsilon^1 |v_z| |v_r| \, r dr$$

$$\leq a \int_0^L \int_0^{2\pi} \int_\varepsilon^1 v_r^2 r dr d\theta dz + \frac{1}{a} \int_0^L \int_0^{2\pi} \int_\varepsilon^1 v_z^2 r dr d\theta dz. \tag{5.26}$$

We write

$$v_r(r, \theta, z, t) = v_{r-w} - \int\limits_r^1 \frac{\partial v_r}{\partial r} dr$$

so that

$$v_r^2 (r, \theta, z, t) = \left(v_{r-w} - \int\limits_r^1 \frac{\partial v_r}{\partial r} dr \right)^2 \leq (1 + b) v_{r-w}^2 + \left(1 + \frac{1}{b} \right) \left(\int\limits_r^1 \frac{\partial v_r}{\partial r} dr \right)^2.$$

By the Schwartz inequality,

$$\left(\int\limits_r^1 \frac{1}{\sqrt{r}} \sqrt{r} \frac{\partial v_r}{\partial r} dr \right)^2 \leq - \ln r \int\limits_r^1 r \left(\frac{\partial v_r}{\partial r} \right)^2 dr$$

so we have that

$$r v_r^2 (r, \theta, z, t) \leq (1 + b) r v_{r-w}^2 - \left(1 + \frac{1}{b} \right) r \ln r \int\limits_\varepsilon^1 r \left(\frac{\partial v_r}{\partial r} \right)^2 dr$$

where we have set $r = \varepsilon$ in the lower integral limit. We now get

$$\int\limits_0^L \int\limits_0^{2\pi} \int\limits_\varepsilon^1 v_r^2 r \, dr \, d\theta \, dz \leq$$

$$\int\limits_0^L \int\limits_0^{2\pi} \int\limits_\varepsilon^1 \left((1 + b) r v_{r-w}^2 - \left(1 + \frac{1}{b} \right) r \ln r \int\limits_\varepsilon^1 r \left(\frac{\partial v_r}{\partial r} \right)^2 dr \right) dr \, d\theta \, dz$$

$$= \frac{1}{2} \left(1 - \varepsilon^2 \right) (1 + b) \int\limits_0^L \int\limits_0^{2\pi} v_{r-w}^2 \, d\theta \, dz$$

$$+ \frac{1}{4} \left(1 - \varepsilon^2 + 2\varepsilon^2 \ln \varepsilon \right) \left(1 + \frac{1}{b} \right) \int\limits_0^L \int\limits_0^{2\pi} \int\limits_\varepsilon^1 r \left(\frac{\partial v_r}{\partial r} \right)^2 dr \, d\theta \, dz. \quad (5.27)$$

For v_z, we have

$$v_z(r, \theta, z, t) = v_{z-w} - \int\limits_r^1 \frac{\partial v_z}{\partial r} dr = - \int\limits_r^1 \frac{\partial v_z}{\partial r} dr,$$

so we get

$$v_z^2 (r, \theta, z, t) = \left(\int\limits_r^1 \frac{1}{\sqrt{r}} \sqrt{r} \frac{\partial v_z}{\partial r} dr \right)^2 \leq - \ln r \int\limits_r^1 r \left(\frac{\partial v_z}{\partial r} \right)^2 dr.$$

and, finally

$$\int_0^L \int_0^{2\pi} \int_\varepsilon^1 v_z^2 r\,dr\,d\theta\,dz \le \int_0^L \int_0^{2\pi} \int_\varepsilon^1 -r\ln r \int_\varepsilon^1 r\left(\frac{\partial v_z}{\partial r}\right)^2 dr\,dr\,d\theta\,dz$$

$$= \frac{1}{4}\left(1-\varepsilon^2+2\varepsilon^2\ln\varepsilon\right) \int_0^L \int_0^{2\pi} \int_\varepsilon^1 r\left(\frac{\partial v_z}{\partial r}\right)^2 dr\,d\theta\,dz. \quad (5.28)$$

Inserting (5.27) and (5.28) into (5.26), and letting $\varepsilon \to 0$, yield (5.25). ∎

The conditions of Lemma 5.1 and 5.2 are assumed to hold throughout the analysis that follows, that is: $v_{\theta-w} = v_{z-w} = 0$, and; v_{r-w} satisfies (5.16).

5.3.4   Optimality

The following theorem incorporates the control design and optimality result.

Theorem 5.1 *The control*

$$v_{r-w} = -k\Delta p, \quad (5.29)$$

with $k \in \left(0, \frac{Re}{4}\right)$ *and* Re *arbitrary, maximizes the cost functional*

$$J\left(v_{r-w}\right) = \lim_{t\to\infty}\left[2\beta E\left(\mathbf{w}\left(t\right)\right) + \int_0^t h\left(\mathbf{w}\left(\tau\right)\right)d\tau\right] \quad (5.30)$$

where

$$\beta = \frac{2k}{\left(1 - \frac{4}{Re}k\right)}$$

and

$$h\left(\mathbf{w}\right) = \frac{2\beta}{Re}m\left(\mathbf{w}\right) + 2\beta \int_0^L \int_0^{2\pi} \int_0^1 v_z v_r \frac{\partial \tilde{V}_z}{\partial r} r\,dr\,d\theta\,dz$$

$$- \left(\frac{\beta}{2}\right)^2 \left(1 + \frac{2\beta}{Re}\right)^{-1} \int_0^L \int_0^{2\pi} \Delta p^2 d\theta\,dz - \int_0^L \int_0^{2\pi} v_{r-w}^2 d\theta\,dz. \quad (5.31)$$

Moreover, solutions of system (2.64)–(2.67) satisfy

$$h\left(\mathbf{w}\right) \le c_1 m\left(\mathbf{w}\right) - c_2 \int_0^L \int_0^{2\pi} \Delta p^2 d\theta\,dz - \frac{1}{2} \int_0^L \int_0^{2\pi} v_{r-w}^2 d\theta\,dz \quad (5.32)$$

for arbitrary values of the control v_{r-w}, and with

$$c_1 = \frac{2\beta}{Re} + \max\left(\frac{1}{4}, 2\beta^2\right) > 0 \quad and \quad c_2 = \left(\frac{\beta}{2}\right)^2 \left(1 + \frac{2\beta}{Re}\right)^{-1} > 0. \qquad (5.33)$$

Proof. By Lemma 5.1, we can write (5.31) as

$$h(\mathbf{w}) = -2\beta \dot{E}(\mathbf{w}) - \beta \int_0^L \int_0^{2\pi} v_{r-w} \Delta p \, d\theta dz - \frac{2\beta}{Re} \int_0^L \int_0^{2\pi} v_{r-w}^2 \, d\theta dz$$

$$- \left(\frac{\beta}{2}\right)^2 \left(1 + \frac{2\beta}{Re}\right)^{-1} \int_0^L \int_0^{2\pi} \Delta p^2 d\theta dz - \int_0^L \int_0^{2\pi} v_{r-w}^2 \, d\theta dz. \quad (5.34)$$

Inserting (5.34) into (5.30) we get

$$J(v_{r-w}) = \lim_{t \to \infty} \left[2\beta E(\mathbf{w}(t)) + \int_0^t \left(\left(-2\beta \dot{E}(\mathbf{w}(\tau)) \right) \right. \right.$$

$$- \beta \int_0^L \int_0^{2\pi} v_{r-w} \Delta p \, d\theta dz - \frac{2\beta}{Re} \int_0^L \int_0^{2\pi} v_{r-w}^2 \, d\theta dz$$

$$\left. \left. - \left(\frac{\beta}{2}\right)^2 \left(1 + \frac{2\beta}{Re}\right)^{-1} \int_0^L \int_0^{2\pi} \Delta p^2 d\theta dz - \int_0^L \int_0^{2\pi} v_{r-w}^2 \, d\theta dz \right) d\tau \right]$$

$$= \lim_{t \to \infty} \left[2\beta E(\mathbf{w}(t)) - 2\beta \int_0^t \dot{E}(\mathbf{w}(\tau)) d\tau \right.$$

$$- \left(1 + \frac{2\beta}{Re}\right) \int_0^t \int_0^L \int_0^{2\pi} \left(v_{r-w}^2 + \beta \left(1 + \frac{2\beta}{Re}\right)^{-1} v_{r-w} \Delta p \right.$$

$$\left. \left. + \left(\frac{\beta}{2}\right)^2 \left(1 + \frac{2\beta}{Re}\right)^{-2} \Delta p^2 \right) d\theta dz d\tau \right]$$

$$= 2\beta E(\mathbf{w}(0)) - \left(1 + \frac{2\beta}{Re}\right) \lim_{t \to \infty} \int_0^t \int_0^L \int_0^{2\pi} \left(v_{r-w} + \frac{\beta}{2} \left(1 + \frac{2\beta}{Re}\right)^{-1} \Delta p \right)^2 d\theta dz d\tau.$$

$$(5.35)$$

The maximum of (5.30) is achieved when the integral in (5.35) is zero. Thus, (5.29) is the optimal control. Inequality (5.32) is obtained by applying Lemma 5.2 with $a = \frac{1}{4\beta}$ and $b = 1$, to (5.31). ∎

The objective of applying the control input (5.29) is to increase the value of $m(\mathbf{w})$. That this objective is targeted in the cost functional (5.30), is clear from inequality

(5.32), which gives an upper bound on $h(\mathbf{w})$ in terms of $m(\mathbf{w})$. Thus, $h(\mathbf{w})$ cannot be made large without making $m(\mathbf{w})$ large, so the cost functional (5.30) is meaningful with respect to our objective. The cost functional also puts penalty on the output. Since the output is fed back to the control input, the output penalty works in conjunction with the input penalty to minimize control effort.

The next theorem writes the result of Theorem 5.1 on a form that puts emphasis on signal gains.

Theorem 5.2 *For all Re and $t \geq 0$, solutions of system (2.64)–(2.67) satisfy*

$$
\max_{\substack{v_{r-w} \\ E(\mathbf{w}(0)) \neq 0}} \left\{ \lim_{t \to \infty} \frac{2\beta E(\mathbf{w}(t)) + \int\limits_0^t g(\mathbf{w}(\tau)) \, d\tau}{2\beta E(\mathbf{w}(0)) + c_2 \int\limits_0^t \int\limits_0^L \int\limits_0^{2\pi} \Delta p^2 d\theta dz d\tau + \frac{1}{2} \int\limits_0^t \int\limits_0^L \int\limits_0^{2\pi} v_{r-w}^2 d\theta dz d\tau} \right\} = 1, \quad (5.36)
$$

where

$$
g(\mathbf{w}) \leq c_1 m(\mathbf{w}). \tag{5.37}
$$

Furthermore, the maximum is achieved with the optimal control (5.29), for which solutions of the closed–loop system satisfy

$$
2\beta E(\mathbf{w}(t)) + c_1 \int\limits_0^t m(\mathbf{w}(\tau)) \, d\tau \geq 2\beta E(\mathbf{w}(0)) + \left(\frac{3}{2} + \frac{2\beta}{Re} \right) \int\limits_0^t \int\limits_0^L \int\limits_0^{2\pi} v_{r-w}^2 d\theta dz d\tau.
$$
$$
\tag{5.38}
$$

Proof. Consider the function

$$
g(\mathbf{w}) \triangleq h(\mathbf{w}) + c_2 \int\limits_0^L \int\limits_0^{2\pi} \Delta p^2 d\theta dz + \frac{1}{2} \int\limits_0^L \int\limits_0^{2\pi} v_{r-w}^2 d\theta dz. \tag{5.39}
$$

Integration of (5.39) with respect to time, and adding $2\beta E(\mathbf{w}(t))$ to each side, gives

$$
2\beta E(\mathbf{w}(t)) + \int\limits_0^t g(\mathbf{w}(\tau)) \, d\tau
$$
$$
= 2\beta E(\mathbf{w}(t)) + \int\limits_0^t h(\mathbf{w}(\tau)) \, d\tau + c_2 \int\limits_0^t \int\limits_0^L \int\limits_0^{2\pi} \Delta p^2 d\theta dz d\tau + \frac{1}{2} \int\limits_0^t \int\limits_0^L \int\limits_0^{2\pi} v_{r-w}^2 d\theta dz d\tau.
$$
$$
\tag{5.40}
$$

The two first terms on the right hand side of (5.40) is $J(v_{r-w})$ (without the limit), so inserting (5.35) we get

$$2\beta E\left(\mathbf{w}\left(t\right)\right) + \int\limits_0^t g\left(\mathbf{w}\left(\tau\right)\right) d\tau$$

$$= 2\beta E\left(\mathbf{w}\left(0\right)\right) - \left(1 + \frac{2\beta}{Re}\right) \int\limits_0^t \int\limits_0^L \int\limits_0^{2\pi} \left(v_{r-w} + \frac{\beta}{2}\left(1 + \frac{2\beta}{Re}\right)^{-1} \Delta p\right)^2 d\theta dz d\tau$$

$$+ c_2 \int\limits_0^t \int\limits_0^L \int\limits_0^{2\pi} \Delta p^2 d\theta dz d\tau + \frac{1}{2} \int\limits_0^t \int\limits_0^L \int\limits_0^{2\pi} v_{r-w}^2 d\theta dz d\tau. \quad (5.41)$$

Dividing both sides of (5.41) by

$$2\beta E\left(\mathbf{w}\left(0\right)\right) + c_2 \int\limits_0^t \int\limits_0^L \int\limits_0^{2\pi} \Delta p^2 d\theta dz d\tau + \frac{1}{2} \int\limits_0^t \int\limits_0^L \int\limits_0^{2\pi} v_{r-w}^2 d\theta dz d\tau,$$

assuming $E\left(\mathbf{w}\left(0\right)\right) \neq 0$, taking the limit as $t \rightarrow \infty$, and then taking the maximum value over v_{r-w}, we obtain

$$\lim_{t\to\infty} \underbrace{\frac{2\beta E\left(\mathbf{w}\left(t\right)\right) + \int\limits_0^t g\left(\mathbf{w}\left(\tau\right)\right) d\tau}{2\beta E\left(\mathbf{w}\left(0\right)\right) + c_2 \int\limits_0^t \int\limits_0^L \int\limits_0^{2\pi} \Delta p^2 d\theta dz d\tau + \frac{1}{2} \int\limits_0^t \int\limits_0^L \int\limits_0^{2\pi} v_{r-w}^2 d\theta dz d\tau}}_{\substack{\max\, v_{r-w} \\ E\left(\mathbf{w}\left(0\right)\right) \neq 0}}$$

$$= 1 - \lim_{t\to\infty} \underbrace{\frac{\left(1 + \frac{2\beta}{Re}\right) \int\limits_0^t \int\limits_0^L \int\limits_0^{2\pi} \left(v_{r-w} + \frac{\beta}{2}\left(1 + \frac{2\beta}{Re}\right)^{-1} \Delta p\right)^2 d\theta dz d\tau}{2\beta E\left(\mathbf{w}\left(0\right)\right) + c_2 \int\limits_0^t \int\limits_0^L \int\limits_0^{2\pi} \Delta p^2 d\theta dz d\tau + \frac{1}{2} \int\limits_0^t \int\limits_0^L \int\limits_0^{2\pi} v_{r-w}^2 d\theta dz d\tau}}_{\substack{\max\, v_{r-w} \\ E\left(\mathbf{w}\left(0\right)\right) \neq 0}}. \quad (5.42)$$

Since the numerator of the last term in (5.42) is non-negative, and the denominator is strictly positive, the maximum on the right hand side of (5.42) is attained when the numerator is zero, which is for the optimal control (5.29). Thus, we obtain (5.36). Inequality (5.37) follows from (5.39) and (5.32). Inserting the optimal control into (5.41) by writing Δp in terms of v_{r-w} using (5.29), we obtain

$$2\beta E\left(\mathbf{w}\left(t\right)\right) + \int\limits_0^t g\left(\mathbf{w}\left(\tau\right)\right) d\tau = 2\beta E\left(\mathbf{w}\left(0\right)\right)$$

$$+ c_2 \left(\frac{2}{\beta}\right)^2 \left(1 + \frac{2\beta}{Re}\right)^2 \int\limits_0^t \int\limits_0^L \int\limits_0^{2\pi} v_{r-w}^2 \, d\theta dz d\tau + \frac{1}{2} \int\limits_0^t \int\limits_0^L \int\limits_0^{2\pi} v_{r-w}^2 \, d\theta dz d\tau. \quad (5.43)$$

Inserting for c_2, as defined in (5.33), and using (5.37), we get (5.38). $\blacksquare$

The result (5.36) was inspired by the work on optimal destabilization of linear systems reported in [92]. In view of (5.37), by maximizing the ratio in the curly brackets of (5.36), we make sure that the input and output signals are small compared to the internal states. This is equivalent to obtaining a large closed-loop gain. In addition, the theorem gives a lower bound on the states in terms of the control input for system (2.64)–(2.67) in closed loop with (5.29). Thus, it establishes the fact that the states cannot be small without the control input being small, and the control input cannot be made large without making the states large. As we shall see in our simulation study, this will lead to good mixing with low control effort.

5.3.5 Detectability of Mixing

Achieving optimality with static output feedback of Δp is remarkable. In this section we explain why this special output is strongly related to mixing and allows its enhancement. The next theorem establishes an open-loop property of system (2.64)–(2.67) that is reminiscent of an integral variant of input/output-to-state-stability (IOSS) for finite dimensional nonlinear systems.

Theorem 5.3 *If $Re \in (0,4)$, then solutions of system (2.64)–(2.67) satisfy*

$$c_3 \int\limits_0^t m\left(\mathbf{w}\left(\tau\right)\right) d\tau \quad \leq \quad 2\beta E\left(\mathbf{w}\left(0\right)\right)$$

$$+ \beta^2 \left(1 + \frac{2\beta}{Re}\right)^{-1} \int\limits_0^t \int\limits_0^L \int\limits_0^{2\pi} \Delta p^2 d\theta dz d\tau$$

$$+ c_4 \int\limits_0^t \int\limits_0^L \int\limits_0^{2\pi} v_{r-w}^2 d\theta dz d\tau, \quad (5.44)$$

for all $t \geq 0$ and for arbitrary values of the control v_{r-w}, with

$$c_3 = \frac{\beta}{4} \left(\frac{4 - Re}{Re}\right) > 0 \ \ and \ \ c_4 = 1 + \beta \left(\frac{4 + Re}{4 - Re}\right) > 0.$$

Proof. From (5.30), (5.31) and (5.35), we get for all $t \geq 0$:

$$2\beta E\left(\mathbf{w}\left(t\right)\right) + \int_0^t \frac{2\beta}{Re} m\left(\mathbf{w}\left(\tau\right)\right) d\tau$$

$$\leq 2\beta E\left(\mathbf{w}\left(0\right)\right) - 2\beta \int_0^t \int_0^L \int_0^{2\pi} \int_0^1 v_z v_r \frac{\partial \tilde{V}_z}{\partial r} r dr d\theta dz d\tau$$

$$+ \left(\frac{\beta}{2}\right)^2 \left(1 + \frac{2\beta}{Re}\right)^{-1} \int_0^t \int_0^L \int_0^{2\pi} \Delta p^2 d\theta dz d\tau + \int_0^t \int_0^L \int_0^{2\pi} v_{r-w}^2 d\theta dz d\tau. \quad (5.45)$$

Using Lemma 5.2 , we obtain

$$2\beta E\left(\mathbf{w}\left(t\right)\right) + \int_0^t \frac{2\beta}{Re} m\left(\mathbf{w}\left(\tau\right)\right) d\tau$$

$$\leq 2\beta E\left(\mathbf{w}\left(0\right)\right) + 2\beta \int_0^t \left(\frac{a}{2}\left(1 + b\right) \int_0^L \int_0^{2\pi} v_{r-w}^2 d\theta dz\right.$$

$$+ \frac{a}{4}\left(1 + \frac{1}{b}\right) \int_0^L \int_0^{2\pi} \int_0^1 \left(\frac{\partial v_r}{\partial r}\right)^2 r dr d\theta dz + \frac{1}{4a} \int_0^L \int_0^{2\pi} \int_0^1 \left(\frac{\partial v_z}{\partial r}\right)^2 r dr d\theta dz \right) d\tau$$

$$+ \left(\frac{\beta}{2}\right)^2 \left(1 + \frac{2\beta}{Re}\right)^{-1} \int_0^t \int_0^L \int_0^{2\pi} \Delta p^2 d\theta dz d\tau + \int_0^t \int_0^L \int_0^{2\pi} v_{r-w}^2 d\theta dz d\tau,$$

so it follows that

$$2\beta E\left(\mathbf{w}\left(t\right)\right) + \int_0^t \frac{2\beta}{Re} m\left(\mathbf{w}\left(\tau\right)\right) d\tau$$

$$\leq 2\beta E\left(\mathbf{w}\left(0\right)\right) + \int_0^t \frac{\beta}{2} \max\left(a\left(1 + \frac{1}{b}\right), \frac{1}{a}\right) m\left(\mathbf{w}\left(\tau\right)\right) d\tau$$

$$+ \left(\frac{\beta}{2}\right)^2 \left(1 + \frac{2\beta}{Re}\right)^{-1} \int_0^t \int_0^L \int_0^{2\pi} \Delta p^2 d\theta dz d\tau + \left(1 + \beta a\left(1 + b\right)\right) \int_0^t \int_0^L \int_0^{2\pi} v_{r-w}^2 d\theta dz d\tau.$$

Rearranging the terms, we obtain

$$2\beta E\left(\mathbf{w}\left(t\right)\right) + \left(\frac{2\beta}{Re} - \frac{\beta}{2} \max\left(a\left(1 + \frac{1}{b}\right), \frac{1}{a}\right)\right) \int_0^t m\left(\mathbf{w}\left(\tau\right)\right) d\tau$$

$$\leq 2\beta E\left(\mathbf{w}\left(0\right)\right) + \left(\frac{\beta}{2}\right)^2 \left(1 + \frac{2\beta}{Re}\right)^{-1} \int_0^t \int_0^L \int_0^{2\pi} \Delta p^2 d\theta dz d\tau$$

$$+ \left(1 + \beta a \left(1 + b\right)\right) \int\limits_0^t \int\limits_0^L \int\limits_0^{2\pi} v_{r-w}^2 \, d\theta dz d\tau,$$

which is (5.44) for $a = 1$ and $b = 2 \left(\frac{Re}{4-Re}\right)$. ∎

The significance of inequality (5.44) is that it provides a notion of detectability of internal states from the output Δp. In particular, if $m(\mathbf{w})$ is large, Δp must be large as well, or if Δp is small, so is $m(\mathbf{w})$. This is reminiscent of an integral variant of the IOSS property for finite-dimensional nonlinear systems, as presented in [79] (and motivated by earlier results in [107, 108]). In the case of (5.44) we have an integral-to-integral property (iiIOSS) with $m(\mathbf{w})$ as a measure of the states, so the "energy" of the states is bounded above by the "energy" of the input and output signals. With $E(\mathbf{w})$ as a measure of the states, we can also find a uniform upper bound (as opposed to an "energy" upper bound) in terms of the input and output signals. That is, system (2.64)–(2.67) has the IOSS property, as stated formally in the next theorem.

Theorem 5.4 *For $Re \in (0, 4)$, solutions of system (2.64)–(2.67) satisfy*

$$E\left(\mathbf{w}\left(t\right)\right)$$

$$\leq E\left(\mathbf{w}\left(0\right)\right) e^{-c_5 t} + \frac{1}{4c_5} \sup_{[0,t]} \left\{ \int\limits_0^L \int\limits_0^{2\pi} \Delta p^2 d\theta dz \right\} + \frac{c_6}{c_5} \sup_{[0,t]} \left\{ \int\limits_0^L \int\limits_0^{2\pi} v_{r-w}^2 d\theta dz \right\}$$

(5.46)

for all $t \geq 0$ and for arbitrary values of the control v_{r-w}, with

$$c_5 = 2 \max\left(\frac{4}{3Re} - 1, \frac{4 - Re}{4 + Re}\right) > 0 \text{ and } c_6 = \max\left(\frac{1}{4}, \frac{1}{4} + \frac{5Re - 4}{Re\left(4 - Re\right)}\right) > 0.$$

Proof. From (5.27), (5.28) and a similar derivation for v_θ, we have

$$2E\left(\mathbf{w}\right) \leq \frac{1}{2} \left(1 + b\right) \int\limits_0^L \int\limits_0^{2\pi} v_{r-w}^2 d\theta dz$$

$$+ \frac{1}{4} \int\limits_0^L \int\limits_0^{2\pi} \int\limits_0^1 \left(\left(1 + \frac{1}{b}\right) \left(\frac{\partial v_r}{\partial r}\right)^2 + \left(\frac{\partial v_\theta}{\partial r}\right)^2 + \left(\frac{\partial v_z}{\partial r}\right)^2\right) r dr d\theta dz, \quad (5.47)$$

and therefore

$$2E\left(\mathbf{w}\right) \leq \frac{1}{2} \left(1 + b\right) \int\limits_0^L \int\limits_0^{2\pi} v_{r-w}^2 d\theta dz + \frac{1}{4} \left(1 + \frac{1}{b}\right) m\left(\mathbf{w}\right). \quad (5.48)$$

From Lemma 5.1 and (5.48) we get

$$\dot{E}(\mathbf{w}) \leq -2 \left(\frac{4}{Re} \left(\frac{b}{1+b} \right) - 1 \right) E(\mathbf{w})$$

$$-\frac{1}{2} \int_0^L \int_0^{2\pi} v_{r-w} \Delta p \, d\theta dz + \frac{2b-1}{Re} \int_0^L \int_0^{2\pi} v_{r-w}^2 \, d\theta dz,$$

so that

$$\dot{E}(\mathbf{w}) \leq -2 \left(\frac{4}{Re} \left(\frac{b}{1+b} \right) - 1 \right) E(\mathbf{w})$$

$$+\frac{1}{4} \int_0^L \int_0^{2\pi} \left(v_{r-w}^2 + \Delta p^2 \right) d\theta dz + \frac{2b-1}{Re} \int_0^L \int_0^{2\pi} v_{r-w}^2 \, d\theta dz.$$

Setting

$$b = \max \left(\frac{1}{2}, \frac{2Re}{4-Re} \right)$$

we obtain

$$\dot{E}(\mathbf{w}) \leq -c_5 E(\mathbf{w}) + \frac{1}{4} \int_0^L \int_0^{2\pi} \Delta p^2 \, d\theta dz + c_6 \int_0^L \int_0^{2\pi} v_{r-w}^2 \, d\theta dz \qquad (5.49)$$

with

$$c_5 = 2 \max \left(\frac{4}{3Re} - 1, \frac{4-Re}{4+Re} \right), \text{ and } c_6 = \max \left(\frac{1}{4}, \frac{1}{4} + \frac{5Re-4}{Re(4-Re)} \right).$$

Inequality (5.46) now follows from the comparison principle [80, Lemma C.5] (and the triangle inequality applied to the two last terms in (5.49)).   ■

In Theorem 5.4, the notation $\sup_{[0,t]}$ denotes the essential supremum taken over the finite time interval $[0, t]$. The detectability properties stated in Theorems 5.3 and 5.4 indicate that our choice of sensing, Δp, is appropriate.

5.3.6   Numerical Simulations

The Computational scheme

The simulations are performed using a flow solver that is based on a second-order staggered grid discretization, second-order time advancement, and a Poisson equation for pressure, based on a scheme designed by Akselvoll and P. Moin [8]. The length of the cylinder is $L = 3\pi$ and the radius is $R = 1$. The grid is structured, single-block with cylindrical coordinates. It is uniform and periodic in z and θ with
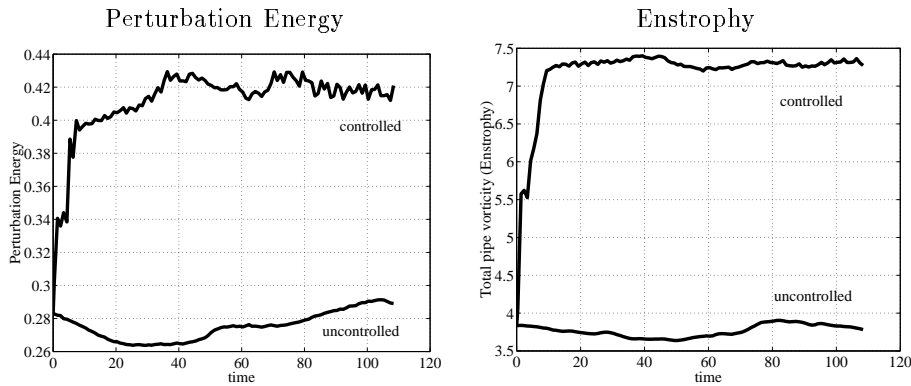
Figure 5.20: Perturbation energy and enstrophy.

Fourier-modes 64 and 128 respectively, and linearly spaced with ratio 8 : 1 in the radial direction in order to achieve high resolution at the wall. The adaptive time step was in the range of 0.06-0.08 with constant CFL number 0.5 and constant 1 volume flux per unit span. The Reynolds number we used was $Re = 2100$ which is slightly higher than the limiting number $Re = 2000$ for nonlinear stability. We ran both the controlled and the uncontrolled case for about 110 time units starting from a statistically steady state flow field with control gain $k = 0.1$ in the controlled case. The initial flow field was obtained from a random perturbation of the parabolic profile over a large time interval using the uncontrolled case.

Measuring mixing

Figure 5.20 shows that our control results in an approximately 50% increase in the perturbation energy and 92% almost instantaneous increase in the enstrophy. While comparison based on perturbation energy is important as it is the part of the cost functional (5.30), enstrophy provides us with a measurement that is more closely related to mixing.

The instantaneous streamwise vorticity along a cross section of the pipe (Figure 5.21) also shows some promise for increased mixing with higher values of vorticity and more complex vortex structures in the controlled case than in the uncontrolled case. Vorticity is increased not only near the wall but everywhere in the pipe.

The method we use to quantify and visualize mixing is the tracking of dye in the flow. We consider the problem of mixing of a single fluid (or similar fluids) governed by the stretching and folding of material elements. We introduce passive tracer dye along the center of the pipe represented by a set of 100 particles, as shown in Figure 5.22. We trace the position of these particles using a particle-line method [78, 112]. The distance between neighboring particles is kept less than 0.1 by introducing new particles to halve the distance if necessary to obtain a connected dye surface at all time. As shown in Figure 5.23, the number of particles, that is, the length of the dye, increases in the controlled case at a much higher rate than

Uncontrolled   Controlled
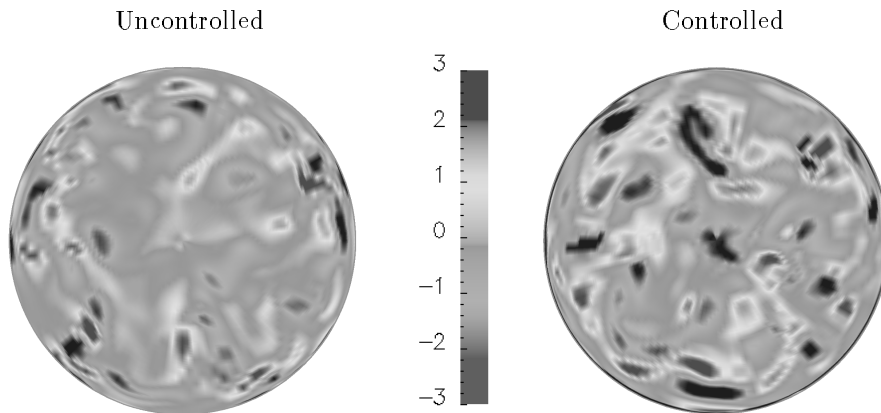
Figure 5.21: Streamwise vorticity.
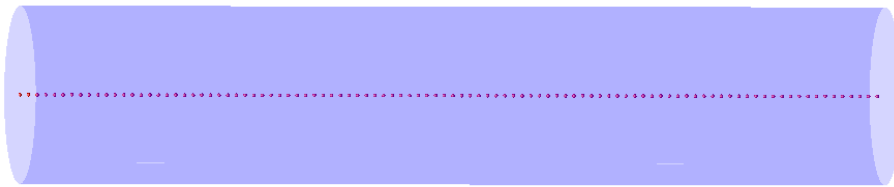
Figure 5.22: Initial particle distribution.

in the uncontrolled case. Adding particles is not feasible computationally for an extended period of time. We stopped adding particles when their number reached two million ($t = 4$ in the controlled case and $t = 8$ in the uncontrolled case), but we continued tracing them. Figure 5.24 shows the distribution of particles inside the pipe. In the controlled case we obtain more uniform particle distribution even for smaller time.

Actuator distribution and bandwidth

Figure 5.25 shows the instantaneous pressure field in a cross section of the pipe along with the boundary velocity that is magnified 500 times for visualization. The control "blows in" when wall pressure is high and "sucks out" when wall pressure is low. Spatial changes in the control velocity are smooth and small, promising that a low number of actuators will suffice in practice. In order to investigate the density and bandwidth of sensors and actuators needed we calculate the power spectral densities of the control. The spectral plots alongside with the original signals are shown in Figure 5.26. Figures 5.26(a,b) show that only about 10-15 actuators/sensors are needed along the pipe length. Similarly, Figures 5.26(c,d) show that we need at most 15-20 actuators/sensors in the angular direction. That
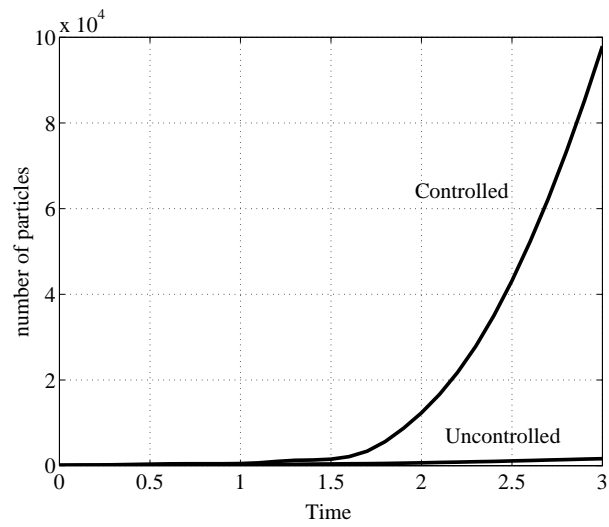
Figure 5.23: Length of dye as a function of time.

Uncontrolled, $t = 38$

Controlled, $t = 19$
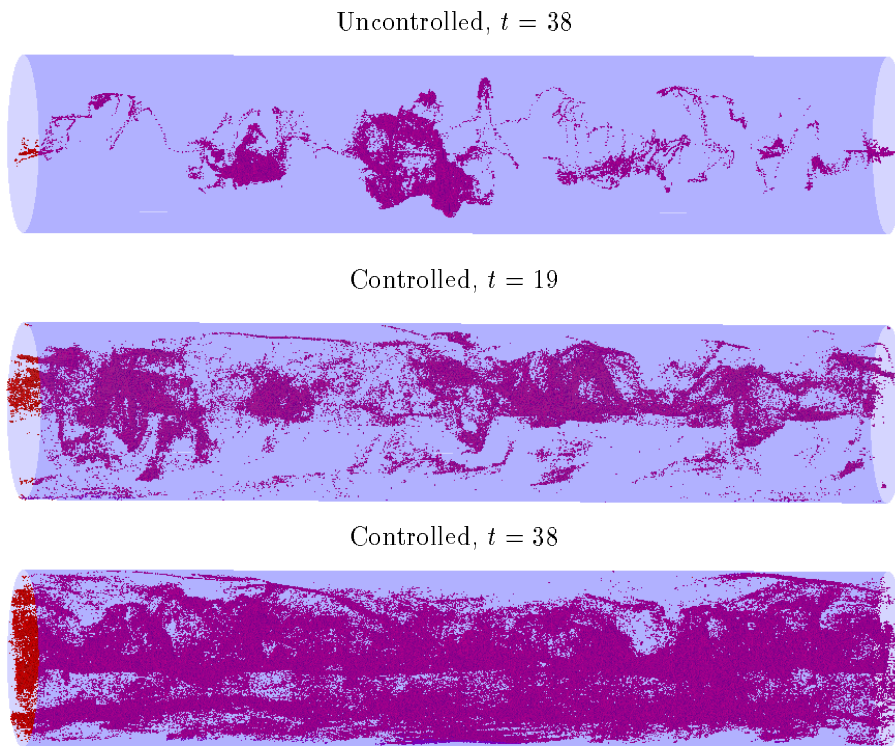
Controlled, $t = 38$

Figure 5.24: Particle distribution.
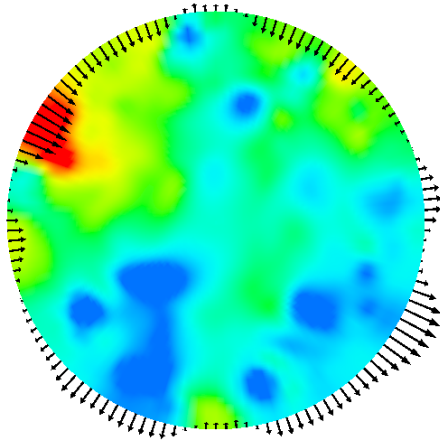
Figure 5.25: Instantaneous pressure field with controlled velocity (magnified) in a cross section of the pipe.

results in approximately 200 micro-actuators/sensors for the whole pipe surface. The time-frequency analysis in Figures 5.26(e,f) shows a bandwidth required for sensing/actuation of only 1.5Hz.

Streamwise frequency

(a) Control signal   (b) Power spectral density

Angular frequency

(c) Control signal   (d) Power spectral density

Time frequency

(e) Control signal   (f) Power spectral density
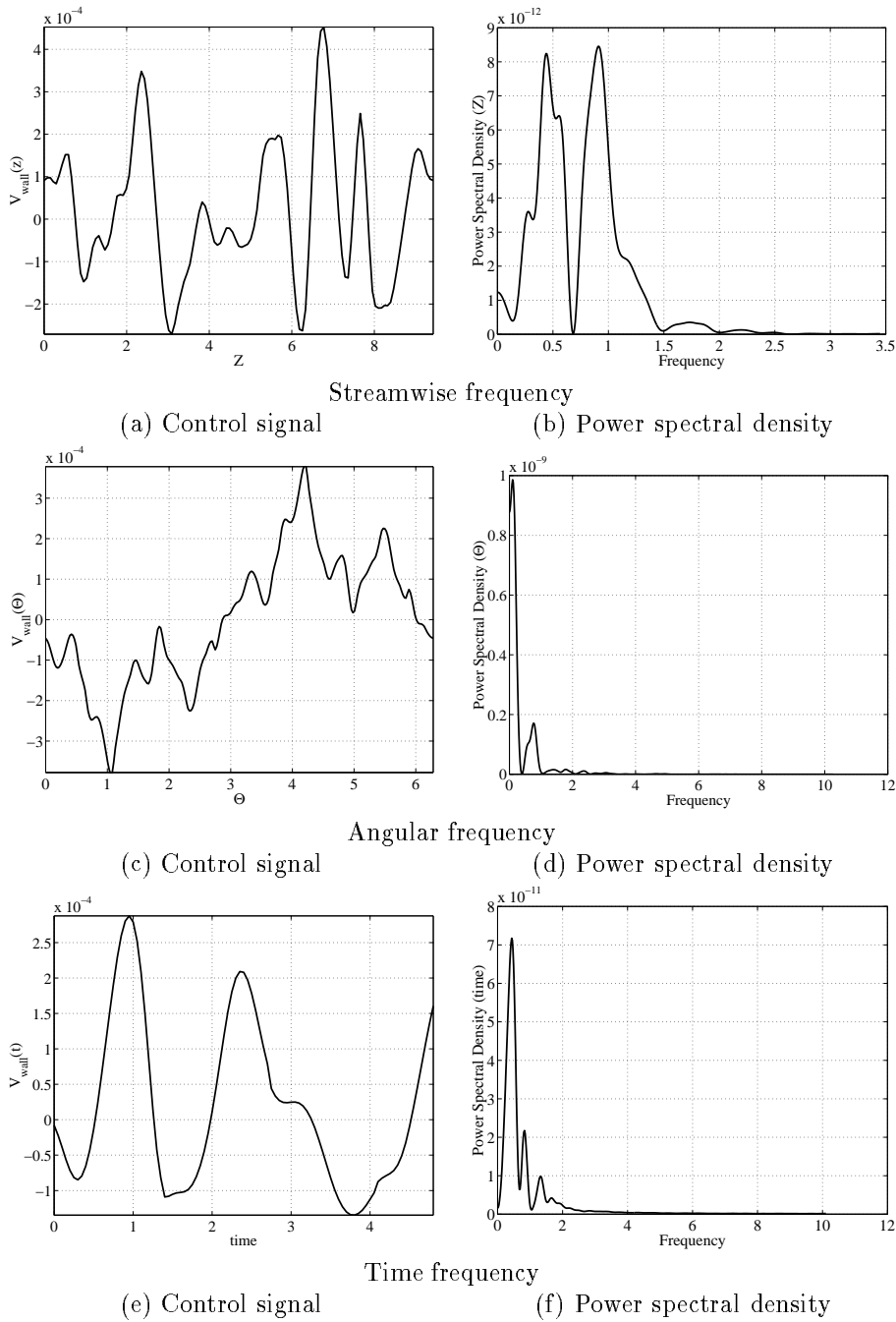
Figure 5.26: Spectral analysis of the control.

5.4   Feedback Control of Particle Dispersion in Bluff Body Wakes

Motivated by the results in Sections 5.2 and 5.3, a simulation study was carried out in [6] investigating the feasibility of enhancing particle dispersion in the wake of a circular cylinder (2D) using similar, pressure-based, feedback control laws. The simulations were performed with **FLUENT** on the grid shown in Figure 4.24. For Reynolds numbers less than the critical Reynolds number $Re_c = 47$, the steady-state flow is symmetric about the streamwise axis. The objective is to initiate vortex shedding for a slightly subcritical case ($Re = 45$), causing increased particle dispersion in the wake.

The initial condition for the simulations is obtained by running **FLUENT** for 500 time units starting from a perturbed velocity field. In this case, which is subcritical, the disturbances are dampened out, as suggested by the time evolution of the lift coefficient, and confirmed by the high degree of symmetry in the vorticity map at $t = 500$, shown in Figure 5.27. The initial condition for the runs with feedback control is thus a *slightly* perturbed velocity field.
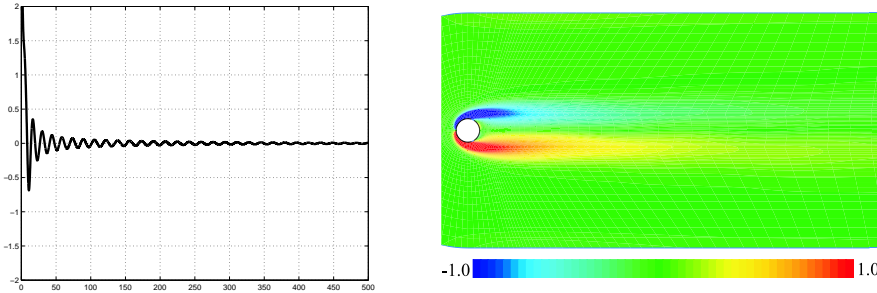
Figure 5.27: Lift coefficient for initial simulation (left graph), and vorticity field at the end of the initial simulation (right graph). The Reynolds number is $Re = 45$.

The feedback law has the form

$$\tau = k\left(a_1 \Delta p_1 + a_2 \Delta p_2 + a_3 \Delta p_3\right) \qquad (5.50)$$

where k, a_1, a_2, and a_3 are constants, and $\Delta p_i = p_i^+ - p_i^-$, for $i = 1, 2, 3$ (see Figure 4.24 for the locations of the pressure sensors; actuation is applied through slot #2). Simulations are performed for three different values of the feedback gain k, as well as for the uncontrolled case.

The lift coefficient plots of Figure 5.28 show that in the uncontrolled case, the lift continues to decrease, while in the controlled cases, the lift coefficients increase and eventually reach a state at which the amplitude remains constant. Figure 5.29 shows the corresponding control signals, and Figure 5.30 shows vorticity plots. The plots consistently show stronger vortices with increased feedback gain. In order to visualize particle dispersion, six strips of massless dye are put into the flow
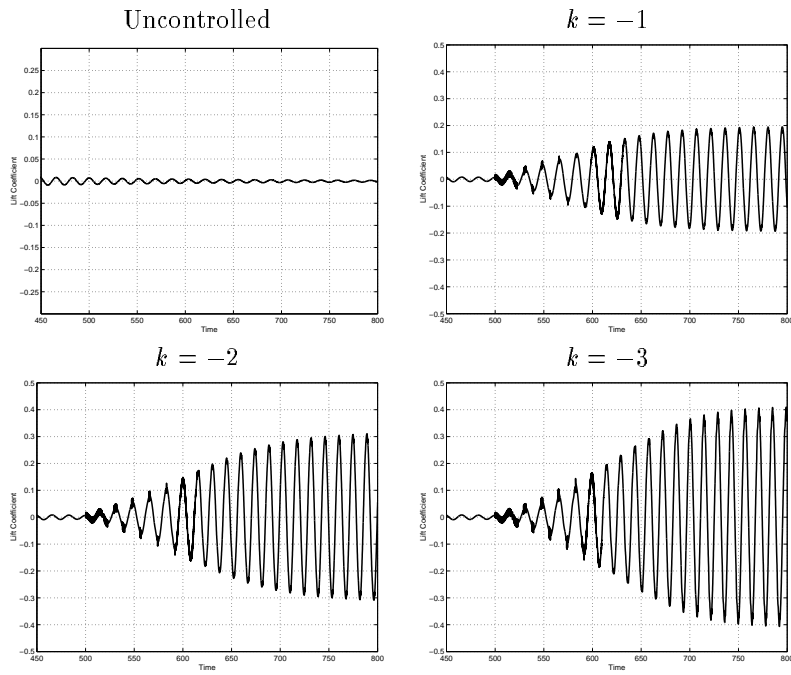
Figure 5.28: Lift coefficient for $Re = 45$.
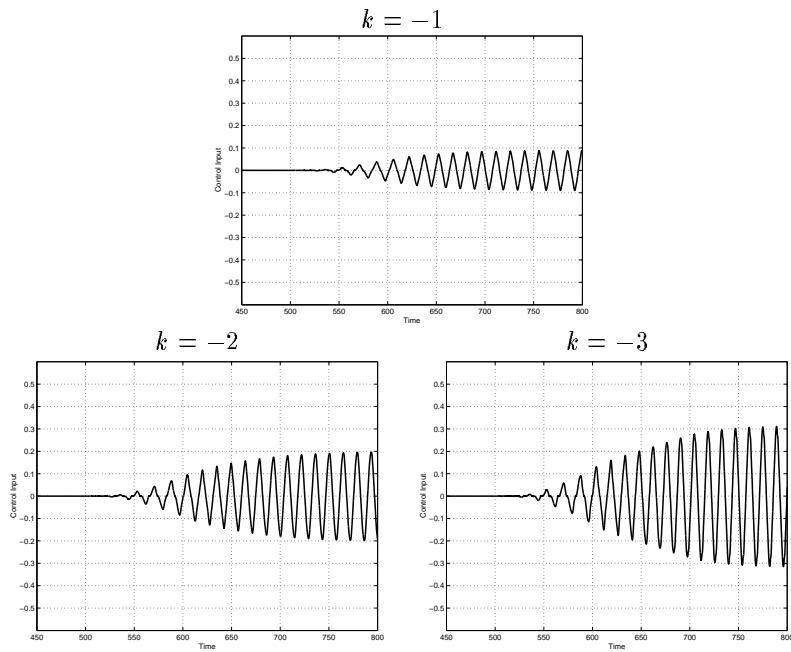
Figure 5.29: Control input for $Re = 45$.

Uncontrolled $k = -1$

$k = -2$ $k = -3$

-1.0   1.0
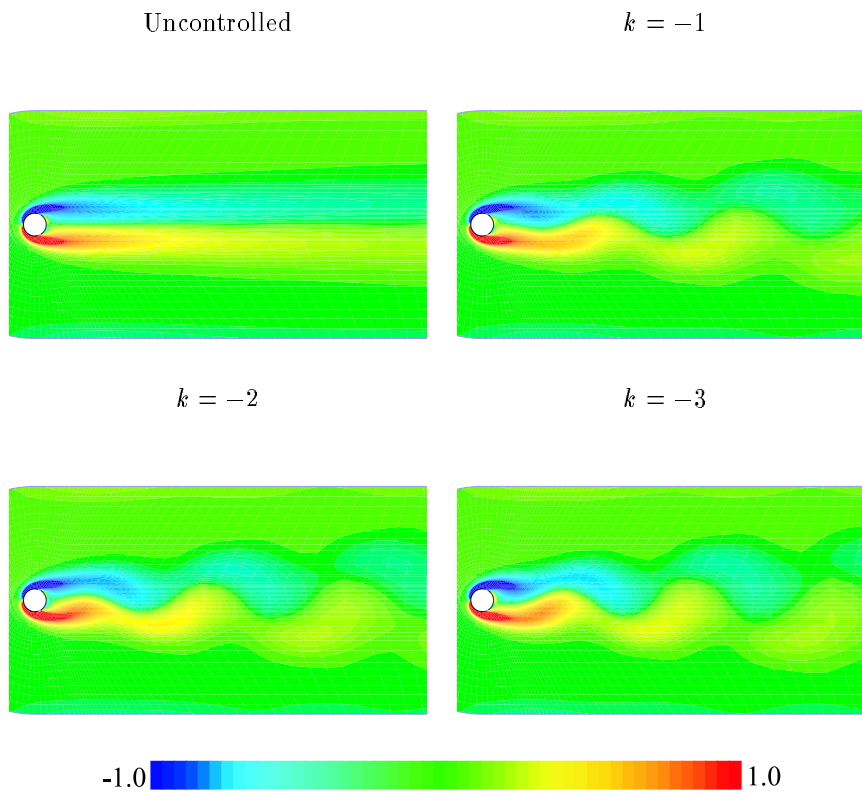
Figure 5.30: Vorticity field for $Re = 45$ at $t = 800$.

some distance upstream of the cylinder, and passively advected with the flow. A
snapshot of the result is shown in Figure 5.31. It is clear that vortex shedding is
initiated by our feedback control. Furthermore, the particles are dispersed more
widely with increasing feedback gain.
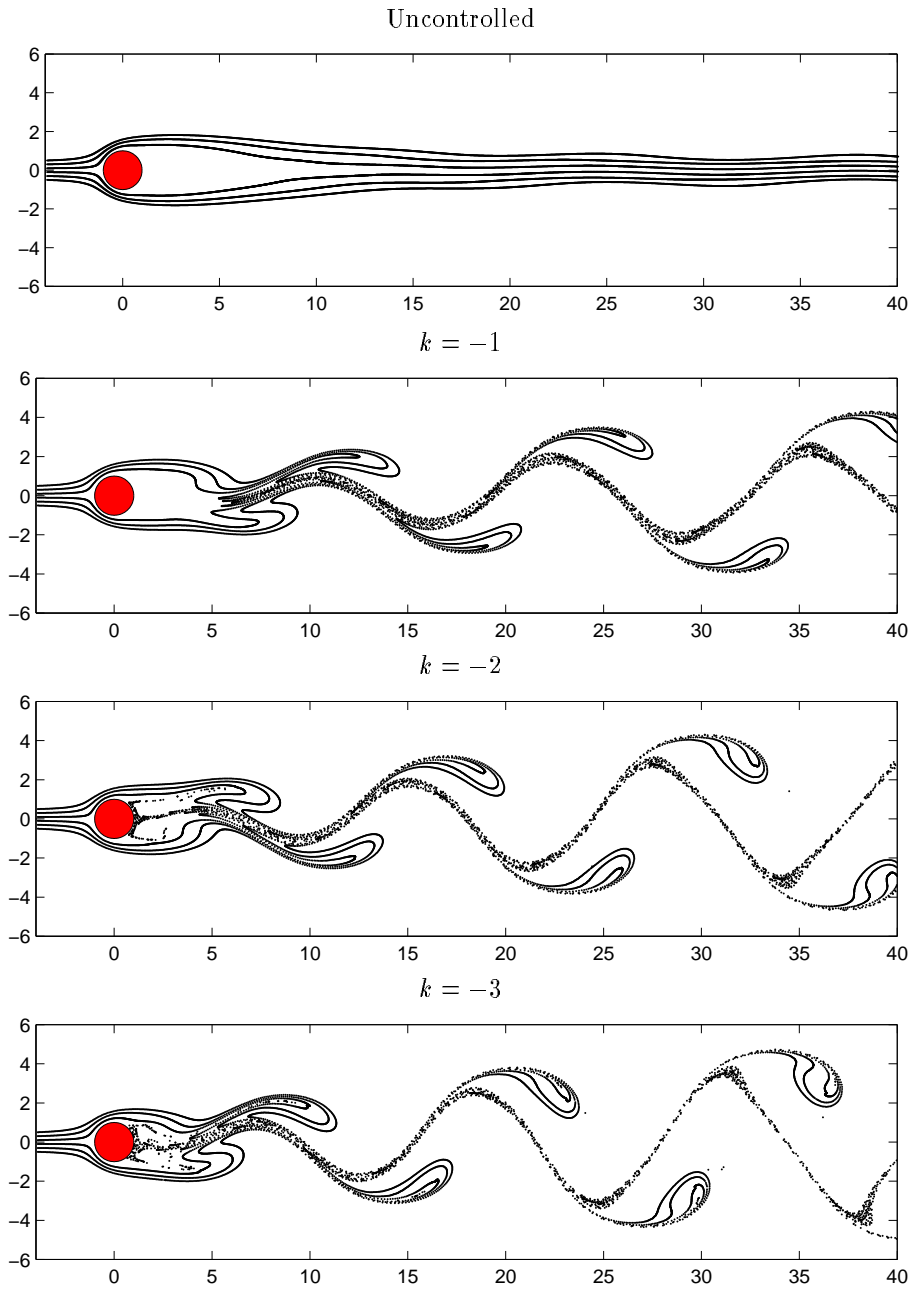
Figure 5.31: Particle distribution for $Re = 45$ at $t = 800$.

Chapter 6

Sensors and Actuators

6.1   Controlling Small-Scale Features

The theoretical and simulation results reviewed in this report are based on the ability to perform real-time distributed control. Distributed control is necessary due to the nature of drag increasing structures in the flow. In [30], high skin friction regions in turbulent flows are reported to occur near streamwise counter-rotating vortex pairs as illustrated in Figure 6.1. These vortex pairs bring high velocity fluid closer to the walls and thereby create local regions of high shear stress that significantly increase the total drag. In order to be able to control the appearance of such structures, we need to be able to sense and actuate at the same length scale, which decreases with increasing Reynolds number. The following example is presented in [30]. For an airflow at Reynolds number 10000, typical vortex pair streaks have width about 1 millimeter and length about 2 centimeters, appear at an approximate frequency of 100 Hertz, and has a life-time of about 1 millisecond. Thus, to have control authority over these structures, the sensors and actuators must have sizes in the order of a few hundred micrometers. The technology to manufacture such small-scale sensors and actuators exists, and selected devices are reviewed in the next section.
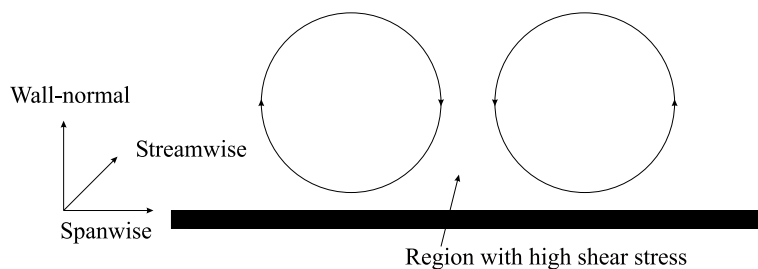
Figure 6.1: Counter-rotating vortex pair producing high shear stress regions.
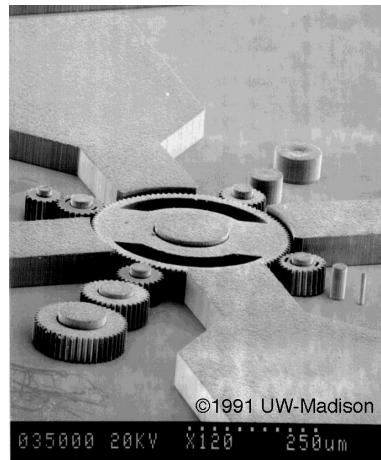
Figure 6.2: Magnetic micromotor fabricated in nickel. Reproduced by courtesy of the University of Wisconsin, Madison.

6.2 Micro-Electro-Mechanical-Systems (MEMS)

6.2.1 General Properties of MEMS

The micromachining technology that was developed over the past decade or two, opens for fabrication of sensors and actuators on the micron scale. As an example of a micromachine, Figure 6.2 shows a photograph of a micromotor. Its rotor has a diameter of about the size of a human hair. This new technology is compatible with the integrated circuit (IC) technology, so that sensors and actuators can be integrated with controller logic into devices that can perform sensing, signal processing and actuation. Thus, for decentralized control strategies, the entire detection-decision-actuation process takes place locally, minimizing the need for wiring and data communication. By integrating a large number of such devices onto one chip, real-time distributed control can be realized. These systems are referred to as micro-electro-mechanical systems (MEMS). Typical micromachined devices are on the order of 100 microns, which is one or more orders of magnitude smaller than conventional sensors and actuators [59, 60]. The small size of the devices not only allows for high spatial resolution sensing and actuation, it also permits substantially faster actuation due to the increased frequency response that follows from decreased inertia. Although technology that permits distributed control of turbulent fluid flows exists, as documented through a number of successful prototype lab experiments [54, 115], commercial off-the-shelf systems are not available at this point. Nevertheless, the impressing progress in the field of MEMS manufacturing has been a driving force for modern flow control research. In the following sections, we will review some of the devices that are designed for flow control.
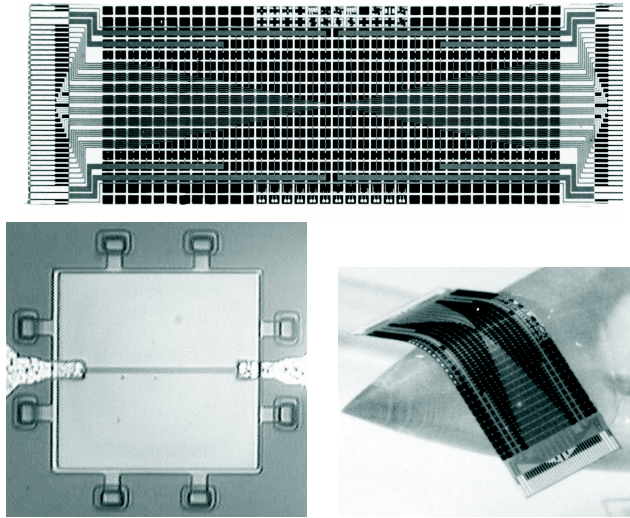
Figure 6.3: Upper picture: Flexible shear stress sensor array containing about 100 sensors. Its dimension is $1 \times 3cm^2$. Left picture: single shear stress sensor ($200 \times 200 \mu m^2$). Right picture: The flexible skin resting on a conic object. The bending is caused by gravitation. All pictures are taken from [68] and shown by courtesy of Dr. Tai of Caltech, USA.

6.2.2   Micro Sensors

Pressure Sensors

Micro pressure sensors represent the most mature application of MEMS devices [60]. [86] describes the development and testing of an array of pressure sensors for obtaining the pressure distribution in a gaseous microchannel flow. Each individual sensor has a size of $250 \times 250 \mu m^2$. For the purpose of measuring intravascular blood pressure, even smaller devices have been manufactured [89], having a size of $100 \times 150 \mu m^2$.

Shear Stress Sensors

Shear stress sensors have been fabricated in sizes of $200 \times 200 \mu m^2$ [62, 87]. Such sensors have been integrated in large numbers on single chips to provide shear stress images of two-dimensional surfaces [67, 77]. They have also been integrated in flexible skins that can be glued on to curved surfaces [68], as shown in Figure 6.3.
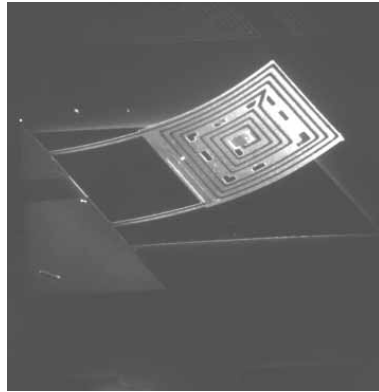
Figure 6.4: A magnetic flap for drag reduction in turbulent flows. Its dimension is $300 \times 300 \mu m^2$. The picture is taken from [114] and shown by courtesy of Dr. Tsao of Caltech, USA.

6.2.3   Micro Actuators

Pumps

For applying wall transpiration by means of suction and blowing of fluid through tiny holes in the wall, micro pumps are needed. A number of micro pumps have been developed using a wide range of actuation principles (see [113, 118] for examples). Many of them consist of a cavity, with a diaphragm that seals the cavity, and inlets and outlets which are controlled by micro valves [105]. The size of these devices vary, but are at this point in the millimeter range.

Flaps

In [114], the use of micro flaps is suggested for pushing areas of high shear stress away from the wall in order to minimize overall drag. The size of this device, shown in Figure 6.4, is $300 \times 300 \mu m^2$. An experiment using this device, in conjunction with shear stress sensors, was conducted in [54], leading to a 2.5% reduction in skin friction.

Rotating Discs

An actuation method based on rotating discs was proposed in [74]. Due to the no-slip boundary condition, small rotating discs are capable of prescribing wall normal vorticity at the wall. Thus, in conjunction with wall normal transpiration, one obtains a two-component actuation device that completely specifies the near-wall flow field in the case of incompressible flow.

6.3   Concluding Remarks

The examples of micro sensors and actuators presented above suggest that distributed control at turbulent scales will be realizable in the near future. This will provide us with a means of testing the control laws reviewed in this report in the laboratory, and will pave the road towards developing commercial flow control systems.

Chapter 7

Conclusions

The field of flow control has picked up pace over the past decade or so, on the promise of real-time distributed control on turbulent scales being realizable in the near future. This promise is due to the micromachining technology that emerged in the 1980s, and developed at an amazing speed through the 1990s. In lab experiments, so called micro-electro-mechanical systems (MEMS) that incorporate the entire detection-decision-actuation process on a single chip, have been batch processed in large numbers and assembled into flexible skins for gluing onto body-fluid interfaces for drag reduction purposes.

Control of fluid flows spans a wide variety of specialities. In this report, we have focused on two specific problems, related to flows in channels and pipes, and flows around bluff bodies: 1) Stabilization for the purpose of drag reduction or vortex shedding suppression, and; 2) Diagnostics of mixing and mixing enhancement by feedback.

Stabilization for the purpose of drag reduction or vortex shedding suppression. The control strategies used for stabilization of flows in channels and pipes include classical control, based on the Nyquist criteria, and various optimal control techniques ($\mathcal{H}_2$, $\mathcal{H}_\infty$), as well as applications of Lyapunov stability theory. The linear approaches are clearly restrictive in that they only provide local stability results. The nonlinear approaches give global stability results, but impose serious restrictions on the Reynolds number. Thus, the problem of stabilizing the parabolic equilibrium profile of channel flow in general, remains open. Nevertheless, stabilization is achieved for large Reynolds numbers in simulations.

A number of authors have studied the flow past a circular cylinder (2D) numerically, and achieved vortex shedding suppression for Reynolds numbers close the critical one, using various, quite simple, control strategies. Despite this success in simulations of the controlled Navier-Stokes equation, rigorous control designs are carried out for simplified models, such as the Ginzburg-Landau model of vortex shedding. A controller based on backstepping was shown to stabilize the Ginzburg-

Landau model for any Reynolds number.

Diagnostics of mixing and mixing enhancement by feedback. Diagnostic tools from dynamical systems theory have been presented that enable detection and quantification of chaotic transport in periodically perturbed systems. However, real systems are generally not periodic, and available measurements or simulations are finite in time. A method for quantifying mixing in finite-time velocity fields has been discussed, and applied to data obtained from simulations of the 2D controlled channel flow. Mixing has traditionally been brought on by open-loop control strategies, such as stirring, jet injection or mixing valves. Applications of active feedback to mixing problems are scarce in the literature, but the idea is currently drawing attention from various research groups. Feedback laws for the purpose of mixing enhancement in 2D and 3D pipe flow have been presented, and simulations show that they induce strong mixing.

Contributions by the author. A new boundary feedback control law for stabilization of the parabolic equilibrium flow in 2D channel flow was derived using Lyapunov stability theory. The control law feeds back from pressure measurements on the wall, to actuation in the form of wall transpiration, that is, suction and blowing of fluid across the wall. Although the analysis was valid for small Reynolds numbers, only, simulations indicate that the control is very efficient in stabilizing the flow at Reynolds numbers several orders of magnitude higher. The pressure based control law performed much better than other Lyapunov-based control laws studied.

The simple pressure-based control law derived for the 2D channel flow was generalized to the 3D pipe flow. As for the 2D channel flow, the analysis is valid for small Reynolds numbers, only. Whether or not stabilization can be obtained for higher Reynolds numbers in simulations, has not been established for this flow.

The pressure-based feedback control law derived for the 2D channel flow results in flow transients with instantaneous drag far lower than that of the corresponding laminar flow. In fact, for the first time, instantaneous total drag in a constant-mass-flow 2D channel flow has been driven to *negative* levels. The physical mechanisms by which this phenomenon occur was explained, and the possibility of achieving sustained drag reductions to below the laminar level by initiating such low-drag transients on a periodic basis was explored. The results add to the evidence that the laminar flow represents a fundamental limit to the drag reduction achievable by wall transpiration.

A state feedback controller that achieves global asymptotic stabilization of a nonlinear Ginzburg-Landau model of vortex shedding from bluff bodies was designed using backstepping. Stabilization was obtained in two steps. First, the upstream and downstream parts of the system were shown to exhibit the input-to-state stability property with respect to certain boundary input terms governed by the core flow in the vicinity of the bluff body. Second, a finite difference approximation of arbitrary order of the core flow was stabilized using the backstepping method. Consequently, all the states in the core flow were driven to zero, including the

boundary input terms of the upstream and downstream subsystems. The control design is valid for any Reynolds number, and simulations demonstrated its performance.

For the first time, active feedback control was used to enhance mixing by exploiting the natural tendency in the flow to mix. By applying the pressure-based feedback control law derived for stabilizing the 2D channel flow, with the sign of the input reversed, enhanced instability of the parabolic equilibrium flow was obtained, which led rapidly to highly complex flow patterns. The mixing enhancement was quantified using various diagnostic tools.

A Lyapunov based boundary feedback controller for achieving mixing in a 3D pipe flow governed by the Navier-Stokes equation was designed. It was shown that the control law maximizes a measure of mixing that incorporates stretching and folding of material elements, while at the same time minimizing the control effort and the sensing effort. The penalty on sensing resulted in a static *output*-feedback control law, rather than full-state feedback. A lower bound on the gain from the control effort to the mixing measure was also derived. For the open-loop system, input/output-to-state stability properties were established, which show a form of detectability of mixing in the interior of the pipe from the chosen outputs on the wall. The effectiveness of the optimal control in achieving mixing enhancement was demonstrated in numerical simulations. Simulation results also showed that the spatial changes in the control velocity were smooth and small, promising that a low number of actuators will suffice in practice.

Motivated by the mixing results in channels and pipes, a simulation study that investigated the feasibility of enhancing particle dispersion in the wake of a circular cylinder was carried out. For a subcritical case, vortex shedding was successfully provoked using feedback.

Bibliography

[1] O.M. Aamo, M. Krstić, and T.R. Bewley, "Control of mixing by boundary feedback in 2d channel flow," submitted to *Automatica*.

[2] O.M. Aamo, M. Krstić, and T.R. Bewley, "Fluid mixing by feedback in Poiseuille flow," *Proceedings of the American Control Conference*, Arlington, Virginia, USA, 2001.

[3] O.M. Aamo, A. Balogh, and M. Krstić, "Optimal mixing by feedback in pipe flow," accepted for presentation at the *15th IFAC World Congress*, Barcelona, Spain, 2002.

[4] O.M. Aamo and M. Krstić, "Global stabilization of a nonlinear Ginzburg-Landau model of vortex shedding," submitted to the *European Journal of Control*.

[5] O.M. Aamo and M. Krstić, "Backstepping design for a semi-discretized Ginzburg-Landau model of vortex shedding," submitted to the *IEEE 2002 Conference on Decision and Control*.

[6] O.M. Aamo and M. Krstić, "Feedback control of particle dispersion in bluff body wakes," in preparation.

[7] F. Abergel and R. Temam, "On some control problems in fluid mechanics," *Theoret. and Comput. Fluid Dynamics*, vol. 1, pp. 303-325, 1990.

[8] K. Akselvoll and P. Moin, "An efficient method for temporal integration of the Navier–Stokes equations in confined axisymmetric geometry," *Journal of Computational Physics,* vol. 125, pp. 454–463, 1996.

[9] B.D.O. Anderson and J.B. Moore, *Optimal Control: Linear Quadratic Methods*, Prentice-Hall, Inc. 1989.

[10] A.M. Annaswamy and A.F. Ghoniem, "Active control in combustion systems," *IEEE Control Systems*, vol. 15, no. 6, pp. 49-63, 1995.

[11] H. Aref, "Stirring by chaotic advection," *Journal of Fluid Mechanics*, vol. 143, pp. 1-21, 1984.

[12] H. Aref and G. Tryggvason, "Vortex dynamics of passive and active interfaces," *Physica D*, vol. 12, pp. 59-70, 1984.

[13] J. Baker, A. Armaou, and P.D. Christofides, "Drag reduction in incompressible channel flow using electromagnetic forcing," *Proceedings of the American Control Conference*, Chicago, Illinois, USA, 2000.

[14] A. Balogh, W-J. Liu, and M. Krstić, "Stability enhancement by boundary control in 2d channel flow–part I: Regularity of solutions," *Proceedings of the 38th Conference on Decision and Control*, Phoenix, Arizona, USA, 1999.

[15] A. Balogh, W-J. Liu, and M. Krstić, "Stability enhancement by boundary control in 2d channel flow," *IEEE Transactions on Automatic Control*, vol. 46, no. 11, pp. 1696-1711, 2001.

[16] A. Balogh, O.M. Aamo, and M. Krstić, "Optimal mixing enhancement in 3d pipe flow," submitted to *IEEE Transactions on Control Systems Technology*.

[17] B. Bamieh, F. Paganini, and M. Dahleh, "Distributed control of spatially-invariant systems," submitted to *IEEE Transactions on Automatic Control*.

[18] V. Barbu, "The time optimal control of Navier-Stokes equations," *Systems & Control Letters*, vol. 30, pp. 93-100, 1997.

[19] V. Barbu and S.S. Sritharan, "$H^{\infty}-$control theory of fluid dynamics," *R. Soc. Lond. Proc. Ser. A Math. Phys. Eng. Sci.*, vol. 454, no. 1979, pp. 3009-3033, 1998.

[20] T.R. Bewley and S. Liu, "Optimal and robust control and estimation of linear paths to transition," *Journal of Fluid Mechanics*, vol. 365, pp. 305-349, 1998.

[21] T.R. Bewley, "Flow Control: New Challenges for a New Renaissance," *Progress in Aerospace Sciences*, vol. 37, pp. 21-58, 2001.

[22] T.R. Bewley and P. Moin. Technical report TF-76, Stanford University, 1999.

[23] T.R. Bewley, P. Moin, and R. Temam, "DNS-based predictive control of turbulence: an optimal benchmark for feedback algorithms," *Journal of Fluid Mechanics*, vol. 447, pp. 179–225, 2001.

[24] T.R. Bewley, R. Temam, and M. Ziane, "A general framework for robust control in fluid mechanics," *Physica D*, vol. 138, pp. 360-392, 2000.

[25] T.R. Bewley and O.M. Aamo, "On the search for fundamental performance limitations in fluid-mechanical systems," *Proceedings of the 2002 ASME Fluids Engineering Division Summer Meeting, Montreal*, Quebec, Canada, 2002.

[26] T.R. Bewley, "Analysis of a versatile moving-belt mechanism for the control of wall-bounded flows," preprint.

[27] R.B. Bird, W.E. Stewart, and E.N. Lightfoot, *Transport Phenomena*, John Wiley & Sons, Inc., 1960.

[28] D.M. Bošković and M. Krstić, "Nonlinear stabilization of a thermal convection loop by state feedback," *Automatica*, vol. 37, no. 12, pp. 2033-40, 2001.

[29] K.M. Butler and B.F. Farrell, "Three-dimensional optimal perturbations in viscous shear flows," *Physics of Fluids A*, vol. 4, pp. 1637-1650, 1992.

[30] J. Cantwell, "Organized motion in turbulent flow," *Annual Review of Fluid Mechanics*, vol. 13, pp. 475-515, 1981.

[31] C. Canuto, M.Y. Hussaini, A. Quarteroni, and T.A. Zang, *Spectral Methods in Fluid Dynamics*. Springer-Verlag, 1988.

[32] W.-L. Chien, H. Rising, and J.M. Ottino, "Laminar mixing and chaotic mixing in several cavity flows," *Journal of Fluid Mechanics*, vol. 170, pp. 355-377, 1986.

[33] P.D. Christofides and A. Armaou, "Nonlinear control of Navier-Stokes equations," *Proceedings of the American Control Conference*, Philadelphia, Pennsylvania, 1998.

[34] J.-M. Coron, "On the controllability of the 2-D incompressible Navier-Stokes equations with the Navier slip boundary conditions," *ESAIM: Control, Optim. Cal. Var.*, vol. 1, pp. 35-75, 1996.

[35] J.-M. Coron, "On null asymptotic stabilization of the 2-D Euler equation of incompressible fluids on simply connected domains," *Prepublications 98-59 Université de Paris-Sud*, Mathematiques, 1998.

[36] L. Cortelezzi, K.H. Lee, J. Kim, and J.L. Speyer, "Skin-friction drag reduction via robust reduced-order linear feedback control," *Int. J. Comput. Fluid Dyn.*, vol. 8, no. 1-2, pp. 79-92, 1998.

[37] L. Cortelezzi and J.L. Speyer, "Robust reduced-order controller of laminar boundary layer transitions," *Physical Review E*, vol. 58, no. 2, 1998.

[38] D. D'Alessandro, M. Dahleh, and I. Mezić, "Control of fluid mixing using entropy methods," *Proceedings of the American Control Conference*, Philadelphia, Pennsylvania, 1998.

[39] D. D'Alessandro, M. Dahleh, and I. Mezić, "Control of mixing in fluid flow: A maximum entropy approach," *IEEE Transactions on Automatic Control*, vol. 44, no. 10, pp.1852-1863, 1999.

[40] H.O. Fattorini and S.S. Sritharan, "Optimal control problems with state constraints in fluid mechanics and combustion," *Appl. Math. Optim.*, vol. 38, no. 2, pp. 159-192, 1998.

[41] E. Fernández-Cara and M. González-Burgos, "A result concerning controllability for the Navier-Stokes equations," *SIAM J. Control Optim.*, vol. 33, no. 4, pp. 1061-1070, 1995.

[42] J.H. Ferziger and M. Perić, *Computational Methods for Fluid Dynamics*, Springer-Verlag, 1999.

[43] A.V. Fursikov, M.D. Gunzburger, and L.S. Hou, "Boundary value problems and optimal boundary control for the Navier-Stokes system: the two-dimensional case," *SIAM J. Control Optim.*, vol. 36, pp. 852-894, 1998.

[44] J.G. Franjione and J.M. Ottino, "Feasibility of numerical tracking of material lines and surfaces in chaotic flows," *Physics of Fluids*, vol. 30, pp. 3641-3643, 1987.

[45] G.F. Franklin, J.D. Powell, and A. Emami-Naeini, *Feedback Control of Dynamic Systems, 3rd edition,* Addison-Wesley, Inc., 1994.

[46] M. Gad-el-Hak, "Modern developments in flow control," *Appl. Mech. Rev.*, vol. 49, no. 7, pp. 365-379, 1996.

[47] M. Gad-el-Hak, *Flow Control: Passive, Active and Reactive Flow Management*, Cambridge University Press, 2000.

[48] A.F. Ghoniem and K.K. Ng, "Numerical study of the dynamics of a forced shear layer," *Physics of Fluids*, vol. 30, no. 3, pp. 706-721, 1987.

[49] M. Green and D.J.N. Limebeer, *Linear robust control*, Prentice-Hall, Inc., 1995.

[50] J. Guckenheimer and P. Holmes, *Nonlinear Oscillations, Dynamical Systems, and Bifurcations of Vector Fields*, Springer-Verlag, 1983.

[51] M.D. Gunzburger, L. Hou, and T.P. Svobodny, "A numerical method for drag minimization via the suction and injection of mass through the boundary," In *Stabilization of Flexible Structures* (ed. J.P. Zolesio), Springer-Verlag, 1990.

[52] M.D. Gunzburger (Editor), *Flow Control*, Springer-Verlag, 1995.

[53] M.D. Gunzburger and H.C. Lee, "Feedback control of Karman vortex shedding," *Transactions of the ASME*, vol. 63, pp. 828–835, 1996.

[54] B. Gupta, R. Goodman, F. Jiang, Y-C. Tai, S. Tung, and C-M. Ho, "Analog VLSI system for active drag reduction," *IEEE Micro*, October, 1996.

[55] G. Haller and A.C. Poje, "Finite time transport in aperiodic flows," *Physica D*, vol. 119, pp.352-380, 1998.

[56] G. Haller, "Finding finite-time invariant manifolds in two-dimensional velocity fields," *Chaos*, vol.10, no. 1, 2000.

[57] G. Haller and G. Yuan, "Lagrangian coherent structures and mixing in two-dimensional turbulence," *Physica D*, vol. 147, pp. 352-370, 2000.

[58] G. Haller, "Distinguished material surfaces and coherent structures in three-dimensional fluid flows," *Physica D*, vol. 149, pp. 248-277, 2001.

[59] C-M. Ho and Y-C. Tai, "REVIEW: MEMS and its applications for flow control," *Journal of Fluids Engineering*, vol. 118, pp. 437-447, 1996.

[60] C-M. Ho and Y-C. Tai, "Micro-electro-mechanical systems (MEMS) and fluid flows," *Annu. Rev. Fluid Mech.*, vol. 30, pp. 579-612, 1998.

[61] L.S. Hou and Y. Yan, "Dynamics for controlled Navier-Stokes systems with distributed controls," *SIAM J. Control Optim.*, vol. 35, no. 2, pp. 654-677, 1997.

[62] J-B. Huang, C-M. Ho, S. Tung, C. Liu, and Y-C. Tai, "Micro thermal shear stress sensor with and without cavity underneath," *Proceedings of the 8th Annual International Workshop on MEMS*, Amsterdam, 1995.

[63] P. Huerre and P.A. Monkewitz, "Local and global instabilities in spatially developing flows," *Annu. Rev. Fluid Mech.*, vol. 22, pp. 473–537, 1990.

[64] M. Högberg and T.R. Bewley, "Spatially-compact convolution kernels for decentralized control and estimation of transition in plane channel flow," preprint.

[65] O.Y. Imanuvilov, "On exact controllability for the Navier-Stokes equations," *ESAIM: Control, Optim. Cal. Var.*, vol. 3, pp. 97-131, 1998.

[66] K. Ito and S. Kang, "A dissipative feedback control synthesis for systems arising in fluid dynamics," *SIAM J. Control Optim.*, vol. 32, no. 3, pp. 831-854, 1994.

[67] F. Jiang, Y-C. Tai, B. Gupta, R. Goodman, S. Tung, J-B. Huang, and C-M. Ho, "A surface-micromachined shear stress imager," *Proceedings of the 9th Annual International Workshop on MEMS*, San Diego, USA, 1996.

[68] F. Jiang, Y-C. Tai, K. Walsh, T. Tsao, G-B. Lee, and C-M. Ho, "A flexible MEMS technology and its first application to shear stress sensor skin," *Proceedings of the 10th Annual International Workshop on MEMS*, Nagoya, Japan, 1997.

[69] J. Jiménez, "Transition to turbulence in two-dimensional Poiseuille flow," *Journal of Fluid Mechanics*, vol. 218, pp. 265-297, 1990.

[70] S.S. Joshi, J.L. Speyer, and J. Kim, "A systems theory approach to the feedback stabilization of infinitesimal and finite-amplitude disturbances in plane Poiseuille flow," *Journal of Fluid Mechanics*, vol. 332, pp. 157-184, 1997.

[71] S.S. Joshi, J.L. Speyer, and J. Kim, "Finite dimensional optimal control of Poiseuille flow," *Journal of Guidance, Control, and Dynamics*, vol. 22, no. 2, pp. 340-348, 1999.

[72] V. Jurdjevic and J.P. Quinn, "Controllability and stability," *Journal of Differential Equations*, vol. 28, pp. 381-389, 1978.

[73] S.M. Kang, V. Ryder, L. Cortelezzi, and J.L. Speyer, "State-space formulation and controller design for three-dimensional channel flows," *Proceedings of the American Control Conference*, San Diego, California, 1999.

[74] L. Keefe, "A normal vorticity actuator for near-wall modification of turbulent shear flows," *AIAA*, 1997.

[75] D.V. Khakhar, H. Rising, and J.M. Ottino, "Analysis of chaotic mixing in two model systems," *Journal of Fluid Mechanics*, vol. 172, pp. 419-451, 1986.

[76] H.K. Khalil, *Nonlinear Systems, second edition*, Prentice-Hall, Inc. 1996.

[77] M. Kimura, S. Tung, J. Lew, and C-M. Ho, "Shear stress imaging micro chip for detection of high shear stress regions," *Proceedings of the 3rd ASME/JSME Joint Fluids Engineering Conference*, San Francisco, USA, 1999.

[78] T.S. Krasnopolskaya, V.V. Meleshko, G.W.M. Peters, and H.E.H Meijer, "Mixing in Stokes flow in an annular wedge cavity," *Eur. J. Mech. B/Fluids*, 18 (1999), 793-822.

[79] M. Krichman, E.D. Sontag, and Y. Wang, "Input-output-to-state stability," *SIAM Journal on Control and Optimization*, vol. 39, no. 6, pp. 1874–1928, 2001.

[80] M. Krstić, I. Kanellakopoulos, P. V. Kokotović, *Nonlinear and Adaptive Control Design*, John Wiley & Sons, Inc., 1995.

[81] M. Krstić, "On global stabilization of Burgers' equation by boundary control," *Systems & Control Letters*, vol. 37, pp. 123-141, 1999.

[82] J.E. Lagnese, D.L. Russell, and L. White (Editors), *Control and optimal design of distributed parameter systems*, Springer-Verlag, 1995.

[83] E. Lauga and T.R. Bewley, "H_∞ control of linear global instability in models of non-parallel wakes," *Proceedings of the Second International Symposium on Turbulence and Shear Flow Phenomena*, Stockholm, Sweden, 2001.

[84] E. Lauga, private communication, 2002.

[85] C.W. Leong and J.M. Ottino, "Experiments on mixing due to chaotic advection in a cavity," *Journal of Fluid Mechanics*, vol. 209, pp. 463-499, 1989.

[86] J. Liu, Y-C. Tai, and C-M. Ho, "MEMS for pressure distribution studies of gaseous flows in microchannels," *Proceedings of the 8th Annual International Workshop on MEMS*, Amsterdam, 1995.

[87] C. Liu, J-B. Huang, Z. Zhu, F. Jiang, S. Tung, Y-C. Tai, and C-M. Ho, "A micromachined flow shear-stress sensor based on thermal transfer principles," *Journal of Microelectromechanical systems*, vol. 8, no. 1, 1999.

[88] N. Malhotra, I. Mezić, and S. Wiggins, "Patchiness: A new diagnostic for Lagrangian trajectory analysis in time-dependent fluid flows," *International Journal of Bifurcation and Chaos*, vol. 8, no. 6, pp. 1053-1093, 1998.

[89] P. Melvås, E. Kälvesten, and G. Stemme, "A surface micromachined resonant beam pressure sensor," *Proceedings of the 14th Annual Conference on MEMS*, Interlaken, Switzerland, 2001.

[90] I. Mezić, *On geometrical and statistical properties of dynamical systems: Theory and applications*, Ph.D. thesis, California Institute of Technology, 1994.

[91] I. Mezić and S. Wiggins, "A method for visualization of invariant sets of dynamical systems based on the ergodic partition," *Chaos*, vol. 9, no. 1, pp.213-218, 1999.

[92] I. Mezić, "Nonlinear dynamics and ergodic theory methods in control of fluid flows: theory and applications," *Proceedings of the 2001 AFOSR Workshop on Dynamics and Control*, 2001.

[93] P.D. Miller, C.K.R.T. Jones, A.M. Rogerson, and L.J. Pratt, "Quantifying transport in numerically generated velocity fields," *Physica D*, vol. 110, pp. 105-122, 1997.

[94] B.R. Noack, I. Mezić, and A. Banaszuk, "Controlling vortex motion and chaotic advection," *Proceedings of the 39th IEEE Conference on Decision and Control*, Sydney, Australia, December 11-15, 2000.

[95] S.A. Orzag, "Accurate solution of the Orr-Sommerfeld stability equation," *Journal of Fluid Mechanics*, vol. 50, part 4, pp. 689-703, 1971.

[96] J.M. Ottino, *The kinematics of mixing: stretching, chaos, and transport*, Cambridge University Press, 1989.

[97] J.M. Ottino, "Mixing, chaotic advection, and turbulence," *Annu. Rev. Fluid Mech.*, vol. 22, pp. 207-53, 1990.

[98] R.L. Panton, *Incompressible flow, Second Edition*, John Wiley & Sons, Inc., 1996.

[99] D.S. Park, D.M. Ladd, and E.W. Hendricks, "Feedback control of von Kármán vortex shedding behind a circular cylinder at low Reynolds numbers," *Physics of Fluids*, vol. 6, no. 7, pp. 2390–2405, 1994.

[100] A.C. Poje, G. Haller, and I. Mezić, "The geometry and statistics of mixing in aperiodic flows," *Physics of Fluids*, vol. 11, no. 10, 1999.

[101] A.C. Poje and G. Haller, "Geometry of cross-stream mixing in a double-gyre ocean model," *Journal of Physical Oceanography*, vol. 29, pp. 1469-1665, 1999.

[102] V. Rom-Kedar, A. Leonard, and S. Wiggins, "An analytical study of transport, mixing and chaos in an unsteady vortical flow," *Journal of Fluid Mechanics*, vol. 214, pp. 347-394, 1990.

[103] K. Roussopoulos and P. A. Monkewitz, "Nonlinear modelling of vortex shedding control in cylinder wakes," *Physica D*, 97, pp. 264–273, 1996.

[104] B.L. Rozhdestvensky and I.N. Simakin, "Secondary flows in a plane channel: their relationship and comparison with turbulent flows," *Journal of Fluid Mechanics*, vol. 147, pp. 261-289, 1984.

[105] M.T.A. Saif, B.E. Alaca, and H. Sehitoglu, "Analytical modeling of electrostatic membrane actuator for micro pumps," *IEEE Journal of Microelectromechanical Systems*, vol. 8, no. 3, pp. 335-345, 1999.

[106] S. Skogestad and I. Postlethwaite, *Multivariable Feedback Control, Analysis and Design*, John Wiley & Sons, Inc., 1996.

[107] E.D. Sontag and Y. Wang, "Output-to-state stability and detectability of nonlinear systems," *Systems & Control Letters*, vol. 29, pp. 279–290, 1997.

[108] E.D. Sontag, "Comments on integral variants of ISS," *Systems & Control Letters*, vol. 34, pp. 93–100, 1998.

[109] S.S. Sritharan, "Dynamic programming of the Navier-Stokes equations," *Systems & Control Letters*, vol. 16, pp. 299-307, 1991.

[110] S.S. Sritharan, "Optimal control of viscous flows." *SIAM*, 1998.

[111] P.D. Swanson and J.M. Ottino, "A comparative computational and experimental study of chaotic mixing of viscous fluids," *Journal of Fluid Mechanics*, vol. 213, pp. 227-249, 1990.

[112] A.A. Ten, Y.Y. Podladchikov, D.A. Yuen, T.B. Larsen, and A.V. Malevsky, "Comparison of mixing properties in convection with the particle-line method," *Geophys. Res. Lett.*, vol. 25, pp. 3205-3208, 1998.

[113] J-H. Tsai and L. Lin, "A thermal bubble actuated micro nozzle-diffuser pump," *Proceedings of the 14th Annual Conference on MEMS*, Interlaken, Switzerland, 2001.

[114] T. Tsao, C. Liu, Y.C. Tai, and C.M. Ho, "Micromachined magnetic actuators for active fluid control," *ASME Application of Microfabrication to Fluid Mechanics*, Chicago, November 6-11, 1994.

[115] T. Tsao, F. Jiang, R. Miller, Y-C. Tai, B. Gupta, R. Goodman, S. Tung, and C-M. Ho, "An integrated MEMS system for turbulent boundary layer control," *Proceedings of the 1997 International Conference on Solid-State Sensors and Actuators*, Chicago, June 16-19, 1997.

[116] S. Wiggins, *Introduction to Applied Nonlinear Dynamical Systems and Chaos*, Springer-Verlag, 1990.

[117] S. Wiggins, *Chaotic Transport in Dynamical Systems*, Springer-Verlag, 1992.

[118] K-S. Yun, I-J. Cho, J-U. Bu, G-H. Kim, Y-S. Jeon, C-J. Kim, and E. Yoon, "A micropump driven by continuous electorwetting actuation for low voltage and low power operations," *Proceedings of the 14th Annual Conference on MEMS*, Interlaken, Switzerland, 2001.

[119] K. Zhou, J.C. Doyle, and K. Glover, *Robust Optimal Control*, Prentice-Hall, Inc., 1995.

Part II

Modelling and Control of Marine Structures

Chapter 8

Modelling and Control of Moored Vessels

8.1 Introduction

Position mooring systems (PM) have been commercially available since the late 1980's, and have proven to be a cost-effective alternative to permanent platforms for offshore oil production. The current research on PM systems is based on the experience obtained from research on dynamic positioning (DP) systems since the 1970's [14]. DP systems based on optimal control theory and Kalman-filtering were proposed in [7], and extended in [8, 9, 24, 25, 26, 44, 45]. In recent years, nonlinear controllers have been developed for DP systems based on integrator backstepping techniques, see [4, 20, 22, 43].

PM systems differ from DP systems in that thruster assistance is used mainly for damping the surge, sway and yaw motions and for keeping the desired heading, whereas the position is kept within an acceptable region by the mooring lines [48]. Thus, fuel consumption is kept to a minimum in normal weather conditions. In rough weather conditions, thruster assistance may be needed for position keeping in order to avoid line tensions rising above safety limits. In [46], a model for the mooring system based on line characteristics found by solving the catenary equations is presented and the optimal controller derived in [45] is extended for this system. In the last few years, more advanced controllers, based on observer backstepping and locally optimal backstepping have been developed in [48, 47].

In traditional testing of the performance of PM systems by means of computer simulations, tabulated static solutions of the cable equation have been coupled to the vessel dynamics. This approach is adequate for shallow waters. However, in deeper waters, dynamic interactions between the vessel and mooring system renders such a quasi-static approach inaccurate [39].

Models and software packages that solve the cable equation by means of the finite

element method (FEM) are readily available (see for instance [11, 32, 37]). However, such general purpose FEM packages are not suited for control system design, and usually slower than software tailored for a given application. Moreover, the theoretical aspects, such as existence and uniqueness of solutions, are often taken for granted. In fact, FEM tools were developed and used, for instance in structural engineering, decades before a sound theoretical foundation was established [49].

In this chapter, a new finite element model of a cable suspended in water is derived. The hydrodynamic loads on the cable are modelled according to *Morison's equation* (see for instance [18]), and are assumed to dominate internal damping, or friction. In other applications, such as space tether systems, where there is practically no external damping involved, internal damping may be important [10]. Furthermore, bending and torsional stiffness are assumed to be negligible. Several authors, dealing with other applications, include bending stiffness in order to avoid the numerical singularity that occurs for zero tension (see for instance [15, 16, 27]). Since mooring cables are pretensioned to avoid the occurrence of zero tension, including bending and torsional stiffness in the model would only serve to increase implementation complexity and computation time.

For a slightly simplified equation describing the motion of a cable having negligible added mass and supported by fixed end-points, we show global existence and uniqueness of solutions of the truncated system, and conjecture a global result for the initial-boundary value problem. The FEM model for the cable is assembled to give a model of a multi-cable mooring system, which, in turn, is coupled to a rigid body model of the floating vessel. The result is a coupled dynamical model of a moored vessel, which can be applied to applications such as turret-based moored ships, or tension leg platforms.

We end this chapter with simulations demonstrating the importance of a full dynamical analysis, as opposed to a quasi-steady approach, for a turret-based moored oil production ship operating in deep waters. The simulations are in agreement with the conclusions in [39]. As a simple application of the simulator, controlling the line tensions dynamically is investigated as an additional means of station keeping.

This chapter is based on [1, 2].

8.2   Mathematical Modelling

8.2.1   Vessel Kinematics

Two reference frames are defined as follows, see Figure 8.1:

- The Earth-fixed frame, denoted $X_E Y_E Z_E$, is placed so that the $X_E Y_E$ plane coincides with the water surface, and the Z_E axis is positive downwards. In vessel positioning applications, the X_E axis is usually chosen to point along the desired heading of the vessel, and the origin is usually placed at the desired position of the vessel.
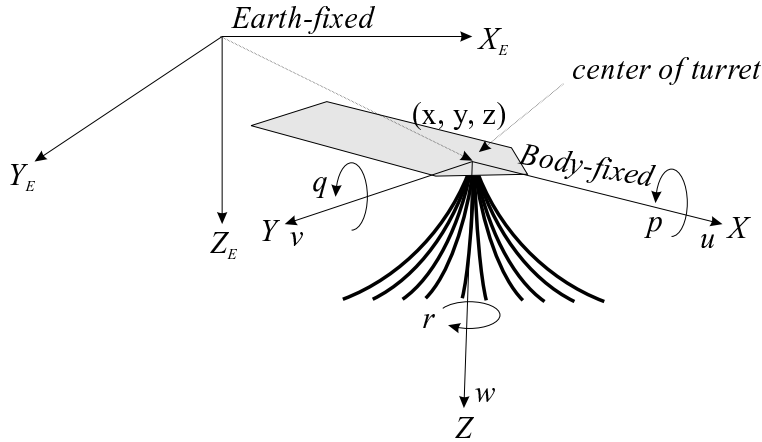
Figure 8.1: Earth-fixed $(X_E Y_E Z_E)$ and body-fixed (XYZ) reference frames.

- The body-fixed frame, denoted XYZ, is fixed to the vessel body, usually in such a way that the origin coincides with the center of gravity. In the case of turret-moored ships, it is common to place the origin at the center of turret, with the X axis directed from aft to fore along the longitudinal axis of the vessel, and the Y axis directed to starboard.

The vessel position and orientation in the Earth-fixed frame are defined by the vectors, $\eta_1 \triangleq [\ x \quad y \quad z\ ]^T \in \mathbb{R}^3$ and $\eta_2 \triangleq [\ [\ \phi \quad \theta \quad \psi\ ]\ ]^T \in \mathbb{S}^3$, respectively ($\mathbb{R}^3$ is the Euclidean space of dimension three, and $\mathbb{S}^3$ is the torus of dimension three). The body-fixed surge, sway and heave translational velocities are defined by the vector $\nu_1 \triangleq [\ u \quad v \quad w\ ]^T \in \mathbb{R}^3$, and the body-fixed roll, pitch and yaw angular velocities are defined by the vector $\nu_2 \triangleq [\ p \quad q \quad r\ ]^T \in \mathbb{R}^3$. The body-fixed velocities are transformed to the Earth-fixed frame by means of the transformation matrices, $\mathbf{J}_1(\eta_2)$ and $\mathbf{J}_2(\eta_2)$, that is

$$\begin{aligned}
\dot{\eta}_1 &= \mathbf{J}_1(\eta_2)\nu_1 \\
\dot{\eta}_2 &= \mathbf{J}_2(\eta_2)\nu_2
\end{aligned}$$

$\mathbf{J}_1(\eta_2)$ is a rotation matrix, given by

$$\mathbf{J}_1(\eta_2) = \mathbf{C}_{z,\psi}^T \mathbf{C}_{y,\theta}^T \mathbf{C}_{x,\phi}^T \in \mathbb{SO}(3)$$

where the matrix $\mathbf{C}_{a,\alpha}$ is the rotation of α radians about the a-axis ($\mathbb{SO}(3)$ is the proper orthogonal group of transformations on $\mathbb{R}^3$). The matrix $\mathbf{J}_2(\eta_2)$ is given by

$$\mathbf{J}_2(\eta_2) = \begin{bmatrix} 1 & \sin\phi\tan\theta & \cos\phi\tan\theta \\ 0 & \cos\phi & -\sin\phi \\ 0 & \sin\phi/\cos\theta & \cos\phi/\cos\theta \end{bmatrix}, \quad \cos\theta \neq 0$$

8.2.2   Vessel Dynamics

The motion of a free-floating vessel in 6 degrees of freedom, can be described by [19]:

$$\mathbf{M}\dot{\nu} + \mathbf{C}(\nu)\nu + \mathbf{D}(\nu)\nu + \mathbf{g}(\eta) = \tau_M + \tau_E + \tau \qquad (8.1)$$

$$\dot{\eta} = \mathbf{J}(\eta)\nu$$

where we have defined

$$\eta \triangleq \left[\begin{array}{c} \eta_1 \\ \eta_2 \end{array} \right], \quad \nu \triangleq \left[\begin{array}{c} \nu_1 \\ \nu_2 \end{array} \right], \quad \mathbf{J}(\eta) \triangleq \left[\begin{array}{cc} \mathbf{J}_1(\eta_2) & \mathbf{0} \\ \mathbf{0} & \mathbf{J}_2(\eta_2) \end{array} \right]$$

$\mathbf{M}$ is the inertia matrix, including hydrodynamic added inertia, $\mathbf{C}$ is the Coriolis and centripetal matrix, $\mathbf{D}$ is the damping matrix, and $\mathbf{g}(\eta)$ is the restoring forces and torques. τ_E constitutes environmental forces and torques, inflicted from winds, currents and waves, τ_M is mooring forces and torques, and τ is propulsion forces and torques.

8.2.3   PDE for the Cable Dynamics

The equation of motion of a cable with negligible bending and torsional stiffness is given by, see for instance [52]:

$$\rho_0 \frac{\partial \vec{\mathbf{v}}(t,s)}{\partial t} = \frac{\partial}{\partial s}(T(t,s)\vec{\mathbf{t}}(t,s)) + \vec{\mathbf{f}}(t,s)(1 + e(t,s))$$

where t is the time variable, and $s \in [0, L]$, $\vec{\mathbf{v}} : [t_0, \infty) \times [0, L] \to \mathbb{R}^3$ and $\vec{\mathbf{t}} : [t_0, \infty) \times [0, L] \to \mathbb{R}^3$ are distance along the unstretched cable, velocity and tangential vector, respectively. L is the length of the unstretched cable, ρ_0 is mass per unit length of unstretched cable, $T : [t_0, \infty) \times [0, L] \to \mathbb{R}$ is tension, $e : [t_0, \infty) \times [0, L] \to \mathbb{R}$ is strain and $\vec{\mathbf{f}} : [t_0, \infty) \times [0, L] \to \mathbb{R}^3$ is the sum of external forces (per unit length of unstreched cable) acting on the cable. By introducing the position vector $\vec{\mathbf{r}} : [t_0, \infty) \times [0, L] \to \mathbb{R}^3$, we get $\vec{\mathbf{t}} = \frac{1}{1+e}\frac{\partial \vec{\mathbf{r}}}{\partial s}$ such that

$$\rho_0 \frac{\partial^2 \vec{\mathbf{r}}}{\partial t^2} = \frac{\partial}{\partial s}\left(\frac{T}{1+e}\frac{\partial \vec{\mathbf{r}}}{\partial s} \right) + \vec{\mathbf{f}}(1 + e)$$

Applying *Hooke's law* yields

$$\rho_0 \frac{\partial^2 \vec{\mathbf{r}}}{\partial t^2} = \frac{\partial}{\partial s}\left(EA_0 \frac{e}{1+e}\frac{\partial \vec{\mathbf{r}}}{\partial s} \right) + \vec{\mathbf{f}}(1 + e)$$

where E is *Young's modulus* and A_0 is the cross-sectional area of the unstretched cable.

External forces

In addition to gravity, a submerged cable is subject to hydrostatic and hydrodynamic forces, i.e.

$$\vec{\mathbf{f}} = \vec{\mathbf{f}}_{(hg)} + \vec{\mathbf{f}}_{(dt)} + \vec{\mathbf{f}}_{(dn)} + \vec{\mathbf{f}}_{(mn)}$$

where $\vec{\mathbf{f}}_{(hg)}$ constitutes the buoyancy (gravity and hydrostatic) force per unit length of unstretched cable, $\vec{\mathbf{f}}_{(dt)}$ and $\vec{\mathbf{f}}_{(dn)}$ are tangential and normal hydrodynamic drag, respectively, per unit length of unstretched cable and $\vec{\mathbf{f}}_{(mn)}$ is the hydrodynamic inertia force per unit length of unstretched cable.

Gravity and hydrostatic forces   It is assumed that we can regard each element of the cable as completely surrounded by water so that

$$\vec{\mathbf{f}}_{(hg)} = \rho_0 \frac{\rho_c - \rho_w}{(1 + e)\rho_c} \vec{\mathbf{g}}$$

where $\vec{\mathbf{g}} \in \mathbb{R}^3$ is the gravitational acceleration, ρ_c is density of the cable and ρ_w is density of the ambient water.

Hydrodynamic forces   From *Morison's equation*, we get the following expression for hydrodynamic drag per unit length of unstretched cable

$$
\begin{aligned}
\vec{\mathbf{f}}_{(dt)} &= -\frac{1}{2} C_{DT} d \rho_w \left| \vec{\mathbf{v}} \cdot \vec{\mathbf{t}} \right| (\vec{\mathbf{v}} \cdot \vec{\mathbf{t}}) \vec{\mathbf{t}} = -\frac{1}{2} C_{DT} d \rho_w \left| \vec{\mathbf{v}}_t \right| \vec{\mathbf{v}}_t \\
\vec{\mathbf{f}}_{(dn)} &= -\frac{1}{2} C_{DN} d \rho_w \left| \vec{\mathbf{v}} - (\vec{\mathbf{v}} \cdot \vec{\mathbf{t}}) \vec{\mathbf{t}} \right| (\vec{\mathbf{v}} - (\vec{\mathbf{v}} \cdot \vec{\mathbf{t}}) \vec{\mathbf{t}}) = -\frac{1}{2} C_{DN} d \rho_w \left| \vec{\mathbf{v}}_n \right| \vec{\mathbf{v}}_n
\end{aligned}
$$

where C_{DT} and C_{DN} are tangential and normal drag coefficients for the cable, respectively, and d is the cable diameter. The hydrodynamic added inertia force per unit length of unstretched cable is given by

$$\vec{\mathbf{f}}_{(mn)} = -C_{MN} \frac{\pi d^2}{4} \rho_w (\vec{\mathbf{a}} - (\vec{\mathbf{a}} \cdot \vec{\mathbf{t}}) \vec{\mathbf{t}}) = -C_{MN} \frac{\pi d^2}{4} \rho_w \vec{\mathbf{a}}_n$$

where C_{MN} is a hydrodynamic mass coefficient and $\vec{\mathbf{a}} : [t_0, \infty) \times [0, L] \to \mathbb{R}^3$ is the acceleration. The subscripts n and t on $\vec{\mathbf{v}}$ and $\vec{\mathbf{a}}$ denote decompositions into the normal and tangential directions, respectively. The motion of slender structures, such as the mooring lines we are considering here, is drag-force dominated, as illustrated in Figure 8.2, taken from [18, page 11]. The diameter of a mooring line is in the order of 10 cm, so for wave heights larger than 1 m, Figure 8.2 shows that viscous forces dominate. However, mooring systems for ships operating in deep waters may consist of cables of light materials, sometimes not much heavier than water. In this case, added mass is important. Thus, we will keep the added mass term in the following derivations, but remark that it may be neglected in certain applications, as shown in Figure 8.2.
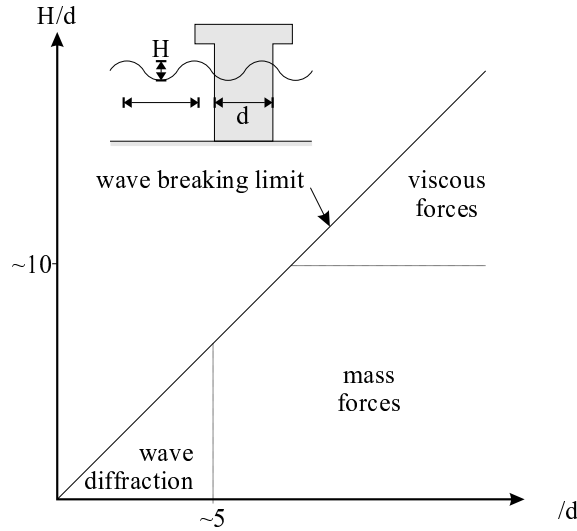
Figure 8.2: Relative importance of mass, viscous drag and diffraction forces on marine structures. Taken from [18, page 11].

Formulation of the initial-boundary value problem   We have the following initial-boundary value problem

$$\rho_0 \frac{\partial^2 \vec{\mathbf{r}}}{\partial t^2} - \frac{\partial}{\partial s} \left(EA_0 \frac{e}{1+e} \frac{\partial \vec{\mathbf{r}}}{\partial s} \right) - (1+e) \left(\vec{\mathbf{f}}_{(hg)} + \vec{\mathbf{f}}_{(dt)} + \vec{\mathbf{f}}_{(dn)} + \vec{\mathbf{f}}_{(mn)} \right) = 0 \quad (8.2)$$

with boundary conditions

$$\vec{\mathbf{r}}(t, 0) = \vec{\mathbf{r}}_0(0), \quad \vec{\mathbf{r}}(t, L) = \vec{\mathbf{r}}_0(L), \quad \text{for all } t \geq t_0$$

and initial conditions

$$\vec{\mathbf{r}}(t_0, s) = \vec{\mathbf{r}}_0(s), \quad \vec{\mathbf{v}}(t_0, s) = \vec{\mathbf{v}}_0(s)$$

Here, $\vec{\mathbf{r}}_0 : [0, L] \to \mathbb{R}^3$ and $\vec{\mathbf{v}}_0 : [0, L] \to \mathbb{R}^3$ are initial cable configuration and initial cable velocity, respectively.

8.2.4   Discretization into Finite Elements

Discretization of the initial-boundary value problem is performed using the Galerkin method and finite elements. This method consists of the following steps

1. The initial-boundary value problem (8.2) is transformed into the corresponding *generalized problem*. This is done by multiplying the equation by the

functions $\vec{\mathbf{w}} \in \mathcal{V}$, and then integrating by parts over $[0, L]$. $\mathcal{V}$ is a suitable space of functions in which to search for a solution.

2. Restriction of $\vec{\mathbf{r}}$ and $\vec{\mathbf{w}}$ to appropriate finite-dimensional subspaces of $\mathcal{V}$, yields the Galerkin method.

3. Choosing the finite-dimensional subspaces such that they are spanned by bases consisting of so-called finite elements, yields a particularly simple set of ordinary differential equations. This is the finite element method.

Generalized problem

We seek a function $\vec{\mathbf{r}} \in \mathcal{V}$ such that

$$
\int_0^L \left(\rho_0 \frac{\partial^2 \vec{\mathbf{r}}}{\partial t^2} - \frac{\partial}{\partial s} \left(E A_0 \frac{e}{1+e} \frac{\partial \vec{\mathbf{r}}}{\partial s} \right) - \vec{\mathbf{f}}(1+e) \right) \cdot \vec{\mathbf{w}} \, ds = 0, \quad \forall t \geq t_0, \quad \forall \vec{\mathbf{w}} \in \mathcal{V} \quad (8.3)
$$

Integrating the second term in (8.3) by parts yields

$$
\int_0^L \left(\rho_0 \frac{\partial^2 \vec{\mathbf{r}}}{\partial t^2} \cdot \vec{\mathbf{w}} + E A_0 \frac{e}{1+e} \frac{\partial \vec{\mathbf{r}}}{\partial s} \cdot \frac{\partial \vec{\mathbf{w}}}{\partial s} - (1+e) \vec{\mathbf{f}} \cdot \vec{\mathbf{w}} \right) ds -
$$

$$
\left[E A_0 \frac{e}{1+e} \frac{\partial \vec{\mathbf{r}}}{\partial s} \cdot \vec{\mathbf{w}} \right]_0^L = 0, \quad \forall t \geq t_0, \quad \forall \vec{\mathbf{w}} \in \mathcal{V} \quad (8.4)
$$

Equation (8.4) is the *generalized problem*.

Galerkin projection

The cable is uniformly partitioned into n segments of length $l = L/n$, and the nodal points are enumerated from 0 to n, as shown in Figure 8.3. Thus, the endpoints of element k are the nodes $k-1$ and k. Let $\mathbb{V}_n$ be a $3 \times (n+1)$-dimensional subspace of $\mathcal{V}$. Using the Galerkin principle, we seek a function $\vec{\mathbf{r}}_n : [t_0, \infty) \times [0, L] \rightarrow \mathbb{R}^3$ such that $\vec{\mathbf{r}}_n \in \mathbb{V}_n$ and satisfies

$$
\int_0^L \left(\rho_0 \frac{\partial^2 \vec{\mathbf{r}}_n}{\partial t^2} \cdot \vec{\mathbf{w}} + E A_0 \frac{e}{1+e} \frac{\partial \vec{\mathbf{r}}_n}{\partial s} \cdot \frac{\partial \vec{\mathbf{w}}}{\partial s} - (1+e) \vec{\mathbf{f}} \cdot \vec{\mathbf{w}} \right) ds -
$$

$$
\left[E A_0 \frac{e}{1+e} \frac{\partial \vec{\mathbf{r}}_n}{\partial s} \cdot \vec{\mathbf{w}} \right]_0^L = 0, \quad \forall t \geq t_0, \quad \forall \vec{\mathbf{w}} \in \mathbb{V}_n \quad (8.5)
$$

Let $(\mathbf{e}_1, \mathbf{e}_2, \mathbf{e}_3)$ be an orthonormal basis for $\mathbb{R}^3$, and define $\varphi_i : [0, L] \rightarrow [0, 1]$ as follows, see Figure 8.4:

$$
\varphi_i(s) = \begin{cases} 0 & s < (i-1)l \\ \frac{1}{l} s - (i-1) & (i-1)l \leq s < il \\ -\frac{1}{l} s + i + 1 & il \leq s < (i+1)l \\ 0 & (i+1)l \leq s \end{cases} , \quad i = 0, 1, 2, ..., n
$$
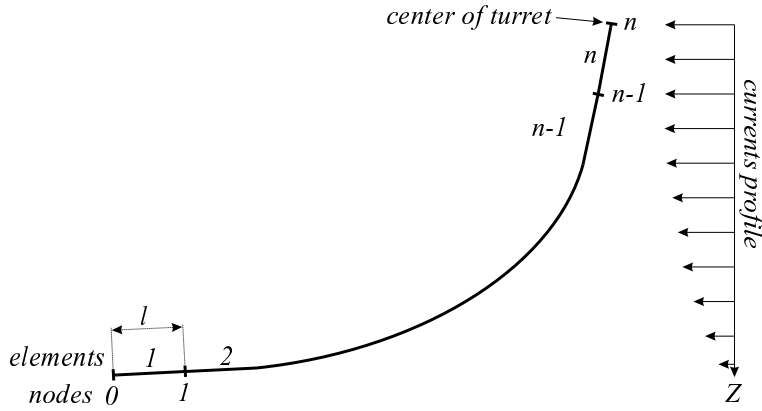
Figure 8.3: Cable configuration with nodal and element indexing.

We now define $\mathbb{V}_n$ as the span of $\{\phi_{ij}\} = \{\varphi_i \mathbf{e}_j\}$, $i = 0, 1, 2, ..., n$, $j = 1, 2, 3$, $\phi_{ij} : [0, L] \rightarrow \mathbb{R}^3$. Note that $\phi_{ij} \perp \phi_{km}$ when $j \neq m$ or $|i - k| > 1$. Thus, $\{\phi_{ij}\}$ is an *almost* orthogonal basis for $\mathbb{V}_n$, with non-zero inner product for adjacent elements only. The unknown solution can now be expanded in terms of the basis functions

$$\vec{\mathbf{r}}_n(t, s) = \sum_{j=1}^{3} \sum_{i=0}^{n} (\mathbf{r}_i(t) \cdot \mathbf{e}_j)\phi_{ij}(s) = \sum_{i=0}^{n} \mathbf{r}_i(t)\varphi_i(s) \qquad (8.6)$$

It follows from the particular choice of basis that the unknown parameters, $\mathbf{r}_i(t) : [t_0, \infty) \rightarrow \mathbb{R}^3$, in (8.6) are exactly the value of the unknown solution, $\vec{\mathbf{r}}_n(t, s)$, at the nodes, i.e., they are nodal position vectors. Since every trial function $\vec{\mathbf{w}} \in \mathbb{V}_n$ is a linear combination of the basis functions, and, since $\mathbf{r}_0(t)$ and $\mathbf{r}_n(t)$ are given by the boundary conditions, it suffices to apply Galerkin's principle to the basis functions $\{\phi_{km}\}$, for $k = 1, 2, 3, ..., n - 1$ and $m = 1, 2, 3$. This yields

$$\int_0^L \left[\sum_{i=0}^{n} \left(\rho_0 \frac{\partial^2 \mathbf{r}_i}{\partial t^2} \varphi_i \varphi_k + E A_0 \frac{e}{1 + e} \mathbf{r}_i \left(\frac{\partial \varphi_i}{\partial s} \frac{\partial \varphi_k}{\partial s} \right) \right) - (1 + e)\varphi_k \mathbf{f} \right] ds$$

$$-E A_0 \sum_{i=0}^{n} \left[\frac{e}{1 + e} \mathbf{r}_i \frac{\partial \varphi_i}{\partial s} \varphi_k \right]_0^L = 0, \quad k = 1, 2, ..., n - 1 \qquad (8.7)$$

Using orthogonality of the basis functions, and noting that the last term in (8.7) vanishes, we get

$$\sum_{i=k-1}^{k+1} \left(\rho_0 \frac{\partial^2 \mathbf{r}_i}{\partial t^2} \int_0^L \varphi_i \varphi_k \, ds + E A_0 \mathbf{r}_i \int_0^L \frac{e}{1 + e} \left(\frac{\partial \varphi_i}{\partial s} \frac{\partial \varphi_k}{\partial s} \right) ds \right) \qquad (8.8)$$

$$= \int_0^L \mathbf{f}(1 + e)\varphi_k \, ds, \quad k = 1, 2, ..., n - 1$$
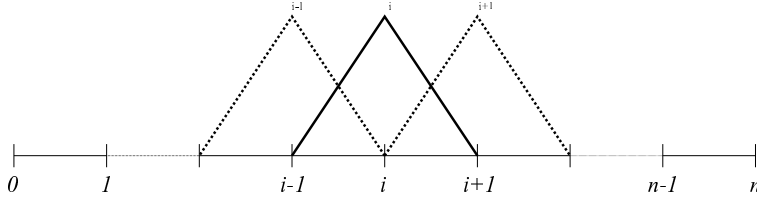
Figure 8.4: The shape of the φ-functions yields an *almost* orthogonal basis.

For the strain, $e(t, s)$, we have the following

$$
e(t, s) \;=\; \left| \frac{\partial}{\partial s} \sum_{i=0}^{n} \mathbf{r}_i(t)\varphi_i(s) \right| - 1 = \frac{1}{l}\,|\mathbf{r}_k(t) - \mathbf{r}_{k-1}(t)| - 1 \triangleq e_k(t)
$$
$$
\text{for } s \;\in\; ((k-1)l,\, kl],\;\; k = 1, 2, ..., n
$$

which shows that the strain is constant within each element. Evaluation of the integrals in (8.8) gives the following set of $3 \times (n-1)$ 2nd-order ordinary differential equations, called the *Galerkin equation*

$$
\frac{\rho_0 l}{6}\left(\ddot{\mathbf{r}}_{k-1} + 4\ddot{\mathbf{r}}_k + \ddot{\mathbf{r}}_{k+1} \right) + E A_0 \left[\frac{e_k}{\varepsilon_k}\mathbf{l}_k - \frac{e_{k+1}}{\varepsilon_{k+1}}\mathbf{l}_{k+1} \right] =
$$
$$
\int_0^L \left(\vec{\mathbf{f}}_{(hg)} + \vec{\mathbf{f}}_{(dt)} + \vec{\mathbf{f}}_{(dn)} + \vec{\mathbf{f}}_{(mn)} \right)(1 + e)\varphi_k\,ds \qquad\qquad (8.9)
$$
$$
k = 1, 2, ..., n-1
$$

where

$$
\mathbf{l}_k \;=\; \mathbf{r}_k - \mathbf{r}_{k-1}
$$
$$
e_k \;=\; \frac{1}{l}\,|\mathbf{r}_k - \mathbf{r}_{k-1}| - 1 = \frac{|\mathbf{l}_k|}{l} - 1
$$
$$
\varepsilon_k \;=\; l(1 + e_k) = |\mathbf{l}_k|
$$
$$
\int_0^L \vec{\mathbf{f}}_{(hg)}(1 + e)\varphi_k\,ds \;=\; l\rho_0\frac{\rho_c - \rho_w}{\rho_c}\begin{bmatrix} 0 & 0 & g \end{bmatrix}^T
$$

and

$$
\int_0^L \vec{\mathbf{f}}_{(dt)}(1 + e)\varphi_k\,ds = -\frac{1}{2}C_{DT}d\rho_w\,\{
$$

$$
\frac{1}{l\varepsilon_k^2}\int_{(k-1)l}^{kl} |(\dot{\mathbf{r}}_{k-1}\varphi_{k-1} + \dot{\mathbf{r}}_k\varphi_k)\cdot\mathbf{l}_k|\,[(\dot{\mathbf{r}}_{k-1}\varphi_{k-1} + \dot{\mathbf{r}}_k\varphi_k)\cdot\mathbf{l}_k]\,\mathbf{l}_k\varphi_k\,ds
$$

$$+ \frac{1}{l\varepsilon_{k+1}^2} \int\limits_{kl}^{(k+1)l} |(\dot{\mathbf{r}}_k \varphi_k + \dot{\mathbf{r}}_{k+1} \varphi_{k+1}) \cdot \mathbf{l}_{k+1}|$$

$$[(\dot{\mathbf{r}}_k \varphi_k + \dot{\mathbf{r}}_{k+1} \varphi_{k+1}) \cdot \mathbf{l}_{k+1}] \mathbf{l}_{k+1} \varphi_k \, ds \}$$

and

$$\int\limits_0^L \vec{\mathbf{f}}_{(dn)} (1+e) \varphi_k \, ds = -\frac{1}{2} C_{DN} d \rho_w \{$$

$$\frac{\varepsilon_k}{l} \int\limits_{(k-1)l}^{kl} \left| \dot{\mathbf{r}}_{k-1} \varphi_{k-1} + \dot{\mathbf{r}}_k \varphi_k - \frac{(\dot{\mathbf{r}}_{k-1} \varphi_{k-1} + \dot{\mathbf{r}}_k \varphi_k) \cdot \mathbf{l}_k}{\varepsilon_k^2} \mathbf{l}_k \right|$$

$$\left(\dot{\mathbf{r}}_{k-1} \varphi_{k-1} + \dot{\mathbf{r}}_k \varphi_k - \frac{(\dot{\mathbf{r}}_{k-1} \varphi_{k-1} + \dot{\mathbf{r}}_k \varphi_k) \cdot \mathbf{l}_k}{\varepsilon_k^2} \mathbf{l}_k \right) \varphi_k \, ds$$

$$+ \frac{\varepsilon_{k+1}}{l} \int\limits_{kl}^{(k+1)l} \left| \dot{\mathbf{r}}_k \varphi_k + \dot{\mathbf{r}}_{k+1} \varphi_{k+1} - \frac{(\dot{\mathbf{r}}_k \varphi_k + \dot{\mathbf{r}}_{k+1} \varphi_{k+1}) \cdot \mathbf{l}_{k+1}}{\varepsilon_{k+1}^2} \mathbf{l}_{k+1} \right|$$

$$\left(\dot{\mathbf{r}}_k \varphi_k + \dot{\mathbf{r}}_{k+1} \varphi_{k+1} - \frac{(\dot{\mathbf{r}}_k \varphi_k + \dot{\mathbf{r}}_{k+1} \varphi_{k+1}) \cdot \mathbf{l}_{k+1}}{\varepsilon_{k+1}^2} \mathbf{l}_{k+1} \right) \varphi_{k+1} \, ds \}$$

and

$$\int\limits_0^L \vec{\mathbf{f}}_{(mn)} (1+e) \varphi_k \, ds = -C_{MN} \frac{\pi d^2}{4} \rho_w \{$$

$$\frac{1}{6} \left[\varepsilon_k \ddot{\mathbf{r}}_{k-1} + 2(\varepsilon_k + \varepsilon_{k+1}) \ddot{\mathbf{r}}_k + \varepsilon_{k+1} \ddot{\mathbf{r}}_{k+1} \right] -$$

$$\frac{1}{6\varepsilon_k} \left[(\ddot{\mathbf{r}}_{k-1} + 2\ddot{\mathbf{r}}_k) \cdot \mathbf{l}_k \right] \mathbf{l}_k - \frac{1}{6\varepsilon_{k+1}} \left[(2\ddot{\mathbf{r}}_k + \ddot{\mathbf{r}}_{k+1}) \cdot \mathbf{l}_{k+1} \right] \mathbf{l}_{k+1} \}$$

Here, g is the length of the gravitational acceleration vector. The subscripts (hg), (dt), (dn) and (mn) stand for hydrostatic and gravity forces, tangential drag forces, normal drag forces, and hydrodynamic inertia forces, respectively. Note that in this form, algebraic expressions for the drag forces cannot be found. However, in Section 8.2.6, approximations are introduced that eliminate the need for numerical integration of these terms.

8.2.5   Existence and Uniqueness of Solutions

In this section we show existence and uniqueness of solutions for a slightly simplified equation under the assumption of strictly positive strain.

Assumption 8.1 *There exists a constant $c > 0$, such that*

    i) $e(t, s) \geq c$ *for $s \in [0, L]$ and for all $t \geq t_0$, and;*

    ii) $e_k(t) \geq c$ *for $k = 1, 2, ..., n$ and for all $t \geq t_0$.*

Neglecting the added mass term $\vec{\mathbf{f}}_{(mn)}$, which means that we assume drag dominated behavior, and considering a damping term in the form

$$\vec{\mathbf{f}}_{(d)} = -\frac{1}{2}C_D\, d\rho_w\, |\vec{\mathbf{v}}|\, \vec{\mathbf{v}}$$

yield the following slightly modified initial-boundary value problem

$$\frac{\partial^2 \vec{\mathbf{r}}}{\partial t^2} = \frac{EA_0}{\rho_0}\frac{\partial}{\partial s}\left(\frac{e}{1+e}\frac{\partial \vec{\mathbf{r}}}{\partial s}\right) + \frac{\rho_c - \rho_w}{\rho_c}\vec{\mathbf{g}} - \frac{1}{2\rho_0}(1+e)C_D\, d\rho_w\, |\vec{\mathbf{v}}|\, \vec{\mathbf{v}} \qquad (8.10)$$

with boundary conditions

$$\vec{\mathbf{r}}(t,0) = \vec{\mathbf{r}}_0(0), \quad \vec{\mathbf{r}}(t,L) = \vec{\mathbf{r}}_0(L), \quad \forall\, t \geq t_0$$

and initial conditions

$$\vec{\mathbf{r}}(t_0,s) = \vec{\mathbf{r}}_0(s), \quad \vec{\mathbf{v}}(t_0,s) = \vec{\mathbf{v}}_0(s)$$

Our goal is to apply Proposition 2.1 in [50, page 370], which states local existence and uniqueness of solutions for symmetrizable hyperbolic systems. Thus, we need to show that (8.10) is symmetrizable. Define $\mathbf{u}(t,s)$ as follows

$$\mathbf{u}(t,s) = \begin{bmatrix} \mathbf{u}_0 \\ \mathbf{u}_1 \\ \mathbf{u}_2 \end{bmatrix} \triangleq \begin{bmatrix} \vec{\mathbf{r}} \\ \frac{\partial \vec{\mathbf{r}}}{\partial s} \\ \frac{\partial \vec{\mathbf{r}}}{\partial t} \end{bmatrix}$$

Carrying out the differentiation in the first term on the right hand side of (8.10), the equation, in terms of $\mathbf{u}$, can be written as

$$\mathbf{A}_0\frac{\partial \mathbf{u}}{\partial t} = \mathbf{A}_1\frac{\partial \mathbf{u}}{\partial s} + \mathbf{g} \qquad (8.11)$$

where

$$\mathbf{A}_0(t,s,\mathbf{u}) = \begin{bmatrix} \mathbf{I} & 0 & 0 \\ 0 & \frac{EA_0}{\rho_0}\left(\frac{\mathbf{u}_1\mathbf{u}_1^T}{(1+e)^3} + \frac{e}{1+e}\mathbf{I}\right) & 0 \\ 0 & 0 & \mathbf{I} \end{bmatrix}$$

$$\mathbf{A}_1(t,s,\mathbf{u}) = \begin{bmatrix} 0 & 0 & 0 \\ 0 & 0 & \frac{EA_0}{\rho_0}\left(\frac{\mathbf{u}_1\mathbf{u}_1^T}{(1+e)^3} + \frac{e}{1+e}\mathbf{I}\right) \\ 0 & \frac{EA_0}{\rho_0}\left(\frac{\mathbf{u}_1\mathbf{u}_1^T}{(1+e)^3} + \frac{e}{1+e}\mathbf{I}\right) & 0 \end{bmatrix}$$

$$\mathbf{g}(t,s,\mathbf{u}) = \begin{bmatrix} \mathbf{u}_2 \\ 0 \\ \frac{\rho_c - \rho_w}{\rho_c}\vec{\mathbf{g}} - \frac{1}{2\rho_0}(1+e)C_D\, d\rho_w\, |\mathbf{u}_2|\, \mathbf{u}_2 \end{bmatrix}$$

In (8.11), we have multiplied the equation by the matrix $\mathbf{A}_0$, which is symmetric positive definite for $s \in [0,L]$ and for all $t \geq t_0$ under Assumption 8.1 (in fact, there exists a constant c, such that $\mathbf{A}_0 \geq c\mathbf{I} > 0$, $s \in [0,L]$, $\forall t \geq t_0$). Notice that the matrix $\mathbf{A}_1$ is rendered symmetric, by means of the *symmetrizer* $\mathbf{A}_0$. Thus,

Proposition 2.1 in [50, page 370], provides local existence of a unique solution to (8.11). However, based on the following arguments, we will conjecture that the solution can be continued for all time. The Galerkin equation corresponding to (8.10) is given by

$$\frac{\rho_0 l}{6}(\ddot{\mathbf{r}}_{k-1} + 4\ddot{\mathbf{r}}_k + \ddot{\mathbf{r}}_{k+1}) + EA_0 \left[\frac{e_k}{\varepsilon_k}\mathbf{l}_k - \frac{e_{k+1}}{\varepsilon_{k+1}}\mathbf{l}_{k+1} \right] =$$

$$\int_0^L \left(\vec{\mathbf{f}}_{(hg)} + \vec{\mathbf{f}}_{(d)} \right)(1+e)\varphi_k \, ds$$

$$k = 1, 2, ..., n-1$$

Defining $\mathbf{v}_k = \dot{\mathbf{r}}_k$, $\mathbf{r} \triangleq [\; \mathbf{r}_1^T \quad \mathbf{r}_2^T \quad \cdots \quad \mathbf{r}_{n-1}^T \;]^T$, and $\mathbf{v} \triangleq [\; \mathbf{v}_1^T \quad \mathbf{v}_2^T \quad \cdots \quad \mathbf{v}_{n-1}^T \;]^T$ we have

$$\left[\begin{array}{c} \dot{\mathbf{r}} \\ \dot{\mathbf{v}} \end{array} \right] = \left[\begin{array}{c} \mathbf{f}_1(\mathbf{v}) \\ \mathbf{f}_2(\mathbf{r},\mathbf{v}) \end{array} \right] \tag{8.12}$$

where

$$\mathbf{f}_1(\mathbf{v}) \quad = \quad \mathbf{v}$$

$$\mathbf{f}_2(\mathbf{r},\mathbf{v}) \quad = \quad \mathbf{M}_n^{-1} \left[\begin{array}{c} EA_0 \left(\frac{e_2}{\varepsilon_2}\mathbf{l}_2 - \frac{e_1}{\varepsilon_1}\mathbf{l}_1 \right) + \int_0^L (1+e)\varphi_1 \left(\vec{\mathbf{f}}_{(hg)} + \vec{\mathbf{f}}_{(d)} \right) ds \\ EA_0 \left(\frac{e_3}{\varepsilon_3}\mathbf{l}_3 - \frac{e_2}{\varepsilon_2}\mathbf{l}_2 \right) + \int_0^L (1+e)\varphi_2 \left(\vec{\mathbf{f}}_{(hg)} + \vec{\mathbf{f}}_{(d)} \right) ds \\ \vdots \\ EA_0 \left(\frac{e_{k+1}}{\varepsilon_{k+1}}\mathbf{l}_{k+1} - \frac{e_k}{\varepsilon_k}\mathbf{l}_k \right) + \int_0^L (1+e)\varphi_k \left(\vec{\mathbf{f}}_{(hg)} + \vec{\mathbf{f}}_{(d)} \right) ds \\ \vdots \\ EA_0 \left(\frac{e_n}{\varepsilon_n}\mathbf{l}_n - \frac{e_{n-1}}{\varepsilon_{n-1}}\mathbf{l}_{n-1} \right) + \int_0^L (1+e)\varphi_{n-1} \left(\vec{\mathbf{f}}_{(hg)} + \vec{\mathbf{f}}_{(d)} \right) ds \end{array} \right]$$

$$\mathbf{M}_n \quad = \quad \frac{\rho_0 l}{6} \left[\begin{array}{ccccccc} 4\mathbf{I}_{3\times 3} & \mathbf{I}_{3\times 3} & & & & & \\ \mathbf{I}_{3\times 3} & 4\mathbf{I}_{3\times 3} & \mathbf{I}_{3\times 3} & & & & \\ & \mathbf{I}_{3\times 3} & 4\mathbf{I}_{3\times 3} & \mathbf{I}_{3\times 3} & & & \\ & & \ddots & \ddots & \ddots & & \\ & & & \mathbf{I}_{3\times 3} & 4\mathbf{I}_{3\times 3} & \mathbf{I}_{3\times 3} \\ & & & & \mathbf{I}_{3\times 3} & 4\mathbf{I}_{3\times 3} \end{array} \right]$$

$\mathbf{I}_{3\times 3}$ is the 3×3 identity matrix. $\mathbf{M}_n$ is symmetric positive definite, and, under Assumption 8.1, $\mathbf{f}_1$ and $\mathbf{f}_2$ are locally Lipschitz in $(\mathbf{r}, \mathbf{v})$. The Lipschitz condition yields *local* existence of solutions of (8.12), but we can prove more by exploiting the dissipativity of the drag term.

Theorem 8.1 *For any $n \in \{2, 3, 4, ...\}$, let the initial state $(\mathbf{r}(t_0), \mathbf{v}(t_0)) = (\mathbf{r}_0, \mathbf{v}_0)$ be given. If Assumption 8.1 holds, then there exists a unique solution of (8.12) for all $t \geq t_0$.*

Proof. Consider the energy function

$$E(\mathbf{r}, \mathbf{v}) = -l\frac{\rho_0}{2}\frac{\rho_c - \rho_w}{\rho_c}\sum_{k=1}^{n}(\mathbf{r}_k + \mathbf{r}_{k-1}) \cdot \vec{\mathbf{g}} + \frac{1}{2}lEA_0\sum_{k=1}^{n}e_k^2 + \frac{1}{2}\mathbf{v}^T\mathbf{M}_n\mathbf{v}$$

Its time derivative along trajectories of (8.12) is

$$\begin{aligned}
\dot{E} &=& \mathbf{v}^T\mathbf{M}_n\dot{\mathbf{v}} + lEA_0\sum_{k=1}^{n}e_k\dot{e}_k - \frac{\rho_0}{2}\frac{\rho_c - \rho_w}{\rho_c}\sum_{k=1}^{n}(\mathbf{v}_k + \mathbf{v}_{k-1}) \cdot \vec{\mathbf{g}}\\
&=& -EA_0\sum_{k=1}^{n-1}\mathbf{v}_k^T\left(\frac{e_k}{\varepsilon_k}\mathbf{l}_k - \frac{e_{k+1}}{\varepsilon_{k+1}}\mathbf{l}_{k+1}\right) + EA_0\sum_{k=1}^{n}\frac{e_k}{\varepsilon_k}\mathbf{l}_k^T(\mathbf{v}_k - \mathbf{v}_{k-1})\\
&& -l\rho_0\frac{\rho_c - \rho_w}{\rho_c}\sum_{k=1}^{n-1}\mathbf{v}_k \cdot \vec{\mathbf{g}} - l\frac{\rho_0}{2}\frac{\rho_c - \rho_w}{\rho_c}(\mathbf{v}_0 + \mathbf{v}_n) \cdot \vec{\mathbf{g}}\\
&& + \int_0^L(1+e)\sum_{k=1}^{n-1}\varphi_k\mathbf{v}_k^T \cdot \vec{\mathbf{f}}_{(d)}ds
\end{aligned}$$

In view of the boundary conditions, $\mathbf{v}_0 = \mathbf{0}$ and $\mathbf{v}_n = \mathbf{0}$, we get

$$\dot{E} = \int_0^L(1+e)\sum_{k=1}^{n-1}\varphi_k\mathbf{v}_k^T \cdot \vec{\mathbf{f}}_{(d)}ds$$

Looking at the integral between $s = jl$ and $s = jl + l/2$, we have that

$$\int_{jl}^{jl+l/2}(1+e)\sum_{k=1}^{n-1}\varphi_k\mathbf{v}_k^T \cdot \vec{\mathbf{f}}_{(d)}ds = -\frac{1}{2}C_D d\rho_w\int_{jl}^{jl+l/2}(1+e)\sum_{k=1}^{n-1}\varphi_k|\vec{\mathbf{v}}|\mathbf{v}_k \cdot \vec{\mathbf{v}}ds$$

$$(8.13)$$

Inserting

$$\vec{\mathbf{v}} = \sum_{i=0}^{n}\mathbf{v}_i\varphi_i$$

into (8.13), and noticing that for $s \in [jl, (j+1)\,l]$, only φ_j and φ_{j+1} are nonzero, we get

$$\int_{jl}^{jl+l/2}(1+e)\sum_{k=1}^{n-1}\varphi_k\mathbf{v}_k^T \cdot \vec{\mathbf{f}}_{(d)}ds =$$

$$-\frac{1}{2}C_D d\rho_w\int_{jl}^{(j+1)l}\sum_{k=1}^{n-1}(1+e)|\mathbf{v}_j\varphi_j + \mathbf{v}_{j+1}\varphi_{j+1}|^3 ds \leq 0$$

so that

$$\dot{E} \leq 0, \quad \forall t \geq t_0$$

Therefore, the solution $(\mathbf{r}(t), \mathbf{v}(t))$ of (8.12) with $(\mathbf{r}(t_0), \mathbf{v}(t_0)) = (\mathbf{r}_0, \mathbf{v}_0)$ stays forever in the set

$$\mathcal{W} = \{(\mathbf{r}, \mathbf{v}) \mid E(\mathbf{r}, \mathbf{v}) \leq E(\mathbf{r}_0, \mathbf{v}_0)\}$$

By continuity of E, $\mathcal{W}$ is closed. Since $\mathbf{r}_0$ and $\mathbf{r}_n$ are fixed (boundary conditions), and $\mathbf{M}_n > 0$, it follows that $E \to \infty$ as $|(\mathbf{r}, \mathbf{v})| \to \infty$. Thus, E is bounded below (by continuity of E), and consequently, $\mathcal{W}$ is bounded. Since $\mathcal{W} \subset \mathbb{R}^{6(n-1)}$ is closed and bounded, it is compact. The theorem now follows from standard results [29, Theorem 2.4]. ∎

Theorem 8.1 implies that $\mathbf{u}_n \in H^k([0, L])$, for $t \geq t_0$, where $H^k([0, L])$ denotes the Sobolev space defined by

$$H^k([0, L]) = \left\{ \mathbf{u} \in L^2([0, L]) \;\middle|\; \frac{\partial^l \mathbf{u}}{\partial s^l} \in L^2([0, L]), \;\; 0 < l \leq k \right\}$$

with the natural norm

$$\|\mathbf{u}\|_{H^k([0,L])} = \sum_{l=0}^{l=k} \left\| \frac{\partial^l \mathbf{u}}{\partial s^l} \right\|_{L^2([0,L])}$$

and $\mathbf{u}_n$ is given in terms of the finite element basis defined in Section 8.2.4, that is

$$\mathbf{u}_n(t, s) = \sum_{i=0}^{n} \begin{bmatrix} \mathbf{r}_i(t)\varphi_i(s) \\ \mathbf{r}_i(t)\frac{\partial \varphi_i(s)}{\partial s} \\ \mathbf{v}_i(t)\varphi_i(s) \end{bmatrix} \tag{8.14}$$

In fact, Theorem 8.1 implies that there exists a constant c, independent of k and n, such that

$$\|\mathbf{u}_n\|_{H^k([0,L])} \leq c, \quad \forall t \geq t_0, \;\; n = 2, 3, \dots$$

Based on the above considerations, along with the results of Chapter 16, Sections 1 and 2 in [50, pages 359–372], we conjecture the following.

Conjecture 8.1 *Suppose Assumption 8.1 holds, and that* $\mathbf{u}(0, s) \in H^k([0, L])$, *with* $k \geq 2$. *Then there exists a unique solution* $\mathbf{u} \in C([t_0, \infty), H^k([0, L]))$, *to the initial-boundary value problem (8.11). Moreover, the sequence of solutions* $\mathbf{u}_n$ *(as given in (8.14)) of the Galerkin equation (8.12), converges to* $\mathbf{u}$ *in the following sense*

$$\|\mathbf{u} - \mathbf{u}_n\|_{H^k([0,L])} \to 0 \; as \; n \to \infty$$

Remark 8.1 *We stress the fact that since Theorem 8.1 and Conjecture 8.1 are stated under Assumption 8.1, global solutions are not guaranteed for all initial conditions. The problem of finding conditions on the initial data under which Assumption 8.1 holds (for all* $t \geq t_0$*), is outside the scope of this work.*

8.2.6 Implementation

It is desirable to apply certain approximations to the terms of (8.9) in order to simplify implementation. Looking at the kth node, we see by inspection of (8.9), that it takes an advantageous form if the following approximations are applied

$$\dot{\mathbf{r}}_{k-1} \approx \dot{\mathbf{r}}_k, \quad \dot{\mathbf{r}}_{k+1} \approx \dot{\mathbf{r}}_k \tag{8.15}$$

$$\ddot{\mathbf{r}}_{k-1} \approx \ddot{\mathbf{r}}_k, \quad \ddot{\mathbf{r}}_{k+1} \approx \ddot{\mathbf{r}}_k. \tag{8.16}$$

These approximations are to be taken locally, in the sense that they do not propagate throughout the cable setting all nodal velocities and accelerations equal. In other words, they represent lumping of the mass onto the nodes. With the approximations (8.15)–(8.16), (8.9) reduces to the following:

$$\left[\left(\rho_0 l + \frac{C_1}{2}(\varepsilon_k + \varepsilon_{k+1}) \right) \mathbf{I}_{3 \times 3} - \frac{C_1}{2} \left(\frac{\mathbf{l}_k \mathbf{l}_k^T}{\varepsilon_k} + \frac{\mathbf{l}_{k+1} \mathbf{l}_{k+1}^T}{\varepsilon_{k+1}} \right) \right] \ddot{\mathbf{r}}_k =$$

$$\mathbf{f}_{k_{(hg)}} + \mathbf{f}_{k_{(dt)}} + \mathbf{f}_{k_{(dn)}} + \mathbf{f}_{k_{(r)}}, \quad k = 1, 2, ..., n - 1 \tag{8.17}$$

where

$$\mathbf{f}_{k_{(r)}} = E A_0 \left[\frac{e_{k+1}}{\varepsilon_{k+1}} \mathbf{l}_{k+1} - \frac{e_k}{\varepsilon_k} \mathbf{l}_k \right]$$

$$\mathbf{f}_{k_{(hg)}} = l \rho_0 \frac{\rho_c - \rho_w}{\rho_c} \begin{bmatrix} 0 & 0 & g \end{bmatrix}^T$$

$$\mathbf{f}_{k_{(dt)}} = -\frac{C_2}{2} \left[|\dot{\mathbf{r}}_k \cdot \mathbf{l}_k| \frac{\mathbf{l}_k \mathbf{l}_k^T}{\varepsilon_k^2} + |\dot{\mathbf{r}}_k \cdot \mathbf{l}_{k+1}| \frac{\mathbf{l}_{k+1} \mathbf{l}_{k+1}^T}{\varepsilon_{k+1}^2} \right] \dot{\mathbf{r}}_k$$

$$\mathbf{f}_{k_{(dn)}} = -\frac{C_3}{2} \left[\varepsilon_k \left| \left(\mathbf{I}_{3 \times 3} - \frac{\mathbf{l}_k \mathbf{l}_k^T}{\varepsilon_k^2} \right) \dot{\mathbf{r}}_k \right| \left(\mathbf{I}_{3 \times 3} - \frac{\mathbf{l}_k \mathbf{l}_k^T}{\varepsilon_k^2} \right) \right.$$

$$\left. + \varepsilon_{k+1} \left| \left(\mathbf{I}_{3 \times 3} - \frac{\mathbf{l}_{k+1} \mathbf{l}_{k+1}^T}{\varepsilon_{k+1}^2} \right) \dot{\mathbf{r}}_k \right| \left(\mathbf{I}_{3 \times 3} - \frac{\mathbf{l}_{k+1} \mathbf{l}_{k+1}^T}{\varepsilon_{k+1}^2} \right) \right] \dot{\mathbf{r}}_k$$

$$C_1 = C_{MN} \frac{\pi d^2}{4} \rho_w, \quad C_2 = \frac{1}{2} C_{DT} d \rho_w, \quad C_3 = \frac{1}{2} C_{DN} d \rho_w$$

The subscript (r) stands for internal reaction forces. Clearly, in the limit as $n \to \infty$, (8.9) and (8.17) are identical. However, simulations suggest that (8.16) imposes fundamental restrictions on the accuracy of the model, so (8.16) may be an undesirable approximation in certain applications. The effect of omitting (8.16) is a fuller mass matrix, that requires more computations to invert.

8.2.7 Comparison With Exact Solutions of the Elastic Catenary Equations

A simple test of the model is performed by comparing the static solution ($\dot{\mathbf{r}}_k \equiv \mathbf{0}$ and $\ddot{\mathbf{r}}_k \equiv \mathbf{0}$ for all k) to the exact solution of the elastic catenary given in [52, Section 1.6]. In this test, L, E, and A_0 are chosen to be 2400 m, 2.55×10^{10}

N/m^2, and 0.0079 m^2, respectively. Figure 8.5 clearly suggests that the finite element solutions converge to the exact solution as the number of elements is increased.

8.2.8   Multi-Cable Mooring System

Modelling a mooring system consisting of several mooring lines is now a matter of assembling the equations from the previous section. For completeness, we will do this exercise for an m-cable mooring system, where the cables may have individual characteristics. As before, each cable is uniformly partitioned into n segments, and the nodal points are enumerated from 0 to n. Let $\mathbf{r}_k^j \in \mathbb{R}^3$ denote the position vector in Earth-fixed coordinates for the kth nodal point of the jth cable, and define the relative velocity $\mathbf{v}_k^j = \dot{\mathbf{r}}_k^j - \mathbf{v}_c(\mathbf{r}_k^j)$ where $\mathbf{v}_c(\mathbf{r}_k^j) \in \mathbb{R}^3$ is the ambient fluid velocity at the node. The boundary conditions are as follows:

1. The first nodal point $\mathbf{r}_0^j$ is fixed for $j = 1, 2, ..., m$.

2. The last nodal point $\mathbf{r}_n^j$ is connected to a fixed point on the vessel, $\mathbf{p}^j$. Thus, $\mathbf{p}^j$ for $j = 1, 2, ..., m$, are constant vectors given in the body-fixed frame.

This leads to the following set of ordinary differential equations:

$$\mathbf{M}_k^j \dot{\mathbf{v}}_k^j + \mathbf{D}_k^j \mathbf{v}_k^j + \mathbf{k}_k^j + \mathbf{g}_k^j \;\; = \;\; \mathbf{0}, \;\; k = 1, 2, ..., n-1, \;\; j = 1, 2, ..., m \quad (8.18)$$

$$\mathbf{M}_n^j \dot{\mathbf{v}}_n^j + \mathbf{D}_n^j \mathbf{v}_n^j + \mathbf{k}_n^j + \mathbf{g}_n^j \;\; = \;\; \mathbf{0}, \;\; j = 1, 2, ..., m \qquad\qquad (8.19)$$

where $\mathbf{M}_k^j \in \mathbb{R}^{3\times3}$, $\mathbf{D}_k^j \in \mathbb{R}^{3\times3}$, $\mathbf{k}_k^j \in \mathbb{R}^3$ and $\mathbf{g}_k^j \in \mathbb{R}^3$. By defining $\varepsilon_k^j \in \mathbb{R}$ and $\mathbf{l}_k^j \in \mathbb{R}^3$ analogous to the previous section, and defining $\mathbf{P}_k^j \in \mathbb{R}^{3\times3}$ as

$$\mathbf{P}_k^j \triangleq \frac{\mathbf{l}_k^j {\mathbf{l}_k^j}^T}{\varepsilon_k^{j^2}}$$

the terms of (8.18) are given by:

$$\mathbf{M}_k^j \;\; = \;\; \left[\rho_o l_j + \frac{C_1^j}{2}(\varepsilon_k^j + \varepsilon_{k+1}^j)\right] \mathbf{I}_{3\times3} - \frac{C_1^j}{2}\left(\varepsilon_k^j \mathbf{P}_k^j + \varepsilon_{k+1}^j \mathbf{P}_{k+1}^j\right)$$

$$\mathbf{D}_k^j \;\; = \;\; \frac{C_2^j}{2}\left[\left|\mathbf{v}_k^j \cdot \mathbf{l}_k^j\right| \mathbf{P}_k^j + \left|\mathbf{v}_k^j \cdot \mathbf{l}_{k+1}^j\right| \mathbf{P}_{k+1}^j\right] +$$

$$\qquad \frac{C_3^j}{2}\left[\varepsilon_k^j \left|(\mathbf{I}_{3\times3} - \mathbf{P}_k^j)\mathbf{v}_k^j\right| (\mathbf{I}_{3\times3} - \mathbf{P}_k^j) +\right.$$

$$\qquad \left. \varepsilon_{k+1}^j \left|(\mathbf{I}_{3\times3} - \mathbf{P}_{k+1}^j)\mathbf{v}_k^j\right| (\mathbf{I}_{3\times3} - \mathbf{P}_{k+1}^j)\right]$$

$$\mathbf{k}_k^j \;\; = \;\; \frac{E_j A_{0_j}}{l_j}\left[\frac{\varepsilon_k^j - l_j}{\varepsilon_k^j}\mathbf{l}_k^j - \frac{\varepsilon_{k+1}^j - l_j}{\varepsilon_{k+1}^j}\mathbf{l}_{k+1}^j\right]$$

$$\mathbf{g}_k^j \;\; = \;\; -l_j \rho_0^j \frac{\rho_c^j - \rho_w}{\rho_c^j}\begin{bmatrix} 0 & 0 & g \end{bmatrix}^T$$
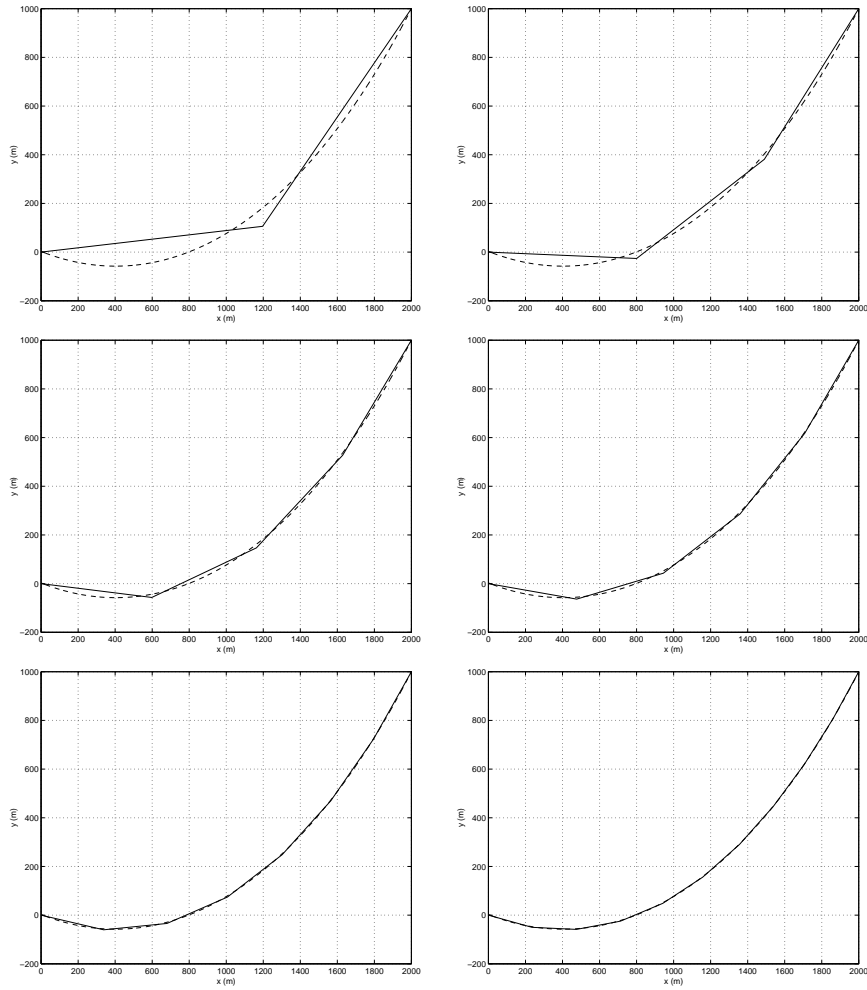
Figure 8.5: Solutions with 2, 3, 4, 5, 7 and 10 elements (solid line) compared to the exact solution (dashed line) of the elastic catenary.

Since the last node of a cable is connected to just one element, the force-terms with subscript $k+1$ vanish from the equations for this particular node. Keeping this in mind, the terms of (8.19) are given by

$$
\begin{aligned}
\mathbf{M}_n^j &= (\rho_o l_j + C_1^j \varepsilon_n^j)\mathbf{I}_{3\times 3} - C_1^j \varepsilon_n^j \mathbf{P}_n^j \\
\mathbf{D}_n^j &= C_2^j \left| \mathbf{v}_n^j \cdot \mathbf{l}_n^j \right| \mathbf{P}_n^j + C_3^j \varepsilon_n^j \left| (\mathbf{I}_{3\times 3} - \mathbf{P}_n^j)\mathbf{v}_n^j \right| (\mathbf{I}_{3\times 3} - \mathbf{P}_n^j) \\
\mathbf{k}_n^j &= \frac{E_j A_{0_j}}{l_j} \frac{\varepsilon_n^j - l_j}{\varepsilon_n^j} \mathbf{l}_n^j \\
\mathbf{g}_n^j &= -\frac{1}{2} l_j \rho_0^j \frac{\rho_c^j - \rho_w}{\rho_c^j} \begin{bmatrix} 0 & 0 & g \end{bmatrix}^T
\end{aligned}
$$

where the constants are defined in the obvious way

$$
C_1^j = C_{MN}^j \frac{\pi d_j^2}{4} \rho_w, \quad C_2^j = \frac{1}{2} C_{DT}^j d_j \rho_w, \quad C_3^j = \frac{1}{2} C_{DN}^j d_j \rho_w
$$

C_{DT}^j and C_{DN}^j are tangential and normal drag coefficients for the jth cable, respectively, and C_{MN}^j is a hydrodynamic mass coefficient for the jth cable. l_j is the length of each element in the jth cable. All forces are expressed in the Earth-fixed frame. The position and velocity of the last nodal points are given by

$$
\mathbf{r}_n^j = \eta_1 + \mathbf{J}_1(\eta_2)\mathbf{p}^j, \quad j = 1, 2, ..., m \tag{8.20}
$$

$$
\mathbf{v}_n^j = \mathbf{J}_1(\eta_2)\nu_1 + \frac{d}{dt}\left(\mathbf{J}_1(\eta_2) \right) \mathbf{p}^j, \quad j = 1, 2, ..., m \tag{8.21}
$$

8.2.9 Coupled Vessel-Mooring Dynamics

When coupling the mooring cables to the vessel, we can safely ignore the inertia, drag, and hydrostatic and gravity effects in (8.19), that is, the terms involving $\mathbf{M}_n^j$, $\mathbf{D}_n^j$, and $\mathbf{g}_n^j$, since the effect of these terms will be negligible when compared to the mass, damping and restoring forces of the vessel. Thus, the mooring forces acting on the vessel will be given by $\mathbf{k}_n^j$, for $j = 1, 2, 3, ..., m$, as follows

$$
\tau_M^1 = \mathbf{J}_1(\eta_2)^T \sum_{j=1}^m \mathbf{k}_n^j, \quad \tau_M^2 = \sum_{j=1}^m \left(\mathbf{J}_1(\eta_2)^T \mathbf{k}_n^j \right) \times \mathbf{p}^j
$$

where we have defined

$$
\tau_M \triangleq \begin{bmatrix} -\tau_M^1 \\ -\tau_M^2 \end{bmatrix} \tag{8.22}
$$

Inserting (8.22) into (8.1) yields the following complete equations of motion for the moored vessel

$$
\mathbf{M}\dot{\nu} + \mathbf{C}(\nu)\nu + \mathbf{D}(\nu)\nu + \mathbf{g}(\eta) + \begin{bmatrix} \tau_M^1 \\ \tau_M^2 \end{bmatrix} = \tau_E + \tau \tag{8.23}
$$

$$
\dot{\eta} = \mathbf{J}(\eta)\nu \tag{8.24}
$$

$$
\mathbf{M}_M \dot{\mathbf{v}}_M + \mathbf{D}_M \mathbf{v}_M + \mathbf{k}_M + \mathbf{g}_M = 0 \tag{8.25}
$$

where we have defined, for notational simplicity, the following quantities for the $n-1$ first nodes

$$
\mathbf{r}_{\mathrm{M}} = \begin{bmatrix} \mathbf{r}_1^1 \\ \vdots \\ \mathbf{r}_{n-1}^1 \\ \vdots \\ \mathbf{r}_1^m \\ \vdots \\ \mathbf{r}_{n-1}^m \end{bmatrix}, \quad
\mathbf{v}_{\mathrm{M}} = \begin{bmatrix} \mathbf{v}_1^1 \\ \vdots \\ \mathbf{v}_{n-1}^1 \\ \vdots \\ \mathbf{v}_1^m \\ \vdots \\ \mathbf{v}_{n-1}^m \end{bmatrix}, \quad
\mathbf{k}_{\mathrm{M}} = \begin{bmatrix} \mathbf{k}_1^1 \\ \vdots \\ \mathbf{k}_{n-1}^1 \\ \vdots \\ \mathbf{k}_1^m \\ \vdots \\ \mathbf{k}_{n-1}^m \end{bmatrix}, \quad
\mathbf{g}_{\mathrm{M}} = \begin{bmatrix} \mathbf{g}_1^1 \\ \vdots \\ \mathbf{g}_{n-1}^1 \\ \vdots \\ \mathbf{g}_1^m \\ \vdots \\ \mathbf{g}_{n-1}^m \end{bmatrix}
$$

$$
\begin{aligned}
\mathbf{M}_{\mathrm{M}} &= \operatorname{diag}\{\mathbf{M}_1^1, ..., \mathbf{M}_{n-1}^1, ..., \mathbf{M}_1^m, ..., \mathbf{M}_{n-1}^m\} \\
\mathbf{D}_{\mathrm{M}} &= \operatorname{diag}\{\mathbf{D}_1^1, ..., \mathbf{D}_{n-1}^1, ..., \mathbf{D}_1^m, ..., \mathbf{D}_{n-1}^m\}
\end{aligned}
$$

8.3 Simulations of the Coupled System

The following simulation example, using the ABB Integrated Vessel Simulator, aims to demonstrate the importance of a coupled dynamic analysis of moored vessels in deep waters as opposed to quasi-static analyses. For simplicity, we will consider a vessel in three degrees of freedom, that is, the horizontal motion of the vessel. We assume that the ship has a turret-based mooring system, and that all cables are connected to the center of turret. The origin of the body-fixed reference frame is also placed in the center of turret. Furthermore, we assume linear viscous damping and negligible Coriolis and centripetal forces for the vessel. These are low speed assumptions, which are common in positioning applications. With these simplifications, equations (8.23)–(8.25) are reduced to the following

$$
\mathbf{M}\dot{\nu} + \mathbf{D}\nu + \mathbf{J}(\psi)\mathbf{k}_n = \tau_E + \tau \tag{8.26}
$$

$$
\dot{\eta} = \mathbf{J}(\psi)\nu \tag{8.27}
$$

$$
\mathbf{M}_{\mathrm{M}}\dot{\mathbf{v}}_{\mathrm{M}} + \mathbf{D}_{\mathrm{M}}\mathbf{v}_{\mathrm{M}} + \mathbf{k}_{\mathrm{M}} + \mathbf{g}_{\mathrm{M}} = \mathbf{0} \tag{8.28}
$$

where $\eta = [\; x \quad y \quad \psi \;]^T$, $\nu = [\; u \quad v \quad r \;]^T$, $\mathbf{M} \in \mathbb{R}^{3 \times 3}$, $\mathbf{D} \in \mathbb{R}^{3 \times 3}$, and

$$
\mathbf{J}(\psi) = \begin{bmatrix} \cos\psi & -\sin\psi & 0 \\ \sin\psi & \cos\psi & 0 \\ 0 & 0 & 1 \end{bmatrix}
$$

$$
\mathbf{k}_n = \mathbf{J}(\psi)^T \begin{bmatrix} \mathbf{I}_{2\times 2} & 0 \\ 0 & 0 \end{bmatrix} \sum_{j=1}^{m} \mathbf{k}_n^j
$$

Open loop simulations (that is, no thruster action is applied) have been performed in order to compare ship movements in two different cases:

1. *Coupled dynamics*, that is, the finite element model is coupled to the vessel dynamics as described by (8.26)–(8.28).
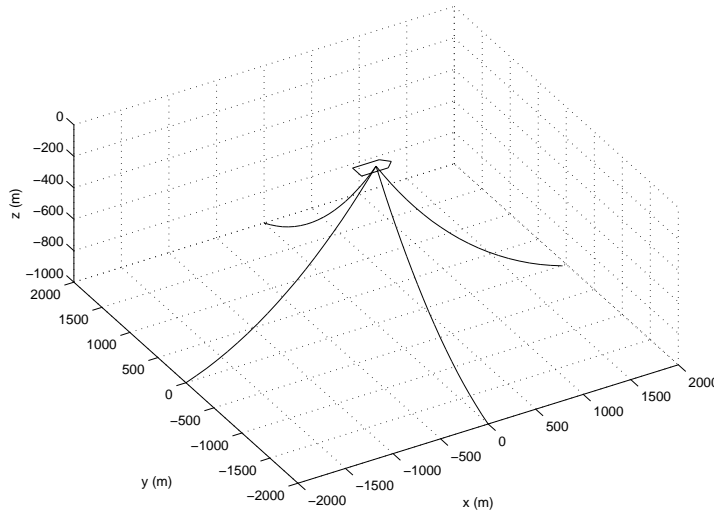
Figure 8.6: Initial condition for simulation.

2. *Quasi-static analysis*, that is, the finite element model is replaced by a look-up table of catenary solutions as a function of ship position.

The input parameters to the model are stated in Table 8.1, and the initial configuration of the system is sketched in Figure 8.6.

Figure 8.7 shows that the distance between trajectories in the two simulation cases exceeds 40 m during the 60 minute simulation. The overall displacement of the ship is about 160 m, which yields a considerable relative error. The difference in heading, shown in Figure 8.8, has a maximum of about 20 degrees, but over a short period of time. Figures 8.9 and 8.10, which show total environmental forces and torques (τ_E) for the quasi-static case, and dynamic case, respectively, are included such that the simulations may be reproduced.

8.4   Controlling Line Tension

The design of a controller for dynamic line tensioning is based on the following two basic assumptions:

1. A DP system has already been designed for the vessel.

2. The mooring line tensions are measured continuously.

Table 8.1: Parameters used in the simulation

Vessel parameters

$$\mathbf{M} = \begin{bmatrix} 9.6 \times 10^7 & 0 & 0 \\ 0 & 1.3 \times 10^8 & -5.3 \times 10^9 \\ 0 & -5.3 \times 10^9 & 5 \times 10^{11} \end{bmatrix}$$

$$\mathbf{D} = \begin{bmatrix} 9.2 \times 10^5 & 0 & 0 \\ 0 & 2.4 \times 10^6 & -9.7 \times 10^7 \\ 0 & -9.7 \times 10^7 & 1.3 \times 10^{10} \end{bmatrix}$$

Mooring system parameters

$$\left. \begin{aligned} L_j &= 2250 \\ C_{DT}^j &= 0.3 \\ C_{DN}^j &= 1 \\ C_{MN}^j &= 1.5 \\ \rho_c^j &= 5500 \\ \rho_0^j &= 27.6 \\ d_j &= 0.08 \\ E_j A_{0_j} &= 230 \times 10^6 \\ l_j &= 112.5 \end{aligned} \right\} \quad j \in [1, 2, 3, 4]$$

$$\mathbf{r}_0^1 = \begin{bmatrix} 1950 & 0 & 1000 \end{bmatrix}^T$$
$$\mathbf{r}_0^2 = \begin{bmatrix} 0 & 1950 & 1000 \end{bmatrix}^T$$
$$\mathbf{r}_0^3 = \begin{bmatrix} -1950 & 0 & 1000 \end{bmatrix}^T$$
$$\mathbf{r}_0^4 = \begin{bmatrix} 0 & -1950 & 1000 \end{bmatrix}^T$$

Environmental parameters

Wind velocity: $8m/s$, wind direction: $45deg$ (w.r.t. Earth-fixed x-axis)
Significant wave height: $2m$, wave period: $5s$
Current velocity: $0.5m/s$, current direction: $45deg$
Density of water: $\rho_w = 1025kg/m^3$
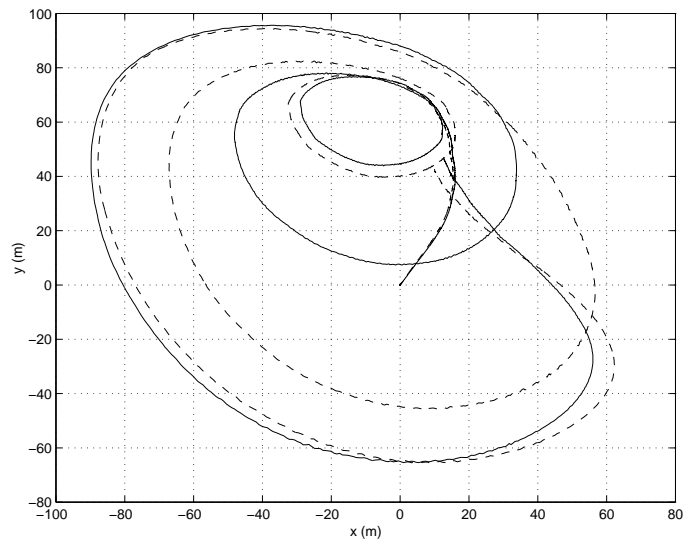
Figure 8.7: Ship movement in the xy-plane for the dynamic case (solid line) and quasi-static case (dashed line).
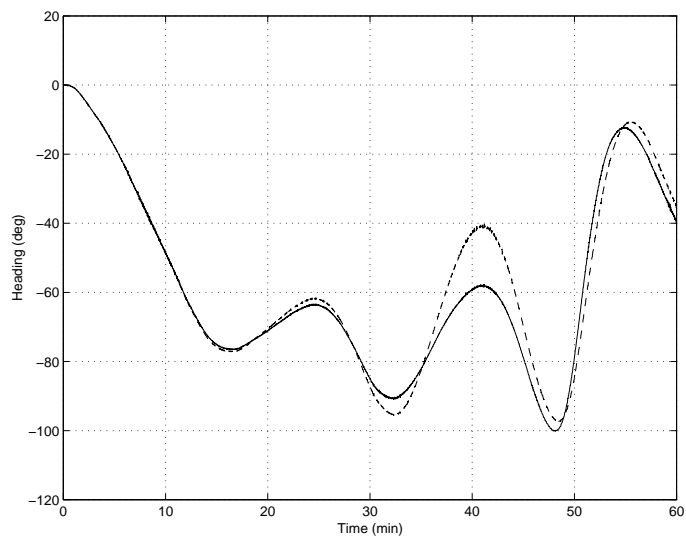

Figure 8.8: Ship heading for the dynamic case (solid line) and quasi-static case (dashed line).
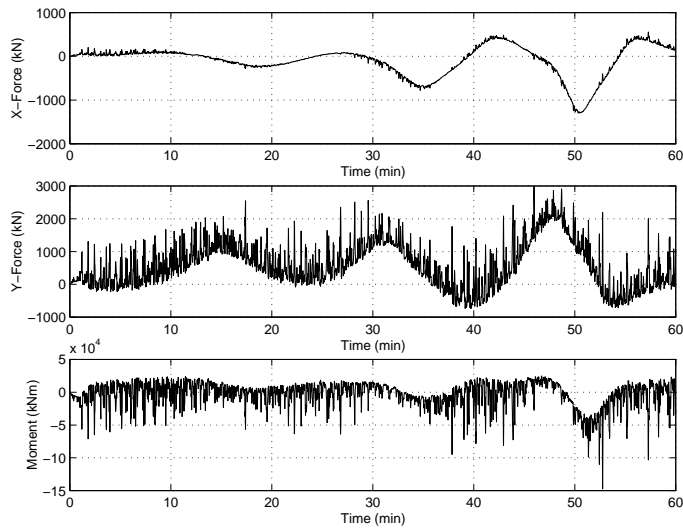
Figure 8.9: Total environmental forces and moments acting on the ship in the quasi-static case. Forces are given in the body-fixed reference frame.
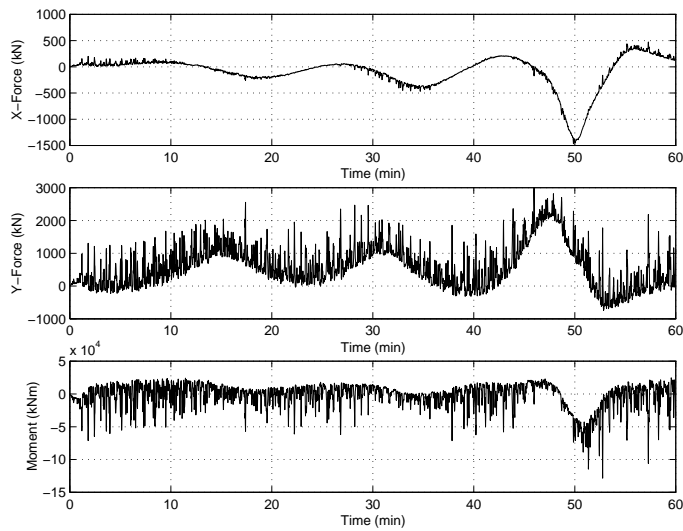

Figure 8.10: Total environmental forces and moments acting on the ship in the dynamic case. Forces are given in the body-fixed reference frame.
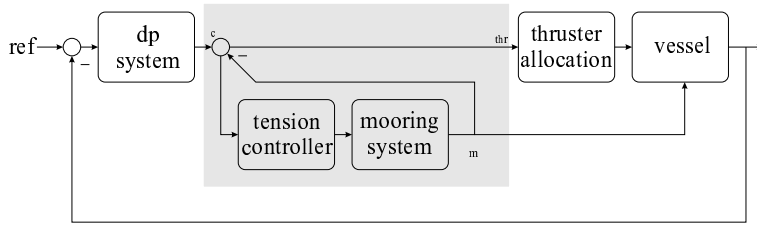
Figure 8.11: Block diagram of the moored vessel, with the dynamic line tensioning system emphasized.

Denoting the commanded force from the DP controller τ_c, and the mooring force projected onto the horizontal plane τ_m, we define the thruster force (see Figure 8.11):

$$\tau_{thr} = \tau_c - \tau_m$$

Thus, the performance of the thruster assisted mooring system is exactly that of the DP system alone. The objective of the dynamic line tensioning controller is to track τ_c, such that as little as possible of the commanded force is passed on to the thrusters. Formally, the control problem is

Problem 8.1 *Consider the initial-boundary-value problem*

$$\rho_0 \frac{\partial \mathbf{v}}{\partial t} = \frac{\partial}{\partial s}\left(EA_0 \frac{e}{1+e} \frac{\partial \mathbf{r}}{\partial s}\right) +$$
$$\left(\mathbf{f}_{(hg)} + \mathbf{f}_{(dt)} + \mathbf{f}_{(dn)} + \mathbf{f}_{(mn)}\right)(1+e), \quad s \in [0, L] \quad (8.29)$$

$$b.c.: \mathbf{v}(s) = \mathbf{v}(L), \quad e(s) = e(L), \quad s \in (L, L_{\max}]$$

$$i.c.: \mathbf{r}(0) = \mathbf{r}_0, \quad \mathbf{r}(L) = \mathbf{0}, \quad \mathbf{v}(L) = [1 + e(L)]\dot{L}\mathbf{t}(L) = u\mathbf{t}(L)$$

where the control input u is related to the cable length L according to

$$\frac{dL}{dt} = \frac{u}{1 + e(L)},$$

and the measurement output is

$$y = EA_0 e(L) = T(L).$$

Given a reference tension T_{ref}, find $u(t)$ such that $y(t)$ regulates to T_{ref}.

In the problem formulation above, $\mathbf{r}(L) = \mathbf{0}$, which is to say that the DP-system is assumed to be perfect in the analysis. Deviation from the desired vessel position is considered noise.

Criterion 8.1 (Well Posedness) T_{ref} *lies within a certain interval given by the static line characteristic. Formally; there exists* $L^* \in [L_{min}, L_{max}]$, $\mathbf{r}^*(s)$ *(and thereby* $e^*(s)$*) such that*

$$\frac{\partial}{\partial s}\left(EA_0 \frac{e^*}{1+e^*} \frac{\partial \mathbf{r}^*}{\partial s}\right) + \mathbf{f}_{(hg)}(1+e^*) = 0, \quad s \in [0, L^*]$$

$$\mathbf{r}^*(0) = \mathbf{r}_0, \quad \mathbf{r}^*(L^*) = \mathbf{0}$$

is satisfied, and $T_{ref} = EA_0 e^*(L^*)$.

Moving the added mass term in equation (8.29) to the left hand side yields:

$$\mathbf{M}_c \left[\begin{array}{c} \dot{\mathbf{v}}_t \\ \dot{\mathbf{v}}_n \end{array}\right] = \frac{\partial}{\partial s}(EA_0 \frac{e}{1+e}\frac{\partial \mathbf{r}}{\partial s}) + $$
$$(\mathbf{f}_{(hg)} + \mathbf{f}_{(dt)} + \mathbf{f}_{(dn)})(1+e)$$

where

$$\mathbf{M}_c = \left[\begin{array}{cc} \rho_0 & 0 \\ 0 & \rho_0 + C_{MN}\frac{\pi d^2}{4}\rho_w(1+e) \end{array}\right]$$

Assumption 8.2 *The inertia matrix including hydrodynamic added inertia is constant, that is:* $\dot{\mathbf{M}}_c = \mathbf{0}$.

Proposition 8.1 *Under Assumption 8.2, the mapping from u to y is (state strictly) passive.*

Proof. Take the storage function

$$V(\mathbf{v}, e) = \frac{1}{2} \int_0^{L_{max}} \mathbf{v}^T \mathbf{M}_c \mathbf{v} ds + \frac{1}{2}EA_0 \int_0^{L_{max}} e^2 ds$$

The derivative of V with respect to time is:

$$\dot{V} = \int_0^{L(t)} \mathbf{v} \cdot \frac{\partial}{\partial s}(EA_0 \frac{e}{1+e}\frac{\partial \mathbf{r}}{\partial s})ds +$$

$$\int_0^{L(t)} \mathbf{v} \cdot \mathbf{f}_{(hg)}(1+e)ds +$$

$$\int_{L(t)}^{L_{max}} \mathbf{v}^T(s)\mathbf{M}_c(L)\dot{\mathbf{v}}(L)ds -$$

$$\frac{1}{2}d\rho_w \int_0^{L(t)} \left(C_{DT}|\mathbf{v}_t|^3 + C_{DN}|\mathbf{v}_n|^3 \right)(1+e)ds +$$

$$\frac{1}{2}EA_0\int\limits_0^{L(t)}\frac{de^2}{dt}ds+\frac{1}{2}EA_0\int\limits_{L(t)}^{L_{\max}}\frac{de(L)^2}{dt}ds \qquad (8.30)$$

Consider the first term in equation (8.30):

$$\int\limits_0^{L(t)}\mathbf{v}\cdot\frac{\partial}{\partial s}(EA_0\frac{e}{1+e}\frac{\partial\mathbf{r}}{\partial s})ds$$

$$= \left[\mathbf{v}\cdot EA_0\frac{e}{1+e}\frac{\partial\mathbf{r}}{\partial s}\right]_0^L - \int\limits_0^{L(t)}\frac{\partial\mathbf{v}}{\partial s}\cdot EA_0\frac{e}{1+e}\frac{\partial\mathbf{r}}{\partial s}ds$$

$$= uy - \int\limits_0^{L(t)}\frac{d\left(\frac{\partial\mathbf{r}}{\partial s}\right)}{dt}\cdot EA_0\frac{e}{1+e}\frac{\partial\mathbf{r}}{\partial s}ds$$

$$= uy - \int\limits_0^{L(t)}\frac{d\left((1+e)\mathbf{t}\right)}{dt}EA_0e\mathbf{t}ds$$

$$= uy - EA_0\int\limits_0^{L(t)}\frac{d\left(e\mathbf{t}\right)}{dt}e\mathbf{t}ds$$

$$= uy - \frac{1}{2}EA_0\int\limits_0^{L(t)}\frac{de^2}{dt}ds \qquad (8.31)$$

Now, consider the second term in equation (8.30):

$$\int\limits_0^{L(t)}\mathbf{v}\cdot\mathbf{f}_{(hg)}(1+e)ds$$

$$= \rho_0\frac{\rho_c-\rho_w}{\rho_c}\left(\frac{d}{dt}\int\limits_0^{L(t)}\mathbf{r}\cdot\mathbf{g}ds-\mathbf{r}(L)\cdot\mathbf{g}\dot{L}\right)=0 \qquad (8.32)$$

Now, consider the third term in equation (8.30):

$$\int\limits_{L(t)}^{L_{\max}}\mathbf{v}^T(s)\mathbf{M}_c(L)\dot{\mathbf{v}}(L)ds$$

$$= \left[\mathbf{v}(s)\cdot EA_0\frac{e(L)}{1+e(L)}\frac{\partial\mathbf{r}}{\partial s}(L)\right]_{L(t)}^{L_{\max}} -$$

$$\frac{1}{2}EA_0 \int\limits_{L(t)}^{L_{\max}} \frac{de(L)^2}{dt}ds$$

$$= -\frac{1}{2}EA_0 \int\limits_{L(t)}^{L_{\max}} \frac{de(L)^2}{dt}ds \qquad (8.33)$$

Inserting (8.31), (8.32) and (8.33) into (8.30) yields:

$$uy \geq \dot{V}(\mathbf{v}, e) + \rho\psi(\mathbf{v})$$

where $\rho \in [0, 1]$ and

$$\psi(\mathbf{v}) = \frac{1}{2}d\rho_w \int\limits_0^{L(t)} \left(C_{DT} |\mathbf{v}_t|^3 + C_{DN} |\mathbf{v}_n|^3 \right)(1 + e)ds$$

∎

Therefore, a passive controller will ensure stability. For dynamically positioned and moored vessels the inertia matrix will be slowly-varying compared to the dynamics of the closed-loop system. Hence, time scale separation suggests that $\dot{\mathbf{M}}_c = 0$ is a good approximation (Assumption 8.2). In general, the inertia matrix will depend on the frequency of the incoming waves, speed of the vessel and strain. These effects are, however, negligible in an industrial control system [19].

8.5   Simulation of Line Tension Control

A simple simulation has been performed in order to demonstrate the potential for energy reduction when using dynamic line tensioning. The simulation is simple in the sense that tidal current is the only disturbance considered. The vessel parameters are the same as in the previous simulation example (see Table 8.1), and Table 8.2 summarizes the mooring system parameters and the specified tidal current. The DP-system described in [21, Section 2.2.3] is used, giving the commanded force τ_c to the tension controller. The mooring-system consists of $m = 4$ cables, with anchor points distributed evenly on a circle of radius $2km$ about the origin. The commanded force is distributed to the cables in such a way that two cables having their anchor points opposite each other with respect to the origin are wound, respectively unwound, at the same speed. This strategy leads to the following P-controller:

$$\mathbf{u} = -k_c \mathbf{B}(\tau_c - \tau_m)$$

where k_c is the controller gain, τ_c is the commanded force and τ_m is the measured mooring force. $\mathbf{B}$ is an $m \times 3$ configuration matrix given by the anchor points:

$$\mathbf{B} = \begin{bmatrix} \mathbf{p}_1 & \mathbf{p}_2 & \cdots & \mathbf{p}_m \end{bmatrix}^T, \quad \mathbf{p}_j = \frac{\mathbf{I}^* \mathbf{r}_0^j}{\left| \mathbf{I}^* \mathbf{r}_0^j \right|}$$

Table 8.2: Parameters used in the simulation

$$
\left.
\begin{array}{l}
L_j = 2250 \\
C_{DT}^j = 0.3 \\
C_{DN}^j = 1 \\
C_{MN}^j = 1 \\
\rho_c^j = 5500 \\
\rho_0^j = 27.6 \\
d_j = 0.08 \\
E_j A_{0_j} = 230 \times 10^6
\end{array}
\right\} \quad j \in [1, 2, 3, 4]
$$

$$
\mathbf{v}_c(z, t) = \begin{bmatrix} -\cos(t/6875) \\ \sin(t/6875) \\ 0 \end{bmatrix} \qquad z \in [0, 1000]
$$

$$\rho_w = 1025$$

$$\mathbf{r}_0^1 = \begin{bmatrix} 2000 & 0 & 1000 \end{bmatrix}^T$$

$$\mathbf{r}_0^2 = \begin{bmatrix} 0 & 2000 & 1000 \end{bmatrix}^T$$

$$\mathbf{r}_0^3 = \begin{bmatrix} -2000 & 0 & 1000 \end{bmatrix}^T$$

$$\mathbf{r}_0^4 = \begin{bmatrix} 0 & -2000 & 1000 \end{bmatrix}^T$$

$$k_c = 2.5 \times 10^{-7}$$

Figure 8.12 shows commanded force from the DP-system compared with the thruster force. As expected, the thruster force is very small, which means that the tension controller follows the commanded force quite closely. Figure 8.13 shows the length of the cables with anchor points on the positive x-axis and positive y-axis. The length of the remaining two cables are in exact opposite phase to the ones shown.

8.6   Conclusions

In this chapter, we have developed a new finite element model for a cable suspended in water. Global existence and uniqueness of solutions of the truncated system is shown for a slightly simplified equation describing the motion of a cable having negligible added mass and supported by fixed end-points. Based on this, along with well known results on local existence and uniqueness of solutions for symmetrizable hyperbolic systems, we conjecture a global result for the initial-boundary value problem. The FEM model for the cable is assembled to give a model of a multi-cable mooring system, which, in turn, is coupled to a rigid body model of the floating vessel. The result is a coupled dynamical model of a moored vessel, which can be applied to applications such as turret-based moored ships, or tension leg platforms. By showing that the mapping from winding velocity of the cable to the upper end tension is passive, we conclude that passive controllers may be used for dynamic line tensioning in a mooring system. Numerical simulations
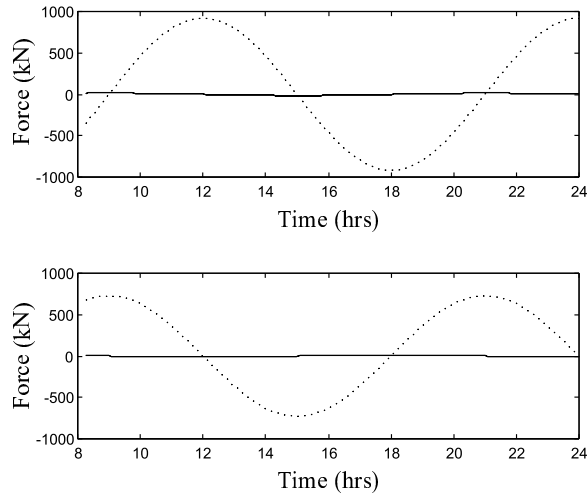
Figure 8.12: Commanded (dotted) and thruster forces (solid) in the x-direction (upper graph) and y-direction (lower graph).
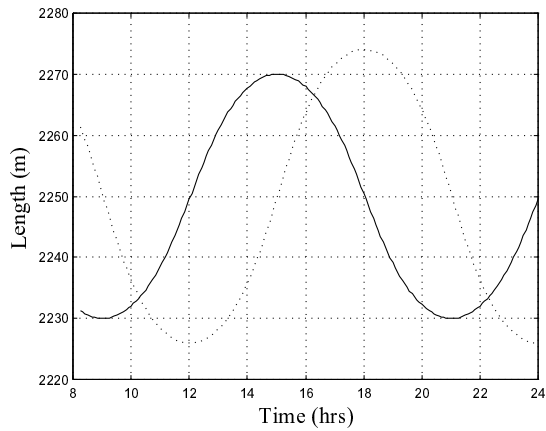
Figure 8.13: Length of cables with anchor point at positive x-axis (dotted) and positive y-axis (solid).

emphasize the importance of having a coupled dynamical model as opposed to using static cable models, and also demonstrate the potential for lowering fuel consumption by letting the mooring system compensate for constant and slowly varying environmental forces. Compensation of fast disturbances should be left to the thrusters, as tear and wear on the mooring cables will be a limitation on the actuation allowed from the tension controller.

$(A - LC)^T P + P(A - LC) = -Q$. Raghavan and Hedrick [41], and later Rajamani [42], provided systematic approaches to finding an observer gain matrix L that satisfies this condition. In two recent papers [5, 6], Arcak and Kokotović remove the global Lipschitz condition on f, and instead require a monotonic damping property to hold. As we will demonstrate, this damping property is of interest in offshore applications.

The papers by Arcak and Kokotović, and a recent paper by Loria and Panteley [36], are the main sources of motivation for this work. In [36], the authors present a separation principle for fully actuated Euler-Lagrange systems that can be transformed, via a global change of coordinates, into the following form

$$\dot{q} = J(q)\nu \tag{9.1}$$
$$M\dot{\nu} + v(q) = \tau \tag{9.2}$$

where q and ν are n-dimensional vectors of generalized positions and velocities, respectively, M is a symmetric positive definite and constant matrix, τ is the control input, and J is an $n \times n$ matrix as a function of q. In contrast to the numerous references made to ship dynamics in [36], the class of systems described by equations (9.1) and (9.2) does not include systems where $\dot{\nu}$ depends on ν. Clearly, this fact excludes offshore structures and ships from the class, since they will be subject to Coriolis and centripetal forces, as well as hydrodynamic drag. In general, these terms are nonlinear functions of the velocities. As already mentioned, nonlinearities in the unmeasured states are not trivial to include in the analysis, and the global output feedback tracking control problem has not been solved for general Euler-Lagrange systems (the global set-point regulation problem has been solved, though [12]). In the special case of one degree-of-freedom systems, Loria [33] presented the first explicit global solution to the problem. In [13], a more elegant solution to the one degree-of-freedom problem was presented. For higher order systems, a semi-global result has been achieved in [34].

We extend the class of systems considered in [36] by adding a term, nonlinear in the unmeasured states, that satisfies the monotone damping property employed for observer design in [6]. Although this property allows the unmeasured states to be raised to any power, it ensures that the *unboundedness observability* property of Mazenc et al. [38] holds. The observer-controller scheme proposed in this paper, renders the origin of the error dynamics uniformly globally asymptotically stable (UGAS). In a separate result, positive definiteness of the linear damping term, or alternatively, an additional assumption on the matrix $J(q)$, is exploited to obtain UGAS by means of a simplified control law.

This chapter is based on [3].

9.2 Problem Statement

In the Lyapunov analysis that follows, we will require a monotone damping property to hold for the function of the unmeasured states (denoted d in (9.6) below). More precisely, we require that the function $d : \mathbb{R}^n \to \mathbb{R}^n$ is locally Lipschitz and

satisfies

$$(x - y)^T P(d(x) - d(y)) \geq 0, \quad \forall x, y \in \mathbb{R}^n \tag{9.3}$$

where $P = P^T > 0$. For the special case when d is continuously differentiable, the following lemma provides a test for this property [40].

Lemma 9.1 (monotone damping property) *Suppose $d : \mathbb{R}^n \to \mathbb{R}^n$ satisfies*

$$P \left[\frac{\partial d}{\partial x} \right] + \left[\frac{\partial d}{\partial x} \right]^T P \geq 0, \quad \forall x \in \mathbb{R}^n \tag{9.4}$$

where $P = P^T > 0$. Then, (9.3) holds for d.

We consider systems in the following form

$$\dot{q} = J(q)\nu \tag{9.5}$$
$$M\dot{\nu} + D\nu + d(\nu) + v(q) = \tau \tag{9.6}$$

where $q, \nu \in \mathbb{R}^n$, M and D are constant matrices satisfying $M = M^T > 0$ and $D + D^T \geq 0$, respectively, and $d(\nu)$ satisfies (9.3) with $P = I$. As in [36] we will assume that $J : \mathbb{R}^n \to \mathbb{R}^{n \times n}$ has the following properties

Property 9.1 *$J(q)$ is invertible and satisfies $0 < k_j \leq \|J(q)\| \leq k_J$ for all $q \in \mathbb{R}^n$.*

Property 9.2 *$\frac{d}{dt} J(q) = \dot{J}(q, \dot{q})$ is globally Lipschitz in $\dot{q}$, uniformly in q, with Lipschitz constant L_j.*

Problem 9.1 (global output feedback tracking control) *Consider the system given by equations (9.5)–(9.6). Let a desired trajectory, $q_d : [t_0, \infty) \to \mathbb{R}^n$, be given, that has continuous first and second derivatives whose norms are bounded above by β_d. Find a controller*

$$\dot{\zeta} = f(t, \zeta, q)$$
$$\tau = h(t, \zeta, q)$$

such that $q \to q_d$, and $\dot{q} \to \dot{q}_d$, as $t \to \infty$.

9.3   Main Results

9.3.1   Observer Design

Copying equations (9.5)–(9.6) and adding output injection terms yield the following observer

$$\dot{\hat{q}} = J(q)\hat{\nu} + K_{o_1}\tilde{q} \tag{9.7}$$
$$M\dot{\hat{\nu}} + D\hat{\nu} + d(\hat{\nu}) + v(q) = \tau + M K_{o_2}(q)\tilde{q} \tag{9.8}$$

Chapter 9

Global Output Tracking Control of Ships

9.1 Introduction

In contrast to the well developed theory of linear systems, results for nonlinear systems do not apply in general, but are restricted to classes of systems for which certain structural properties can be exploited. For instance, when only a subset of the states are available for measurement, simple algebraic tests are available for linear systems, that, if confirmative, ensure that the problem of output feedback tracking is solvable by means of an observer in conjunction with a state feedback control law. Moreover, the observer and the control law can be designed independently, a fact which is referred to as the *separation principle* for linear systems. For nonlinear systems in general, even an estimate that converges exponentially fast to the actual state, does not guarantee stability of the closed loop system when used in a state feedback control law.

Among the first papers on observer design for systems with nonlinearities in the unmeasured states was one by Thau [51], whose results were later generalized by Kou et al. [30]. They considered systems in the form

$$\begin{aligned} \dot{x} &= Ax + g(t, u, y) + f(t, u, x) \\ y &= Cx \end{aligned}$$

where f is assumed to be globally Lipschitz in x with Lipschitz constant γ. They went on to construct an observer as follows

$$\dot{\hat{x}} = A\hat{x} + g(t, u, y) + f(t, u, \hat{x}) + L(y - C\hat{x})$$

where L is the observer gain matrix. Their main result stated that the estimate $\hat{x}$ will converge to the true state x, provided that $\gamma < \lambda_{\min}(Q)/2\lambda_{\max}(P)$, where P and Q are symmetric positive definite matrices satisfying the Lyapunov equation

with error dynamics, in terms of $\tilde{q} \triangleq q - \hat{q}$ and $\tilde{\nu} \triangleq \nu - \hat{\nu}$, as follows

$$\dot{\tilde{q}} = -K_{o_1}\tilde{q} + J(q)\tilde{\nu} \tag{9.9}$$
$$\dot{\tilde{\nu}} = -K_{o_2}(q)\tilde{q} - M^{-1}[D\tilde{\nu} + d(\nu) - d(\hat{\nu})] \tag{9.10}$$

The error dynamics (9.9)–(9.10) are time-varying, since the measurement q is time-varying. Now, consider the Lyapunov function candidate given by

$$V_o(t, \tilde{q}, \tilde{\nu}) = \frac{1}{2}\left(\tilde{q}^T P_o \tilde{q} + \tilde{\nu}^T M \tilde{\nu}\right) \tag{9.11}$$

where $P_o = P_o^T > 0$. Setting $K_{o_2}(q) = M^{-1}J(q)^T P_o$, the time derivative of V_o along the trajectories of (9.9)–(9.10) is

$$\dot{V}_o(t, \tilde{q}, \tilde{\nu}) = -\frac{1}{2}\tilde{q}^T(P_o K_{o_1} + K_{o_1}^T P_o)\tilde{q} + \tilde{q}^T P_o J(q)\tilde{\nu}$$
$$-\tilde{\nu}^T M K_{o_2}(q)\tilde{q} - \frac{1}{2}\tilde{\nu}^T\left(D + D^T\right)\tilde{\nu} - \tilde{\nu}^T[d(\nu) - d(\hat{\nu})]$$

Since d satisfies (9.3) with $P = I$, we get

$$\dot{V}_o(t, \tilde{q}, \tilde{\nu}) \le -\frac{1}{2}\tilde{q}^T(P_o K_{o_1} + K_{o_1}^T P_o)\tilde{q} - \frac{1}{2}\tilde{\nu}^T\left(D + D^T\right)\tilde{\nu} \tag{9.12}$$

Clearly, for $D + D^T$ positive definite, the origin $(\tilde{q}, \tilde{\nu}) = (0, 0)$ of (9.9)–(9.10) is UGES, provided that K_{o_1} is chosen such that $P_o K_{o_1} + K_{o_1}^T P_o$ is positive definite. Now, what happens if the damping and friction forces cannot be represented by a positive definite $D + D^T$, that is, $D + D^T$ is only positive *semi*-definite? This is, for instance, the case for offshore vessels and structures for which the hydrodynamic drag is modelled by Morison's equation, and for ships not possessing straight-line stability. In [36], UGAS and ULES of the origin $(\tilde{q}, \tilde{\nu}) = (0, 0)$ of (9.9)–(9.10) is shown by using Theorem 1 in [23] (also in [35]), under the assumption that the trajectories of (9.5)–(9.6) are uniformly bounded. The idea of this theorem is to decompose the system into one part, for which the origin is ULES, plus a perturbation whose norm is bounded, on any compact subset of the state space, by a linear function of $\|\tilde{q}\|$. Direct application of this theorem requires a global Lipschitz condition to hold for d, but in our case, d is only locally Lipschitz. A small modification of the theorem, taking (9.3) into account, resolves this problem.

Proposition 9.1 *Let $P_o = P_o^T > 0$, and suppose the observer gain matrices are chosen according to*

$$0 < P_o K_{o_1} + K_{o_1}^T P_o$$
$$K_{o_2}(q) = M^{-1}J(q)^T P_o$$

If the trajectories $\nu(t)$ are uniformly globally bounded, then the origin of (9.9)–(9.10) is uniformly globally asymptotically stable (UGAS) and uniformly locally exponentially stable (ULES). Moreover, if $D + D^T > 0$ then it is uniformly globally exponentially stable (UGES).

Proof. The UGES part of the proposition is clear from equations (9.11) and (9.12). We prove the UGAS/ULES part. In reference to Definition 3.3, we need to prove uniform global stability (UGS) and uniform attractivity. From equations (9.11) and (9.12), and by the positive definiteness of $P_o K_{o_1} + K_{o_1}^T P_o$, there exists a strictly positive constant c_1, such that

$$\dot{V}_o(t, \tilde{q}, \tilde{\nu}) \leq -c_1 \|\tilde{q}\|^2 \leq 0 \tag{9.13}$$

So the origin is UGS, which means that there exists a class $\mathcal{K}_\infty$ function, γ, such that $\|x(t)\| \leq \gamma(\|x(t_0)\|)$, where we have defined $x \triangleq (\tilde{q}, \tilde{\nu})$ to simplify notation. In order to prove uniform attractivity, we rewrite the system (9.9)–(9.10) as

$$\dot{x} = f(t, x) + g(t, x) \tag{9.14}$$

where

$$f(t, x) = \begin{bmatrix} -\tilde{q} + J(q)\tilde{\nu} \\ -M^{-1}J(q)^T\tilde{q} - M^{-1}D\tilde{\nu} - M^{-1}[d(\nu) - d(\hat{\nu})] \end{bmatrix}$$

and

$$g(t, x) = \begin{bmatrix} -K_{o_1}\tilde{q} + \tilde{q} \\ -M^{-1}J(q)^T P_o \tilde{q} + M^{-1}J(q)^T \tilde{q} \end{bmatrix}$$

We start by proving that, for any $r > 0$, the origin of $\dot{x} = f(t, x)$ is ULES for initial states belonging to B_r. Define $\omega \triangleq \gamma(r)$ and consider the Lyapunov function candidate $V_2 : [t_0, \infty) \times B_\omega \to \mathbb{R}_+$ defined by

$$V_2(t, x) = \frac{1}{2}\left(\tilde{q}^T\tilde{q} + \tilde{\nu}^T M\tilde{\nu}\right) - \varepsilon\tilde{q}^T J(q)\tilde{\nu} \tag{9.15}$$

Since $M = M^T > 0$, there exist constants c_a and c_b, with $c_a \geq c_b$, such that

$$c_b\|x\|^2 - \varepsilon\tilde{q}^T J(q)\tilde{\nu} \leq V_2(t, x) \leq c_a\|x\|^2 - \varepsilon\tilde{q}^T J(q)\tilde{\nu}$$

so, by imposing $\varepsilon \leq c_b/k_J$, we have that

$$\frac{c_b}{2}\|x\|^2 \leq V_2(t, x) \leq \frac{3c_a}{2}\|x\|^2, \quad \forall(t, x) \in [t_0, \infty) \times B_\omega \tag{9.16}$$

The time derivative of $V_2(t, x)$ along trajectories of $\dot{x} = f(t, x)$ is

$$
\begin{aligned}
\dot{V}_2(t, x) \leq\ & -\tilde{q}^T\tilde{q} + \varepsilon\tilde{q}^T J(q)M^{-1}J(q)^T\tilde{q} + \varepsilon\tilde{q}^T J(q)M^{-1}[d(\nu) - d(\hat{\nu})] \\
& + \varepsilon\tilde{q}^T J(q)M^{-1}D\tilde{\nu} - \varepsilon\tilde{q}^T \dot{J}(q, \dot{q})\tilde{\nu} + \varepsilon\tilde{\nu}^T J(q)^T\tilde{q} - \varepsilon\tilde{\nu}^T J(q)^T J(q)\tilde{\nu} \\
\leq\ & -\|\tilde{q}\|^2 - \varepsilon k_j^2\|\tilde{\nu}\|^2 + \varepsilon k_J^2\|M\|^{-1}\|\tilde{q}\|^2 + \varepsilon k_J\|M^{-1}\|\|d(\nu) - d(\hat{\nu})\|\|\tilde{q}\| \\
& + \left(\varepsilon k_J\|M^{-1}\|\|D\| + \varepsilon\|\dot{J}(q, \dot{q})\| + \varepsilon k_J\right)\|\tilde{q}\|\|\tilde{\nu}\|
\end{aligned}
$$

Notice that since d is locally Lipschitz, we can find a Lipschitz constant, L_{d_ω}, for d on the compact set B_ω. Thus, $\|d(\nu) - d(\hat{\nu})\| \leq L_{d_\omega}\|\tilde{\nu}\|$. Furthermore, since $\nu(t)$ is assumed to be UGB, there exists a constant, $b(\|\nu(t_0)\|)$, such that $\|\nu(t)\| \leq$

$b\left(\|\nu(t_0)\|\right)$. Thus, using Properties 9.1 and 9.2, we get the following bound on $\left\|\dot{J}(q,\dot{q})\right\|$

$$\left\|\dot{J}(q,\dot{q})\right\| \le L_j \left\|J(q)\nu\right\| \le L_j k_J b\left(\|\nu(t_0)\|\right) \triangleq \beta_j$$

Defining $c = k_J \left\|M^{-1}\right\| L_{d_\omega} + k_J \left\|M^{-1}\right\| \|D\| + \beta_j + k_J$, we get

$$\dot{V}_2(t,x) \le -\left(\frac{1}{2} - \varepsilon k_J^2 \|M\|^{-1}\right) \|\tilde{q}\|^2 - \frac{1}{4}\|\tilde{q}\|^2 - \frac{\varepsilon k_j^2}{2}\|\tilde{\nu}\|^2$$
$$-\frac{1}{2}\left[\begin{array}{c} \|q\| \\ \|\nu\| \end{array}\right]^T \left[\begin{array}{cc} \frac{1}{2} & -\frac{\varepsilon c}{2} \\ -\frac{\varepsilon c}{2} & \frac{\varepsilon k_j^2}{2} \end{array}\right] \left[\begin{array}{c} \|q\| \\ \|\nu\| \end{array}\right]$$

If we pick ε such that

$$\varepsilon \le \min\left\{\frac{c_b}{k_J}, \left(\frac{k_j}{c}\right)^2\right\}$$

then

$$\dot{V}_2(t,x) \le -c_2 \|x\|^2 \tag{9.17}$$

with

$$c_2 = \min\left(\frac{1}{4}, \frac{\varepsilon k_j^2}{2}\right)$$

It remains to show uniform attractivity of the full system (9.14). Consider the Lyapunov function candidate $\mathcal{V} : [t_0, \infty) \times B_\omega \to \mathbb{R}_+$ defined by $\mathcal{V}(t,x) \triangleq \mu V_o(t,x) + V_2(t,x)$ where $\mu > 0$ is to be specified later. From equations (9.11) and (9.16), it is clear that there exist constants c_a' and c_b', with $c_a' > c_b'$, such that

$$c_b' \|x\|^2 \le \mathcal{V}(t,x) \le c_a' \|x\|^2 \tag{9.18}$$

From equations (9.13), (9.14), and (9.17) we have

$$\dot{\mathcal{V}}(t,x) \le -c_1 \mu \|\tilde{q}\|^2 - c_2 \|x\|^2 + \left\|\frac{\partial V_2}{\partial x}(t,x)\right\| \|g(t,x)\| \tag{9.19}$$

Using Property 9.1 we can find a positive constant c_3, such that

$$\|g(q,\nu,t)\| \le c_3 \|\tilde{q}\| \tag{9.20}$$

Let $j_i(q)$ denote the ith column of $J(q)$, that is

$$J(q) = \left[\begin{array}{cccc} j_1(q) & j_2(q) & \cdots & j_n(q) \end{array}\right]$$

The Jacobian of $j_i(q)$, $\frac{\partial j_i(q)}{\partial q}$, is bounded uniformly in q, otherwise Property 9.2 would not hold. Thus, we can find a constant, $\beta_{\partial j}$, such that

$$\left\|\frac{\partial j_i(q)}{\partial q}\right\| \le \beta_{\partial j}, \quad \forall q \in \mathbb{R}^n$$

The Jacobian of $V_2(t, x)$ is

$$
\frac{\partial V_2}{\partial x}(t, x) = \left[\begin{array}{cc} \tilde{q}^T - \varepsilon \tilde{\nu}^T \frac{\partial}{\partial \tilde{q}}(J(\tilde{q}+\hat{q})^T \tilde{q}) & \tilde{\nu}^T M - \varepsilon \tilde{q}^T J(q) \end{array} \right]
$$

$$
= \left[\begin{array}{cc} \tilde{q}^T - \varepsilon \tilde{\nu}^T \left(J(q)^T + \left[\begin{array}{c} \tilde{q}^T \frac{\partial j_1(\tilde{q}+\hat{q})}{\partial \tilde{q}} \\ \tilde{q}^T \frac{\partial j_2(\tilde{q}+\hat{q})}{\partial \tilde{q}} \\ \vdots \\ \tilde{q}^T \frac{\partial j_n(\tilde{q}+\hat{q})}{\partial \tilde{q}} \end{array} \right] \right) & \tilde{\nu}^T M - \varepsilon \tilde{q}^T J(q) \end{array} \right]
$$

By noticing that

$$
\left\| \left[\begin{array}{c} \tilde{q}^T \frac{\partial j_1(\tilde{q}+\hat{q})}{\partial \tilde{q}} \\ \tilde{q}^T \frac{\partial j_2(\tilde{q}+\hat{q})}{\partial \tilde{q}} \\ \vdots \\ \tilde{q}^T \frac{\partial j_n(\tilde{q}+\hat{q})}{\partial \tilde{q}} \end{array} \right] \right\| \leq \sqrt{n} \beta_{\partial j} \|\tilde{q}\| \leq \sqrt{n} \beta_{\partial j} \omega
$$

and, by using Property 9.1, we get

$$
\left\| \frac{\partial V_2}{\partial x}(x, t) \right\|^2 \leq (1 + \varepsilon^2 k_J^2) \|\tilde{q}\|^2 + 2\varepsilon \left(k_J \|M\| + (k_J + \sqrt{n} \beta_{\partial j} \omega) \right) \|\tilde{q}\| \|\tilde{\nu}\|
$$
$$
+ \left(\|M\| + \varepsilon^2 (k_J + \sqrt{n} \beta_{\partial j} \omega)^2 \right) \|\tilde{\nu}\|^2
$$

Thus, we can find a positive constant c_4, such that

$$
\left\| \frac{\partial V_2}{\partial x}(x, t) \right\| \leq c_4 \|x\| \tag{9.21}
$$

Inserting the bounds (9.20) and (9.21), into (9.19), we get

$$
\dot{\mathcal{V}}(t, x) \leq -c_1 \mu \|\tilde{q}\|^2 - c_2 \|x\|^2 + c_3 c_4 \|x\| \|\tilde{q}\|
$$
$$
= -c_1 \mu \|\tilde{q}\|^2 - \frac{c_2}{2} \|x\|^2 + \frac{(c_3 c_4)^2}{2c_2} \|\tilde{q}\|^2 - (\sqrt{\frac{c_2}{2}} \|x\| - \frac{c_3 c_4}{\sqrt{2c_2}} \|\tilde{q}\|)^2
$$
$$
\leq -\left(c_1 \mu - \frac{(c_3 c_4)^2}{2c_2} \right) \|\tilde{q}\|^2 - \frac{c_2}{2} \|x\|^2 \tag{9.22}
$$

Thus, for sufficiently large μ, $\dot{\mathcal{V}}(t, x)$ is negative definite on $[t_0, \infty) \times B_\omega$. From equation (9.18), and the last term in equation (9.22), we conclude that the origin $x = 0$ of (9.14) is ULES, that is, there exist strictly positive constants k and γ_3 such that

$$
\|x(t)\| \leq k \|x(t_0)\| e^{-\gamma_3(t-t_0)}
$$

for all $t \geq t_0$ and $x(t_0) \in B_r$. Now, given $\epsilon > 0$ (recall that $r > 0$ is already given), we have that (3.16) holds with $T = \ln\left(\frac{\epsilon}{kr}\right)/\gamma_3$. ∎

Under an additional assumption on $J(q)$, and by following the lines of [5], we can find an observer that renders the error dynamics UGES, even in the case of only positive semi-definite $D + D^T$.

Assumption 9.1 *A locally Lipschitz function,* $\phi : \mathbb{R}^n \to \mathbb{R}^n$, *is known, such that*

$$\frac{\partial \phi}{\partial q}(q) J(q) + \left(\frac{\partial \phi}{\partial q}(q) J(q) \right)^T > \epsilon I, \quad \forall q \in \mathbb{R}^n$$

for some $\epsilon > 0$.

We will use the knowledge of such a function to perform a change of variables. Define the new variable as follows

$$y = \nu - \phi(q)$$

where ϕ satisfies Assumption 9.1. Writing the system (9.5)–(9.6) in terms of q and y, we obtain

$$\dot{q} = J(q)y + J(q)\phi(q)$$

$$\dot{y} = -M^{-1}\left(D(y + \phi(q)) + d(y + \phi(q)) + v(q) - \tau \right) - \frac{\partial \phi}{\partial q}(J(q)y + J(q)\phi(q))$$

Now, consider the observer

$$\dot{\hat{q}} = J(q)\hat{y} + J(q)\phi(q) + K_{o_1}\tilde{q} \tag{9.23}$$

$$\dot{\hat{y}} = -M^{-1}\left(D(\hat{y} + \phi(q)) + d(\hat{y} + \phi(q)) + v(q) - \tau \right)$$
$$\qquad - \frac{\partial \phi}{\partial q}(J(q)\hat{y} + J(q)\phi(q)) + K_{o_2}(q)\tilde{q} \tag{9.24}$$

with error dynamics, in terms of $\tilde{q} \triangleq q - \hat{q}$ and $\tilde{y} \triangleq y - \hat{y}$, as follows

$$\dot{\tilde{q}} = -K_{o_1}\tilde{q} + J(q)\tilde{y} \tag{9.25}$$

$$\dot{\tilde{y}} = -K_{o_2}(q)\tilde{q}$$
$$\qquad -M^{-1}D\tilde{y} - M^{-1}\left[d(y + \phi(q)) - d(\hat{y} + \phi(q)) \right] - \frac{\partial \phi}{\partial q}J(q)\tilde{y} \tag{9.26}$$

Proposition 9.2 *Suppose the observer gain matrices in (9.23)–(9.24) are chosen as in Proposition 9.1. If Assumption 9.1 holds, then the origin of (9.25)–(9.26) is uniformly globally exponentially stable (UGES).*

Proof. Using the Lyapunov function candidate $V_o(t, \tilde{q}, \tilde{y}) = \frac{1}{2}\left(\tilde{q}^T P_o \tilde{q} + \tilde{y}^T M \tilde{y} \right)$, and setting $K_{o_2}(q) = M^{-1}J(q)^T P_o$, the time derivative of V_o along the trajectories of (9.25)–(9.26) is

$$\dot{V}_o(t, \tilde{q}, \tilde{y}) = -\frac{1}{2}\tilde{q}^T \left(P_o K_{o_1} + K_{o_1}^T P_o \right)\tilde{q} + \tilde{q}^T P_o J(q)\tilde{y} - \tilde{y}^T J(q)^T P_o \tilde{q}$$

$$\qquad -\frac{1}{2}\tilde{y}^T \left(D + D^T \right)\tilde{y} - \tilde{y}^T \left[d(y + \phi(q)) - d(\hat{y} + \phi(q)) \right]$$

$$\qquad\qquad\qquad -\frac{1}{2}\tilde{y}^T \left(\frac{\partial \phi}{\partial q}J(q) + \left(\frac{\partial \phi}{\partial q}J(q) \right)^T \right)\tilde{y}$$

Since d satisfies (9.3) with $P = I$, we get

$$\dot{V}_o(t, \tilde{q}, \tilde{\nu}) \leq -\frac{1}{2}\tilde{q}^T(P_oK_{o_1} + K_{o_1}^T P_o)\tilde{q} - \frac{1}{2}\tilde{y}^T\left(\frac{\partial\phi}{\partial q}J(q) + \left(\frac{\partial\phi}{\partial q}J(q)\right)^T\right)\tilde{y}$$

In view of Assumption 9.1, UGES of the origin $(\tilde{q}, \tilde{y}) = 0$ of (9.25)–(9.26) follows from standard results [29, Corollary 3.4]. ∎

9.3.2 Controller Design

Now, moving on to controller design, we define the virtual tracking error as

$$\hat{z} \triangleq J(q)\hat{\nu} - \dot{q}_d + K_p q_e$$

where $q_e \triangleq q - q_d$ and $K_p + K_p^T > 0$. Then,

$$\dot{q}_e = -K_p q_e + \hat{z} + J(q)\tilde{\nu} \tag{9.27}$$

and

$$\dot{\hat{z}} = \dot{J}(q, \dot{q})\hat{\nu} + J(q)M^{-1}\left(\tau + MK_{o_2}(q)\tilde{q} - D\hat{\nu} - d(\hat{\nu}) - v(q)\right)$$
$$- \ddot{q}_d + K_p\left(J(q)\nu - \dot{q}_d\right) \tag{9.28}$$

The theorem below covers the general case, that is, when $D + D^T$ is only positive semi-definite, and we cannot find a ϕ that satisfies Assumption 9.1. In this case, we achieve UGAS of the origin of the error dynamics.

Theorem 9.1 *Let $P_o = P_o^T > 0$, and set $K_{o_2} = M^{-1}J(q)^T P_o$. Suppose that the matrices K_{o_1}, K_p, and K_d, are chosen such that*

$$P_oK_{o_1} + K_{o_1}^T P_o > 0$$
$$K_p = K_p^T > 0$$
$$K_d = K_d^T > 0$$

Then, the nonlinear output feedback tracking controller

$$\tau = MJ(q)^{-1}\left\{-q_e - \left(K_d + \|q_e\|^2 I + \|\hat{z}\|^2 I\right)\hat{z} + \ddot{q}_d + K_p\dot{q}_d\right.$$
$$\left.-K_pJ(q)\hat{\nu} - \dot{J}(q, J(q)\hat{\nu})\hat{\nu}\right\}$$
$$+ v(q) + D\hat{\nu} + d(\hat{\nu}) \tag{9.29}$$

renders the origin $\xi = (\tilde{q}, \tilde{\nu}, q_e, \hat{z}) = 0$ of the error dynamics (9.9)–(9.10) and (9.27)–(9.28) uniformly globally asymptotically stable (UGAS).

Proof. Inserting the control law (9.29) into (9.28), we obtain

$$\dot{\hat{z}} = -q_e - \left(K_d + \|q_e\|^2 I + \|\hat{z}\|^2 I\right)\hat{z}$$
$$+ J(q)M^{-1}J(q)^T P_0\tilde{q} + \left[\dot{J}(q, J(q)\nu) - \dot{J}(q, J(q)\hat{\nu})\right]\hat{\nu}$$
$$+ K_pJ(q)\tilde{\nu} \tag{9.30}$$

The derivative of $V_c(t, q_e, \hat{z}) = \frac{1}{2} \|q_e\|^2 + \frac{1}{2} \|\hat{z}\|^2$ along the trajectories of (9.27) and (9.30) is

$$
\begin{aligned}
\dot{V}_c(t, q_e, \hat{z}) &= -q_e^T K_p q_e - \hat{z}^T K_d \hat{z} - \|q_e\|^2 \|\hat{z}\|^2 - \|\hat{z}\|^4 \\
&\quad + \hat{z}^T J(q) M^{-1} J(q)^T P_0 \tilde{q} + \hat{z}^T \left[\dot{J}(q, J(q)\nu) - \dot{J}(q, J(q)\hat{\nu}) \right] \hat{\nu} \\
&\quad + \hat{z}^T K_p J(q) \tilde{\nu} + q_e^T J(q) \tilde{\nu}
\end{aligned}
\tag{9.31}
$$

Using Properties 9.1 and 9.2, we get

$$
\hat{z}^T \left[\dot{J}(q, J(q)\nu) - \dot{J}(q, J(q)\hat{\nu}) \right] \hat{\nu} \leq L_j k_J \|\hat{z}\| \|\tilde{\nu}\| \|\hat{\nu}\|
\tag{9.32}
$$

and, since $J(q)\hat{\nu} = \hat{z} + \dot{q}_d - K_p q_e$, we get

$$
\|\hat{\nu}\| \leq k_{J^{-1}} \|\hat{z}\| + k_{J^{-1}} \|K_p\| \|q_e\| + k_{J^{-1}} \beta_d
\tag{9.33}
$$

where $k_{J^{-1}}$ is an upper bound on $\|J(q)^{-1}\|$ (which exists by Property 9.1). Inequalities (9.32) and (9.33) imply

$$
\hat{z}^T \left[\dot{J}(q, J(q)\nu) - \dot{J}(q, J(q)\hat{\nu}) \right] \hat{\nu} \leq L_j k_J k_{J^{-1}} \left(\|\hat{z}\| + \|K_p\| \|q_e\| + \beta_d \right) \|\hat{z}\| \|\tilde{\nu}\|
\tag{9.34}
$$

Substitution of inequality (9.34), along with the inequalities

$$
\begin{aligned}
\hat{z}^T J(q) M^{-1} J(q)^T P_0 \tilde{q} &\leq k_J^2 \|M^{-1}\| \|P_0\| \|\hat{z}\| \|\tilde{q}\| \tag{9.35} \\
\hat{z}^T K_p J(q) \tilde{\nu} &\leq k_J \|K_p\| \|\hat{z}\| \|\tilde{\nu}\| \tag{9.36} \\
q_e^T J(q) \tilde{\nu} &\leq k_J \|q_e\| \|\tilde{\nu}\| \tag{9.37}
\end{aligned}
$$

into equation (9.31), yields

$$
\begin{aligned}
\dot{V}_c \leq\; &-\frac{1}{2} q_e^T K_p q_e - \frac{1}{2} \hat{z}^T K_d \hat{z} + \left(-\frac{1}{4} \lambda_{\min}(K_d) \|\hat{z}\|^2 + k_J^2 \|M^{-1}\| \|P_0\| \|\hat{z}\| \|\tilde{q}\| \right) \\
&+ \left(-\|\hat{z}\|^4 + L_j k_J k_{J^{-1}} \|\hat{z}\|^2 \|\tilde{\nu}\| \right) \\
&+ \left(-\|q_e\|^2 \|\hat{z}\|^2 + L_j k_J k_{J^{-1}} \|K_p\| \|q_e\| \|\hat{z}\| \|\tilde{\nu}\| \right) \\
&+ \left(-\frac{1}{2} \lambda_{\min}(K_p) \|q_e\|^2 + k_J \|q_e\| \|\tilde{\nu}\| \right) \\
&+ \left(-\frac{1}{4} \lambda_{\min}(K_d) \|\hat{z}\|^2 + (L_j k_J k_{J^{-1}} \beta_d + k_J \|K_p\|) \|\hat{z}\| \|\tilde{\nu}\| \right)
\end{aligned}
$$

where $\lambda_{\min}(K_?)$ denotes the smallest eigenvalue of the matrix $K_?$. Upon completion of squares, one can find a constant c such that

$$
\dot{V}_c(t, q_e, \hat{z}) \leq -\frac{1}{2} q_e^T K_p q_e - \frac{1}{2} \hat{z}^T K_d \hat{z} + c \|(\tilde{q}, \tilde{\nu})\|^2
\tag{9.38}
$$

which proves, using standard results [29, Theorem 5.2], that the $(q_e, \hat{z})$-subsystem is ISS with input $(\tilde{q}, \tilde{\nu})$. From the proof of Proposition 9.1, $\|(\tilde{q}, \tilde{\nu})\|$ is UGB, so

it follows from (9.38) that q_e and $\hat{z}$ are UGB. Therefore, ν is UGB. The theorem now follows from [29, Lemma 5.6] along with Proposition 9.1.　　■

In the control law (9.29) of Theorem 9.1, the variables q_e and $\hat{z}$ are raised to the third power in order to dominate the estimation error. This may be undesirable due to practical issues such as measurement noise, saturation in the actuators, and unmodelled actuator dynamics. The next result covers the case when an exponentially convergent observer is available, in which case we can achieve UGAS of the origin of the overall system with less control effort. Moreover, we achieve exponential convergence to any ϵ-neighborhood of the origin. Before we state the theorem, we need the following lemma.

Lemma 9.2 *Let $x = 0$ be an equilibrium point for the nonlinear system*

$$\dot{x} = f(t, x), \qquad x(t_0) = x_0 \tag{9.39}$$

where $f : [t_0, \infty) \times \mathbb{R}^n \to \mathbb{R}^n$ is piecewise continuous in t and locally Lipschitz in x. Let $V : [t_0, \infty) \times \mathbb{R}^n \to \mathbb{R}_+$ be a continuously differentiable function such that

$$k_1 \|x\|^c \quad \leq \quad V(t, x) \leq k_2 \|x\|^c \tag{9.40}$$

$$\frac{\partial V}{\partial t} + \frac{\partial V}{\partial x} f(t, x) \quad \leq \quad -k_3 \|x\|^c + g(\|x\|) \sigma(\|x(t_0)\|, t - t_0) \tag{9.41}$$

$\forall t \geq t_0$, $\forall x \in \mathbb{R}^n$, where k_1, k_2, k_3, and c, are strictly positive constants, $g : \mathbb{R}_+ \to \mathbb{R}$ is continuous, and σ is a class $\mathcal{KL}$ function satisfying

$$\int_{t_0}^{\infty} \sigma(r, s)\, ds \leq \sigma_\infty r \tag{9.42}$$

for some constant σ_∞. Suppose that there exist constants $k > 0$, and $r \geq 0$ such that $k \|x\|^c \geq g(\|x\|)$, $\forall \|x\| \geq r$. Then, the equilibrium point $x = 0$ of (9.39) is uniformly globally asymptotically stable (UGAS).

Proof. First we show that solutions can be continued for all time. From (9.40) and (9.41), we get

$$\|x(t)\|^c \quad \leq \quad \frac{V(t, x)}{k_1} \leq \frac{V(t_0, x_0)}{k_1} + \frac{1}{k_1} \int_{t_0}^{t} \dot{V}(\tau, x)\, d\tau \tag{9.43}$$

$$\leq \quad \frac{k_2}{k_1} \|x_0\|^c + \frac{1}{k_1} \int_{t_0}^{t} g(\|x\|) \sigma(\|x_0\|, t - t_0)\, d\tau$$

Define

$$\beta_r = \sup_{\|x\| < r} g(\|x\|)$$

By continuity of g on $\mathbb{R}_+$, β_r is finite. We then get

$$\|x(t)\|^c \leq \frac{k_2}{k_1} \|x_0\|^c + \frac{\beta_r \sigma_0}{k_1} (t - t_0) + \int_{t_0}^t \frac{k\sigma_0}{k_1} \|x(\tau)\|^c \, d\tau$$

where we have set $\sigma_0 = \sigma(\|x_0\|, 0)$, and used the fact that $k\|x\|^c \geq g(\|x\|)$ for sufficiently large $\|x\|$. Using Gronwall's inequality [29, Lemma 2.1], it follows that

$$\|x(t)\|^c \leq \frac{k_2}{k_1} \|x_0\|^c + \frac{\beta_r \sigma_0}{k_1} (t - t_0)$$
$$+ \frac{k\sigma_0}{k_1} \left(\frac{k_2}{k_1} \|x_0\|^c (t - t_0) + \frac{\beta_r \sigma_0}{2k_1} (t - t_0)^2 \right) e^{\frac{k\sigma_0}{k_1}(t - t_0)}$$

which shows that solutions exist for all $t \geq t_0$. We proceed to show that the solutions are in fact bounded. Since $\sigma \in \mathcal{KL}$ there exists a time $t_* \geq t_0$, dependent on the initial state, such that $\sigma(\|x_0\|, t_* - t_0) < \frac{k_3}{2k}$. Thus, we get

$$\dot{V} \leq -k_3 \|x\|^c + \frac{k_3 g(\|x\|)}{2k} \leq -\frac{k_3}{2} \|x\|^c, \ \forall \|x\| \geq r, \ \forall t > t_*$$

Again we have used the fact that $k\|x\|^c \geq g(\|x\|)$ for sufficiently large $\|x\|$. This shows that the set $\mathcal{S} = \{x : \|x\| \leq r\}$ is globally attractive, that is, the distance between x and $\mathcal{S}$ tends to 0 as $t \to \infty$, for all initial states x_0. Thus, boundedness of solutions follows. We finish the proof by showing uniform attractivity. Since the solutions are bounded, given β, there exists $\beta_b > 0$, such that for all $\|x_0\| < \beta$, $\|x(t)\| < \beta_b$ for all $t > t_0$. Now, define

$$\beta_g = \sup_{\|x\| < \beta_b} g(\|x\|)$$

By continuity of g on $\mathbb{R}_+$, β_g is finite. From (9.40)–(9.41), and (9.43), we get

$$\|x(t)\|^c \leq \frac{k_2}{k_1} \|x_0\|^c + \int_{t_0}^t \left[-\frac{k_3}{k_1} \|x(\tau)\|^c + \frac{1}{k_1} g(\|x(\tau)\|) \sigma(\|x_0\|, \tau - t_0) \right] d\tau$$

$$\leq \frac{k_2}{k_1} \|x_0\|^c + \int_{t_0}^t \left[-\frac{k_3}{k_1} \|x(\tau)\|^c + \frac{\beta_g}{k_1} \sigma(\|x_0\|, \tau - t_0) \right] d\tau$$

$$\leq \frac{k_2}{k_1} \beta^c + \frac{\beta_g \sigma_\infty \beta}{k_1} + \int_{t_0}^t \left[-\frac{k_3}{k_1} \|x(\tau)\|^c \right] d\tau$$

where we have used (9.42) in the last step. Using Gronwall's inequality, it follows that

$$\|x(t)\|^c \leq \left(\frac{k_2}{k_1} \beta^c + \frac{\beta_g \sigma_\infty \beta}{k_1} \right) e^{-\frac{k_3}{k_1}(t - t_0)}$$

and finally that

$$\|x(t)\| \le \left(\frac{k_2}{k_1} \beta^c + \frac{\beta_g \sigma_\infty \beta}{k_1} \right)^{\frac{1}{c}} e^{-\frac{k_3}{ck_1}(t-t_0)} \tag{9.44}$$

■

Theorem 9.2 *Let* $P_o = P_o^T > 0$ *be a symmetric, positive definite matrix, and set* $K_{o_2} = M^{-1}J(q)^T P_o$. *Suppose that the matrices* K_{o_1}, K_p, *and* K_d, *are chosen such that*

$$\begin{aligned} P_o K_{o_1} + K_{o_1}^T P_o &> 0 \\ K_p &= K_p^T > 0 \\ K_d &= K_d^T > 0 \end{aligned}$$

If Assumption 9.1 holds (respectively, $D + D^T$ *is positive definite), then, the nonlinear output feedback tracking controller*

$$\tau = MJ(q)^{-1} \left\{ -q_e - K_d\hat{z} + \ddot{q}_d + K_p\dot{q}_d - K_pJ(q)\hat{\nu} - \dot{J}(q, J(q)\hat{\nu})\hat{\nu} \right\}$$
$$+ v(q) + D\hat{\nu} + d(\hat{\nu}) \tag{9.45}$$

renders the origin $\xi = (\tilde{q}, \tilde{y}, q_e, \hat{z}) = 0$ *(respectively,* $\xi = (\tilde{q}, \tilde{\nu}, q_e, \hat{z}) = 0$*) of the error dynamics (9.25)–(9.26) (respectively, (9.9)–(9.10)) and (9.27)–(9.28) uniformly globally asymptotically stable (UGAS).*

Proof. Inserting the control law (9.45) into (9.28), we obtain

$$\dot{\hat{z}} = -q_e - K_d\hat{z} + J(q)M^{-1}J(q)^T P_0\tilde{q} + \left[\dot{J}(q, J(q)\nu) - \dot{J}(q, J(q)\hat{\nu}) \right] \hat{\nu} + K_pJ(q)\tilde{\nu} \tag{9.46}$$

The derivative of $V_c(t, q_e, \hat{z}) = \frac{1}{2}\|q_e\|^2 + \frac{1}{2}\|\hat{z}\|^2$ along the trajectories of (9.27) and (9.46) is

$$\begin{aligned} \dot{V}_c(t, q_e, \hat{z}) &= -q_e^T K_p q_e - \hat{z}^T K_d\hat{z} + \hat{z}^T J(q)M^{-1}J(q)^T P_0\tilde{q} \\ &\quad + \hat{z}^T \left[\dot{J}(q, J(q)\nu) - \dot{J}(q, J(q)\hat{\nu}) \right] \hat{\nu} \\ &\quad + \hat{z}^T K_p J(q)\tilde{\nu} + q_e^T J(q)\tilde{\nu} \end{aligned} \tag{9.47}$$

As in the proof of Theorem 9.1, substitution of inequalities (9.34), and (9.35)-(9.37) into equation (9.47), and noticing that $\|\hat{z}\| \le \|\xi\|$ and $\|q_e\| \le \|\xi\|$, yields

$$\dot{V}_c \le -q_e^T K_p q_e - \hat{z}^T K_d\hat{z} + \left(c_1\|\xi\| + c_2\|\xi\|^2 \right) \|(\tilde{q}, \tilde{\nu})\|$$

where we have defined

$$\begin{aligned} c_1 &\triangleq k_J \left(k_J \|M^{-1}\| \|P_0\| + L_j k_{J^{-1}} \beta_d + \|K_p\| + 1 \right) \\ c_2 &\triangleq L_j k_J k_{J^{-1}} (1 + \|K_p\|) \end{aligned}$$

In view of Proposition 9.2 (respectively, the UGES part of Proposition 9.1), the positive definiteness of K_p and K_d, ensures the existence of a strictly positive constant c, such that the time derivative of $V = V_o + V_c$ is bounded above as follows

$$\dot{V} \leq -c \left\| \xi \right\|^2 + \left(c_1 \left\| \xi \right\| + c_2 \left\| \xi \right\|^2 \right) \left\| (\tilde{q}, \tilde{\nu}) \right\|$$

Proposition 9.2 (respectively, the UGES part of Proposition 9.1) provides the following bound on $\left\| (\tilde{q}, \tilde{\nu}) \right\|$

$$\left\| (\tilde{q}, \tilde{\nu}) \right\| \leq k_1 \left\| (\tilde{q}(t_0), \tilde{\nu}(t_0)) \right\| e^{-\gamma(t-t_0)} \leq k_1 \left\| \xi(t_0) \right\| e^{-\gamma(t-t_0)}$$

where k_1 and γ are strictly positive constants. Thus, we get

$$\dot{V} \leq -c \left\| \xi \right\|^2 + g(\left\| \xi \right\|) \sigma(\left\| \xi(t_0) \right\|, t - t_0)$$

where we have defined

$$g(\rho) \triangleq c_1 \rho + c_2 \rho^2$$

and

$$\sigma(\rho, \tau) \triangleq k_1 \rho e^{-\gamma \tau}$$

Clearly, σ is integrable in its second argument on $\mathbb{R}_+$. Also, if we pick $r = 1$ and $k_2 = c_1 + c_2$, we have $g(\rho) \leq k_2 \rho^2$, for all $\rho \geq r$. Thus, we can apply Lemma 9.2 to conclude that the origin $\xi = 0$ is UGAS. ∎

Remark 9.1 *Notice from (9.44), that for any $\epsilon > 0$, we can find a constant k_ϵ, such that*

$$\left\| x(t) \right\| \leq k_\epsilon \left\| x(t_0) \right\| e^{-\frac{k_3}{ck_1}(t-t_0)}, \quad \forall \left\| x(t) \right\| > \epsilon$$

In other words, we have exponential convergence of the trajectories of (9.25)–(9.26) (respectively, (9.9)–(9.10)) and (9.27)–(9.28) to any ϵ-neighborhood of the origin.

Remark 9.2 *Notice that in both theorems above, a separation principle holds in the sense that the proposed controller, which clearly stabilizes the system when the full state is available, in conjunction with the proposed observer, renders the origin of the overall system UGAS. In addition, the controller gains and the observer gains can be chosen independently of each other.*

9.4   Examples

Example 9.1 *Consider the mass-spring-damper system*

$$m\ddot{x} + d_1 \dot{x} + d_2 \left| \dot{x} \right| \dot{x} + d_3 \left| \dot{x} \right|^2 \dot{x} + d_4 \left| \dot{x} \right|^3 \dot{x} + \cdots + d_n \left| \dot{x} \right|^{n-1} \dot{x} + k(x)x = u \quad (9.48)$$

where $m > 0$, d_1, d_2, d_3,...,$d_n \geq 0$, $n \in \mathbb{N}$, $k(x)$ is a spring constant (possibly nonlinear), and u is the control input. Defining $\nu = \dot{x}$, and $q = x$, (9.48) can be written in the form (9.5)-(9.6) with

$$J(q) = 1, \quad M = m, \quad D = d_1,$$
$$d(\nu) = d_2 |\nu| \nu + d_3 |\nu|^2 \nu + d_4 |\nu|^3 \nu + \cdots + d_n |\nu|^{n-1} \nu, \quad v(q) = k(q)q, \quad and \ \tau = u$$

It is clear that $J(q)$ satisfies Properties 9.1 and 9.2, and since $d/d\nu(|\nu|^i \nu) = (i+1)|\nu|^i \geq 0$ for all $\nu \in \mathbb{R}$ and for all $i \in 1, 2, \ldots, n$, $d(\nu)$ satisfies (9.3) by Lemma 9.1. Thus, Theorem 9.1 is applicable. Clearly, if $d_1 > 0$ then Theorem 9.2 is also applicable. In fact, Theorem 9.2, is applicable for $d_1 = 0$ as well, since Assumption 9.1 holds (pick $\phi(q) = q$).

Example 9.2 (omni-directional intelligent navigator (ODIN)) *ODIN is a spherical autonomous underwater vehicle developed at the Autonomous Systems Laboratory at the University of Hawaii [17]. Motion on a horizontal plane (constant depth) is governed by [28]*

$$\begin{aligned} M\dot{\xi} + C(\xi)\xi + D(\xi)\xi &= \tau \\ \dot{\eta} &= J(\eta)\xi \end{aligned}$$

where

$$M = \begin{bmatrix} 2m & 0 & 0 \\ 0 & 2m & 0 \\ 0 & 0 & \frac{8}{15}\pi\rho R^5 \end{bmatrix}, \quad C(\xi) = \begin{bmatrix} 0 & 0 & -2mv \\ 0 & 0 & 2mu \\ 2mv & -2mu & 0 \end{bmatrix}$$

$$D(\xi) = \begin{bmatrix} d_t |(u,v)| & 0 & 0 \\ 0 & d_t |(u,v)| & 0 \\ 0 & 0 & d_1 |r| + d_2 \end{bmatrix}, \quad J(\eta) = \begin{bmatrix} c\psi & -s\psi & 0 \\ s\psi & c\psi & 0 \\ 0 & 0 & 1 \end{bmatrix}$$

$\xi = [\ u \quad v \quad r\ ]^T$ is the velocity in body-fixed coordinates, $\eta = [\ x \quad y \quad \psi\ ]^T$ is the position and orientation in earth-fixed coordinates, and τ is the control input. $s\psi$ and $c\psi$ denote the sine of ψ and cosine of ψ, respectively. M is the mass matrix including hydrodynamic added mass, C is the Coriolis and centripetal matrix including hydrodynamic added mass, and D is the hydrodynamic damping matrix. m and R are the mass and radius of the ODIN, respectively. d_t, d_1 and d_2 are positive constants for the hydrodynamic damping forces, and ρ is the water density. This system fits directly into the form of (9.5)-(9.6) by setting $q = \eta$, $\nu = \xi$, $v(q) = 0$, and $d(\nu) = (C(\nu) + D(\nu))\nu$. $J(\eta)$ is orthogonal, and clearly satisfies Properties 1 and 2. However, $d(\xi)$ does not satisfy the condition of Lemma 9.1, and in particular, it can be shown that (9.3) does not hold. This problem is resolved by transforming the equation of motion into earth-fixed coordinates as follows

$$\begin{aligned} M_\eta &= J(\psi)MJ^T(\psi) = M \\ C_\eta(\dot{\eta}) &= J(\psi)\left[C(\xi) - MJ^T(\psi)\dot{J}(\psi) \right] J^T(\psi) = \begin{bmatrix} 0 & 2m\dot{\psi} & -2m\dot{y} \\ -2m\dot{\psi} & 0 & 2m\dot{x} \\ 2m\dot{y} & -2m\dot{x} & 0 \end{bmatrix} \end{aligned}$$

$$D_\eta\left(\eta,\dot{\eta}\right) = J(\psi)\left[D(\xi)\right]J^T(\psi)$$

$$= \begin{bmatrix} c^2\psi d_t\left|u\right| + s^2\psi d_t\left|v\right| & c\psi s\psi d_t\left|u\right| - s\psi c\psi d_t\left|v\right| & 0 \\ s\psi c\psi d_t\left|u\right| - s\psi c\psi d_t\left|v\right| & s^2\psi d_t\left|u\right| + c^2\psi d_t\left|v\right| & 0 \\ 0 & 0 & d_1\left|\dot{\psi}\right| + d_2 \end{bmatrix}$$

*where we have kept $u = \dot{x}c\psi + \dot{y}s\psi$ and $v = -\dot{x}s\psi + \dot{y}c\psi$ in the expression for D_η
for notational simplicity. Defining $q = \eta$, and $\nu = \dot{\eta}$, the elements of (9.5)–(9.6)
become*

$$J(q) = I, \quad M = \begin{bmatrix} 2m & 0 & 0 \\ 0 & 2m & 0 \\ 0 & 0 & \frac{8}{15}\pi\rho R^5 \end{bmatrix}, \quad D = \begin{bmatrix} 0 & 0 & 0 \\ 0 & 0 & 0 \\ 0 & 0 & d_2 \end{bmatrix}$$

$$d(q,\nu) = \left[C_\eta(\nu) + D_\eta\left(q,\nu\right)\right]\nu = \begin{bmatrix} c\psi d_t\left|u\right|u - s\psi d_t\left|v\right|v \\ s\psi d_t\left|u\right|u + c\psi d_t\left|v\right|v \\ d_1\left|\dot{\psi}\right|\dot{\psi} \end{bmatrix}, \quad v(q) = 0$$

*The fact that q appears in the expression for d, does not present a problem, since q
is measured. In order to apply Lemma 9.1, we need the Jacobian of d (with respect
to ν) which is*

$$\frac{\partial d}{\partial \nu} = \begin{bmatrix} 2c^2\psi d_t\left|u\right| + 2s^2\psi d_t\left|v\right| & 2s\psi c\psi d_t\left|u\right| - 2s\psi c\psi d_t\left|v\right| & 0 \\ 2s\psi c\psi d_t\left|u\right| - 2s\psi c\psi d_t\left|v\right| & 2s^2\psi d_t\left|u\right| + 2c^2\psi d_t\left|v\right| & 0 \\ 0 & 0 & 2d_1\left|\dot{\psi}\right| \end{bmatrix}$$

so we get

$$\left[\frac{\partial d}{\partial \nu}\right] + \left[\frac{\partial d}{\partial \nu}\right]^T$$

$$= \begin{bmatrix} 4c^2\psi d_t\left|u\right| + 4s^2\psi d_t\left|v\right| & 4s\psi c\psi d_t\left|u\right| - 4s\psi c\psi d_t\left|v\right| & 0 \\ 4s\psi c\psi d_t\left|u\right| - 4s\psi c\psi d_t\left|v\right| & 4s^2\psi d_t\left|u\right| + 4c^2\psi d_t\left|v\right| & 0 \\ 0 & 0 & 4d_1\left|\dot{\psi}\right| \end{bmatrix} \quad (9.49)$$

*Since all the principal submatrices of (9.49) have nonnegative determinants, (9.49)
is positive semi-definite for all $(\dot{x},\dot{y},\dot{\psi}) \in \mathbb{R}^3$ (and for all ψ). Therefore, by
Lemma 9.1, (9.3) holds for d with $P = I$. We can now apply Theorem 9.1.
D is not positive definite, but Assumption 9.1 holds (simply choose ϕ equal to the
identity on $\mathbb{R}^3$). Thus, we can also apply Theorem 9.2. Based on Theorem 9.2,
we construct the following controller*

$$\begin{bmatrix} \dot{\hat{q}} \\ \dot{\hat{y}} \end{bmatrix} = \begin{bmatrix} -K_{o_1} & I \\ -M^{-1}P_o & -(I+K) \end{bmatrix}\begin{bmatrix} \hat{q} \\ \hat{y} \end{bmatrix}$$

$$+ \begin{bmatrix} K_{o_1} + I & 0 & 0 & 0 \\ M^{-1}P_o - 2I - K - K_d K_p & I + K_d K_p & K & I \end{bmatrix}\begin{bmatrix} q \\ q_d \\ \dot{q}_d \\ \ddot{q}_d \end{bmatrix}$$
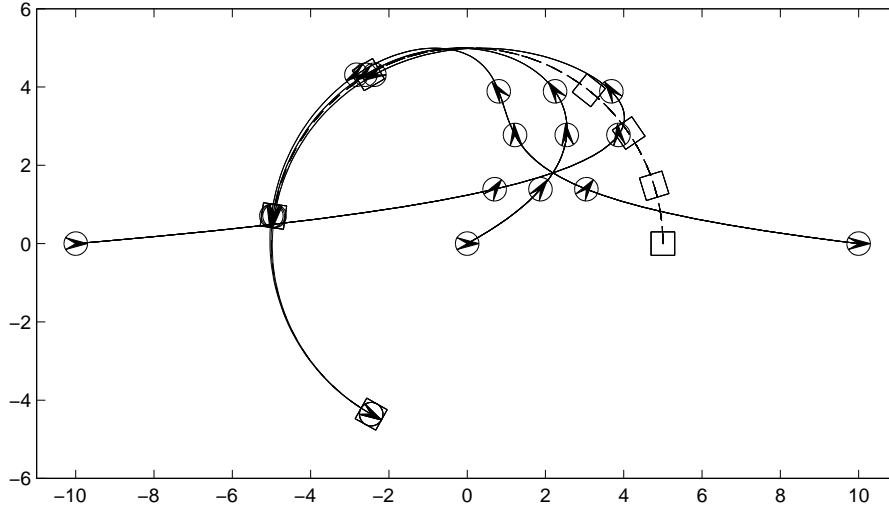
Figure 9.1: Simulation of output tracking of the ODIN. The desired trajectory (dashed line) is constant velocity of $1.5m/s$ on a circle with radius $5m$, starting in the location $(x, y) = (5, 0)$ at $t = 0$. The desired heading is in the direction of travel. Trajectories of the ODIN are shown for three different initial conditions: 1) $(x, y, \psi) = (-10, 0, 0)$; 2) $(x, y, \psi) = (0, 0, 0)$; and 3) $(x, y, \psi) = (10, 0, 0)$. The initial velocity is zero in all cases. The initial condition of the observer is zero position and zero velocity. A box is plotted at the desired position for seven time instances. At the same time instances, circles with arrows are plotted indicating the position and heading of the ODIN.

$$\tau = d(\hat{y} + q) + (D - MK)\hat{y}$$

$$+ \begin{bmatrix} D - M\left(I + K + K_d K_p\right) & M\left(I + K_d K_p\right) & MK & M \end{bmatrix} \begin{bmatrix} q \\ q_d \\ \dot{q}_d \\ \ddot{q}_d \end{bmatrix}$$

where $K = K_p + K_d$. Simulations (see figure 9.1) confirm that tracking is obtained for this test case. The numerical values used in the simulations are summarized below (the physical parameters for the ODIN model are taken from [28]).

$$R = 0.3m, \quad m = 150kg, \quad \rho = 1kg/m^3,$$

$$d_t = 48N\left(\frac{s}{m}\right)^2, \quad d_1 = 80Ns^2/m, \quad and \quad d_2 = 30Ns,$$

$$K_{o_1} = I, \quad P_o = I, \quad K_p = 10I, \quad K_d = 0.5I$$

9.5   Conclusions

In this chapter, we have addressed the problem of output feedback tracking control of a class of Euler-Lagrange systems subject to nonlinear dissipative loads. By imposing a monotone damping condition on the nonlinearities of the unmeasured states, the common restriction that the nonlinearities be globally Lipschitz is removed. The proposed observer-controller scheme renders the origin of the error dynamics uniformly globally asymptotically stable, in the general case. Under certain additional assumptions, the result continue to hold for a simplified control law that is less sensitive to noise and unmodelled phenomena.

Bibliography

[1] O. M. Aamo and T. I. Fossen, "Controlling line tension in thruster assisted mooring systems," *Proceedings of the 1999 IEEE International Conference on Control Applications*, Hawaii, USA, 1999.

[2] O. M. Aamo and T. I. Fossen, "Finite element modelling of moored vessels," *Mathematical and Computer Modelling of Dynamical Systems*, vol. 7, no. 1, pp. 47-75, 2001.

[3] O. M. Aamo, M. Arcak, T. I. Fossen, and P. V. Kokotović, "Global output tracking control of a class of Euler-Lagrange systems with monotonic nonlinearities in the velocities," *International Journal of Control*, vol. 74, no. 7, pp. 649-658, 2001.

[4] M. F. Aarset, J. P. Strand, and T. I. Fossen, "Nonlinear vectorial observer backstepping with integral action and wave filtering for ships," *Proceedings of the IFAC Conference on Control Applications in Marine Systems (CAMS'98)*, Fukuoka, Japan, 1998.

[5] M. Arcak and P. V. Kokotović, "Nonlinear observers: A circle criterion design," *Proceedings of the 38th IEEE Conference on Decision and Control*, Phoenix, Arizona, USA, 1999.

[6] M. Arcak and P. V. Kokotović, "Observer-based stabilization of systems with monotonic nonlinearities," *Asian Journal of Control*, vol. 1, pp. 42–48, 1999.

[7] J. G. Balchen, N. A. Jenssen, and S. Sælid, "Dynamic positioning using Kalman filtering and optimal control theory," *Proceedings of the IFAC/IFIP symposium*, Amsterdam, The Netherlands, 1976.

[8] J. G. Balchen, N. A. Jenssen, E. Mathisen, and S. Sælid, "A dynamic positioning system based on Kalman filtering and optimal control," *Modelling, Identification and Control*, vol. 1, no. 3, pp. 135–163, 1980.

[9] J. G. Balchen, N. A. Jenssen, and S. Sælid, "Dynamic positioning of floating vessels based on Kalman filtering and optimal control," *Proceedings of the 19th IEEE Conference on Decision and Control*, Albuquerque, New Mexico, USA, 1980.

[10] V. V. Beletsky and E. M. Levin, *Dynamics of space tether systems*, American Astronautical Society, 1993.

[11] R. Berger, *Instationäre Bewegung und Stabilitätsverhalten eindimensionaler Kontinua* (in german), Technical Report 189, Fortschritt-Berichte VDI, 1996.

[12] H. Berghuis and H. Nijmeijer, "Global regulation of robots using only position measurements," *Systems & Control Letters*, vol. 21, pp. 289–293, 1993.

[13] G. Besançon, "Simple global output feedback tracking control for one-degree-of-freedom Euler-Lagrange systems," *Proceedings of the IFAC Conference on Systems Structure and Control*, 1998.

[14] A. W. Brink, J. B. Van Den Brug, C. Ton, R. Wahab, and W. R. Van Wijk, *Automatic position and heading control of a drilling vessel*, Technical report, Inst. TNO for Mechanical Constructions, The Netherlands, 1972.

[15] J. J. Burgess, "Modeling of undersea cable installation with a finite difference method," *Proceedings of the first international offshore and polar engineering conference*, Edinburgh, UK, 1991.

[16] J. J. Burgess, "Bending stiffness in a simulation of undersea cable deployment," *Journal of Offshore and Polar Engineering*, vol. 3, no. 3, pp. 197–204, 1993.

[17] S. K. Choi, J. Yuh, and G. Y. Takashige, "Design of an omni-directional intelligent navigator," *in* J. Yuh (ed.), *Underwater Robotic Vehicles*, TSI Press, 1995.

[18] O. M. Faltinsen, *Sea Loads on Ships and Offshore Structures*, Cambridge University Press, 1990.

[19] T. I. Fossen, *Guidance and Control of Ocean Vehicles*, John Wiley & Sons, Inc., 1994.

[20] T. I. Fossen and Å. Grøvlen, "Nonlinear output feedback control of dynamically positioned ships using vectorial observer backstepping," *IEEE Transactions on Control Systems Technology*, vol. 6, no. 1, pp. 121–128, 1998.

[21] T. I. Fossen and J. P. Strand, *Nonlinear ship control*, Tech. Rep. 98-19-W, Dept. of Eng. Cybernetics, Norwegian Univ. of Sci. and Tech., 1998.

[22] T. I. Fossen and J. P. Strand, "Passive nonlinear observer design for ships using lyapunov methods: Full-scale experiments with a sypply vessel," *Automatica*, vol. 35, no. 1, pp. 3–16, 1999.

[23] T. I. Fossen, A. Loria, and A. Teel, "A theorem for UGAS and ULES of (passive) nonautonomous systems: Robust control of mechanical systems and ships," *International Journal of Robust and Nonlinear Control*, vol. 11, pp. 95–108, 2001.

[24] P. T. Fung and M. J. Grimble, "Dynamic ship positioning using self-tuning Kalman filter," *IEEE Transactions on Automatic Control*, vol. 28, no. 3, pp. 339–349, 1983.

[25] M. J. Grimble, R. J. Patton, and D. A. Wise, "The design of dynamic ship positioning control systems using stochastic optimal control theory," *Optimal Control Applications and Methods*, pp. 167–202, 1980.

[26] M. J. Grimble, R. J. Patton, and D. A. Wise, "Use of Kalman filtering techniques in dynamic ship positioning systems," *IEE proceedings, Control theory and applications*, pp. 93–102, 1980.

[27] M. A. Grosenbaugh, C. T. Howell, and S. Moxnes, S. "Simulating the dynamics of underwater vehicles with low-tension tethers," *International Journal of Offshore and Polar Engineering*, vol. 3, no. 3, pp. 213–218, 1993.

[28] E. Kardash, *Sonar-based navigation and control of autononmous underwater vehicles*, M.Sc. thesis, Department of Engineering Cybernetics, NTNU, Norway, 1998.

[29] H. K. Khalil, *Nonlinear Systems*, Prentice-Hall, Inc., 1996.

[30] S. R. Kou, D. L. Elliot, and T. J. Tarn, "Exponential observers for nonlinear dynamic systems," *Information and Control*, vol. 29, pp. 204–216, 1975.

[31] M. Krstić, I. Kanellakopoulos, P. V. Kokotović, *Nonlinear and Adaptive Control Design*, John Wiley & Sons, Inc., 1995.

[32] J. Lindahl and A. Sjöberg, *Dynamic analysis of mooring cables*, Technical Report 9, Chalmers University of Technology, 1983.

[33] A. Loria, "Global tracking control of one degree of freedom Euler-Lagrange systems without velocity measurements," *European Journal of Control*, vol. 2, pp. 144–151, 1996.

[34] A. Loria and H. Nijmeijer, "Bounded output feedback tracking control of fully actuated Euler-Lagrange systems," *Systems & Control Letters*, vol. 33, pp. 151–161, 1998.

[35] A. Loria, T. I. Fossen, and A. Teel, "UGAS and ULES of nonautonomous systems: Applications to integral control of ships and manipulators," *Proceedings of the European Control Conference*, Karlsruhe, Germany, 1999.

[36] A. Loria and E. Panteley, "A separation principle for a class of Euler-Lagrange systems," *in* H. Nijmeijer and T. I. Fossen (eds), *New Directions in Nonlinear Observer Design*, Springer-Verlag London, 1999.

[37] MARINTEK. *Riflex - Program Documentation*, SINTEF, 1995.

[38] F. Mazenc, L. Praly, and W. P. Dayawansa, "Global stabilization by output feedback: examples and counterexamples," *Systems & Control Letters*, vol. 23, pp. 119–125, 1994.

[39] H. Ormberg, I. J. Fylling, K. Larsen, and N. Sødal, "Coupled analysis of vessel motions and mooring and riser system dynamics," *Proceedings of the 16th International Conference on Offshore Mechanics and Arctic Engineering*, New York, USA, 1997.

[40] R. Ortega and W. C. Rheinboldt, *Iterative solutions of nonlinear equations in several variables*, Academic Press, New York, 1970.

[41] S. Raghavan and J. K. Hedrick, "Observer design for a class of nonlinear systems," *International Journal of Control*, vol. 59, pp. 515–528, 1994.

[42] R. Rajamani, "Observers for Lipschitz nonlinear systems," *IEEE Transactions on Automatic Control*, vol. 43, pp. 397–401, 1998.

[43] A. Robertsson and R. Johansson, "Comments on: Nonlinear output feedback control of dynamically positioned ships using vectorial observer backstepping," *IEEE Transactions on Control Systems Technology*, vol. 6, no. 3, pp. 439–441, 1998.

[44] S. Saelid, N. A. Jenssen, and J. G. Balchen, "Design and analysis of a dynamic positioning system based on Kalman filtering and optimal control," *IEEE Transactions on Automatic Control*, vol. 28, no. 3, pp. 331–339, 1983.

[45] A. J. Sørensen, S. I. Sagatun, and T. I. Fossen, "Design of a dynamic positioning system using model-based control," *Journal of Control Engineering Practice*, vol. 4, no. 3, 1996.

[46] J. P. Strand, A. J. Sørensen, and T. I. Fossen, "Modelling and control of thruster assisted position mooring systems for ships," *Proceedings of the IFAC Conference on Maneuvering and Control of Marine Craft*, pp. 160–165. IFAC, 1997.

[47] J. P. Strand, K. Ezal, T. I. Fossen, and P. V. Kokotović, "Nonlinear control of ships: A locally optimal design," *Proceedings of the IFAC NOLCOS'98*, Enschede, The Netherlands, 1998.

[48] J. P. Strand, *Nonlinear Position Control Systems Design for Marine Vessels*, PhD thesis, Dept. of Eng. Cybernetics, Norwegian Univ. of Sci. and Tech., June 1999.

[49] G. Strang and G. J. Fix, *An analysis of the finite element method*, Prentice-Hall, Inc., 1973.

[50] M. E. Taylor, *Partial Differential Equations III*, Springer-Verlag New York, Inc., 1996.

[51] F. E. Thau, "Observing the state of nonlinear dynamic systems," *International Journal of Control*, vol. 17, pp. 471–479, 1973.

[52] M. S. Triantafyllou, *Cable mechanics with marine applications, lecture notes*, Department of Ocean Engineering, Massachusetts Institute of Technology, Cambridge, MA 02139, USA, 1990.

Appendix A

Coefficients for the Ginzburg-Landau Equation

The numerical coefficients below are taken from [103, Appendix A], with modifications given by [84].

$$Re_c = 47 \tag{A.1}$$

$$x^t = 1.183 - 0.031i \tag{A.2}$$

$$\omega_0^t = 0.690 + 0.080i + (-0.00159 + 0.00447i)(Re - Re_c) \tag{A.3}$$

$$k_0^t = 1.452 - 0.844i + (0.00341 + 0.011i)(Re - Re_c) \tag{A.4}$$

$$\omega_{kk}^t = -0.292i \tag{A.5}$$

$$\omega_{xx}^t = 0.108 - 0.057i \tag{A.6}$$

$$k_x^t = 0.164 - 0.006i \tag{A.7}$$

$$\omega_0(x) = \omega_0^t + \frac{1}{2}\omega_{xx}^t \left(x - x^t\right)^2 \tag{A.8}$$

$$k_0(x) = k_0^t + k_x^t \left(x - x^t\right) \tag{A.9}$$

$$a_1(x) = -\omega_{kk}^t k_0(x) \tag{A.10}$$

$$a_2 = -\frac{1}{2}i\omega_{kk}^t \tag{A.11}$$

$$a_3 = -0.638 + 0.191i + (0.0132 - 0.00399i)\left(Re - Re_c\right) \tag{A.12}$$

$$a_4(x) = \left(\omega_0 + \frac{1}{2}\omega_{kk}^t k_0^2(x)\right)i \tag{A.13}$$

$$a_5 = -0.0225 + 0.0671i. \tag{A.14}$$

Based on these parameters, we obtain

$$a_{R_1}(x) = 0.242\,89 - 0.003212\left(Re - Re_c\right) + 1.752 \times 10^{-3}x \tag{A.15}$$

$$a_{I_1}(x) = 0.367\,39 + 0.00099572\left(Re - Re_c\right) + 4.788\,8 \times 10^{-2}x \tag{A.16}$$

$$a_{R_2} = -0.146 \tag{A.17}$$

$$a_{I_2} = 0 \tag{A.18}$$

$$a_{R_3} = -0.638 + 0.0132\,(Re - Re_c) \tag{A.19}$$

$$a_{I_3} = 0.191 - 0.00399\,(Re - Re_c) \tag{A.20}$$

$$
\begin{aligned}
a_{R_4}(x) = \; & 9.391\,7 \times 10^{-2} - 5.454\,1 \times 10^{-4}\,(Re - Re_c) \\
& -1.596\,8 \times 10^{-5}\,(Re - Re_c)^2 - 1.198\,5 \times 10^{-2}x \\
& +1.825\,7 \times 10^{-4}\,(Re - Re_c)\,x + 3.242\,2 \times 10^{-2}x^2
\end{aligned}
\tag{A.21}
$$

$$
\begin{aligned}
a_{I_4}(x) = \; & 0.457\,83 + 1.623\,0 \times 10^{-3}\,(Re - Re_c) \\
& +1.095\,3 \times 10^{-5}\,(Re - Re_c)^2 - 0.168\,04x \\
& +5.207\,9 \times 10^{-4}\,(Re - Re_c)\,x + 5.371\,3 \times 10^{-2}x^2
\end{aligned}
\tag{A.22}
$$

$$a_{R_5} = -0.0255 \tag{A.23}$$

$$a_{I_5} = 0.0671. \tag{A.24}$$